Surface Micromachined Widely Tunable VCSEL and OAM-Filter for Optical Data Transmission

Dem Fachbereich Elektrotechnik und Informationstechnik
der Technische Universität Darmstadt
zur Erlangung des akademischen Grades eines
Doktor-Ingenieurs (Dr.-Ing)
vorgelegte Dissertation

von

Sujoy Paul, M.Sc.

geboren am 01. Januar 1985
in Chittagong

Referent:	**Prof. Dr.-Ing. Franko Küppers**
Korreferent:	**Prof. Dr. rer. nat. Ulrich Lemmer**
Tag der Einreichung:	**30. April 2018**

D17
Darmstadt 2018

Paul, Sujoy: Surface Micromachined Widely Tunable VCSEL and OAM-Filter for Optical Data Transmission
Darmstadt, Technische Universität Darmstadt
Jahr der Veröffentlichung der Dissertation auf TUprints: 2019
URN: urn:nbn:de:tuda-tuprints-87996
Tag der mündlichen Prüfung: 29.04.2019
Veröffentlicht unter CC BY-SA 4.0 International
https://creativecommons.org/licenses/

Erklärung laut §9 PromO

Ich versichere hiermit, dass ich die vorliegende Dissertation allein und nur unter Verwendung der angegebenen Literatur verfasst habe. Die Arbeit hat bisher noch nicht zu Prüfungszwecken gedient.

Unterschrift: _____

Datum: _____

To my family

Acknowledgements

This doctoral thesis has been conducted during my engagement as a research associate at the Institute for Microwave engineering and Photonics (IMP) in Technische Universität Darmstadt, Germany.

I would like to acknowledge all the contributions that help me successfully accomplish my doctoral research. I must first express my gratitude towards my *Doktorvater* Prof. Franko Küppers for his continuous support throughout my research. He kept his trust in me, gave me the freedom in my research and most importantly, provided the financial support to implement my ideas. We had many interesting discussions regarding not only my research but on different paths of life. I hope this will continue in future also. I would also like to thank my coreferee Prof. Ulrich Lemmer for his insightful comments and encouragement.

I would like to mention the successful cooperation between the four partners (Vertilas GmbH, Adva optical networking, DEV systemtechnik and TU Darmstadt) within the framework *Verbundprojekts VCSEL-TRX* supported by the Federal Ministry of Education and Research, Germany. A significant portion of my doctoral thesis has been implemented within this project.

My sincere gratitude goes to Dr. Christian Gierl, who mentored me in the initial phase of my research, shared me his vast technological experience in the MEMS VCSEL field. I appreciate his great support during the MEMS fabrication and not least the enjoyable communication over the years.

I am grateful to Julijan Cesar in many ways. Staring from cleanroom processing to proof-reading this thesis, it is a long list. He always came up with helping hands with smiling face whenever I needed. Thank you, Julijan! I really enjoyed the long working hours with you in the cleanroom during the release of the tiny stubborn MEMS.

My heartfelt thanks goes to Dr. Vladimir Lyubopytov for the experiments regarding OAM-filters. I have learned a lot from the fruitful discussions. I would like to mention Dr. Pedro Martin for the efficient collaboration for the spectroscopy experiments. Special thanks to Mohammadreza Malekizandi and Dr. Quang Trung Le for the technical help during the fiber optic transmission experiments and Tanvir Haidar for the productive discussions about the linewidth measurements. My sincere gratitude goes to Dr. Andreas Molitor for conducting the polarization measurement in his setup. I am also thankful to Dr. Oktay Yilmazoglu for taking time to read my thesis, and to give valuable suggestions to make it better. Dr. Holger Maune was always helpful with his tremendous expertise in different measurements tools and techniques. I also thank Dr. Shihab Al-Daffai and Ahid Hajo for sharing lab instruments time to time. I would like to convey special thanks to all previous and present Photonics lab mates including Dr. Karolina Zogal, Dr. Estefania

Prior, Dr. Ali Emsia, Dr. Arkadi Chupuline, and Alla Jumma. It was fantastic experience to share the laboratory with all of you during my stay in Darmstadt. I am also grateful to all staffs at the IMP for their unfailing supports.

My sincere thanks to Niels Heermeier, who had conducted both his Bachelor and Master thesis under my supervision. I am tremendously benefited from your well-organized work.

Last but not the least, my gratitude to my parents, my siblings and brother in-law has no limit. They were always there when I needed them. I am especially thankful to my sister for always supporting me mentally not only during my research but my whole life. Anubha, the nice person I met halfway my research and eventually married her, fulfilled the missing part of my life. I sincerely thank you for being so loving, supportive, encouraging, and patient. Your faithful support during the final stage of the Doctoral research as well as the working phase in Switzerland is beyond appreciation. I am also grateful to my in-law parents who have supported me mentally along the way.

Sujoy Paul
Technische Universität Darmstadt
April 2018

Abstract

The implication of wavelength division multiplexed passive optical network (WDM-PON) is becoming more evident as the traffic demands of the mobile network operators keep increasing. It offers a cost-efficient solution to handle the bandwidth and latency requirements of the mobile fronthaul. The key component of such a WDM-PON system is a centralized wavelength-controlled tunable laser. The biggest challenge up to now is the lack of low-cost wideband 1550 nm tunable lasers with 10 Gbit/s transmission capacity. In the first part of this work, a widely-tunable microelectromechanical system vertical-cavity surface-emitting laser (MEMS VCSEL) is developed. The cost-efficient, directly-modulated laser can be utilized for 10 Gbit/s transmission over relevant reach. It also offers simplicity for wideband autonomous tuning. The device is suitable for applications including hot backup and fixed wavelength laser replacement for inventory reduction.

Within the framework of this work, a PECVD-deposited MEMS distributed Bragg reflector (DBR) mirror is surface-micromachined on top of a short-cavity active VCSEL structure. The MEMS-DBR consisting of SiN_x/SiO_y dielectric materials has a very high reflectivity with wide stopband. Wavelength tuning is realized by the electrothermal actuation of the MEMS electrode. The fabrication steps of the MEMS aiming for large volume production is discussed in detail. A comprehensive static and dynamic characterizations of MEMS VCSEL including far-field, linewidth, polarization behavior, modulation capacity and relative intensity noise is presented. The effect of the temperature change on its tuning behavior as well as on the static and dynamic performance is investigated. The obtained wavelength tuning range of more than 100 nm covers the complete telecom C-band (1530–1565 nm) and part of L-band (1565–1625 nm). A small-signal amplitude modulation bandwidth of up to 8.35 GHz is demonstrated for the center emission wavelength around 1550 nm. This enables to implement a directly-modulated MEMS VCSEL based back-to-back link at 10 Gbit/s data transmission for 76 nm tuning range. Also, quasi error-free 10 Gbit/s transmission over 40 km standard single-mode fiber for a tuning range of more than 60 nm validates its potential for the above mentioned novel WDM-PON system. Apart from optical communication, the scope of this tunable source is investigated in applications such as dispersion spectroscopy and tunable terahertz (THz) signal generation. Experimental validation of multi-species dispersion spectroscopy using MEMS VCSEL is presented for the first time in this work, where concurrent detection of acetylene (C_2H_2), hydrogen cyanide (HCN), and carbon monoxide (CO) is demonstrated.

The second part of the work constitutes demonstration and experimental validation of a novel optical component called MEMS orbital angular momentum (OAM) filter.

The filter consists of a micro-sized spiral phase plate (SPP) which is integrated to the MEMS-DBR of a Fabry-Pérot optical filter by means of direct laser writing. The on-chip devices are suitable for distinguishing different OAM modes for a broad tuning range around 1550 nm emission and considered as a compact, robust and cost-effective solution for simultaneous OAM- and WDM optical communications. The utilization of the OAM modes as an additional orthogonal basis of information carriers in both free space and optical fiber communication systems potentially enhances the transmission capacity tremendously. Four devices with OAM orders of 0 (i.e., no SPP on MEMS), 1, 2 and 3 have been investigated. They are capable of generating/receiving the OAM beam of corresponding order over a continuous tuning range of more than 30 nm, for which the designed SPPs work with high mode purity. The system performance is evaluated by multiplexing two wavelength- and two OAM channels. Error-free free-space transmission at 10 Gbit/s suggests that OAM-filters functioning over a wide wavelength range could be employed as an additional degree of freedom for increasing the capacity of free-space communication to a great extent.

Zusammenfassung

Die Verwirklichung eines passiven optischen Wellenlängenmultiplex-Netzwerks (WDM-PON) wird immer dringender, sobald die Datenanforderungen der Mobilfunknetzbetreiber weiter zunehmen. Es bietet eine kosteneffiziente Lösung, um die Bandbreiten- und Latenzanforderungen des mobilen Fronthauls zu erfüllen. Die Schlüsselkomponente eines solchen WDM-PON-Systems ist ein zentralisiert wellenlängengesteuerbarer Laser. Die größte Herausforderung ist bisher das Fehlen von kostengünstigen, abstimmbaren Breitband-1550-nm-Lasern, die eine Übertragung von 10 Gbit/s ermöglichen. Im ersten Teil dieser Arbeit wurde eine mikroelektromechanisch weit abstimmbare Oberflächen-emittierende Laserdiode mit Vertikalresonator (engl. micro-electro-mechanical system vertical-cavity surface-emitting laser, MEMS-VCSEL) entwickelt, der eine kostengünstige, direkt modulierte 10 Gbit/s Übertragung über die relevante Reichweite ermöglicht und eine Vereinfachung für das autonome Breitband-Tuning bietet. Das Bauteil ist für Anwendungen geeignet, die einen Ersatz durch Hot Backup und Laser mit fester Wellenlänge zur Reduzierung des Lagerbestands umfassen.

Im Rahmen dieser Arbeit wird ein PECVD-abgeschiedener MEMS-Bragg-Spiegel (engl. distributed Bragg reflector, DBR) auf einer aktiven VCSEL-Struktur für hoher Modulationsgeschwindigkeiten mittels Oberflächenmikromachining aufgebracht. Der MEMS-DBR, der aus dielektrischen SiN_x/SiO_y-Materialien besteht, weist eine sehr hohe Reflektivität mit einem breiten Stoppband auf. Die Wellenlängenabstimmung wird durch elektrothermische Aktuation der MEMS-Elektrode erreicht. Die Herstellung der MEMS mit dem Ziel der Großserienproduktion wird ausführlich diskutiert. Eine umfassende statische und dynamische Charakterisierung von MEMS-VCSELn einschließlich Fernfeld, Linienbreite, Polarisationsverhalten, Modulationskapazität und relativem Intensitätsrauschen wird vorgestellt. Die Auswirkung der Temperaturänderung auf ihren Abstimmbereich, sowie auf die statischen und dynamischen Eigenschaften wird untersucht. Der erhaltene Wellenlängen-Abstimmbereich von ca. 100 nm umfasst das komplette Telekom-C-Band (1530 - 1565 nm) und einen Teil des L-Bandes (1565 - 1625 nm). Eine Kleinsignalamplitudenmodulationsbandbreite von bis zu 7 GHz wird bei 1550 nm Emission demonstriert. Dies ermöglicht die Implementierung einer direkt modulierten MEMS-VCSEL-basierten Back-to-Back-Verbindung bei 10 Gbit/s Datenübertragung über einen Abstimmbereich von 76 nm. Außerdem bestätigt eine quasi fehlerfreie 10-Gbit/s-Übertragung über eine Standard-Einmodenfaser von 40 km für einen Abstimmbereich von mehr als 60 nm ihr Potential für das oben erwähnte neue WDM-PON-System. Neben der optischen Kommunikation wird der Anwendungsbereich dieser abstimmbaren Quelle in Anwendungen wie der Dispersionsspektroskopie und der abstimmbaren Terahertz (THz)-Signalerzeugung untersucht. Die experimentelle Validierung der Multispezies-Dispersionsspektroskopie mit MEMS-VCSEL wird erstmals in dieser Arbeit vorgestellt, in der der

gleichzeitige Nachweis von Cyanwasserstoff, Acetylen und Kohlenmonoxid demonstriert wird.

Der zweite Teil der Arbeit stellt die Demonstration und experimentelle Validierung einer neuartigen optischen Komponente dar, die als MEMS Orbitaldrehimpuls (engl. orbital angular momentum, OAM)-Filter bezeichnet wird. Das Filter besteht aus einer mikroskopisch kleinen Spiralphasenplatte (SPP), die (durch direktes Laserschreiben) in den MEMS-DBR eines optischen Fabry-Pérot-Filters integriert ist. Die On-Chip-Bausteine eignen sich zur Unterscheidung verschiedener OAM-Modi für einen breiten Abstimmbereich um die 1550-nm-Emission und werden als kompakte, robuste und kostengünstige Lösung für gleichzeitige optische OAM- und WDM-Kommunikation betrachtet. Die Verwendung der OAM-Modi als zusätzliche orthogonale Basis von Informationsträgern sowohl in Freiraum- als auch optischen Faserkommunikationssystemen erhöht möglicherweise die Übertragungskapazität enorm. Vier Chips mit OAM-Ordnungen von 0 (kein SPP auf MEMS), 1, 2 und 3 wurden untersucht. Sie sind in der Lage, den OAM-Strahl entsprechender Ordnung über einen kontinuierlichen Abstimmbereich von mehr als 30 nm zu erzeugen / zu empfangen, wofür die entworfenen SPPs mit hoher Modenreinheit arbeiten. Die Systemleistung wird beim Multiplexen von zwei Wellenlängen- und zwei OAM-Kanälen ausgewertet. Eine fehlerfreie Übertragung bei 10 Gbit/s in freiem Raum legt nahe, dass OAM, das über einen weiten Wellenlängenbereich funktioniert, ein nützlicher Freiheitsgrad sein könnte, um die Kapazität der Datenübertragung im freien Raum enorm zu erhöhen.

List of Figures

1.1 A standard VCSEL epitaxial structure. Highly reflective distributive Bragg reflector (DBR) mirrors are required for compensating its short axial length of the gain region. . . . 20
1.2 Development of electrically pumped tunable VCSELs in the last two decades, and the tuning range has reached above 100 nm. . . . 23
1.3 Integrated Backhaul- und Fronthaul-Network with BBU: base band unit, RRH: remote radio head, VM: virtual machine, vBBU: virtual BBU (cite). 24

2.1 Multiple reflections of light beam in a Fabry-Pérot (FP) resonator with two parallel mirrors of identcal proprties. . . . 29
2.2 Simulated reflectance of a symmetrical ($R_1 = R_2$) FP resonator as a function of the optical resonator length normalized to wavelength, shown for different mirror reflectances. . . . 30
2.3 Two different configurations of half-symmetric resonators with curved top mirrors: (a) Stable resonator with $\mathrm{RoC}_1 > \mathrm{L}_c$, (b) unstable resonator with $\mathrm{RoC}_1 < \mathrm{L}_c$. . . . 31
2.4 Simulated reflection spectrum of a DBR consisting of 11.5 pairs of $\mathrm{SiN}_x/\mathrm{SiO}_y$ dielectrics for Bragg wavelength $\lambda_{\mathrm{Bragg}} = 1550$ nm. . . . 34
2.5 Principle of a continuously tunable laser with a short resonator. Lasing mode is realised as the material gain of the active zone outweighs the cavity losses. . . . 40
2.6 Large-signal digital modulation of a standard VCSEL with a set of bias points. . . . 42
2.7 The SNR of the measured eye with a bit rate of B measured with an oscilloscope. . . . 44
2.8 The helical wavefronts of different Laguerre-Gaussian modes. The index ℓ refers to the topological charge number. The handedness of the helical wave fronts of the LG modes is linked to the sign of the index ℓ, and can be chosen by convention. . . . 45
2.9 SPPs of different topological charge and their conjugates. . . . 47
2.10 OAM conversion of $\ell = 0$ (Gaussian TEM_{00}) $\rightarrow \ell = 2$ is achieved by using a second order SPP, i.e., $\ell_{\mathrm{SPP}} = 2$. . . . 48
2.11 Different multiplexing techniques in optical fiber communications: OTDM: optical time-division multiplexing, WDM: wavelength-division multiplexing, SDM: spatial-division multiplexing, MDM: mode-division multiplexing, and PDM: polarization-division multiplexing. OAM beams can be regarded as the analogue of MDM with theoretically unlimited orthogonal degree of freedom for data multiplexing. . . . 49

3.1 (a) Optical image of a half-VCSEL. The semiconductor around the VCSEL mesa is replaced by BCB. (b) Scanning electron microscopy (SEM) image of a part of a fully processed wafer. Inset shows a close view of a single device. The free-standing circular dish supported by four suspension beams consitute the movavle MEMS-DBR. 52
3.2 Schematic cross-section of a MEMS VCSEL. The MEMS-DBR consisting of 11.5 SiN_x/SiO_y pairs is surface-micromachined on the half-VCSEL structure. Wavelength tuning is realized by applying an electro-thermal actuation current to the MEMS electrode. Note: The picture is not scaled to the actual dimensions of the device. 53
3.3 Cross-sectional view of the BTJ in the half-VCSEL structure. 54
3.4 (a) Electro-luminescence (EL) spectrum of two half-VCSELs (with and without ARC) measured at room temperature. (b) EL peaks plotted as a function of substrate temperature. 55
3.5 Simulated and measured reflectivity of a top MEMS DBR consisting of 11.5 pairs of SiN_x/SiO_y dielectric materials. Inset highlights that MEMS-DBR has 99.6% of reflectance for a wavelength range of $\approx 125\,\text{nm}$. 58
3.6 MEMS surface micromachining steps. 59
3.7 Half-VCSEL with AlO_z ARC. Surface roughness measured using a profiler – (a) before and (b) after wet-etching of Ni sacrificial layer with diluted HNO_3. 62
3.8 (a) AlO_z ARC layer is attacked by TFG which can be seen by mechanically removing the MEMS. (b) TFG damages SiO_y, penetrates thorough it and etches the InP semiconductor layer. 64
3.9 (a) Histograms of single layer stress measurements of (a) SiN_x (compressive), (b) SiN_x (tensile), and (c) SiO_y (compressive) dielectrics. 67
3.10 RIE etch rate determination of two types of layer-pairs. Compressive SiN_x/SiO_y pairs have higher etch rate compared to tensile SiN_x/SiO_y pairs. Moreover, rinsing the wafer during the etching has a significant influence on the etch rate. 68
3.11 The release of the MEMS can be visually observed by looking at the beams – dark color indicates the Ni sacrificial layer is completely etched and the MEMS is released. 70
3.12 Cross-section of a MEMS tunable OAM-filter. 72
3.13 (a) Optical images of a 2-D array of MEMS OAM-filters with SPP orders, $\ell_{SPP} = 1$, 2 and 3. The devices on the left column ($\ell_{SPP} = 0$) have no SPP. (b) Si wafer of 2-D arrays conjugate SPPs of corresponding orders. 72
3.14 SEM images (top and side view) of a SPP of order 1 on a glass substrate. 74

4.1 (a) The continuous-wave (CW) tunable spectrum of a MEMS VCSEL at 30 °C is recorded by sweeping the actuation current I_{MEMS}. I_{bias} is set to 20 mA. The spectrum moves to higher wavelength values (red-shifted) with increasing I_{MEMS}. (b) Emission wavelength λ as a function of I_{MEMS}. Inset shows the linear relationship between emission wavelength and actuation power $P_{heat} \propto \lambda$. 77
4.2 Side-mode suppression ratio (SMSR) values calculated from the tuning spectra, plotted as a function of wavelength for different substrate temperature. 78

4.3 Tuning range distribution of 123 MEMS VCSELs from different positions of the wafer. The mean and standard deviation of the data set is 83.57 nm and 11.45 nm, respectively. The devices are measured after mounting and bonding to a silicon submount, as shown in the inset. 79
4.4 Thermal characteristics of a 14 µm aperture device. (a) Tunable emission spectra of a MEMS VCSEL measured at a constant laser current $I_{\mathrm{bias}} = 20\,\mathrm{mA}$, operating at 20 °C. (b) Wavelength-shift over temperature shown for two consecutive modes; I_{MEMS} is set to 0 mA. (c) Maximum (λ_{max}), minimum (λ_{min}) and center wavelength (λ_{c}) of the tuning range at different heat sink temperature. (d) Tuning range and the corresponding FSR as a function of temperature. 81
4.5 (a) Fiber coupled optical power (L) as a function of injection current I_{bias}, measured at a heat-sink temperature of 23 °C for 1550 nm emission wavelength. (b-f) L-I plots for five tuning wavelengths at different heat sink temperatures. 83
4.6 (a) Threshold currents (a), fiber-coupled maximum optical output powers (b), and corresponding thermal rollover current (c) measured at five heat sink temperatures and plotted as a function of tunable emission wavelengths. 85
4.7 (a) Maximum output power over temperature. The linear fit gives a slope $\mathrm{d}P_{\mathrm{opt,max}}/\mathrm{d}T \approx -0.021\,\mathrm{mW/K}$. (b) $\mathrm{d}P_{\mathrm{opt,max}}/\mathrm{d}T$ values plotted for different emission wavelengths. 86
4.8 (a) Laser voltages vs. injection current (V-I) characteristics of a 14 µm BTJ-diameter MEMS VCSEL. (b) corresponding fiber-coupled maximum optical output power on temperatures for different wavelengths. 86
4.9 (a) Emission spectrum recorded for increasing injection curret I_{bias} at a constant sunstrate teperature of 18 °C and zero I_{MEMS}. (b) Wavelength peaks versus I_{bias} at 18 °C, 32 °C, and 57 °C. 87
4.10 Far-field measurement setup. 89
4.11 (a) Three dimensional color gradient of the far-field at 1568 nm emission wavelength at thermal rollover current of 35 mA and 20 °C heat sink temperature. (b) Relative optical intensity against divergence angle. (c) $1/\mathrm{e}^2$ divergence angle for different tuning wavelengths. 90
4.12 Linewidth measurements based on delayed self-heterodyne (DSH) method using fiber-based Mach-Zehnder interferometer. 92
4.13 (a) Normalized power density spectrum of the beat note of self-heterodyne linewidth measurement of an MEMS VCSEL with a fiber delay length of 5 km. The total linewidth of this VCSEL is extracted to be 42 MHz. (b) Power density spectra of the beat signals for different operating currents. (c) Linewidth over the inverse optical power. (d) Voigt-fitted linewidth for different tuning wavelengths. 93
4.14 Sketch of the experimental setup for polarization measurements using Stokes vector parameters. The emitted light is collimated by a lens, passes a combination of a quarter-wave plate with revolvable fast axis and a polarizer with fixed transmission axis and is finally detected by a photo detector. 96
4.15 Normalized Stokes polarization parameters S_1 (red star), S_2 (blue cross), and S_3 (green circle) together with DOP (magenta square) as a function of laser injection current I_{bias} recorded at six emission wavelngths. 97
4.16 Degree of Polarization (DOP) of the device for six wavelngths. 98

4.17 Setup for measuring the small-signal transfer function. The microscope image shows how the MEMS VCSEL is contacted on-wafer with a coplanner ground-signal (G-S) probe for dynamic measurements. The light output is butt-coupled to lensed single-mode fiber. 99
4.18 (a) Small-signal modulation response of a 14 µm BTJ-diameter MEMS VCSEL for different injection currents above $I_{th} \approx 3.00\,mA$. The laser is emitting at around 1550 nm at a heat sink teperature of 12 °C. (b) Maximum 3-dB bandwidths $f_{3dB,max}$ for different emission wavelengths at 12 °C and 57 °C. 100
4.19 (a) Small-signal 3-dB modulation bandwidth f_{3dB} as a function of $(I - I_{th})^{1/2}$, shown for 12 °C. (b) The slopes of the plots (f_{3dB} versus $(I - I_{th})^{1/2}$) are the corresponding MCEF values, which are plotted as a funtion of emission wavelength for two heat sink temeratures: 12 °C and 57 °C. . 101
4.20 Resonance frequency f_R against the square root of the bias-current above threshold $(I - I_{th})^{1/2}$ shown for 12 °C (b) The slopes of the plots (f_R versus $(I - I_{th})^{1/2}$) are the corresponding D-factor values plotted as a funtion of emission wavelength for two heat sink temeratures: 12 °C and 57 °C. 102
4.21 (a) Intrinsic damping factor γ vs. square of f_R plot shown for 12 °C. and (b) The K-factors that are obtained from a linear fit to the data, obtained for 12 °C and 57 °C for different tuning wavelengths. 102
4.22 Experimental setup for RIN measurement. 104
4.23 (a) RIN spektum at 1550 nm emission for $I_{bias} = 1.5 I_{th}$. (b) RIN values as a function of bias-current. (c) resonance frequency f_R against the square root of the bias-current above threshold $(I - I_{th})^{1/2}$ for 15 °C, (d) Calculted D-factors for the RIN measurement. 105
4.24 Frequency response of the MEMS under electro-thermal actuation. The static tuning range of 70 nm reduces to half at a modulation frequency $f_{3\text{-}dB} = 200 Hz$. 107

5.1 Experimental setup for large-signal data transmission. SG: signal generator, PPG: pulse pattern generator, LDC: laser diode controller, Iso: isolator, SSMF: standard single-mode fiber, OSA: optical spectrum analyzer, VOA: variable optical attenuator, PIN PD: *p-i-n* photodiode, A: preamplifier, OPM: optical power meter, LPF: electrical low-pass filter, BERT: bit-error rate tester, SO: sampling oscilloscope. The maximum operating frequency of 12.5 Gbit/s of the BERT is the maximum data transmission capacity of the setup. 109
5.2 BER performance as a function of received optical power, operation at 10 Gbit/s NRZ direct modulation in back-to-back configuration. (a) BER curves for three PRBS word lengths with reference to a MZM, measured to 1550 nm emission. (b) BER performance for six tunable emission spectra with a fixed PRBS length of $2^{15} - 1$. 111
5.3 Optical eye diagrams including SNRs and corresponding recieved optical powers for six tunable emission spectum. The eyes are recorded for quasi error-free transmission at 10 Gbit/s. 112
5.4 (a) Minimum and maximum wavelength for quasi error-free transmission in dependency of temperature operated in BTB configuration. (b) Tuning range as well as the minimum/maximum wavelengths (at which 10 Gbit/s transmission rate can be obtained) as functions of substrate temperature. 114

5.5 BER performance as a function of received optical power for BTB 12.5 Gbit/s NRZ direct modulation. 115
5.6 (a) The shortest (λ_{min}) and the longest (λ_{max}) emission wavelengths capable of transmitting error-free 10 Gbit/s transmission are plotted as a function of the fiber length at two temperature levels. (b) Corresponding tuning range achieved for 10 Gbit/s transmission at same temperature levels. 115
5.7 Fiber-coupled power, SMSR and corresponding MEMS actuation power $P_{MEMS} = I^2_{MEMS} \times R_{MEMS}$ of a packaged MEMS VCSEL plotted against its tunable emission wavelength. 117
5.8 (a) A concept of a WDM-PON system based on low-cost tunable MEMS VCSEL. TX: transmitter, RX: receiver, AWG: arrayed waveguide grating, PD: photodetector, PT: pilot-tone. (b) Experimental setup. VOA: variable optical attenuator, EDFA: Erbium-doped fiber amplifier, SSMF: standard single-mode fiber„ DCF: dispersion compensating fiber, AWG: arrayed waveguide gratings, BERT: bit-error rate tester, OLT: optical line terminal, ODN: optical distribution network, optical ONU: optical network unit. 118
5.9 (a) Back-to-back BER performance vs. received power for various wavelengths. (b) Receiver sensitivity measured as BER vs. receied optical power for different emission wavelengths after 1-40 km standard single-mode fiber (SSMF) and dispersion compensating fiber (DCF) matched to 40 km SSMF [**?**]. 119
5.10 (a) Refractive index in the vicinity of a molecular transition with center ω_c. (b) Spectrum of an intensity modulated optical carrier centered in the dispersion line. 122
5.11 Experimental setup of the HPSDS system based on a MEMS-VCSEL. MOD: Optical intensity modulator, SG: Signal generator, Mix: Frequency mixer, APD: Avalanche photodiode, Lock-in: Lock-in amplifier. 124
5.12 Tunable emission spectrum of the MEMS VCSEL. The dotted line refers to the continuous spectra with intensity fluctuations of up to 17 dB. . . . 124
5.13 HPSDS phase signal of three samples for the entire spectral range. HPSDS signal is shown in degrees. A absorption spectroscopy signal in arbitrary units is also highlighted. Inset diagrams show comparative scenario between direct absorption spectrum (TDLAS) and the HPSDS outcome. 126

6.1 Experimental setup for characterizing the transmission characteristics of a MEMS tunable Fabry-Pérot filter. 129
6.2 (a) Tuning spectra of a MEMS tunable Fabry-Pérot optical filter. (b) Tuning wavelength vs. MEMS actuation power, and (c) Tuning wavelength as a function of substrate temperature. 130
6.3 Experimental setup for generation, detection and characterization of different OAM modes. ECL: External cavity laser, PC: Polarization controller, xyz: Three axis positioning stage, MO1-MO5: Microscope objectives, POL: Polarizer, BS1-BS2: Beam splitters, M1-M4: Mirrors, QWP: Quarter wave plate, ATT: Variable attenuator, TEC: Thermoelectric cooler , DUT: Device under test, CCD: Charge coupled device camera. . . . 131
6.4 Transmittance of the SPP modes with $l = 0$, 1, 2 and 3 as a function of resonance wavelength. 132

6.5 Intensity distributions for the main resonance mode of the MEMS OAM-filters with the 4 azimuthal orders ($l_p = 0$, 1, 2, and 3) at a resonance wavelength of 1540 nm. . . . 134
6.6 Measured phase distributions for the main resonance mode of the MEMS OAM-filters with the 3 azimuthal orders ($l_p = 1$, 2, 3) at different resonance wavelengths. . . . 134
6.7 Normalized power of OAM states in the generated vortex beams using SPPs of orders 1 (a), 2 (b) and 3 (c), respectively. . . . 135
6.8 Schematic drawing of the experimental setup for the BER measurements. 137
6.9 BER vs. ROP curves and penalties for demultiplexing wavelength and OAM channels when transmitting the Gaussian channel and the OAM channel of order: (a),(b) $l_p = 1$; (c),(d) $l_p = 2$; and (e),(f) $l_p = 3$. The left [(a),(c),(e)] and the right [(b),(d),(f)] columns correspond to OOK and BPSK modulations, respectively. . . . 140
6.10 BER vs. ROP curves and penalties for OOK modulation when four (two wavelength and two OAM) channels are being transmitted for different spacing between wavelength channels. Each graph corresponds to transmission of the Gaussian channel and the OAM channel of order: $l_p = 1$; (c),(d) $l_p = 2$; and (e),(f) $l_p = 3$. The left column [(a),(c),(e)] and the right column [(b),(d),(f)] correspond to the cases when the received channel has higher and lower wavelength, than the filtered channel, respectively. . . . 141

B.1 A unit cell showing the overlay of all photolithography masks used in MEMS surface micromachining. . . . 158

D.1 Optimal space utilization of an SFP+ module by two printed circuit boards on both sides (green and blue). . . . 163

E.1 Schematic of the THz setup, broadband tunability is obtained by employing a tunable MEMS VCSEL. . . . 166
E.2 Homodyne detection of 2.75 THz using a MEMS VCSEL and a DFB laser ($\lambda_{\mathrm{VCSEL}} < \lambda_{\mathrm{DFB}}$ [107]. The individual DFB sweeps are indicated by color sequences. . . . 166

List of Tables

3.1 Layer structure and properties of the MEMS-DBR. 57
3.2 PECVD process parameters. 61
3.3 PECVD deposition parameters for SiN_x ARC. 62
3.4 Different sacrificial layers investigated for MEMS surface micromachining. 65
3.5 Resulting air-gaps for two MEMS-DBRs with different combination of stress values. The compressive stress of SiN_x is the key variant in this case. 66
3.6 RIE parameters for DBR etching. With the following parameters, the gas combination etches at a rate of 150 ($\pm$5) nm/min. 69
3.7 Layer structure of the MEMS OAM-filter. The Bragg layers are adapted for 1550 nm wavelength. 73

4.1 Device parameters of the MEMS VCSEL at 1555 nm emission, derived from the small-signal analysis. 103

6.1 Average transmittance of four MEMS OAM-filters. 133
6.2 Penalties at the FEC BER thresholds for four (two OAM and two wavelength) channels, $\Delta\lambda = 0.8$ nm. 142
6.3 Maximum penalties at the FEC BER thresholds for multiplexing four channels, $\Delta\lambda = 0.4$ nm in reference to $\Delta\lambda = 0.8,$ nm. 143

D.1 Measured basic electro-optical characteristics of the first batch of TOSAs. 163

Contents

Declaration of Authorship **2**

Acknowledgements **4**

Abstract **6**

List of Figures **10**

List of Tables **15**

1 Introduction **19**
1.1 Tunable VCSELs . . . 21
1.2 Wavelength Tunable OAM-Filter . . . 25
1.3 Thesis Overview . . . 26

2 Theoretical Background **28**
2.1 Fabry-Pérot Resonator . . . 28
2.2 Vertical-Cavity Surface-Emitting Laser . . . 34
2.2.1 Principles of Operation . . . 35
2.2.2 Rate Equations . . . 35
2.2.3 Optical Data Transmission using VCSEL . . . 41
2.3 Orbital Angular Momentum of Light . . . 44
2.3.1 MEMS OAM-Filters and Their Application . . . 48

3 Device Structures and Fabrication **51**
3.1 MEMS VCSEL . . . 51
3.1.1 Half-VCSEL: Design and Structure . . . 52
3.1.2 MEMS-DBR: Structure and Fabrication . . . 56
3.2 MEMS OAM-Filter: Structure and Fabrication . . . 71

4 Characterization of MEMS VCSEL **76**
4.1 Static Characterizations . . . 76
4.1.1 Electro-thermal Tuning . . . 76
4.1.2 Light–Current–Voltage Measurement . . . 83
4.1.3 Far-Field Measurements . . . 88

4.1.4 Linewidth Measurements . . . 91
4.1.5 Polarization Measurements . . . 95
4.2 Dynamic Characterizations . . . 99
4.2.1 Small-Signal Modulation Response . . . 99
4.2.2 Relative Intensity Noise (RIN) . . . 104
4.2.3 Tuning Speed . . . 106

5 Applications of MEMS VCSELs 108
5.1 Optical Data Transmission . . . 108
5.1.1 Back-to-Back Transmission . . . 108
5.1.2 Data Transmission Using Single-Mode Fiber . . . 115
5.1.3 Applications using Packaged MEMS VCSEL . . . 116
5.2 Other Applications using MEMS VCSELS . . . 120
5.2.1 Heterodyne Phase Sensitive Dispersion Spectroscopy . . . 120
5.2.2 Tunable Terahertz (THz) Generation . . . 127

6 Tunable MEMS OAM-Filter 128
6.1 MEMS Filter Characterization . . . 128
6.2 OAM beam Generation and Detection . . . 130
6.3 Optical Data Transmission Experiments . . . 136

7 Summary and Outlook 144
7.1 Future Work . . . 147

Acronyms 149

Symbols 153

A Differential Analysis of the Rate Equations 154

B Photolithography Masks 158

C MEMS Surface Micromachining Process 159

D TOSA Packaging and Characterizations 163

E MEMS VCSEL-based THz Photomixing 165

Bibliography 168

Publications 179

Supervised Theses 184

Curriculum Vitae 185

Chapter 1

Introduction

The concept of utilizing light for transmitting signals dates back a long time, but one of the first proposals to use it as information carrier may be traced back to the 1860's [1]. It was however, only after the first experimental demonstration of a functional laser by T. Maiman in 1960 [2] that an intensive research effort has been carried out in this field. Among different types of lasers, *p-n* junction based semiconductor laser diodes had been specially attractive for optical communication systems due to their compact size, large digital modulation bandwidth and cost. The advancement of the optical communication today is an accumulated outcome of continuous research triggered by the demonstration of the first continuous-wave (CW) double heterostructure laser diode at room temperature in 1970 [3] followed by the introduction of a very low-loss (0.47 dB/km) optical fiber as transmission medium in 1976 [4].

In principle, a laser diode emits light through a process of optical amplification based on the stimulated emission of electromagnetic radiation. Like any other laser, it includes a gain medium which is incorporated into an optical resonator. By supplying optical or electrical energy from an external source, electrons in the gain medium can be excited to higher energy states. Thus any incident radiation can be amplified rather than absorbed by stimulating the de-excitation of these electrons along with the generation of additional radiation [5]. If the resulting gain is sufficient enough to overcome different losses of an oscillating optical mode inside the cavity, a coherent light of same wavelength, phase, and polarization is emitted from the laser. Edge emitting lasers (EELs) were the first semiconductor lasers in the large scale production due to their relatively simple epitaxial growth. The pump current required for stimulated emission in EELs is injected vertical to the wafer surface whereas the photons are emitted horizontally along the wafer edge. The light wave propagating through a long active region ($\approx$ 0.1–1 mm) undergoes a large amplification. Therefore, simple cleaved semiconductor facets with reflectivity of only 30% can be used as mirrors [6]. However, due to waveguide-type geometry, the radiated

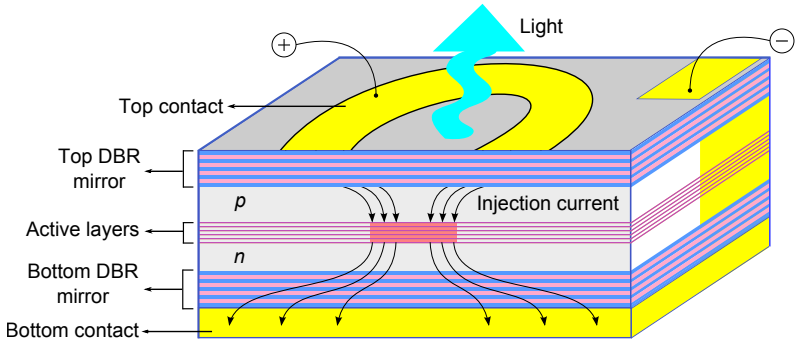

FIGURE 1.1: A standard VCSEL epitaxial structure. Highly reflective distributive Bragg reflector (DBR) mirrors are required for compensating its short axial length of the gain region.

beam is vastly elliptical. As a result, additional corrective optics are often required for light-coupling – which makes the process inefficient.

A new concept of the semiconductor laser was proposed by K. Iga in 1977 [7], where light emits perpendicular to the wafer surface, and hence named as vertical-cavity surface-emitting laser (VCSEL). A simple VCSEL resonator consists of a thin active zone ($< 100\,\text{nm}$) with few quantum wells (QWs) sandwiched between two distributed Bragg reflector (DBR) mirrors parallel to the wafer, as shown in Fig. 1.1. The vertically injected current is confined through the active region mostly by ion implantation, lateral oxidation or tunnel junction formation depending on the material system [6]. The planar DBR mirrors comprise layers with alternating high and low refractive indices yielding intensity reflectivity above 99%, which is required to compensate their short axial length of the gain region and moderate optical confinement factors.

The evolution of VCSELs as high-speed optical source has taken a lot of research initiatives. The very first VCSELs were based on the technologically-challenging InGaAsP-InP mixed compound semiconductors [8]. A major breakthrough occurred in the late 1980s with the demonstration of the first CW-operating GaAs-based VCSEL using metal and dielectric mirrors [9]. First-generation commercial lasers were based on proton-implanted current confinement [10, 11] and made from GaAs-AlGaAs materials for an emission around 850 nm. Until today, 850 nm spectral region has remained dominant specially in local area networks (LANs) due to their high modulation bandwidth and high optical output power. The reported highest data rate has reached up to 71 Gbit/s [12], targeting at data center applications with $<$100 m link-length. After an extraordinary evolution over the past four decades, they have entirely replaced EELs in multimode fiber (MMF) based Gbit/s optical transmission networks and interconnection of various types of computer clusters. The so-called long-wavelength VCSELs emitting in the 1300–1600 nm regime, on the other hand, have suffered from many technological issues [6]. For example, the active regions cannot be grown on GaAs substrates using technologically mature materials such as InGaAsP or InGaAlAs. Due to low refractive index

contrast between the consecutive DBR-layers of InGaAsP or InGaAlAs materials, more layer-pairs are required for a required reflectivity of $> 99\%$. Moreover, longer emission wavelength requires higher layer thickness. As a result, the epitaxial mirror stacks of the InP-based VCSELs become very thick. Considering the small thermal conductivity of the ternary/quaternary layers being about one order of magnitude smaller than GaAs and AlAs, the thermal resistances of the epitaxial mirrors for the InP-based VCSELs are 20–40 times larger than GaAs-based counterparts. Furthermore, the lateral steam oxidation technique is not available for the InP-based material systems [6]. All these challenges required a considerable research effort to obtain functioning long wavelength VCSEL. However, they have accomplished a noticeable level of maturity in terms of high digital modulation in the last decade [13, 14]. By increasing the strain of the QWs, reducing the optical volume by shortening the cavity length, and optimizing the thermal design by incorporating gold heat sinks, hybrid GaAs-DBRs and thin dielectric mirrors, 40 Gbit/s direct modulation using 1550 nm VCSEL has been demonstrated [13]. With minimum fiber losses around this spectrum, they are highly attractive optical sources for the fast-growing applications such as access networks, interconnects and communications between wireless base stations.

In general, the significant features of VCSELs with regard to optical data transmission include low operating current due to their compact structure; thus reducing total power consumption, excellent digital modulation behavior, high power conversion efficiencies thus low power dissipation, circular beam profiles with small divergence angles which simplify the design of beam-shaping optics, wide ambient temperature ranges enabling uncooled operation even in automobiles, complete testing and device selection on the wafer level – yielding enormous cost reduction, formation of homogeneous two-dimensional (2-D) laser arrays as the key to compact space division multiplexed (SDM) data transmission, and very high reliability with projected lifetimes of the order of ten million hours at room temperature [6].

1.1 Tunable VCSELs

Among different performance characteristics (e.g., output power, spectral linewidth, modulation speed, wavelength tuning, polarization etc.) continuous tunability is one of the most interesting topics for laser scientists. Tunable VCSELs have attracted immense attention due to their single-mode operation and continuous tuning range; thus constantly instigating wavelength-specific new applications. VCSELs inherit two important aspects which make them impeccable as ultra-wide tunable optical source. Firstly, the short cavity length of the VCSEL enables a large spectral spacing between two consecutive longitudinal modes – which is known as free spectral range (FSR). Due

to comparatively longer cavity lengths of EELs, selection of a single longitudinal resonant mode is a problem when it comes to continuous wavelength tuning. For a properly designed VCSEL resonator, FSR is the ultimate limit for a mode-hop free tuning [15]. Secondly, their vertical resonator structure facilitates easier wafer-level integration of photonic components such as microelectromechanical systems (MEMS) and spiral phase plate (SPP) etc. in 2-D arrays for mass fabrication [16, 17]. Consequently, MEMS VCSELs are highly desirable optical sources in optical communication [14, 16, 18], gas sensing [19], optical coherence tomography (OCT) [20], fiber Bragg-grating (FBG) sensing [21, 22], tunable Terahertz (THz) generation [23] and light detection and ranging (LIDAR) [24] due to their continuous tuning characteristics around different emission wavelengths.

In principle, the emission wavelength of any laser diode can simply be tuned by altering the refractive index (i.e., optical length) of the resonator. Refractive index of resonator mainly depends on temperature and carrier density; hence the resultant tuning range is limited to only few nanometers. For instance, wafer-fused InAlGaAs-InP 1550 nm-VCSELs with GaAs-based DBRs exhibit high thermal conductivity, enabling 15 nm tuning by operating it well above the thermal rollover region [25]. However, a large variation in injection current leads to a significant change in the output power across emission range. Thus, changing geometric length is a prerequisite for wide tunability. This can be achieved by integrating a movable mirror such as a MEMS-DBR or a MEMS high-contrast grating (HCG) which can be externally actuated to obtain a variable optical cavity length. There are different techniques for integrating the movable mirror into the active VCSEL structure.

Micromachining is a widely used technology for MEMS integration. In case of bulk micromachining the active VCSEL and the curved movable mirror are processed separately. One can combine deposited dielectrics and epitaxial semiconductors to obtain relatively large values of refractive index difference to reduce the effective cavity length due to small mirror thickness [26]. However, bulk-micromachined MEMS structures possess several drawbacks. Multiple independent epi-growths/depositions are required to produce a working device, which is rather costly. Additionally, all of the mirrors that are fabricated by bulk-micromachining are bulky and heavy. The resulting MEMS structures have very large spring constants and require high actuation voltages (electro-static actuation) or currents (electro-thermal actuation), which involve additional electronics. The bonding process is rather complicated and lacks uniformity. It also destroys the adjacent devices during the bonding process, making it a time- and cost-inefficient and not suitable for mass production. In comparison, surface micromachining eliminates the need for wafer-bonding and uses deposited dielectric DBR mirrors instead, which on one hand leads to better alignment accuracy along with better uniformity control and on the other hand facilitates cost-effective mass production in 2-D arrays. Different

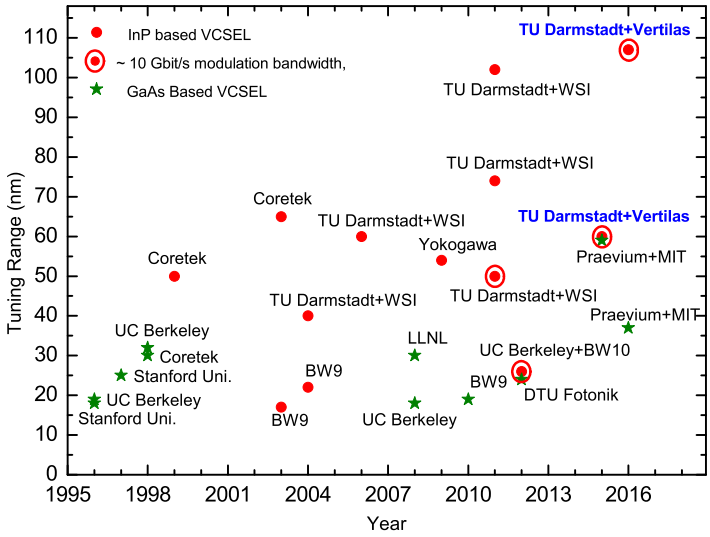

FIGURE 1.2: Development of electrically pumped tunable VCSELs in the last two decades, and the tuning range has reached above 100 nm.

commonly used approaches involve cantilever-type movable reflectors [27] and movable membrane structures using HCG [14] or DBR [15, 28]. HCGs are sub-wavelength gratings that are fully surrounded by lower refractive-index materials and that can behave as ultra-broadband, highly-reflective mirror. HCG-VCSELs can be grown monolithically, thus offering a large fabrication tolerance. They have shown great performance in terms of polarization mode selection, fast tuning speed and high digital modulation rate. Nonetheless, due to relatively large penetration into the bottom mirror the FSR is reduced. The tuning range reported in literature is limited to 30 nm [14].

Obtaining wider tunability depends on the pumping scheme. In comparison to electrically pumped MEMS VCSELs, optically pumped devices with their shorter cavities exhibit very wide tuning ranges [28]. The optical pump structure eliminates the need for doping in the cavity, which reduces both free carrier absorption losses and threshold gain. Also, the optical pump does not have a resistive heating problem that detunes the Fabry-Pérot (FP) cavity and active material gain peak. However, an additional pump source makes the system bulky and yet, direct modulation at a high data rate is not possible. Figure 1.2 summarizes the progress of the electrically pumped tunable VCSELS, including both GaAs-based and InP-based tunable devices, over last two decades. The blue-color text refers to the widely tunable high-speed VCSELs resulting from the collaboration between TU Darmstadt/Vertilas within this thesis work.

Applications in Optical Communication

The expansion of cellular networks over the past decades has gone through an astonishing evolution. Networks are now adapting to ever increasing data-traffic loads, which was initially designed solely for voice traffic. Mobile operators primarily depended on network of macro cells to provide a sound balance of wireless coverage and capacity, are currently deploying more cells in the purpose of coping with exponentially increasing traffic demands [29]. Due to centralized network functions the splitting of the generation/processing of radio frequency (RF) signal in centralized base band units (BBUs) and the baseband-RF conversion in remote radio heads (RRHs) has become inevitable. However, this split imposes rigorous bandwidth- and latency requirements on the so-called mobile fronthaul (MFH) system, which is the transport link between BBUs and RRHs [30]. A network that covers both back-hauls and front-office applications is shown schematically in Fig. 1.3. To systematically overcome the bandwidth and latency issues, an inventive cost-efficient wavelength division multiplexed passive optical network (WDM-PON) operating around 1550 nm has been proposed between a central station (e.g., BBU) and a multitude of distributed points (e.g., RRH) [31]. Such a system is standardized in the G.metro project (ITU-T SG15), with the distributed transceivers should automatically adjust their wavelengths which is centrally controlled. The biggest challenge up to now was the lack of low-cost wideband tunable lasers for high-speed transmission. MEMS VCSELs have potential for low cost, 10 Gbit/s transmission over the relevant reach ($\approx$ 20 km), and offer simplicity for wideband autonomous tuning. MEMS VCSEL based WDM-PON is a viable solution to cope with the pressing MFH needs. Moreover, a widely tunable VCSEL can not only be used as hot backup and sparing for inventory reduction, but also can potentially supersede current fixed-wavelength distributed-feedback (DFB) laser in WDM systems. They give network designers an additional degree of flexibility to lower overall system cost concerning fiber-to-the-home (FTTH) and data

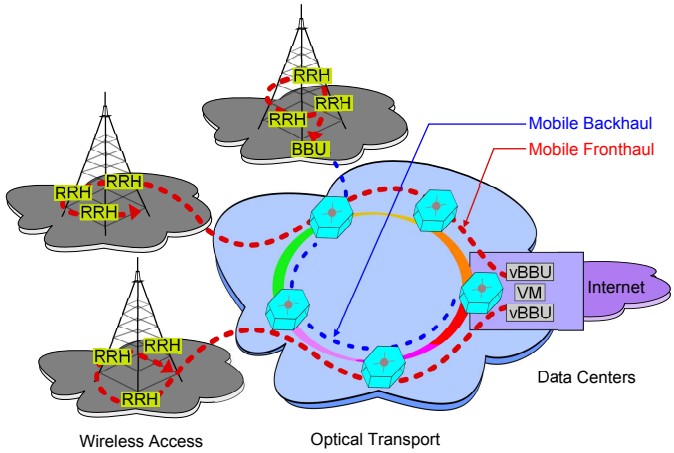

FIGURE 1.3: Integrated Backhaul- und Fronthaul-Network with BBU: base band unit, RRH: remote radio head, VM: virtual machine, vBBU: virtual BBU (cite).

center applications. In addition to that, the so called colorless sources can meet the performance criteria for communication among wireless base stations and interconnects in high-performance computers and data center networks.

1.2 Wavelength Tunable OAM-Filter

As discussed in the previous section, a MEMS VCSEL is a promising source for WDM applications, where wavelength tuning of the optical source is of main interest. However, owing to the exponential growth of Internet traffic the bandwidth capabilities of current broadband services and transmission equipment require significant improvement. This has lead to the investigation of using other physical properties of a lightwave for data encoding and channel addressing. More recently spatially orthogonal modes have been under intense investigation.

A special case of SDM is the utilization of orthogonal spatially overlapping and co-propagating spatial modes, known as mode-division multiplexing (MDM). In such case, each mode can carry an independent data channel, and the orthogonality enables efficient (de)multiplexing and low inter-modal cross-talks among multiple modes. There are several different types of orthogonal modal basis sets that are potential candidates for such MDM systems. One such set is orbital angular momentum (OAM). Over the last decade, OAM beams has grown immense interests due to its potential in a diverse range of applications. In comparison to polarized lightwaves, an OAM beam twists through space like a corkscrew and theoretically, an infinite range of "twists" per wavelength can be obtained. OAM of light is particularly promising in the field of optical communications for the following reasons. Firstly, coaxially OAM beams with different azimuthal states are mutually orthogonal corresponding to an additional degree of freedom as independent information channel. Secondly, inter-beam cross-talks can be effectively minimized. Finally, different OAM states can be multiplexed and demultiplexed. Importantly, OAM multiplexing does not rely on the wavelength or polarization, indicating that OAM could be used in addition to WDM and PDM techniques to improve system capacity. Additionally, in comparison, to other MDM methods, OAM might have some implementation advantages stemming from the circular symmetry of the modes, which makes it well suited for many optical component technologies.

Currently several successful implementations of OAM-multiplexed transmission over relevant distances have been demonstrated in both free space and optical fibers [32, 33]. However, processes of generation, modulation, (de)multiplexing and detection of OAM beams are provided as a rule by bulky optical devices. For generation and (de)multiplexing of OAM carrying signals liquid crystal spatial light modulators (SLMs) [33, 34] or separate spiral phase plates (SPPs) [35, 36] are usually utilized. Such systems

based on discrete components cannot provide robustness and repeatability, thus cannot be effectively introduced into industrial applications. Development of compact, on-chip integrable optical components providing all the functions for processing OAM-carrying signals is necessary for launching next generation energy- and cost-effective OAM-based communications.

In this work a novel on-chip micro-sized device, capable of generating wavelength-selective OAM beams, is proposed. This MEMS OAM-filter is combination of a electro-thermally tunable MEMS Fabry-Pérot (FP) optical filter and a SPP – which is integrated onto a top MEMS-DBR. It is capable of functioning simultaneously in both wavelength and OAM domains around telecom wavelength. In optical communication, the device can be used for simultaneous multiplexing of wavelength and OAM beams [37, 38].

1.3 Thesis Overview

In this thesis, two tunable components are presented mainly for optical communication based applications. First, a MEMS-DBR is integrated into 1550 nm short-cavity active VCSEL structure by means of surface micromachining technology which is suitable for mass fabrication in 2-D arrays. The device is optimized for high speed applications at 10 Gbit/s. The semiconductor around the VCSEL mesa structure is replaced by Benzocyclobutene (BCB) with lower dielectric constant k. The significant part of this work is to develop a process compatible surface micromachining of the MEMS-DBR on the BCB surface, providing that the fabrication process does not destroy any layer of the active-VCSEL structure. After successful fabrication of the devices, a comprehensive set of electro-optical characterizations are carried out. Optical data transmission experiments at 10 Gbit/s for a wide tuning rang range shows the compatibility of the MEMS tunable VCSEL as a cost-effective optical source in the proposed WDM-PON system.

In the second part a MEMS tunable OAM-filter has been demonstrated and experimentally validated. The tunable filter is designed for working around 1550 nm telecom wavelengths and can be put in both transmitting and receiving end. Thus it can effectively both generate/detect an OAM beam for a desired wavelength. In this work, it has been shown that a device with a fixed order (number of twists) of OAM beam can generate/detect not only for a specific wavelength it is designed for, but for a certain tuning range around the target wavelength. The on-chip device can especially be useful for communication applications, where the distance is short but high data rates are desirable. It can also be considered as the first prototype towards MEMS OAM-VCSEL, which can provide a directly-modulated wavelength-tunable OAM beam as a compact, cost-effective, ultra-high-bandwidth optical transmitter.

The dissertation is organized as follows. **Chapter 2** reviews relevant theoretical basics of tunable VCSEL and MEMS OAM-filter. **Chapter 3** presents the structure and fabrication of the devices. The surface micromachining technology of the MEMS-DBR is presented in detail. **Chapter 4** deals with the electro-optic characterization of the MEMS VCSEL. Both static and dynamic properties are characterized and discussed. Data transmission experiments using directly-modulated on-wafer and packaged MEMS VCSELs are demonstrated in **Chapter 5**. It also addresses the potential of tunable VCSEL in other demanding areas such as gas spectroscopy and tunable THz-signal generation. **Chapter 6** experimentally discusses how OAM beams are generated using MEMS OAM-filters. Also, OAM- and wavelength multiplexing/demultiplexing of four channels with different data stream is shown in this chapter. Finally, **Chapter 7** summarizes the essential findings of this work and provides an outlook on future work for both components and possible improvements for different applications.

Chapter 2

Theoretical Background

In this chapter the working mechanism of a MEMS VCSEL is elaborated based on Fabry-Pérot (FP) resonator theory. Different aspects of optical data transmission experiments are briefly discussed. Afterwards, the basics of orbital angular momentum (OAM) beam as well as its generation technique using spiral phase plate (SPP) is shortly introduced.

2.1 Fabry-Pérot Resonator

The working principle of a FP resonator is based on the interference of multiple beams. In a simplified FP resonator comprising two identical, coplanar, highly-reflecting mirrors with negligible thickness, an incoming beam is split into many beams (due to numerous internal reflections) which interfere with each other. The transmission and reflection properties of a FP resonator can be described using one-dimensional propagation of plane electromagnetic wave, $E(z,t) = E_0 \cdot \exp[j(\omega t - kz)]$. Here, the electric field is considered to propagate along the longitudinal $(+z)$ direction with an amplitude E_0, an angular frequency ω and a propagation constant $k = \frac{\omega n_c}{c} = \frac{2\pi n_c}{\lambda}$, where n_c is the refractive index of the cavity medium, λ is the wavelength, and c is the vacuum light speed. For the subsequent calculations three assumptions are made: (i) the mirrors are infinitely extended in two lateral (x and y) directions, (ii) the refractive index is independent of the wavelength, and (iii) the resonator medium is loss-free and thus the imaginary part of n_c responsible for the attenuation of the signal is ignored. Figure 2.1 shows the multi-beam interference of a FP resonator with two coplanar mirrors at a distance L_c. The geometric length of the cavity L_c can be converted into an optical length $L_o = n_c L_c$. For vertical light-incident, the mirrors are characterized by their reflection coefficient r_i $(i = 1, 2)$ as the ratio of the field amplitudes of the reflected and the incident beams, and the transmission coefficient t_i as the ratio of the field amplitudes of the transmitted

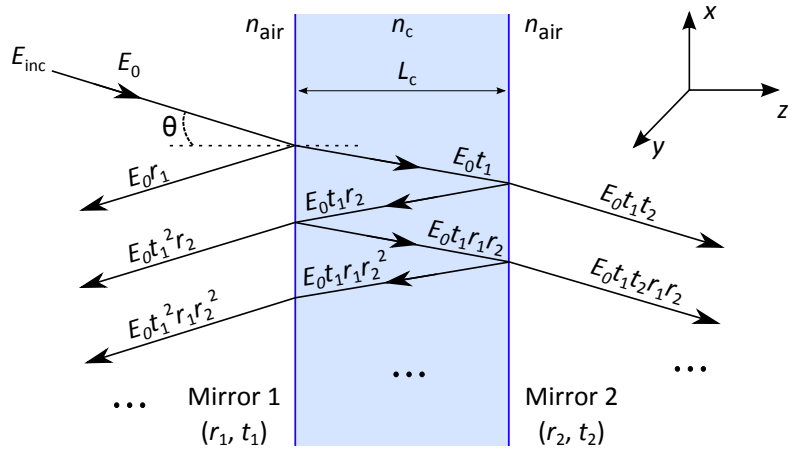

FIGURE 2.1: Multiple reflections of light beam in a Fabry-Pérot (FP) resonator with two parallel mirrors of identcal proprties.

and the incident beams. For an incident field amplitude E_0, the amplitudes of the reflected and transmitted beams can be written as: $E_0r_1, E_0{t_1}^2r_2, E_0{t_1}^2r_1{r_2}^2, ...$ and $E_0t_1t_2, E_0t_1t_2r_1r_2, E_0t_1t_2{r_1}^2{r_2}^2, ...$, respectively. As the transmitted field amplitude of the incoming light beam results from the superposition of infinitely many partial beams, the corresponding phase of each beam has to be taken care of. The successive transmitted pair have a path difference of $2n_cL_c\cos(\theta)$, where θ is the angle of incident. Thus, the corresponding phase difference δ is given by:

$$\delta = \frac{2\pi}{\lambda} \cdot 2n_cL_c\cos(\theta). \tag{2.1}$$

If the resulting phase difference is taken into account, a sum of the amplitudes of the transmitted beam result in:

$$E_{tran} = E_0t_1t_2 + E_0t_1t_2r_1r_2\exp[j\delta] + E_0t_1t_2{r_1}^2{r_2}^2\exp[j2\delta] + ... \tag{2.2}$$

$$= E_0\frac{t_1t_2}{1 - r_1r_2\exp[j\delta]} \tag{2.3}$$

The intensities of the incident, the transmitted and the reflected beams are given by $I_0 \sim |E_0|^2$, $I_{tran} \sim |E_{tran}|^2$ and $I_{refl} \sim |E_{refl}|^2$ respectively, where E_{refl} is the sum of the amplitudes of the reflected beams. With respect to intensities, the reflectance $R = I_{refl}/I_0 = |r_i|^2$ and the transmittance $T = I_{tran}/I_0 = |t_i|^2$ are being applied. Equation (2.3) can be formulated as:

$$T = \frac{I_{tran}}{I_0} = \frac{T_1T_2}{1 + R_1R_2 - 2\sqrt{R_1R_2}\cos\delta} \tag{2.4}$$

$$R = \frac{I_{refl}}{I_0} = \frac{R_1 + R_2 - 2\sqrt{R_1R_2}\cos\delta}{1 + R_1R_2 - 2\sqrt{R_1R_2}\cos\delta} \tag{2.5}$$

Figure 2.2 shows the reflectance of a lossless, symmetrical ($R_1 = R_2$) FP resonator. A standing wave is formed within the resonator (due to constructive interference for multiple reflections from the mirrors) for circulating phases of $\delta = m \cdot 2\pi$ or optical resonator lengths of $L_o = m \cdot \frac{\lambda}{2}$ (for a wave with wavelength, λ). Other wavelengths that do not meet the above resonance condition are canceled out in the FP resonator by destructive interference. Certain mirror distances and wavelengths correspond to an optical path length difference ($2n_c L_c \cos(\theta)$) between each transmitted beam equal to an integer multiple of the wavelength and thus, maximum transmittance ($T = \frac{I_{tran}}{I_0} = 1$) can be obtained. In an practical application of the FP resonator as an optical filter or tunable VCSEL, the value of R_1 and R_2 should be close to unity.

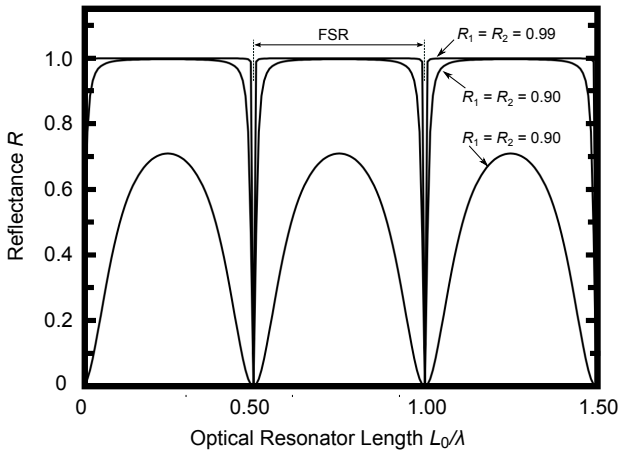

FIGURE 2.2: Simulated reflectance of a symmetrical ($R_1 = R_2$) FP resonator as a function of the optical resonator length normalized to wavelength, shown for different mirror reflectances.

The resonances in the FP resonator are referred as longitudinal modes and distinguished by m, where m is the number of minima (nodes) of the intensity distribution in the resonator. The spectral spacing between two consecutive longitudinal modes is defined as free spectral range (FSR) of the resonator,

$$\mathrm{FSR} = \lambda_m - \lambda_{m+1} = \frac{-\lambda^2}{2n_c L_c \left(1 - \frac{\lambda}{n_c}\frac{\mathrm{d}n_c}{\mathrm{d}\lambda}\right)} \approx \frac{\lambda^2}{2n_c L_c} \tag{2.6}$$

where $\left(1 - \frac{\lambda}{n}\frac{\mathrm{d}n}{\mathrm{d}\lambda}\right)$ is the dispersion term which is negligible.

Stability of the resonator

The FP resonator considered in the previous subsection has two plane mirrors. However, MEMS based devices presented in this work possess concavely bent top mirror. Therefore, it is of utmost importance to analyze the stability of these half-symmetric

resonators. A resonator is stable when the distribution of the electric field traveling within the cavity remains unchanged after one round trip. This is only possible if the curvature of the phase front of the electric field matches to the radius of curvature (RoC) of the MEMS mirror. The resonator stability also depends on the cavity length L_c as well as on the geometric alignment of the curved mirror. The following equation shows the limiting conditions for a stable resonator:

$$0 < \left(1 - \frac{L_c}{\mathrm{RoC}_1}\right) \cdot \left(1 - \frac{L_c}{\mathrm{RoC}_2}\right) < 1, \tag{2.7}$$

where RoC_1 and RoC_2 refer to the corresponding RoC of Mirror-1 (top) and Mirror-2 (bottom), respectively. Two different configurations of half symmetric resonator geometries are shown in Fig. 2.3. In the case of Fig. 2.3 (a), the RoC of the bottom mirror (RoC_2) is infinite; whereas RoC of the top mirror (RoC_1) is smaller than the cavity length L_c. In this case, Eq. (2.7) is clearly not satisfied. A stable half symmetric resonator satisfying Eq. (2.7) is shown in Fig. 2.3(b), where, $\mathrm{RoC}_1 > L_c$ and the $\mathrm{RoC}_2 = \infty$.

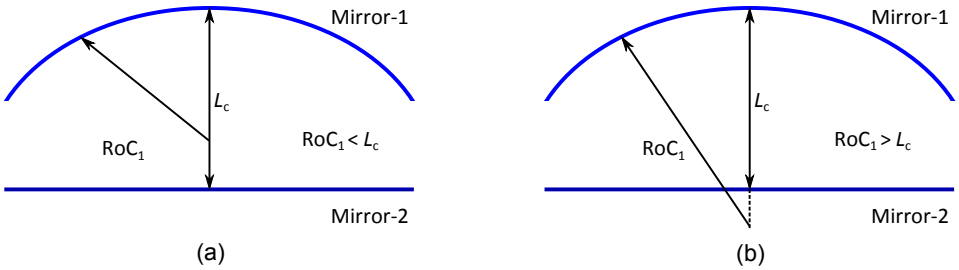

FIGURE 2.3: Two different configurations of half-symmetric resonators with curved top mirrors: (a) Stable resonator with $\mathrm{RoC}_1 > \mathrm{L}_c$, (b) unstable resonator with $\mathrm{RoC}_1 < \mathrm{L}_c$.

Transverse Resonator Modes

A stable resonator satisfies some specific steady-state solutions for field distributions on the resonator mirrors. Such an eigensolution $E_i(x, y)$ on mirror M_i ($i = 1,2$) will reproduce itself after each round trip. In terms of electric fields, these solutions are standing electrical fields within the resonator. The condition for forming standing electrical fields in longitudinal direction has already been introduced. In a real resonator, this condition must be extended to the transverse field distribution. The field distribution $E_1(x, y)$ on one of the two mirrors must be identical to the field distribution $E_2(x, y)$, after a round trip, up to a constant factor γ as in

$$E_2(x, y) = \gamma E_1(x, y) \tag{2.8}$$

The field distribution $E_2(x, y)$ can be calculated from a given field distribution $E_1(x, y)$ using the Collins-integral [39]. The Gaussian beam, as the simplest solution of the Collins-integral, reproduces itself under the conditions in Eq. (2.7) after a round trip and simultaneously represents the fundamental mode of the resonator. In addition to the Gaussian fundamental mode, transversal modes of higher order also satisfy the eigenvalue problem of Eq. (2.8) [40]. Due to the rounded shape of the concave mirror, the eigenmodes must have a circular symmetry. It is shown that Gauss-Laguerre modes solve the eigenvalue problem in Eq. (2.8) under the given boundary conditions [40]. The electric field distribution $E(r, \Phi)$ and the corresponding eigenvalue γ of the resonator mirrors on the two mirrors M_i can be described by the following functions [39]:

$$E_{\rho\ell}{}^{(i)}(r, \Phi) = E_0 \left(\frac{\sqrt{2}r}{\omega_i}\right)^{\ell} L_\rho{}^{(\ell)} \left(\frac{2r^2}{{\omega_{i,j}}^2} \exp\left(\frac{-r^2}{{\omega_{i,j}}^2}\right) \cdot \cos(\ell\Phi)\right), \tag{2.9}$$

$$\gamma = \exp\left[jk\left(2L - \frac{\lambda_0}{\pi}(2\rho + \ell + 1)\arccos\left(\sqrt{\left(1 - \frac{L_\mathrm{c}}{\mathrm{RoC}_1}\right) \cdot \left(1 - \frac{L_\mathrm{c}}{\mathrm{RoC}_2}\right)}\right)\right)\right]. \tag{2.10}$$

The field distribution is in polar coordinates with the radial and azimuthal coordinate of r and Φ, respectively is indicated. The Laguerre polynomials are denoted by $L_\rho{}^{(\ell)}$, where ρ and ℓ refer to the radial and the angular mode numbers. The beam radius $\omega_{i,j}$ on the corresponding mirrors $M_{i,j}$ $(i, j = 1, 2)$ are given by

$$\omega_{i,j} = \sqrt{\frac{\lambda L_\mathrm{c}}{\pi}} \sqrt{\frac{1 - L_\mathrm{c}/\mathrm{RoC}_{i,j}}{1 - L_\mathrm{c}/\mathrm{RoC}_{i,j}\left(1 - \left(1 - \frac{L_\mathrm{c}}{\mathrm{RoC}_1}\right) \cdot \left(1 - \frac{L_\mathrm{c}}{\mathrm{RoC}_2}\right)\right)}}, \quad \text{with } i \neq j. \tag{2.11}$$

For the beam radius on the flat mirror, the following results

$$\omega_1 = \omega_0 = \sqrt{\frac{\lambda}{\pi}\sqrt{L_\mathrm{c}(\mathrm{RoC}_2 - L_\mathrm{c})}}, \tag{2.12}$$

with the beam diameter $2\omega_0$ on the flat mirror. For the higher order modes the beam waist $\omega_{\rho\ell}$ results in:

$$\omega_{\rho\ell} = \omega_1\sqrt{2\rho + \ell + 1}. \tag{2.13}$$

According to Eq. (2.13), transverse modes with orders $\rho, \ell > 0$ have larger lateral extension compared to the fundamental mode. As a consequence, higher modes can be strongly suppressed by an introduction of a circular mode-confining structure into the resonator. For this purpose, the diameter of the circular aperture must be adapted to the beam waist $2\omega_0$, as this enables significant losses for higher order transverse modes. An optimized symmetric RoC of the bent top mirror allows the beam waist perfectly fitting to the circular current confinement area to obtain maximum overlap between them. The gain of the fundamental lasing mode can also be increased in this way.

Distributed Bragg Reflector Mirror

The mirrors of an EEL can simply be formed by cleaving the semiconductor-air interface perpendicular to the cavity. Depending on the refractive index of the semiconductor, a mirror reflectivity of around 30% can be obtained [41]. However, due to short resonator related small round trip gain of photons, VCSELs require mirrors with very high reflectivity. Distributed Bragg reflector (DBR) can provide up to 99.9% reflectivity and hence, are widely used as mirrors for VCSELs. A DBR comprises a stack of thin layers with an alternating sequence of high n_{H} and low refractive index n_{L} (n_{H}, n_{L}, n_{H}, ...). Each individual layer has an optical thickness of $d = \lambda_{\mathrm{Bragg}}/4$, where λ_{Bragg} is the Bragg wavelength. Thus, the electromagnetic fields are partially reflected at the interface of the refractive index transitions and interfere constructively with each other due to an optical path difference of a multiple of half wavelength. In addition, the reflected wave undergoes a phase jump of π at the interface, if the transition from an optically thinner to an optically denser medium occurs (not vice versa). The maximum reflectivity is established at λ_{Bragg}, and can be adjusted via

$$R_{\mathrm{max}} = \left(\frac{1 - \frac{n_{\mathrm{out}}}{n_{\mathrm{in}}} \left(\frac{n_{\mathrm{L}}}{n_{\mathrm{H}}} \right)^{2M}}{1 + \frac{n_{\mathrm{out}}}{n_{\mathrm{in}}} \left(\frac{n_{\mathrm{L}}}{n_{\mathrm{H}}} \right)^{2M}} \right)^2 . \tag{2.14}$$

Here, n_{in} is the refractive index of the medium from which the wave penetrates into the mirror, n_{out} is the refractive index of the medium where the wave exists from the mirror and M is the number of mirror-pairs. It is important to choose n_{in}, $n_{\mathrm{out}} < n_{\mathrm{H}}$, so that a phase-matched overlay is guaranteed. If any of the two surrounding media has a larger refractive index than n_{H}, the DBR with the optically thinner layer (n_{L}) must be faced to this layer in order to obtain the necessary phase shift of π during the transition to the optically denser medium. This situation must be taken into account in the manufacture of wavelength tunable filters on a semiconductor based substrate as described in Chapter 3. Equation (2.14) makes clear that for a large ratio of $n_{\mathrm{H}}/n_{\mathrm{L}}$, very high reflectivities can be achieved even with a small value of M. This plays an important role in the selection of the DBR materials, since not only the maximum reflectivity but also the spectral reflection stopband depends on the refraction indices. In general, the larger the differences, $\Delta n = n_{\mathrm{H}} - n_{\mathrm{L}}$, the wider the stopband. The stopband width can be calculated using the matrix transfer method [40]. The stopband can be roughly estimated from [6]

$$\lambda_{\mathrm{stop}} \approx \frac{2\lambda_{\mathrm{Bragg}}\Delta n}{\pi n_{\mathrm{gr}}}, \tag{2.15}$$

with group index $n_{\mathrm{gr}} = n - \lambda \frac{dn}{d\lambda}$ at λ_{Bragg}. A simulated reflection spectra correspond to a DBR of 11.5 pairs of SiN_x/SiO_y with $n_{\mathrm{L}} = 1.44$ and $n_{\mathrm{H}} \approx 1.90$ ($\Delta n = 0.46$) is

shown in Fig. 2.4. The dielectric material combination exhibits a 3-dB stop bandwidth $\Delta\lambda_{\text{stop,3-dB}}$ of $= 333\,\text{nm}$.

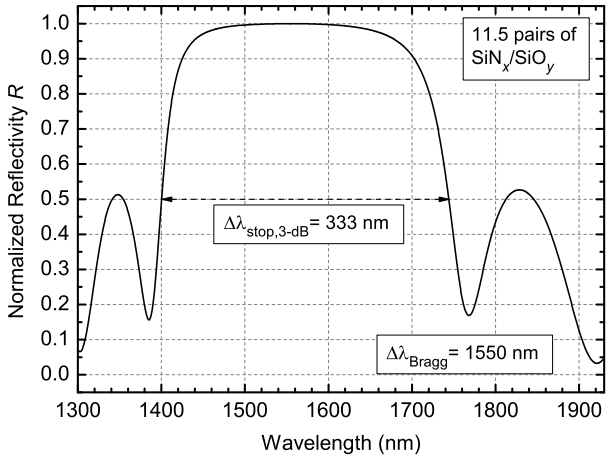

FIGURE 2.4: Simulated reflection spectrum of a DBR consisting of 11.5 pairs of $\text{SiN}_x/\text{SiO}_y$ dielectrics for Bragg wavelength $\lambda_{\text{Bragg}} = 1550\,\text{nm}$.

For calculating the total cavity length, one has to consider the depth of the DBR up to which the electromagnetic field can effectively penetrates. As the partial reflection takes place at each interface, the amplitude of the field also decays as it propagates further. This results in an exponentially decay along the DBR layers. For small refractive index differences $\Delta n \ll n_{\text{L}}$, the effective penetration depth $L_{\textbf{eff}}$ in a DBR mirror with M pairs can be calculated as follows:

$$L_{\text{eff}} = \frac{\lambda_{\text{Bragg}}}{4\Delta n} \cdot \tanh\left(\frac{{n_{\text{H}}}^2 - {n_{\text{L}}}^2}{2n_{\text{H}}n_{\text{L}}} \cdot M\right) \approx \frac{\lambda_{\text{Bragg}}}{4\Delta n} \tag{2.16}$$

However, the condition $\Delta n \ll n$ is only valid for semiconductor based DBRs, where only a small change in refractive index can be achieved by gradually changing tertiary or quaternary material composition.

2.2 Vertical-Cavity Surface-Emitting Laser

Although a FP resonator differs, in principle, in many ways from an active device like VCSEL, the significant difference lies in the light emitting material within the resonator. Many of the approximations regarding mode spacing in the FP resonator are not valid in the case of laser resonators. Nevertheless, the theories related to the beam waist of the sustained mode, the geometry of the top DBR and the mode propagation persist in this case.

2.2.1 Principles of Operation

A basic VCSEL resonator consists of a light-emitting active zone sandwiched between two mirrors. The optical axis of the VCSEL resonator is perpendicular to the wafer plane and thus, along the growth direction of the semiconductor crystals. Hence, a VCSEL resonator length is much shorter compared to that of an EEL. Accordingly, the active zone is also short – enabling a small round-trip gain for the photons generated through stimulated emission. Therefore, VCSELs require special measures for reducing the losses. These include integration of highly reflective mirrors such as DBRs ensuring the proportion of the out-coupled light is reduced. The active zone is predominantly embedded in a *p*-*n* junction. An electrical voltage across the junction results in a diode current of electrons and holes leading to the injection of free charge carriers into the active zone, where an occupancy inversion can be achieved. These electron-hole pairs are then available for the radiative recombination, i.e., for generation and multiplication of photons. In order to further increase the recombination rate in the active zone, quantum wells (QW) surrounded by energy barriers are integrated into the VCSEL structure. These heterostructures lead to a strong localization of the electrons and holes and also favor the recombination of electron-hole pairs. In order for lasing to occur, the gain provided by the active region must outweigh the overall losses of the resonator. By creating the active zone at a maxima of the standing-wave field, the light-matter interaction can be further strengthened. An electric pump current is inserted from ohmic contacts situated on the top epitaxial side (see Fig 1.1). The conductive backside of the substrate completes the circuit. Several methods have been successfully implemented to confine the current to a well-defined active region. Widely used confinement techniques are simple mesa etching of the top mirror, additional ion implantation (creates highly resistive semiconductor regions), selective lateral oxidation of a semiconductor layer with high aluminum (Al) content (for example, $Al_{0.98}Ga_{0.02}As$ or even AlAs) [6] and implementation of buried tunnel juctions (BTJs).

2.2.2 Rate Equations

A single mode laser can be well described with a reservoir theory ensuring the conservation of the particles [5]. The change of the density rate of free carriers i.e., electrons in the conduction band and photons in the optical energy in the laser cavity are formulated in a set of two equations, which are widely known as rate equations of lasers. The rate equations for a semiconductor diode laser can be written as:

$$\frac{dN}{dt} = \frac{\eta_\mathrm{i} I_\mathrm{L}}{qV} - (R_\mathrm{sp} + R_\mathrm{nr} + R_\mathrm{l}) - \upsilon_\mathrm{g} g S \tag{2.17}$$

$$\frac{dS}{dt} = \Gamma \upsilon_\mathrm{g} g S - \frac{S}{\tau_\mathrm{p}} + \Gamma R'_\mathrm{sp}. \tag{2.18}$$

The first equation states the temporal increase of the carrier density N by combining the generation and recombination contributions. With a injection current I_{L}, the number of electrons per second being injected to the active region can be referred to $\eta_{\mathrm{i}} I_{\mathrm{L}}/qV$, where, η_{i} represents the fraction of electron effectively injected to the QWs and V is the active region volume occupied by electrons. The recombination processes include spontaneous recombination R_{sp}, non-radiative recombination R_{nr} (mostly due to crystal defects or surface imperfection as well as Auger recombination), and carriers leakage R_{l} (due to splashing out of the active region by thermionic emission of lateral diffusion). The last term $\upsilon_{\mathrm{g}} g S$ with g being gain per unit length and S being the number of photons, represents the photon-stimulated net electron-hole recombination which generates more photons through a gain process.

Equation (2.18) relates different gain and loss mechanisms contributing to the temporal change of S. Since the cavity volume occupied by photons, V_{P} is usually larger than V, the photon density generation rate R_{st} is multiplied by the confinement factor $\Gamma = (V/V_{\mathrm{P}})$. The photons leaves the cavity at a rate of S/τ_{p}, where τ_{p} is the decay constant at which photons decay constantly in the absence of and generation mechanism. A part of it is the out-coupled light coming through the mirror whereas the rest of the photons exit the cavity through free carrier absorption in active region, absorption outside active region and scattering at the rough surface. The term R'_{sp} is the amount of spontaneous emission that is resonant with the cavity and within the same longitudinal mode as the coherent light.

By setting the time derivatives to zero, one can obtain the steady-state solution of Eqs. (2.17) and (2.18) [5]. Solving Eq. (2.18) for the steady-state photon density and Eq. (2.17) for the DC current, one obtains the following equations as function of N:

$$S(N) = \frac{\Gamma R'_{\mathrm{sp}}(N)}{1/\tau_{\mathrm{p}} - \Gamma \upsilon_{\mathrm{g}} g(N)}, \tag{2.19}$$

$$I(N) = \frac{qV}{\eta_{\mathrm{i}}}(R_{\mathrm{sp}}(N) + R_{\mathrm{nr}}(N) + \upsilon_{\mathrm{g}} g(N) S(N)). \tag{2.20}$$

Solving for $\upsilon_{\mathrm{g}} g S$ in Eq. (2.19), and using the relationships in Eq. (2.22) below to define g_{th}, Eq. (2.20) can alternatively be written as

$$I(N) = \frac{qV}{\eta_{\mathrm{i}}}(R_{\mathrm{sp}}(N) - R'_{\mathrm{sp}}(N) + R_{\mathrm{nr}}(N) + \upsilon_{\mathrm{g}} g_{\mathrm{th}} S(N)). \tag{2.21}$$

The threshold gain and carrier density are

$$\Gamma \upsilon_{\mathrm{g}} g_{\mathrm{th}} \equiv \frac{1}{\tau_{\mathrm{p}}} \qquad \text{and} \qquad g(N_{\mathrm{th}}) = g_{\mathrm{th}}. \tag{2.22}$$

As $N \to N_{\mathrm{th}}$ and $\Gamma \upsilon_{\mathrm{g}} g \to 1/\tau_{\mathrm{p}}$, one can evaluate all terms in Eqs. (2.19) and (2.20) at N_{th} except for the denominator of (2.19) which contains the difference between the

threshold gain and the actual gain:

$$S(N) = \frac{R'_{\mathrm{sp}}(N_{\mathrm{th}})/\upsilon_{\mathrm{g}}}{g_{\mathrm{th}} - g(N)}, \tag{2.23}$$

$$I(N) = \frac{qV}{\eta_{\mathrm{i}}}(R_{\mathrm{sp}}(N_{\mathrm{th}}) + R_{\mathrm{nr}}(N_{\mathrm{th}})) + \frac{qV}{\eta_{\mathrm{i}}}\upsilon_{\mathrm{g}} g_{\mathrm{th}} S(N)). \tag{2.24}$$

The threshold current of the laser is defined as

$$I_{\mathrm{th}} = \frac{qV}{\eta_{\mathrm{i}}}(R_{\mathrm{sp}}(N_{\mathrm{th}}) + R_{\mathrm{nr}}(N_{\mathrm{th}})). \tag{2.25}$$

By using Eq. (2.25), one can represent the relation between the optical output power P_0 with the current above threshold as

$$I = I_{\mathrm{th}} + \frac{q}{h\nu}\frac{P_0}{\eta_{\mathrm{i}}\eta_0}. \tag{2.26}$$

Small-Signal Modulation Behavior

When the injection current of a VCSEL is modulated in small-signal domain, the response from the device comprises the individual responses of the internal and package parasitic networks as well as the intrinsic device properties. To attain high modulation bandwidths with directly modulated VCSELs, both the extrinsic device parasitics and the intrinsic modulation properties have to be taken care of. In ideal case, a VCSEL is divided into three main cascaded subsections: the package or mount parasitics, the parasitics associated with the semiconductor chip, and the intrinsic laser (active layer and cavity) properties. Parasitics associated with the package generally include bond-wire inductance, small capacitance between the input terminals and the capacitance originated from the submount. However, these parasitics can be either reduced to a great extent or completely eliminated if the laser is monolithically integrated with its drive circuitry [42]. Therefore, it is wise approximation to scheme a cascaded two-port model to separately discuss intrinsic and parasitic influences on the modulation response. In such cases, the overall electrical modulation frequency response can be written as a linear convolution of the parasitic network response with the internal response of the intrinsic laser in the small-signal domain which is as follows:

$$H(f) = \eta_{\mathrm{L}}\eta_{\mathrm{PD}} \cdot \frac{f_{\mathrm{R}}^2}{f_{\mathrm{R}}^2 + j\frac{\gamma}{2\pi}f - f^2} \cdot \frac{1}{1 + j\frac{f}{f_{\mathrm{par}}}}. \tag{2.27}$$

Here, the constant terms namely, η_{L} and η_{PD} are the differential quantum efficiencies of the VCSEL and photodetector, respectively. The following two factors constitute a three-pole filter function of the relaxation resonance frequency f_{R}, intrinsic damping

coefficient γ and a parasitic cut-off frequency f_{par}. The first factor describes the intrinsic modulation response whereas the second factor represents the parasitic effect. In Appendix A, a detailed mathematical derivation of the term f_{R} according to the rate-equation analysis is attached [5]. f_{R} can be written as

$$f_{\mathrm{R}} = \sqrt{\frac{\upsilon_{\mathrm{g}} a N_{\mathrm{P}}}{\tau_{\mathrm{P}}}} = \sqrt{\frac{\upsilon_{\mathrm{g}} a \eta_{\mathrm{i}}}{q V_{\mathbf{P}}}} \sqrt{I - I_{\mathrm{th}}} \equiv D\sqrt{I - I_{\mathrm{th}}} \tag{2.28}$$

for a single-mode VCSEL. The proportionality factor D is denoted as the D-factor of the laser. In practice, a large D-factor is favorable for reaching a high f_{R} before thermal saturation comes into play. As can be seen, an increased differential gain a and reduced photon lifetime τ_{P} would yield the favored increase in f_{R}. On the other hand, adding strain to the quantum wells and reducing the mode-volume V_{P} raises a and lowers τ_{P}, respectively. Consequently, f_{R} can be increased. Since f_{R} saturates at high ambient temperatures, the D-factor is evaluated at low currents, where self-heating effects are negligible. At higher temperatures, the D-factor is lowered by the reduction in η_i due to carrier leakage from the QWs, and the reduced a due to the higher carrier concentration required to reach the threshold material gain at elevated temperatures. As another figure of merit, the modulation current efficiency factor (MCEF) specifies the increase of the 3-dB corner frequency of the modulation response against the square root of the current above threshold.

$$\mathrm{MCEF} = \frac{f_{3dB}}{\sqrt{(I - I_{\mathrm{th}})}}. \tag{2.29}$$

Using the simplified definition of f_{R} one can rewrite the damping factor as

$$\gamma = K f_{\mathrm{R}}^2 + \gamma_0 \tag{2.30}$$

where,

$$K = 4\pi^2 \tau_p \left[1 + \frac{\Gamma a_p}{a}\right] \qquad \text{and} \qquad \gamma_0 = \frac{1}{\tau_{\Delta N}} + \frac{\Gamma R'_{\mathrm{sp}}}{S} \tag{2.31}$$

The so-called K-factor describes the damping of the response for large f_{R}. The damping factor offset γ_0 is important at low powers where the f_{R} is small. Its significance arises from the fact that the maximum 3-dB modulation corner frequency is related to K-factor as

$$f_{\text{3-dB, max}} = \sqrt{2}\frac{2\pi}{K}. \qquad (\gamma/\omega_{\mathrm{R}} = \sqrt{2}) \tag{2.32}$$

indicating the intrinsic modulation limit of the laser without any parasitic effects [6, 43]. In practice, K and γ_0 are used as fitting parameters to be extracted from the laser modulation response. The K-factor is usually determined by plotting γ as a function of

the and f_R squared, where both γ and f_R are obtained from curve fits to the measured data. The VCSEL f_R will keep increasing with $\sqrt{(I - I_{th})}$ until the photon density saturates due to thermal effects. By setting $\gamma = 0$ in the first factor (intrinsic modulation response) of Eq. (2.32), the thermally limited modulation bandwidth can be estimated as

$$f_{3\text{-dB}} = f_R\sqrt{1+\sqrt{2}} \approx 1.55 f_R \qquad (\gamma/\omega_R \ll 1) \tag{2.33}$$

The modulation bandwidth increases linearly with f_R and remains about 50% larger than f_R until damping becomes strong [6]. With strong damping the bandwidth is compromised and eventually decreases with further increases in f_R and γ. The optimum damping and maximum bandwidth can be determined by the K-factor, which in turn is determined by the photon lifetime of the cavity. The K-factor therefore defines the intrinsic modulation bandwidth capabilities of the laser.

Relative Intensity Noise (RIN)

Statistical fluctuations in the output power of a VCSEL occurs due to random recombination processes, even without modulation or noise of the current source. The measurement of relative intensity noise (RIN) provides a measure of the intensity fluctuations (optical intensity noise) as well as an alternative and very simple method for determining the intrinsic laser dynamics, excluding parasitic influences and transport effects. Besides small-signal modulation analysis and RIN measurements, the high-resolution measurement of the optical spectrum is e.g., in the heterodyne method, provides the third possibility for determining the relaxation oscillation frequency [22]. RIN can be associated with the signal-to-noise ratio (SNR) in analog data transmission. It relates the spectral power density of the intensity noise $S_p(f)$ to the average value of the output power (with coefficients A and B) [5, 22]:

$$\frac{\text{RIN}}{\Delta f} = \frac{S_p(f)}{{P_{0,\text{opt}}}^2} = \frac{1}{P_{0,\text{opt}}}\left(\frac{A + Bf^2}{{f_R}^4}|H(f)|^2 + \frac{h\nu}{\eta_{\text{PD}}}\right), \tag{2.34}$$

The RIN is alo relative to the filter bandwidth Δf of the electrical spectrum analyzer used in the measurement and expressed in the unit dB/Hz [22]. The second frequency-independent term describes the lower limit by the quantum shot noise in the receiver with photodetector sensitivity η_{PD}. The RIN is small at lower frequencies, independent of the attenuation [$Bf^2 \gg A$] (unlike $|H(f)|^2$) [5], and maximum at the relaxation resonance frequency. With increasing output power (or operating current), the first term decreases with ${P_{0,\text{opt}}}^{-3}$, the maximum at f_R flattens and shifts to higher frequencies.

Resonance Wavelength Tuning

The main mechanism for tuning a laser is to change the effective optical cavity length L_0 and thus the emission wavelength λ, as can be seen from

$$L_0 = n_c L_c = m\frac{\lambda}{2}, \tag{2.35}$$

where L_c is the geometrical cavity length, n_c the effective refractive index, m is the mode number. In the case of a laser resonator integrated with a gain medium, the tuning of the wavelength may be caused by the change in the temperature and charge carrier-dependent refractive index. The small decrease in refractive index with increasing carrier density, has a negligible effect on the emission wavelength compared to the thermal wavelength shift, e.g., caused by self-heating with the operating current. An increase of the temperature leads to a change of the refractive index and thus to an increase of the wavelength. The wavelength change over temperature is typically 0.09 to 0.12 nm/°C and limited to a continuous tuning range of few nanometers for standard VCSEL. The third mechanism is to change the cavity length mechanically by implementing, for example, a microelectromechanical system (MEMS) movable mirror. In this work a concavely bent MEMS-DBR is used for wavelength tuning. The curved top mirror and the flat bottom mirror of the active VCSEL structure form a plane-concave FP cavity. This type of cavity is much more insensitive to tilt angles between the two mirrors as compared to cavities consisting of two plane mirrors. One can clearly see from Eq. (2.6) the advantage of having a shorter cavity length as far as wide mode-hop free tuning is concerned. For an $L_c \approx 10\lambda$, as an example, the $\mathrm{FSR}_\lambda \approx \lambda/20 \approx 80\,\mathrm{nm}$ at a wavelength of $\lambda = 1550\,\mathrm{nm}$. Because of the limited amplification bandwidth g of the gain medium and the losses α of the passive resonator, only one longitudinal mode has a sufficient amplification for lasing in case of a large FSR. Figure 2.5 illustrates the principle of a continuously tunable laser based on its wavelength-selective elements. The intrinsic longitudinal single-mode behavior of the MEMS VCSEL allows a continuous tuning of the wavelength. Another advantage is the tuning efficiency. A change in the distance of the two resonator mirrors

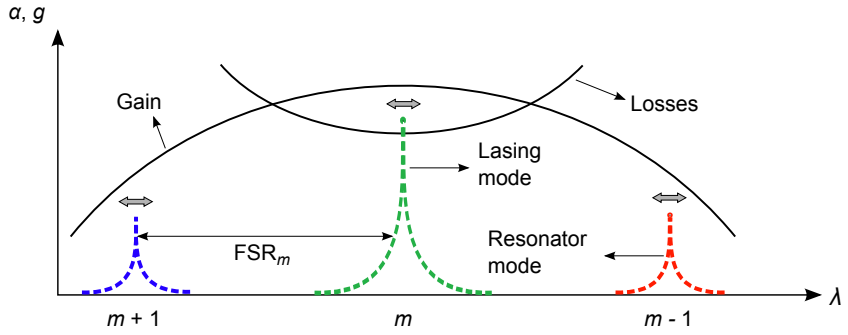

FIGURE 2.5: Principle of a continuously tunable laser with a short resonator. Lasing mode is realised as the material gain of the active zone outweighs the cavity losses.

of $\Delta\lambda$ leads to a linear shift of the wavelength $\Delta\lambda$ with

$$\Delta\lambda = \Delta L \frac{2}{m} \tag{2.36}$$

whereas m is the order of the longitudinal mode. In a typical resonator length of $L = 10\lambda$ one gets $m = 20$ and consequently $\Delta\lambda = 0.1\Delta L$. Whereas a typical edge emitter with $L = 450\lambda$ has a tuning efficiency of only $\Delta\lambda\ /\Delta L \approx 0.005$ which is twenty times smaller. Thus a reduction in the resonator length also increases the tuning efficiency. Nevertheless, a tuning over the whole FSR requires a change of the resonator length of $\Delta\lambda = \lambda/2 \approx 780\,\text{nm}$, which is independent of the resonator length.

2.2.3 Optical Data Transmission using VCSEL

In this work, direct current amplitude modulation using binary signal is employed for optical data transmission using MEMS VCSEL. For analyzing the received signal and for qualitatively evaluating the transmission system, bit error ratio (BER) measurements and optical eye-diagrams are briefly discussed.

Large-Signal Digital Modulation

Although small-signal analysis gives an estimation of the bandwidth capability of a the VCSEL, modulation analysis in the large-signal domain are often essential to evaluate the performance in real digital data transmission systems. An electrically modulated signal of certain amplitude with peak-to-peak voltage (V_{pp}) is applied to the VCSEL using a bias-tee. The bias-tee combines the modulation signal with the DC bias point and prevents the DC to enter the AC signal generator. As shown in Fig. 2.6 the value of V_{pp} is selected in a way so that the dynamic range of the light–current–voltage (L-I-V) characteristics can be fully utilized in order to attain a high SNR at the receiving end. Consequently, an appropriate operating bias point is set in the linear region to fit the modulation current range between the VCSEL threshold and the rollover current. Thus the minimum and maximum currents result in a modulation of the optical power between $P_{1'}$ and $P_{0'}$, as indicated in Fig. 2.6.

In comparison to small-signal modulation, the large-signal measurement quantifies important parameters such as rise and fall times, Extinction ratio, modulation amplitude, and jitter – which play important roles in digital data transmission. While the bandwidth can be estimated mostly from the 3-dB small-signal bandwidth, further parameter such as turn on delay and turn on jitter in case of bias-free operation with $I_{'0'} < I_{\text{th}}$ or pattern effects are of importance in high speed VCSELs. In addition, one should consider the

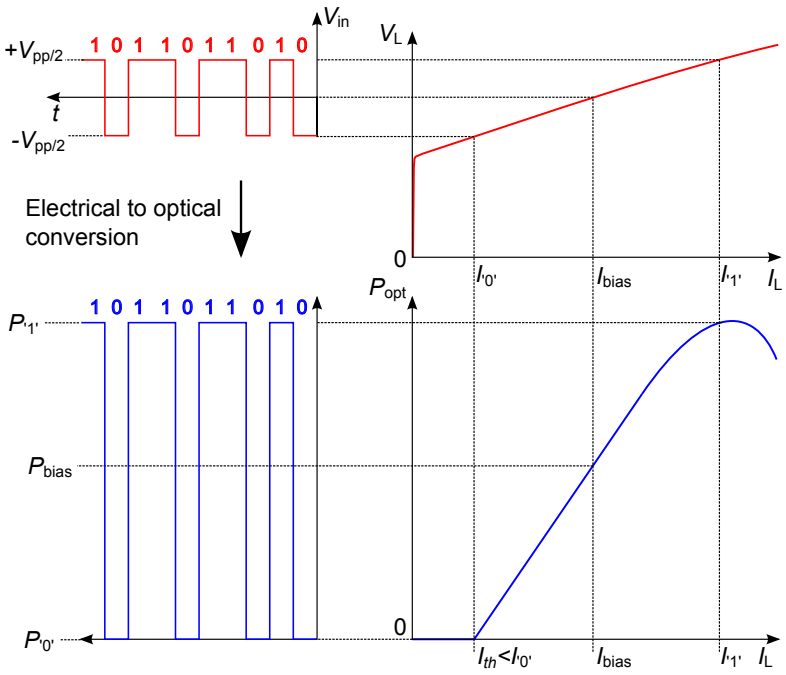

FIGURE 2.6: Large-signal digital modulation of a standard VCSEL with a set of bias points.

intensity noise originating from the mode completion between the transverse modes of different order or polarization, since it will degrade the SNR at the receiver [44].

Bit Error Ratio (BER)

In digital data transmission a common system-evaluation method is to count the number of erroneous bits received over a sufficiently long period of time. The number of received errors over the number of transmitted bits during a certain time interval is usually defined as bit error rate (BER) and usually expressed as ten to a negative power. Unlike many other forms of assessment, BER estimates the actual performance of a system in operation to be tested, rather than testing the component parts. For fiber optic systems, bit errors mainly result from imperfections in the components used to make the link including the optical driver, receiver, connectors and the fiber itself. The main reasons for the degradation of a data channel due to dispersion and attenuation and the corresponding BER is noise, interference, and phase jitter along the propagation path.

A knowledge of the BER also enables other features of the link such as the power and bandwidth, etc. to be tailored to enable the required performance to be obtained. The interference levels present in a system are generally set by external factors and cannot be changed by the system design. Different orders of modulation schemes plays an important role. Another approach that can be adopted to reduce the BER is to reduce the bandwidth. Lower levels of noise will be received and therefore the signal to

noise ratio will improve. However, this is at the expense of data throughput. However, even with a BER below what is ideally required, further trade-offs can be made in terms of the levels of error correction that are introduced into the data being transmitted. Although more redundant data has to be sent with higher levels of error correction, this can help mask the effects of any bit errors that occur, thereby improving the overall bit error rate. One can obtain the value of BER by simply diving the error rate by the sent bit rate B. The relation between BER, the incident average optical power and the bit rate can be written as

$$\mathrm{BER} = \frac{1}{2} \exp\left[\frac{2\eta_{\mathrm{PD}}\langle P_{\mathrm{opt.i}}\rangle}{B \cdot \hbar\omega_{\mathrm{opt}}}\right] \tag{2.37}$$

Which can be further formulated to

$$\ln(\mathrm{BER}) = \ln\frac{1}{2} - \frac{2\eta_{\mathrm{PD}}\langle P_{\mathrm{opt.i}}\rangle}{B \cdot \hbar\omega_{\mathrm{opt}}}. \tag{2.38}$$

This relation results in a set of liner curves with a parameter B, if plotted in a semi-logarithmic Cartesian system. The probability of errors per bit of BER $\approx 10^{-9}$ is often required for a quasi error-free optical data transmission.

Optical Eye Diagram

An optical eye diagram is an intuitive graphical representation often used for evaluating the quality of a received digital waveform. The signal quality such as amount of intersymbol interference (ISI), amplitude variations, and time variations (jitter) can be assessed from the appearance of the eye. In an eye a digital signal from a receiver is repeatedly sampled and applied to the vertical input, while the data rate B is used to trigger the horizontal sweep. When the binary signals are received at the photodetector, discrete mean photocurrents of $\langle I_1\rangle$ and $\langle I_0\rangle$ corresponding to logical 1 and 0, respectively, are generated. The probability density of these photocurrents have their Gaussian distributions of $\langle I_1\rangle$ and $\langle I_0\rangle$, respectively. Then, the eyes can be generated by an oscilloscope that is triggered by the symbol timing clock. An exemplary optical eye is shown in Fig. 2.7, where the number of logical 0s and 1s are sent with equal probability (50%). Different communication applications have their standard eye masks which define the quality requirements for the protocols. One aspect of the eye opening is the difference between the amplitudes of the different logical stages which are included in the modulation of the communication link. The eye-opening, often defined by the extinction ratio (ER), is considered as one of the most significant indicators of the quality of a transmission link. For a binary transmission it is the difference between the respective amplitude levels which represent the 0-bit and 1-bit logic level. To obtain a small BER performance, a significant separation between the corresponding logical ‘1’ and logical

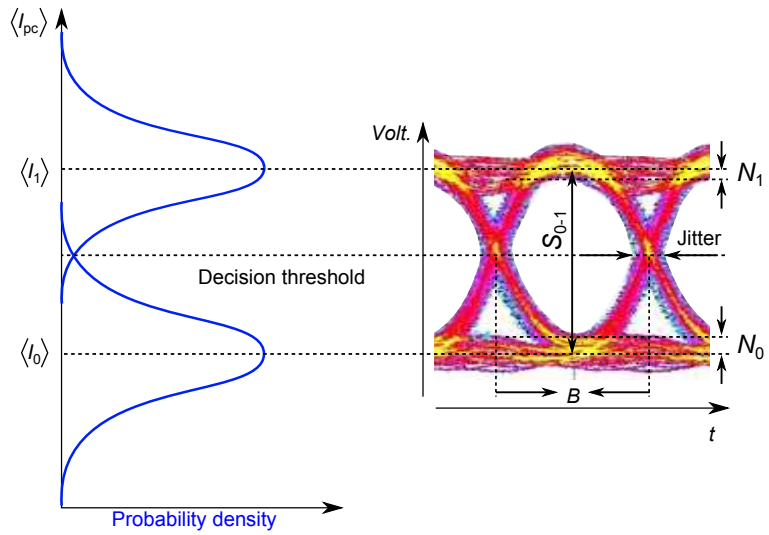

FIGURE 2.7: The SNR of the measured eye with a bit rate of B measured with an oscilloscope.

'0' power level is required. In order for the extinction ratio to be independent on the absolute position of the logic levels and thus solely representing the opening of the eye, the distance to either logic level has to measure from a predefined and calibrated reference level. Superposing all the various symbol transitions of a long pseudo-randomly generated bit sequence is one bit period and at their respective decision times, one can obtain the eye diagram as shown in Fig. 2.7. For a small BER, the eye should be as open as possible. Thus, an estimation of the system performance is obtainable by measuring the width and height of the eye opening in horizontal and vertical direction, respectively. Jitter, for example, caused by variations of the pulse durations (phase noise) or the imprecise recovery of the symbol clock, will close the eye in horizontal direction. Thus, the optimum sampling point for the decision level is decided at the time of highest vertical opening. The amplitude noise and the effects of ISI in the system reduce the vertical eye opening. Therefore, the sampling point corresponds to the time of the maximum SNR whose value from the measured eye diagram can be automatically performed by the oscilloscope (Fig 2.7). Here, N_0 and N_1 are the standard deviations of the electrical noise amplitude at 0 and 1 level, respectively, whereas $S_{0\text{-}1}$ is the distance between both mean signal levels. Due to the relations $\langle P_{\text{opt.i}} \rangle$ is proportionate to the photocurrent I_{pc}, the SNR $= S_{0\text{-}1}/(N_0 + N_1)$ of the electrical signal is also corresponds to the SNR of the optical signal.

2.3 Orbital Angular Momentum of Light

Orbital angular momentum (OAM) is one of the most fundamental physical quantities in both classical and quantum mechanics. Light carries angular momentum comprising

both spin angular momentum (SAM) which is associated with polarization, and OAM component originating from the spatial profile of light intensity and the phase. Due to photon helicity SAM can exist in left- or right-handed circularly polarized light. In 1992, Allen *et al.* identified that any helically phased optical vortex (OV) beam carrying a topological charge within an azimuthal term $\exp(i\ell\varphi)$ inherently possesses an OAM of $\ell\hbar$ ($\hbar = h/2\pi$) carried by each single photon; where integer ℓ is the topological charge, φ is the azimuthal angle, and h is the Planck constant [45]. An OV is a special kind of optical singularity that possesses a spiral phase wave front around a singularity point, and universally characterized by the dark central region – a consequence of destructive interference phenomena that gives the beam the typical doughnut-shaped intensity distribution. The spiral phase of vortex beams rotates around the optical axis which causes the wavefront of the light to twist like a corkscrew as it propagates. The higher the number of the twist, the faster the light is spinning around the propagation axis. Topological charges correspond to the strength of the central singularity and can be distinguished by the number of twists the light experiences in one wavelength of propagation. The number of topological charge can be positive or negative, depending on the handedness of the twist. The OAM in an OV beam can be adjusted by either changing ℓ, or by increasing the photon flux. However, since the radius of an OV scales with its helicity, applications that need controlled geometry or photon density is limited to fixed OAM [46].

In the paraxial regime, OAM beams can be described as a superposition of Laguerre–Gaussian (LG) modes. Considering cylindrical coordinates, in a plane orthogonal to the beam propagation direction and passing through the beam waist, the amplitude of the LG modes can be written as:

$$u(r,\varphi,z) = E_0 \left(\frac{\sqrt{2}r}{w}\right)^{l} {L_\rho}^{\ell}\left(\frac{2r^2}{w^2}\right) \frac{w_0}{w(z)} \exp\left[-i\phi_{\rho\ell}(z)\right] \exp\left[-i\frac{kr^2}{2q(z)}\right] \exp(i\ell\varphi) \quad (2.39)$$

where ρ is the number of radial nodes on a plane perpendicular to the direction of propagation (the intensity pattern exhibits $\rho+1$ concentric rings around the central dark zone of phase singularity), ℓ is the topological charge, ${L_\rho}^{\ell}(x)$ is the associated Laguerre

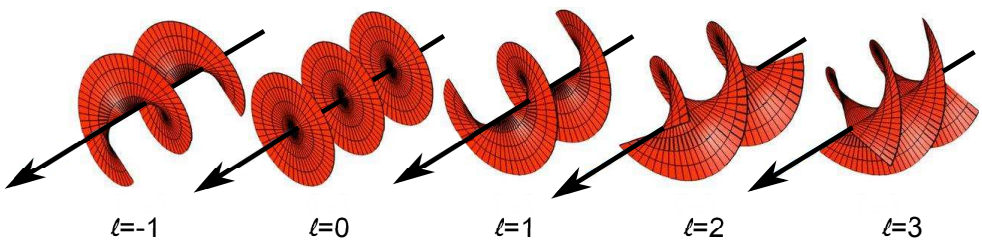

FIGURE 2.8: The helical wavefronts of different Laguerre-Gaussian modes. The index ℓ refers to the topological charge number. The handedness of the helical wave fronts of the LG modes is linked to the sign of the index ℓ, and can be chosen by convention.

polynomials, $w(z)$ is Gaussian beam size, $\phi_{\rho\ell}(z) = (2\rho+l+1)\tan^{-1}(z/z_0)$ is Gouy phase shift and $z_0 = \pi {w_0}^2/\lambda$ is Rayleigh range. For $l = \rho = 0$, the solution reduces to the fundamental Gaussian beam solution. For $l \neq 0$, the LG mode has a vortex phase term $\exp(il\varphi)$. Here φ represents the distinctive, transverse vortex phase profile, impressing a linear phase increase in the azimuthal direction to the field. In contrast to SAM which has only two possible polarization states $\pm\hbar$, OAM can provide an infinite range of states due to its theoretically unlimited values of ℓ. Figure 2.8 shows the helical wavefronts of Laguerre-Gaussian (${LG^{\ell}}_{\rho}$) modes with 5 different values of ℓ. The handedness of the helical wave fronts is linked to the sign of the index ℓ. The utilization of these OAM modes as an additional orthogonal basis of information carriers in both free space [33, 47] and optical fiber [32] communication systems potentially enhances the transmission capacity tremendously. In addition, since the first demonstration of OAM beams they found their ways to a diverse range of applications including but not limited to optical manipulation [48], quantum information [49, 50], optical trapping [51], optical tweezers [52], optical vortex knots [53], astronomy [54], optical microscopy [55], remote sensing [56] and imaging [57].

OAM Beam Generation

OAM beams can be obtained by applying a spiral phase distribution onto an input Gaussian beam. This can be readily realized by employing phase modifying devices (PMDs). However, as far as current realizations of OAM-based transmission systems are concerned both generation and detection of OVs is predominantly provided by discrete, bulk optical devices such as liquid crystal (LC) based spatial light modulators (SLMs) [33, 34]. Both reflective and transmissive SLMs are commercially available in the market. LC SLMs are either optically or electrically addressed and can modulate the amplitude, the phase, or both, for the input field. For phase-only LC SLMs, birefringent LC molecules can be viewed as individual wave plates whose fast axis are modeled as directors. By applying electric field across LC molecules, the angle between the wave vector k of the input electric field and the director, or fast axis of the wave plate can be changed. Thus the birefringence of the LC molecules can be adjusted by varying the voltage applied. Other techniques used for OAM beam generation include separate spiral phase plate (SPP) [35, 36], computer generated hologram (CGH) [58], deformable mirror [59], diffractive optical elements (DOEs) [60], and optic fiber [61], glued hollow axicons [62], form-birefringent elements [63, 64] and microscopic ring resonators [65]. In case of segmented deformable mirrors, the tilt of every segment is controlled to get a helical surface in order to generate the OAM beam although it is still difficult to control and not convenient. However, most of the above mentioned approaches require operations with free space beams as well as precise alignment of the elements. Moreover, high sensitivity of the system to mechanical vibrations, and increased losses due to reflection

are also matters of concern. This type of construction cannot provide robustness and repeatability, and the efficiency of their involvement into industrial applications appears questionable. Hence, development of the compact, on-chip integrated optical components for generation, processing and detection of vortices is the next significant step towards robust, energy- and cost-effective OAM-based communication systems. This is the motivation to utilize the micro-sized SPPs.

Spiral Phase Plate

A spiral phase plate (SPP) is a passive helicoidal transmission optical element whose optical thickness increases azimuthally while preserving the direction of the optical axis. The phase difference between the starting and the ending point determines the generated topological charge. SPPs are built for a specific wavelength at which the maximum fainting along the optical axis is obtained. Therefore, the height of the spiral needs to be precisely engineered to produce the desired topological charge from the incident wavelength. A nano-fabrication process to produce this kind of structure is needed to precisely control the spiral geometry and to accurately fulfill the design requirements of the optical device. In particular, the optical quality of the fabricated SPP mask depends on a good shape definition of the spiral, on the smoothness of the mask, and on the resolution of central singularity and phase step. Two photon abortion lithography represents a powerful tool to generate this kind of structure, due to the possibility to realize continuous surface profiles, high flexibility in the elements design, and good optical quality of the fabricated reliefs [66]. The "spiral staircase" with a certain number of steps progressively build the total phase gap h_s after a complete rotation of the azimuthal angle φ. When the number of steps N is finite, a so-called multi-level or stepped SPP is constructed, where each equidistant step introduces a constant phase variation. Figure 2.9 shows SPPs of different orders where the thickness of the plates

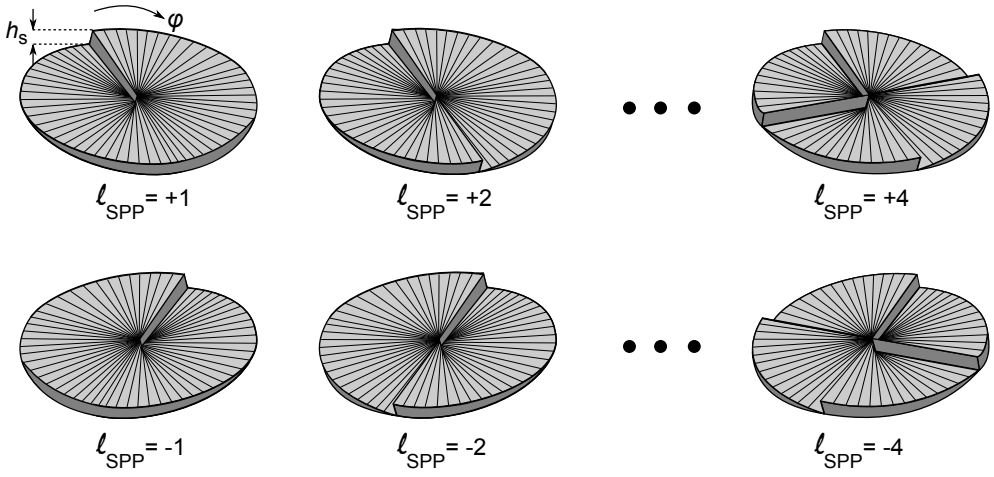

FIGURE 2.9: SPPs of different topological charge and their conjugates.

increases azimuthally around the central axis of the plate. In case of a continuous SPP with $N \to \infty$ the phase of the light is modulated smoothly and continuously. Consequently, the quality of the output beam also increases with the number of phase steps. For an ℓ-fold SPP with an estimated height h_s depends on the azimuthal angle φ according to:

$$h_s(\varphi) = \frac{\varphi \ell \lambda_0}{2\pi(n_p - n_0)}, \tag{2.40}$$

where n_p and n_0 are the refractive indices of the material of the SPP and the surrounding medium (air), respectively. Ideally, the n_p is chosen in a way that SPP is transparent for the transmission wavelength with minimum scattering losses. Figure 2.10 shows how a Gaussian beam ($\ell = 0$) is converted to a OAM beams of $\ell = 2$ using a second order SPP, $\ell_{\mathrm{SPP}} = 2$.

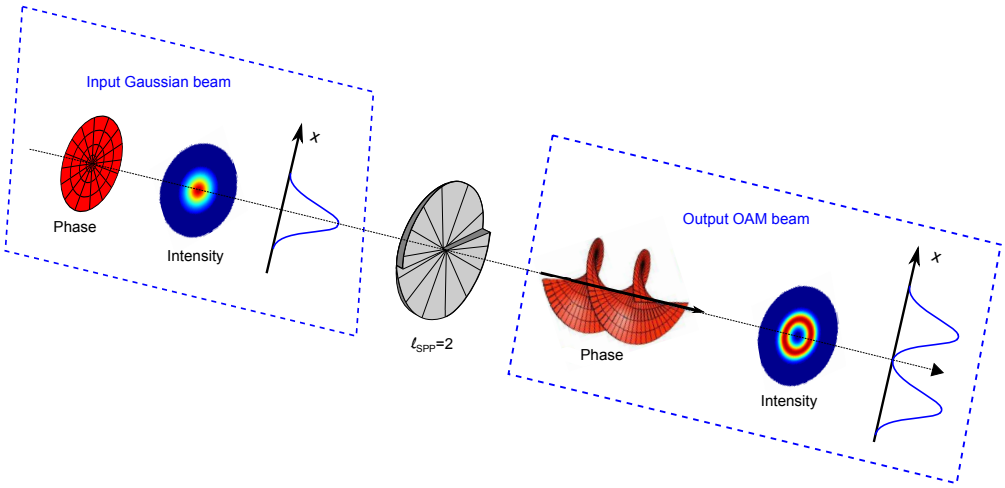

FIGURE 2.10: OAM conversion of $\ell = 0$ (Gaussian TEM_{00}) $\to \ell = 2$ is achieved by using a second order SPP, i.e., $\ell_{\mathrm{SPP}} = 2$.

2.3.1 MEMS OAM-Filters and Their Application

The capacity of optical communication systems based on the existing multiplexing techniques in the time- and frequency domains is often restricted by the nonlinear Shannon limit for single-mode transmission. As a result, bandwidth of the optical communication proves to be insufficient to satisfy the exponentially growing demands for data transfer in the foreseeable future. It is worth mentioning that for a plethora of modern communication applications not only the capacity to length product, but also such factors as energy consumption, space efficiency, latency, and finally the cost of deployment should be involved into consideration. One of the considered ways to prevent the impending capacity crunch is the employment of OAM as an additional degree of freedom. Since

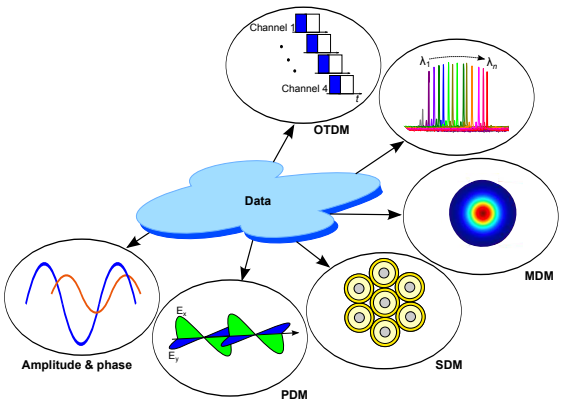

FIGURE 2.11: Different multiplexing techniques in optical fiber communications: OTDM: optical time-division multiplexing, WDM: wavelength-division multiplexing, SDM: spatial-division multiplexing, MDM: mode-division multiplexing, and PDM: polarization-division multiplexing. OAM beams can be regarded as the analogue of MDM with theoretically unlimited orthogonal degree of freedom for data multiplexing.

optical vortices, carrying distinct OAM, form a basis of orthogonal functions, their applicability as independent signal carriers allows for further multiplication of the capacity of optical communication links. In other words, OAM-multiplexing can be treated as a special case of spatial division multiplexing (SDM), where the modal basis is represented by optical vortices. Recently fixed-wavelength VCSEL based direct OAM beam generation has been demonstrated [17]. A dielectric stepped SPP has been deposited on the aperture of a single-mode 860 nm device. However, for future communications based on the converged OAM- and WDM devices capable of functioning simultaneously in both wavelength and OAM domains would be of key importance. Moreover, for communication applications OAM generation at the long-wavelength regime (1300–1600 nm) would be preferred. In this work a novel micro-sized wavelength-tunable component with integrated SPP is proposed and termed as MEMS OAM-filter. The device is basically a FP optical filter which is capable of generating/receiving an orbital angular momentum (OAM) beam of a specific order for a certain wavelength range around the design wavelength of 1550 nm. Figure 2.11 shows different multiplexing techniques in optical fiber communications. A MEMS OAM-filter can be implemented in optical transmission system combing two of those degree of freedoms namely, wavelength and OAM. However, introducing of new techniques should lean upon the achievements of matured, commercially successful techniques. Even though the OAM can provide a theoretically infinite range of discrete states $l\hbar$, practically the efficiency of their excitation decreases with higher values of ℓ. Thus, to multiply the capacity of current optical communications, OAM-multiplexing should be superimposed over the WDM technique. Let us consider a simple optical data transmission system, where N wavelength channels and M OAM channels are multiplexed. Then at the transmitter side N wavelengths from N lasers, carrying $M \times N$ independent information channels, are sent to a set of M SPPs of different azimuthal orders. At the receiver WDM-demultiplexing has to be applied to

each demultiplexed OAM-channel (or vice versa), so the integration of wavelength- and OAM-demultiplexing functions in the same device evidently is advantageous regarding miniaturization and minimization of losses. But in case of using fixed-wavelength WDM filters, the receiver must contain $M \times N$ filters of different types, regardless which wavelength channels are actually in use in each OAM channel. Thus a filter with wide spectral tunability is highly desirable for colorless (de)multiplexing in converged wavelength- and OAM-multiplexed optical networks. First, this approach can provide identity of the devices for the same azimuthal order, as the tunable filters cover the whole spectral range used for WDM transmission and a nomenclature of filters for different wavelengths is not needed. Second, tunable devices provide the possibility for dynamical reconfiguration of the WDM part of the transmission system, which is especially important to enable functionality of software-defined networks (SDN).

There are many challenges both in optical to recover/demultiplex an OAM beam. A major challenge is to determine precisely how much twist the OAM beam contains, if only a small fraction of the beam is captured. The number of OAM beams is theoretically infinite – which will create more difficulties as higher-order OAM beams with more twists spread out faster than lower-order ones. Careful system design will be needed for practical deployment. Specially in fiber communications when OAM signals will be transmitted through silica based core, temperature changes and bends in the fiber can easily alter the beam's phase profile so that some of its power shows up as a wave with a different value of OAM. One possible way of mitigating this issue is with a vortex fiber [32]. In comparison to a normal fiber with a uniform glass core to guide waves, this special fiber contains a waveguide that forms a ring in cross section. It turns out that the size of an OAM beam depends on the amount of twist it has, so beams with different values of OAM will have different levels of overlap with the waveguide. The level of overlap alters the speed at which an OAM beam can travel down the fiber, which helps reduce interaction between beams with different values of OAM. These components can open a big potential in short links inside high-performance computing and data centers.

Chapter 3

Device Structures and Fabrication

The fabrication of high-quality MEMS tunable VCSEL and OAM-filter requires three major undertakings: (*i*) device design, (*ii*) basic structure growth/deposition (without MEMS layers) and processing, and (*iii*) MEMS integration. These tasks are very closely interconnected. After the basic characterization of the fabricated devices, necessary design optimizations are carried out and the above mentioned steps are iterated. This chapter discusses the construction and the fabrication of two devices in separate sections. The first section deals with the short-cavity MEMS VCSEL which includes the structure of the active VCSEL and the integration process of the top MEMS mirror. In the second part, the fabrication of the MEMS OAM-filters are illustrated briefly. The MEMS-DBRs for both components are identical, but the OAM-filters require additional processing steps for integrating the SPPs on to the MEMS.

3.1 MEMS VCSEL

One of the main objectives of this work is to integrate a movable DBR mirror on top of a benzocyclobuthene (BCB)-planarized short-cavity (SC) active VCSEL structure by means of surface micromachining. The bottom active VCSEL structure is fabricated separately on a standard 2-inch InP wafer utilizing a so-called two chip concept[‡]. In order to obtain functioning device it is of utmost importance that the surface micromachining of the MEMS is compatible to the active VCSEL structure processing.

The tunable MEMS VCSEL essentially comprises two parts: The active laser structure which is termed as "half-VCSEL" and the MEMS top DBR. Figure 3.1 (a) shows the top view of a half-VCSEL. The device has a footprint of 420 µm × 420 µm. Both

[‡]The half-VCSEL wafer is grown and processed at VERTILAS GmbH, Garching, Germany within the framework "*Verbundprojekts VCSEL-TRX*".

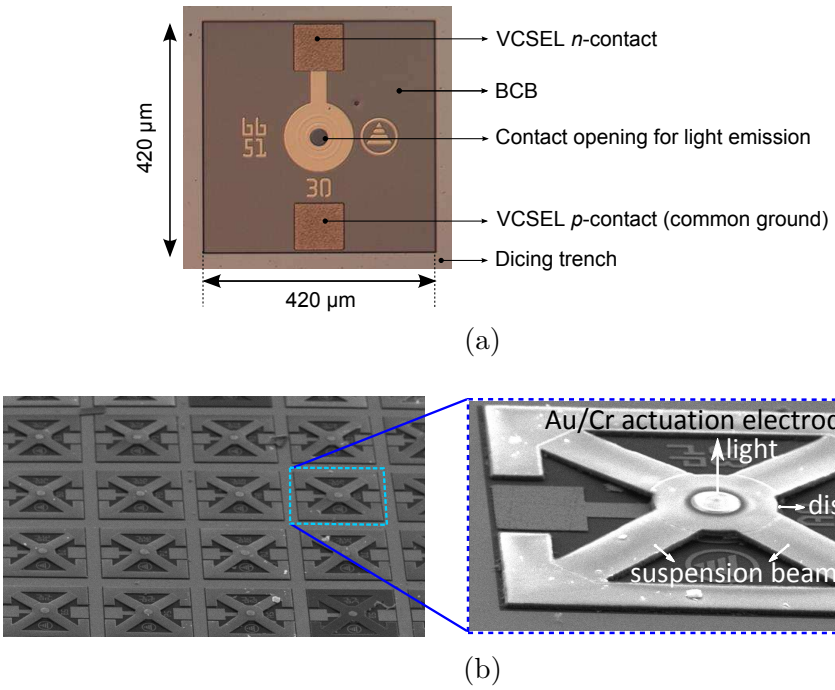

FIGURE 3.1: (a) Optical image of a half-VCSEL. The semiconductor around the VCSEL mesa is replaced by BCB. (b) Scanning electron microscopy (SEM) image of a part of a fully processed wafer. Inset shows a close view of a single device. The free-standing circular dish supported by four suspension beams consitute the movavle MEMS-DBR.

p-type and n-type contacts are placed on the top side. This dual-top contact configuration allows on-wafer MEMS VCSELs (in a two dimensional array) to be contacted using coplanar probe for high-speed measurements. A scanning electron microscopy (SEM) image of a fully fabricated MEMS VCSEL array is shown in Fig. 3.1 (b). The concavely bent MEMS-DBR has a characteristic shape of circular dish suspended with the help of four beams which are fixed at the other ends. The DBR and planner half-VCSEL construct an air-gap between them. The variable air-gap allows altering the resonator length resulting in a tunable emission. On top of the mirror, an actuation metal-electrode is evaporated. The light comes out of the VCSEL through a circular opening in the electrode (as shown in Fig. 3.1 (b) inset) and can be coupled to a lens or a standard lensed single-mode fiber (SMF).

3.1.1 Half-VCSEL: Design and Structure

The half-VCSEL mainly consists of an InGaAlAs-based active region, two InP heat- and current-spreader layers, a buried tunnel junction (BTJ) and a fixed bottom DBR mirror. The active region has seven compressively strained InGaAlAs quantum-wells (QWs) separated by lattice-matched InGaAlAs barriers. A schematic cross-section of a MEMS VCSEL is shown in Fig. 3.2. The electrical current is laterally confined by an aperture defined by a low-bandgap p^+-InGa(Al)As/n^+-InGaAs BTJ. There are several advantages

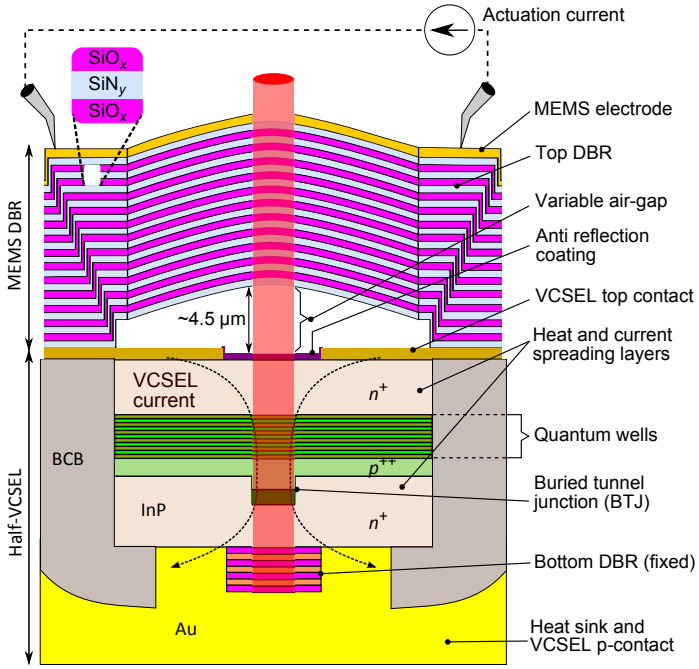

FIGURE 3.2: Schematic cross-section of a MEMS VCSEL. The MEMS-DBR consisting of 11.5 SiN_x/SiO_y pairs is surface-micromachined on the half-VCSEL structure. Wavelength tuning is realized by applying an electro-thermal actuation current to the MEMS electrode. Note: The picture is not scaled to the actual dimensions of the device.

of using a BTJ in VCSEL structure [67]. It defines the geometrical dimensions of the current aperture using well-established processes of photolithography and etching. The lateral mesa is formed by etching away the upper n^+-InGaAs layer and covering the remaining bottom p^+-layer by moderately doped n-InP in a second epitaxial run. As shown schematically in Fig. 3.3, the BTJ is laterally extended to diameter D_{BTJ} which is equal to or smaller than the total diode diameter D_0. Therefore, a blocking p^+n^+-structure is formed underneath the BTJ when a reverse bias is applied [67]. An equal bias onto both the BTJ and the area beneath results in an effective lateral current confinement to the BTJ area. Also, the placement of the tunnel junction within the p-side of the VCSEL ensures the overlap of a major part of the electrical field and the n-InGaAs layer. As a result, electron-hole conversion occurs in the tunnel junction and p-type layers can be replaced by n-type layers, leading to a large reduction of optical absorption loss. In addition, as electrons in n-type layers have high mobilities, the differential resistance decreases significantly. As a result, heat generation within the laser structure is reduced. Another advantage includes applying low-resistive n-type contacts on both sides of the VCSEL. The thickness difference caused by the etching is preserved up to the top layer by epitaxial growth engineering. If the difference is smaller $\lambda_{\mathrm{Bragg}}/4n$, this leads to a positive effective index difference Δn_{eff} between the BTJ and the outer region [67, 68].

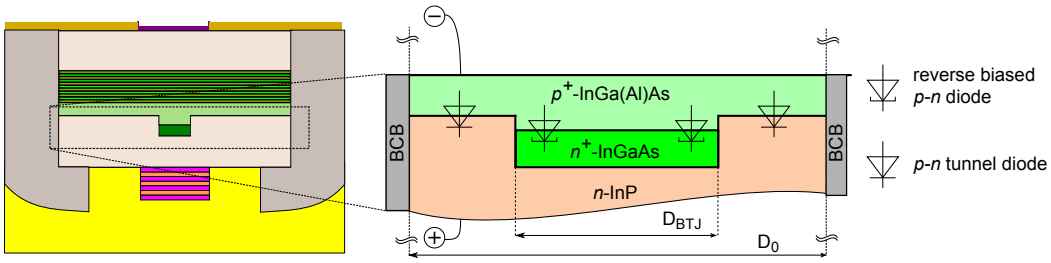

FIGURE 3.3: Cross-sectional view of the BTJ in the half-VCSEL structure.

To partly compensate the fiber-coupling loss, high single-mode output power is desired. Therefore, devices with larger BTJ diameters are favorable. In a fixed wavelength VCSEL with flat top DBR, larger active diameters exhibit current crowding at the BTJ edges and suffer from increased index guiding. This leads to a stronger pumping of higher order transversal modes resulting in multimode emission. Therefore, in order to conserve single-mode operation with a larger BTJ diameter, a planarizing metal-organic vapor phase epitaxy (MOVPE) regrowth is applied instead of the standard, non-planarizing molecular beam epitaxy (MBE) overgrowth. Due to planarization, the lateral index step and the related index guiding for higher order modes are minimized. In that way, single-mode high intensity emission is possible for nontunable devices with active diameters as large as 11 µm [69, 70]. To achieve a high amplification of the fundamental Gaussian mode, the overlap between the gain profile and the optical mode has to be optimal. This can only be achieved if the beam waist fits the radius of the BTJ. Consequently, higher order modes experience a smaller overlap with the gain profile due to their different lateral intensity distribution. This leads to a lower amplification of the side-modes resulting in higher SMSR. An appropriate combination of D_{BTJ} and corresponding RoC of the MEMS assure fundamental transverse mode emission even for significantly larger aperture sizes compared to those of standard non-tunable VCSELs.

In contrast to typical non-high-speed long-cavity (LC) VCSELs, SC half-VCSELs utilize bottom DBRs with significantly lower penetration-depths. For the used fluoride and sulphide based dielectric layer materials (CaF_2/ZnS) a refractive index contrast $\Delta n = 0.95$ is achieved at $\lambda_{\mathrm{Bragg}} = 1550\,\mathrm{nm}$. The 3.5-pairs DBR exhibits a penetration depth of 410 nm, which is more than a factor of 5 smaller than that of the epitaxial mirror implemented in a comparable LC devices. Therefore, the SC-VCSELs used in this work feature a relatively small effective cavity length L_{eff} of only 2.1 µm compared to 4.5 µm for the LC-VCSEL. The half-VCSEL is processed and embedded in a gold-electroplated substrate. The combination of gold (Au) and aforementioned dielectric DBR enables a reflectivity R of almost 100% over the entire tuning range and $R > 99.8\%$ for a bandwidth of 350 nm. This enhances the tuning range of the MEMS VCSEL, as the length of the cavity has direct impact on the FSR.

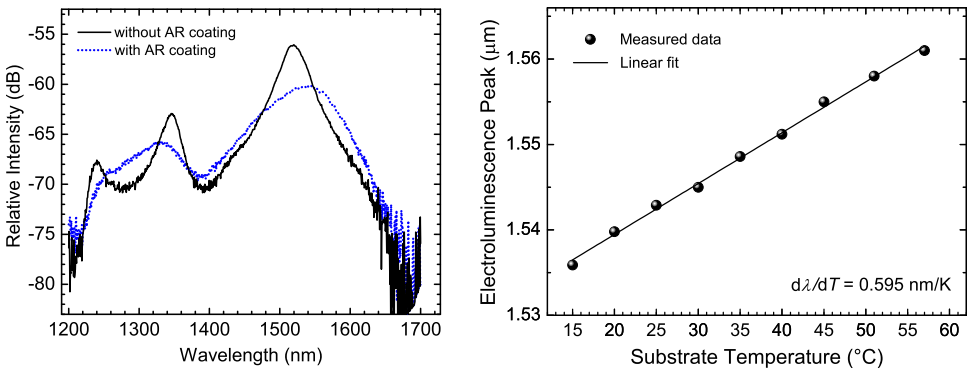

(a) (b)

FIGURE 3.4: (a) Electro-luminescence (EL) spectrum of two half-VCSELs (with and without ARC) measured at room temperature. (b) EL peaks plotted as a function of substrate temperature.

At elevated temperatures and in the high current regime, VCSELs typically show a thermal rollover in their characteristic properties like optical output power and relaxation-resonance frequency. In order to guarantee operation at elevated temperature and to avoid fast thermal degradation of the modulation performance with increasing bias currents, proper heat management of SC-VCSELs is necessary. The Au encapsulation (pseudosubstrate) offers efficient sinking of the dissipated heat.

The major challenge in pushing CW tunable VCSELs to the high-speed region is determined to a great extent by the reduction of the associated *RC*-parasitics. One important restriction is MEMS-VCSEL's naturally larger footprints compared to their fixed-wavelength genre. In SC VCSELs, the pad capacitance is reduced by replacing the semiconductor with a low-κ dielectric BCB (dielectric constant, $\kappa \approx 2.65$) and minimizing contact pad areas [71]. Low mesa diameters with typical values between 25–30 µm lead to a reduction of the mesa capacitance that is dominated by the depletion capacitance of the space-charge region formed by the blocking, reverse-biased $p+$ n-junction in the outer part of the mesa. The n-InP regrowth with low doping leads to an extension of the depletion region and a strong decrease of its capacitance. The mesa resistance accounts for the p- and n-contact resistances as well as parts of the vertical layer resistance. To enhance the modulation bandwidth further, highly strained quantum wells are incorporated to increase the differential gain and reduce the threshold carrier density, which benefits both large-tuning-range and high-speed operation.

Spectral Property of the Half-VCSEL

In order to achieve a wide tuning range DBRs with large reflection bandwidths and active materials with large gain bandwidths are prerequisites. Before integrating the MEMS-DBR, therefore, it is of utmost importance to identify the spectral gain distribution of

the half-VCSEL. The material gain of the active region and its spectral distribution are significant parameters for the threshold current, the output power and the attainable tuning range. The center of the reflection bandwidth of the MEMS-DBR is supposed to coincide with the gain spectrum maxima of the active material. The spectrum of the active material gain can be estimated from the electro-luminescence (EL) spectrum of the electrically pumped half-VCSEL. To obtain the EL spectrum, the spontaneous emission of the half-VCSEL is coupled into a multi-mode fiber and measured by means of an optical spectrum analyzer (OSA). The pump current is deliberately held at 2 mA to keep the additional self-heating of the laser caused by the electric current low. Figure 3.4 (a) shows the EL spectra of two half-VCSELs (with and without ARC) with optical resonator lengths of $12\lambda_{\mathrm{Bragg}}/4$. The EL spectra of the non-ARC half-VCSEL can be seen clearly from the periodically occurring longitudinal modes of the resonator. The EL spectrum is dominated by FP filter characteristics due to the large refractive index jump at the semiconductor (InP, $n_{\mathrm{InP}} = 3.17$ at 1550 nm)–air ($n_{\mathrm{air}} = 1.00$) interface and the resulting reflectivity of $\approx 27\%$. With an ARC applied to the half-VCSEL surface the reflectivity at the semiconductor/air interface is reduced. The FSR of the half-VCSEL resonator according to Eq. (2.6) is 174 nm (1521.0 nm – 1347 nm). The full-width at half-maximum (FWHM) of the transmission spectrum for half-VCSEL with ARC is 110 nm. The temperature dependence of the EL spectra of the $12\lambda_{\mathrm{Bragg}}/4$ long half-VCSEL with ARC is measured. Figure 3.4 (b) shows the EL maxima values plotted as a function of the temperature. The temperature of the heat sink is varied in the range from 15 °C to 57 °C. As the temperature increases, the EL spectrum of the half-VCSEL shifts to higher wavelengths and the modal gain decreases due to broadening of the Fermi distribution [5]. A linear fitting curve reveals a red-shift of 0.59 nm/K. The displacement of the EL maximum as well as of gain peak with increasing heat supplied from the outside is equal to that caused by the increase of the temperature with increasing pump current.

3.1.2 MEMS-DBR: Structure and Fabrication

Layer Structure

In order to obtain tunable lasing operation, a movable MEMS-DBR is integrated to the BCB-planarized SC half-VCSEL by means of surface-micromachining. The MEMS consists of 11.5 layer-pairs of SiN_x/SiO_y dielectric materials as well as a heating electrode with an circular opening for optical emission, as shown in Fig. 3.1 (b). The circular dish with a diameter of 135 µm is suspended on four flexible beams with length and width of 135 µm and 40 µm, respectively. The selection of the dielectric materials is strongly encouraged due to wide stop-band provided by the DBR. Table 3.1 summarizes the layer properties of the MEMS-DBR structure. The stack starts with SiN_x layer for its better

adherence (compared to SiO_y) to BCB. SiN_x also has higher refractive index value (cf. Table 3.1), which ensures higher refractive index contrast with respect to air. Each of the Bragg layers has an optical thickness $d_{opt} = n \cdot d_{geo} = \lambda_{Bragg}/4$, where $\lambda_{Bragg} = 1550\,nm$, n is the refractive index at λ_{Bragg} and d_{geo} is the film thickness of the corresponding DBR layer. The total thickness of the DBR results in $\approx 5.15\,\mu m$.

TABLE 3.1: Layer structure and properties of the MEMS-DBR.

Au/Cr MEMS actuation electrode				
No. of pairs	Dielectric	Geometric thickness	Refractive index	Stress
5	SiN_x	184 nm	1.94	-200 MPa
	SiO_y	269 nm	1.44	-110 MPa
6	SiN_x	211 nm	1.82	+70 MPa
	SiO_y	269 nm	1.44	-110 MPa
0.5	SiN_x	211 nm	1.82	+70 MPa
Initial air-gap				
Anti reflection coating				
Half-VCSEL substrate				

In this work, an ICP-CVD[†] system is used for the development and manufacturing of MEMS-DBR mirror. It is also used for depositing the bottom fixed DBR of the OAM-filter as well as the ARC of both devices. The ICP-CVD technique allows variation in both refractive index (thus, the optical layer properties of the DBR) and the mechanical stress. By deliberately incorporating built-in stress in the alternating dielectric mirror layers, one can influence the mechanical properties of the MEMS-DBR. This leads to an influence on the RoC and the air-gap L_{air}. The curvature of the MEMS dish is rotational symmetric. As shown in Table 3.1, the dielectric layers of the MEMS are provided with different stress in such a way that the resulting overall stress is compressive and the DBR is concavely meandered after releasing from the half-VCSEL. The stress in the SiO_y layers is kept consistent ($\approx$ -110 MPa) throughout the DBR stack, whereas the stress of SiN_x layers in the upper 5 layer-pairs ($\approx$ -200 MPa) is different than the rest of the 6.5 layer-pairs ($\approx$ +70 MPa). As both dielectrics in the upper 5 layer-pairs possess compressive stress, the overall stress is also compressive. However, the lower 6.5 layer-pairs have compressive contribution from the SiO_y layers and tensile contribution from the SiN_x layers. Due to higher absolute value of the compressive stress ($|-110\,MPa| > |+70\,MPa|$) contributed by the SiO_y layers, the resulting stress of the lower 6.5 layer-pairs is also compressive. Thus an intrinsic stress gradient along the deposited layers is obtained. However, the stress gradient also includes a shift in the refractive index of the SiN_x dielectric which has to be taken care of for stop-band calculation.

Due to short-cavity related intrinsic low gain and moderate confinement factor inside the active region of VCSELs, it is essential (for achieving low threshold current and high output power) that both mirrors provide sufficiently high reflectivities across the entire

[†]PlasmaLab System 100, Oxford Instruments

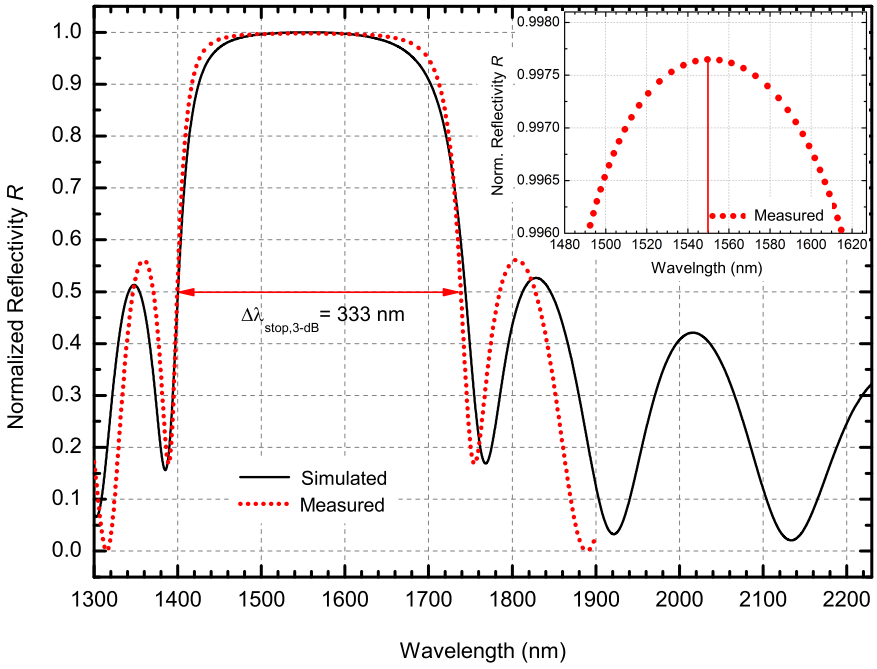

FIGURE 3.5: Simulated and measured reflectivity of a top MEMS DBR consisting of 11.5 pairs of SiN_x/SiO_y dielectric materials. Inset highlights that MEMS-DBR has 99.6% of reflectance for a wavelength range of $\approx 125\,\text{nm}$.

tuning range. Figure 3.5 shows both simulated and measured reflectivity spectra of a DBR consisting of 11.5 pairs of SiN_x/SiO_y dielectric materials. The stop-band $\Delta\lambda_{\text{DBR}}$ as well as the maximum reflectivity R is calculated using the transfer matrix method [72]. Factors such as optical losses, material dispersion and the temperature dependence of the refractive index are not taken into account here. In addition, it is assumed that the layers are infinitely extended in the lateral direction. The measurement is carried out using a multiple-angle laser ellipsometer[†]. With a refractive index difference between SiN_x (compressive) and SiO_y of $\Delta n_{\text{comp}} \approx 0.5$, and between SiN_x (tensile) and SiO_y of $\Delta n_{\text{tens}} \approx 0.4$, the MEMS-DBR exhibits a maximum R of 99.76%. The measured stop-bandwidth results in a Bragg wavelength of $\lambda_{\text{Bragg}} \approx 1550\,\text{nm}$, a 99.6% stop-bandwidth of $\lambda_{99.60} = 125\,\text{nm}$ (1490–1615 nm), and a 3-dB stop-bandwidth of $\lambda_{\text{stop,3-dB}} = 333\,\text{nm}$ (1735–1402 nm).

MEMS Surface Micromachining

The MEMS-DBR is deposited and processed directly on the half-VCSEL wafer. During different lithographic steps, one has to be cautious about using chemical solutions (wet-etchant or developer) that do not destroy any layer of the active VCSEL structure. For facilitating the processing, the half-VCSEL wafer is diced into $10\,\text{mm} \times 5\,\text{mm}$ pieces and glued to glass substrates for further processing. The fabrication starts with an ICP-CVD

[†]SENTECH SE 400adv multiple angle laser ellipsometer

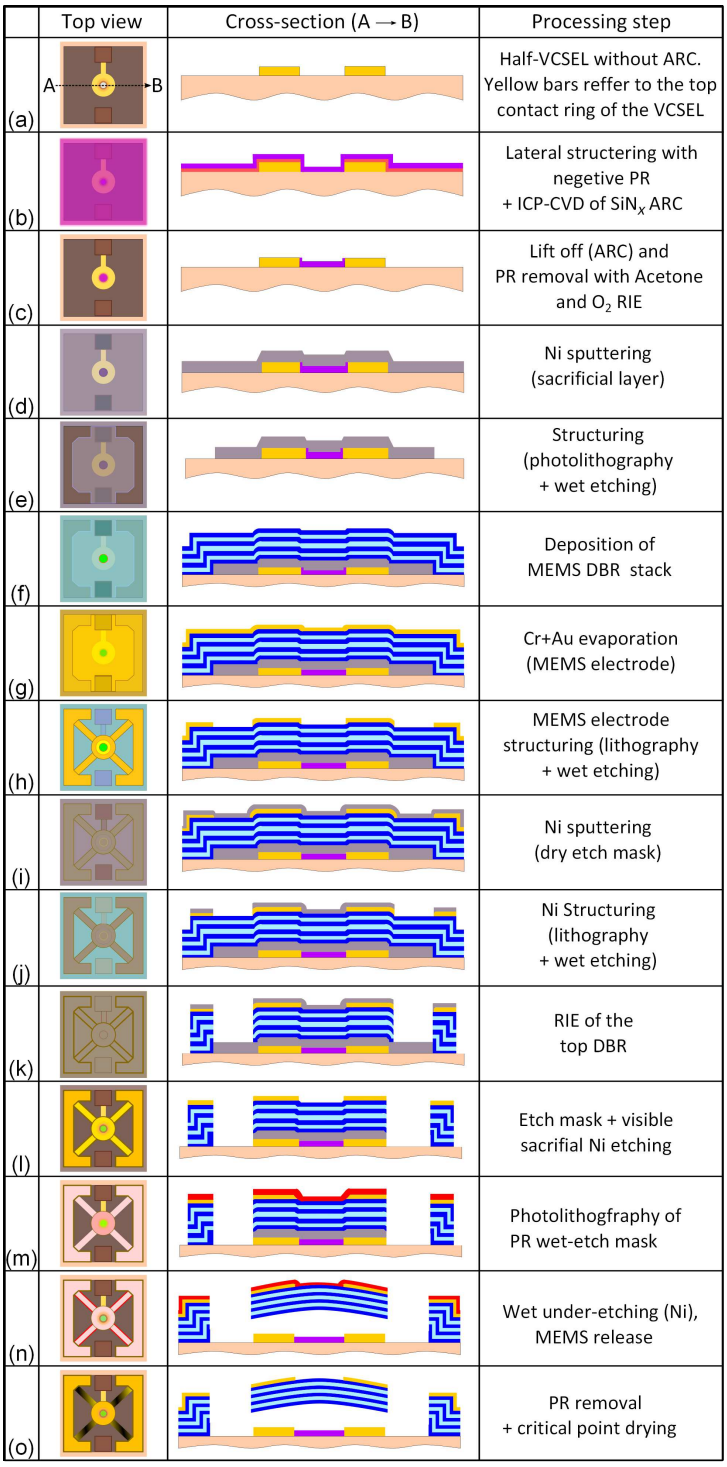

FIGURE 3.6: MEMS surface micromachining steps.

deposition of an ARC layer. The key processing steps of the entire MEMS surface micromachining are illustrated in Fig. 3.6. The fabrication includes five photolithographic steps. Before discussing the individual MEMS processing steps, a brief description of ICP-CVD technique is discussed in the following.

ICP-CVD Technique

In ICP-CVD plasma-excited gaseous species react on a solid surface and form solid layers (for example, different oxides and nitrides etc.). The plasma for the deposition is ignited by an electromagnetic alternating field which is induced by an induction coil. The advantage is the deposition of dielectric layers below T_{dep} <100 °C with a layer quality which is comparable to the layer quality of a PECVD layer at $T_{\mathrm{dep}} = 300\,^{\circ}\mathrm{C}$ [72]. This lower temperature CVD process can be advantageous for the direct deposition on temperature sensitive materials such as BCB. The target wafer is not directly exposed to the plasma and hence not to the ion bombardment either.

For SiN_x deposition SiH_4 and N_2 process gases are used whereas for SiO_y, SiH_4 and N_2O are used. The reaction sequences for the dielectric layers are as follows:

$$SiH_4 + N_2 \xrightarrow{\text{plasma}} SiN_x + H_2 + N_2 \tag{3.1}$$

$$SiH_4 + N_2O \xrightarrow{\text{plasma}} SiO_y + H_2 + N_2 \tag{3.2}$$

A precise stoichiometric specification is not possible because of the complex processes within the plasma. The process gases N_2 and N_2O are injected into the chamber from top and SiH_4 is injected through a ring slightly above the sample. By injecting the SiH_4 through the ring, uniform deposition is realized in the center where the sample is located. The gas flows measured by the unit of standard cubic centimeters (sccm), are controlled by a computer-regulated mass flow controllers (MFC). Two RF plasma generators can separately or together ignite and maintain the plasma. One is connected to an induction coil via an adaptive network, has a maximum power of 600 W and operates at a frequency of 13.56 MHz. The inductively induced power, P_{ICP} is characterized as a process parameter. The second RF plasma generator operates at the same frequency and is connected to the lower substrate electrode via a matching network. This generator couples the power P_{RF} in the plasma and accelerates the ions to the substrate electrode on which the wafer is located. This can be considered as a parallel plate reactor, in which the power is coupled into the plasma capacitively. The temperature of the substrate electrode T_{dep} is regulated with a water circulation system with a maximum operation temperature of 95 °C. Table 3.2 summarizes five process parameters, which can be adjusted within the given ranges for layer deposition.

The 2-inch wafer is fixed to quartz substrate. Helium (He) is introduced between the wafer and the substrate electrode for better thermal conductivity as well as for back-side cooling. The pumping system for the ICP-CVD consists of a turbo pump (operates efficiently under a pressure of approx. 0.1 Torr) and is supported by a rotary slide pump. The pressure p which is a process parameter is regulated by means of a computer-controlled flap valve. Fluctuations in the plasma can occur when the pressure

TABLE 3.2: PECVD process parameters.

Process parameter	Adjustable range
Deposition temperature, T_{dep}	20 to 95°C
Inductive plasma generator, P_{ICP}	max. 600 W at 13.56 MHz
Capacitive plasma generator, P_{RF}	max. 300 W at 13.56 MHz
Pressure, P_{dep}	0 to 100 mTorr (high vacuum)
Process gas flow rate	SiH_4: max. 30 sccm
	N_2, N_2O: max. 50 sccm

is too low. In the case of the ICP-CVD, it is possible to ignite the plasma at a higher pressure and gradually lower the pressure within the container after the ignition. One important thing about DBR deposition is that the relative accuracy of the optical layer thickness in the ICP-CVD is 3%. The deviation from the target value of the deposited optical layer thickness which is defined by $d_{opt} = n \cdot d_{geo}$, is caused by a process-related change in the deposition rate. The change in the refractive index due to small changes in the deposition parameters is very low. Hence, the deviation is attributed mainly to the change in the geometrical thickness. For this reason, one must carry out a reflectivity measurement for determining the absolute spectral position and the stopband-width of the DBR after deposition (cf. Fig. 3.5).

Deposition of ARC Layer

The large discontinuity of the refractive index at the semiconductor/air interface in a MEMS VCSEL acts as an additional mirror with a reflectivity of $R = 27\%$. This also results in two semiconductor coupled cavities (SCCs). The refractive index jump can be nearly compensated by applying an ARC to the semiconductor surface. A quarter wavelength ($\lambda_{Bragg}/4$) thick ARC decouples the resonators as the reflection at the semiconductor/air interface is canceled out by destructive interference. The MEMS VCSEL thus becomes a two-mirror resonator with an extended cavity. The quality of the ARC is very important as it influences directly the tuning performance [73]. As far as the fabrication is concerned, the integration of the ARC should be compatible with the subsequent processes. The stress should also be low to save it from peeling off from the surface and for enhancing the device life time. The ideal refractive index of the ARC, n_{AR} is given by the geometric mean of the two surrounding indices,

$$n_{AR} = \sqrt{n_{air} \cdot n_{sc}} = \sqrt{1 \cdot 3.16} = 1.78 \tag{3.3}$$

where, n_{air} and n_{sc} are the refractive indices of the surrounding layers namely air and InP (top semiconductor layer of the half-VCSEL emission region), respectively. In order to investigate the process compatibility issues, three different ARC layers have been investigated in this work: (*i*) silicon nitride (SiN_x) with refractive index of 1.82, (*ii*)

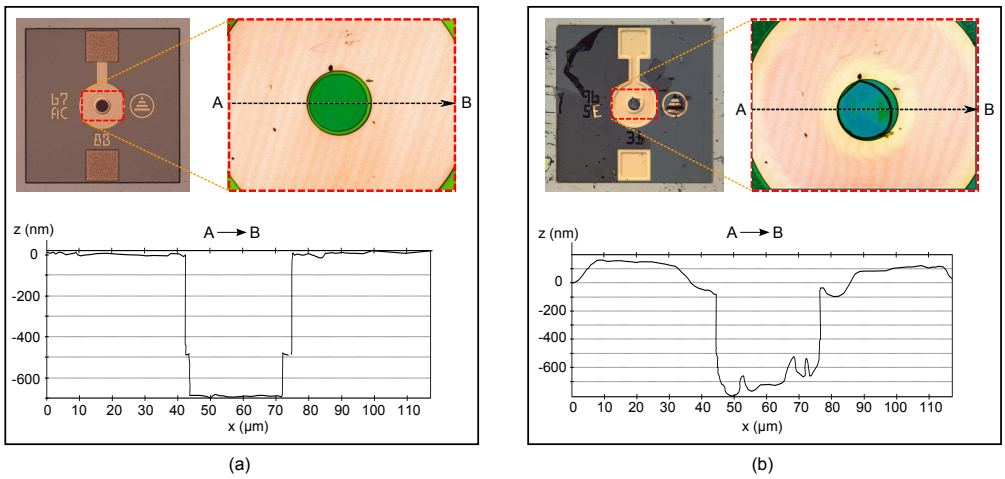

FIGURE 3.7: Half-VCSEL with AlO_z ARC. Surface roughness measured using a profiler – (a) before and (b) after wet-etching of Ni sacrificial layer with diluted HNO_3.

silicon oxide (SiO_y) with refractive index of 1.44, and (*iii*) aluminum oxide (AlO_z) with refractive index of 1.62. All layers are deposited using ICP-CVD. For lateral structuring of such small dimensions lift-off process using image-reversal photoresist is preferred. The formed undercut allows lift-off of ICP-CVD coated films with thicknesses even exceeding the resist film thickness. The mask sets used at different photolithography steps of MEMS surface micromachining are summarized in Appendix B.

Both AlO_z and SiO_y are found to be incompatible with respect to the sacrificial layer etching step. The AlO_z layer is partially etched by two different nickel (Ni) etchants used for sacrificial layer etching. This is shown in Fig. 3.7 (see also Fig. 3.8). A rough ARC layer within laser cavity can cause significant scattering losses and increases the threshold current. The SiO_y coating deposited in low-temperature ICP-CVD is porous, thus the InP layer underneath the ARC is attacked by the wet chemical etchant (HNO_3) of the sacrificial layer. These issues are illustrated in the following subsection. The SiN_y layer has survived during the sacrificial layer etching and is chosen as a compatible solution in the subsequent iterations. The deposition parameters of SiN_x are summarized in Table 3.3.

TABLE 3.3: PECVD deposition parameters for SiN_x ARC.

Temperature	RF power	ICP power	Pressure	SiH_4 rate	N_2 flow rate
80 °C	0 W	200 W	9 mTorr	7 sccm	6 sccm

After the deposition, the photoresist is lifted off using acetone and isopropanol as shown in Fig. 3.6 (b,c). A reactive ion etching (RIE)[†] with oxygen O_2 plasma ensures that the residuals are removed completely.

[†]PlasmaLab 80 Plus, Oxford Instruments

Sacrificial Layer Formation

Surface micromachining allows building a movable structure on the half-VCSEL by incorporating a so-called sacrificial layer. The movable DBR is separated from the active layer structure by the sacrificial layer which is etched away in the very last processing step to create the necessary air-gap in the vertical direction. In case of previous generation non-high-speed MEMS VCSELs, sputtered nickel is applied as a sacrificial layer [40] on top of silicon oxynitride (SiO_xN_y) ARC. Sputtered nickel provides a smooth surface with an average roughness of 5 nm for a scan length of 25 µm within the VCSEL eye area. The average roughness is measured using a surface profiler[‡]. Ni is also used as hard-mask for RIE of the DBR. Therefore, they can be etched in a single wet-chemical etching step. Diluted nitric acid (HNO_3) has been effectively used to etch the Ni layers. However, this standard wet-etchant attacks the top n-contact ring, reaches the semiconductor beneath and releases the ARC layer. This is shown in Fig. 3.7. The surface roughness of ≈30 nm measured across the VCSEL emission area shows that the semiconductor beneath the ARC is damaged. Compared to non-high-speed VCSELs, the BCB based high-speed VCSEL has a significantly smaller contact ring diameter (for reducing parasitic capacitance). Device failure analysis of a high-resistance VCSEL cross-section confirms that titanium (Ti) in n-type contact metal stack is completely removed during HNO_3 etching. This results in a very high-ohmic resistance or open-circuit connection in the laser diode.

To overcome the compatibility issue, a number of alternative solutions are first identified and then systematically performed. Firstly, Ti in the n-contact metal stack is replaced with chromium (Cr). However, the outcome is similar as it is also attacked by HNO_3 and results in a very high ohmic resistance. Secondly, different sacrificial layers such as aluminum (Al) (both sputtered and evaporated) and photoresists are applied. Al can be wet-etched by standard KOH-based developers. That means, one can eventually etch the Al sacrificial layer during the development of the photoresist used for the lateral structuring of Al (before DBR deposition). The etch time can be visually determined as Al on the glass holder is also removed simultaneously. However, the average roughness for sputtered Al is in the range of ≈ 80 nm. This value is very high as far as a high-reflectivity mirror is concerned, as it will cause a high scattering loss of the emitted light. Alternatively, the Al sacrificial layer is evaporated and the resultant average roughness is ≈ 30 nm. After the deposition of the DBR it has been observed that the roughness is translated to the following DBR layers and ends up in big bumps (average roughness of ≈ 100 nm) in the MEMS emission area. In addition, the required etching (lateral etching of the Al layer underneath the MEMS circular dish and the beams) time of 7 hours is not a viable solution for industrial manufacturing. Another issue concerning very long wet etching is the following. The MEMS VCSELs are required to be diced and bonded

[‡]Dektak 6M Stylus profiler, Veeco Instruments Inc.

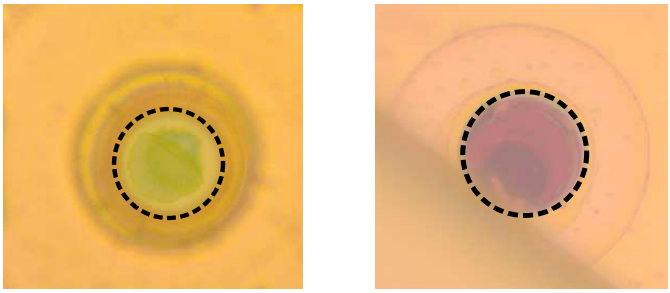

FIGURE 3.8: (a) AlO_z ARC layer is attacked by TFG which can be seen by mechanically removing the MEMS. (b) TFG damages SiO_y, penetrates thorough it and etches the InP semiconductor layer.

to submount for packaging. The adhesive that holds the diced MEMS VCSEL on the Si submount can not withstand the long etch time and thus is solved in the etchant solution.

The next attempt is to apply photoresist (PR) sacrificial layer as a cost-effective solution for mass fabrication. Instead of expensive wet chemical etching, it can be dry-etched using O_2 plasma. Therefore the need for critical point drying during MEMS release can also be avoided. The challenge is to obtain a plane surface inside the circular trench ($\approx 500\,nm$ profile from metal ring to the ARC surface) in the center of the VCSEL, as it tends to make a convex profile in the VCSEL eye. The measured average surface roughness is in the range of 5–10 nm. However, photoresist removal by an O_2 plasma, as well as by the solvent (acetone, N-Methyl-2-Pyrrolidone (NMP)) have not been successful. The excessive heat generated during the DBR layer deposition hardens the resist. The sample is also exposed to ultra-violet (UV) radiation of the plasma (DBR deposition) which is responsible for of polymer curing. In addition, during the dry-etching of the MEMS-DBR, it is exposed to the reactive gases. Thus, the resist become very hard and impossible to remove. As a solution, an additional thin Cr layer (20 nm) is evaporated on the resist in order to reduce the UV exposure. However, cracks formed in the resist during the vapor deposition process, which has made further processing impossible. Therefore, the resist (positive) is replaced by a negative resist which remains intact after Cr evaporation. Despite the existing Cr layer, the resist is hardened strongly during DBR deposition and can not be removed. Moreover, lateral etching of the thin Cr below the MEMS-DBR is not technologically feasible i.e., the release of the MEMS is also not possible.

As a replacement of HNO_3, a nitrate-based commercial Ni etchant namely TFG[†] is used. It does not damage Ti in the n-contact metal stack. However, it etches the exposed electro-thermal actuators (gold layer on the MEMS). This problem is solved by covering

[†]Nickel Ethant TFG, Transene Co INC.

the MEMS electrode by a photoresist at the cost of an additional photolithographic step. The resist must be removed after release of the MEMS. TFG also attacks both AlO_z, and SiO_y ARCs, which can be clearly seen in Fig. 3.8. The pictures are taken after removing the MEMS from the half-VCSEL structures. For this reason, SiN_x has been chosen as an ARC for the high-speed MEMS VCSEL.

After the process is developed, a 400 nm thick nickel layer is sputtered. The thickness of Ni layer influences the initial air-gap (hence, the FSR) as well as its etch rate underneath the circular dish and the beams of the MEMS. It is structured by photolithography and wet etching with diluted HNO_3, as shown in Fig. 3.6 (d and e). As both ARC and the n-contact ring are covered with Ni, they are not attacked by HNO_3. Table 3.4 summarizes various approaches and the associated conclusions mentioned in this subsection.

TABLE 3.4: Different sacrificial layers investigated for MEMS surface micromachining.

Sacrificial layer	Wet-/dry etchant	Average surface roughness	Observation/ Outcome
Al (sputtered)	KOH	80 nm	InP is etched in VCSEL eye
Al (evaporated)	KOH	30 nm	InP is etched in VCSEL eye
Ni (sputtered)	Diluted HNO_3	5 nm	Ti of VCSEL contact is damaged
Ni (sputtered)	TFG	5 nm	long etching time, but functioning device
+ve PR (spin-coated)	O_2 RIE	5-10 nm	unsuccessful etch
-ve PR (spin-coated)	O_2 RIE	5-10 nm	unsuccessful etch

Deposition of the DBR Layers

In order to achieve a flexible DBR, the layers are deposited on top of the sacrificial layer, which is later etched away to release the MEMS. A stress gradient is intentionally incorporated in the dielectric materials so that the mirror is bent concavely after releasing. In the following step, 11.5 pairs of SiN_x/SiO_y DBR will be deposited in ICP-CVD. A single iteration of DBR deposition involves several steps in sequence. Prior to the DBR deposition, therefore, it is essential to calculate the deposition rate and the stress of the particular dielectric layer. The disposition environment changes slightly each time after cleaning the chamber. There is no in-situ control over deposition rate or the thickness of the layer. Three single side polished (SSP) Si wafers are used to deposit single layers of SiN_x (both tensile and compressive stress) and SiO_y. By using

an ellipsometer, one can measure the refractive index n and the thickness d_{film} of the deposited layer for a wide range of wavelength. Hence, the deposition rate R_{dep} can be calculated according to: $R_{\text{dep}} = d_{\text{film}}/t_{\text{dep}}$, where t_{dep} is the deposition time for a single layer. Once R_{dep} is obtained, the required deposition time $t_{\text{film-DBR}}$ for depositing a individual Bragg layer with a geometrical thickness $d_{\text{film-DBR}}$ can be determined from the following relationships:

$$d_{\text{opt}} = \frac{\lambda_{\text{Bragg}}}{4} = n \cdot d_{\text{film-DBR}} = n \cdot R_{\text{dep}} \cdot t_{\text{film-DBR}} \tag{3.4}$$

$$t_{\text{film-DBR}} = \frac{1550\,nm}{4 \cdot n \cdot R_{\text{dep}}} \tag{3.5}$$

where d_{opt} is the optical length of the single Bragg layer and n is considered at λ_{Bragg} wavelength.

The successful fabrication of the MEMS-DBR also requires proper control over the stress within the subsequent layers. Therefore, the single layer-deposited SSP wafers are used for calculating the stress before final deposition. The mechanical stress of the individual dielectric film can be calculated using Stoney's equation:

$$\sigma \quad = \tfrac{1}{6}\left(\tfrac{1}{R_{\text{post}}} - \tfrac{1}{R_{\text{pre}}}\right)\tfrac{E_{\text{s}}}{1-\nu_{\text{s}}}\tfrac{{d_{\text{sub}}}^2}{d_{\text{film}}}, \tag{3.6}$$

where σ is the stress in the film after deposition, R_{pre} and R_{post} are the substrate RoCs before and after deposition, respectively, E_{s} is Young's modulus, ν_{s} is Poisson's ratio, d_{sub} and d_{film} is substrate- and film thickness, respectively. The RoC is measured before and after the deposition using a surface profiler.

The reproducibility of the stress values for the identical deposition parameters is the next point of investigation. The statistical overviews of the single layer stresses of SiN_x (both compressive and tensile) and SiO_y are shown in Fig. 3.9. The analysis is carried out for sixty single layer-deposited wafers for each stress category over a time span of 1.5 years. It can be seen that the compressive SiO_y and tensile SiN_x materials show relatively stable stress values with standard deviations of 13.10 MPa and 13.90 MPa, respectively over 1.5 years; the compressive stress of the SiN_x layer fluctuates with

TABLE 3.5: Resulting air-gaps for two MEMS-DBRs with different combination of stress values. The compressive stress of SiN_x is the key variant in this case.

SiN_x (compressive)	SiN_x (tensile)	SiO_y (compressive)	Air-gap
-190 MPa	75 MPa	-114 MPa	4.3 µm
-194 MPa	110 MPa	-110 MPa	4.1 µm
-210 MPa	80 MPa	-141 MPa	4.6 µm
-244 MPa	77 MPa	-109 MPa	7.0 µm
-190 MPa	127 MPa	-114 MPa	4.0 µm
-240 MPa	72 MPa	-120 MPa	7.1 µm

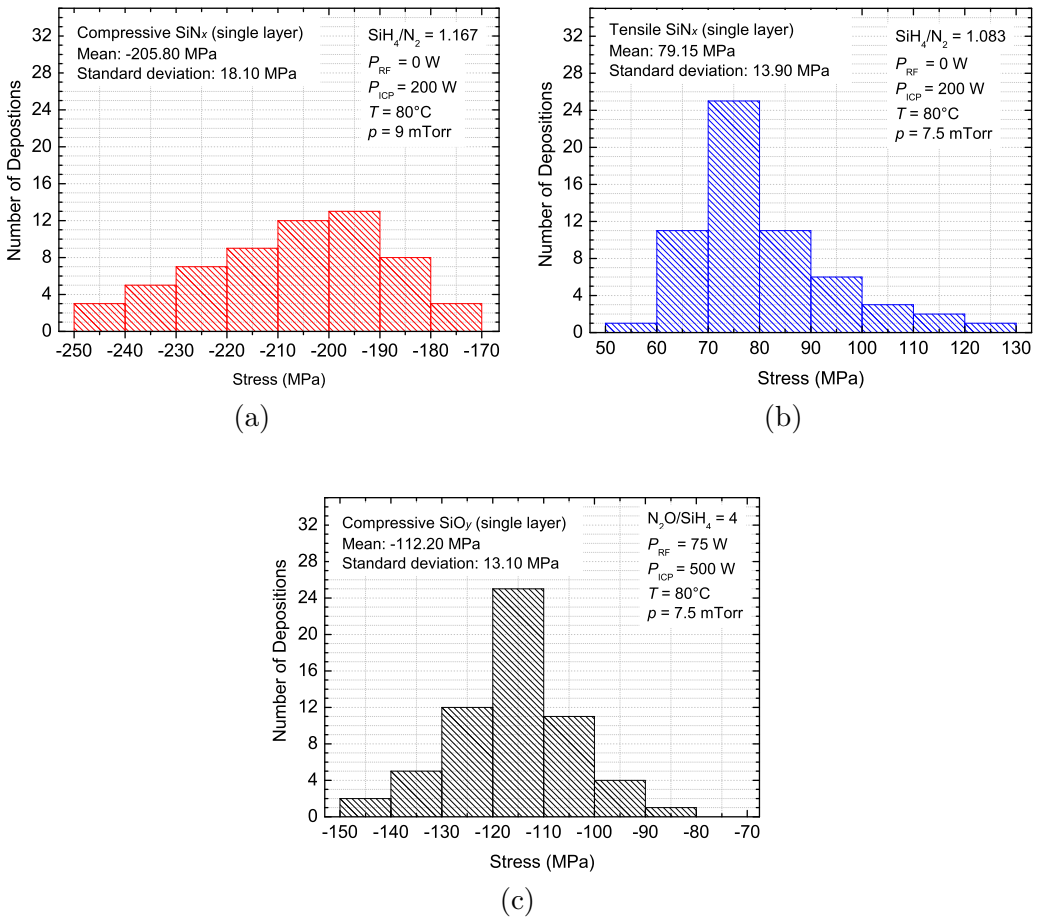

FIGURE 3.9: (a) Histograms of single layer stress measurements of (a) SiN_x (compressive), (b) SiN_x (tensile), and (c) SiO_y (compressive) dielectrics.

standard deviations of 18.10 MPa. In order to see the impact of the stress variations on the air-gap, six MEMS-DBRs are fabricated on silicon wafers. The corresponding stresses of the single layers and the resultant air-gaps are summarized in Table 3.5. As can be seen, the changes in the stress values of the tensile SiN_x and the compressive SiO_y do not make a significant change in the air-gap. It is mostly influenced by the compressive SiN_x layer. By keeping, the other two stress values fairly constant, change in the compressive SiN_x stress from -190 MPa to -240 MPa increases the air-gap by $\approx 65\%$ (from 4.3 µm to 7.1 µm). In oder to reach the target stress, one can alter the depositions parameters mentioned in Table 3.3 until a reproducible stress value is reached.

Electrode for Electro-Thermal Actuation

The next step is to form a metal circuit for electro-thermal actuation, as shown in Fig. 3.6 (h). By using a thermal evaporator, first a 10 nm Chromium (Cr) layer and then a 40 nm gold (Au) layer is evaporated. Cr works as a good adhesion layer between dielectric/semiconductor and Au layers. A glow discharge is performed in the evaporator to increase the surface roughness of the dielectric for better adhesion to the metal that

will be evaporated. Then the characteristic shape of the MEMS electrode with a circular emission window in the center of the dish is formed by photolithography and wet-etching. For Au etching, an in-house prepared etchant[§] is used. The bottom Au heat-sink of the half-VCSEL is protected by PR so that it is not etched away. Afterwards, Cr is wet-etched with a standard perchloric acid ($HClO_4$) based solution. Finally the PR is removed with Acetone and then the residuals are cleaned with O_2 plasma.

Reactive Ion Etching of MEMS-DBR

Next, the DBR is dry-etched from the region defined by a protective hard mask with the characteristic shape of the MEMS-DBR (cf. Fig. 3.6 (j)). The choice of hard mask material depends on the substrates material, structure, fabrication techniques and etch selectivity. In this work a sputtered 400 nm Ni (same metal as sacrificial layer) is used as hard mask against RIE etching of the DBR. After a lithographic step, Ni is wet-etched with HNO_3 from the exposed area.

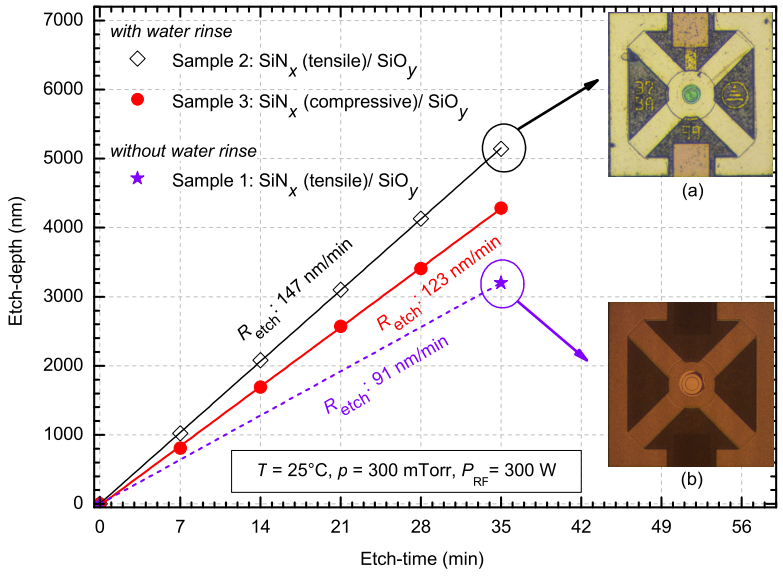

FIGURE 3.10: RIE etch rate determination of two types of layer-pairs. Compressive SiN_x/SiO_y pairs have higher etch rate compared to tensile SiN_x/SiO_y pairs. Moreover, rinsing the wafer during the etching has a significant influence on the etch rate.

For plasma etching of SiN_x and SiO_y, usually gases containing fluorine are used. The use of multi-component gas mixtures is essential as etching conditions for two dielectric materials should be optimized. A mixture of Tetrafluoromethane (CF_4) – Fluoroform (CHF_3) – Oxygen (O_2) are commonly used for etching SiN_x, whereas Fluoroform – Argon (Ar) are the etch gases used for SiO_y. Therefore, a mixture of CF_4–CHF_3–Ar–O_2

[§]mixture of 82.3 g of ceric ammonium nitrate ($(NH_4)_2[Ce(NO_3)_6]$), 45 ml of nitric acid (HNO_3) and 500 ml of deionized water (H_2O)

is used for RIE etching of the SiN_x/SiO_y DBR. The RIE parameters are summarized in Table 3.6. As the hard mask and the etch-stop layer are both metal (Ni), the etch selectivity with respect to dielectrics is very high (>50). To determine the etch rate of the top DBR, three samples with different alternative-layer combination are prepared. The first and the second samples are DBR mirrors consisting of compressive SiN_x and SiO_y layer-pairs. The thirds DBR sample comprises only tensile SiN_x and SiO_y layers. All three samples have Ni hard mask and are etched separately using the same RIE etchant combination mentioned in Table 3.6. The sample is etched uninterruptedly for 35 min and then the surface profile is measured without rinsing it. Figure 3.10 shows the etch-depth as a function of etch-time for three samples. The slopes of the curves are the corresponding etch-rate R_{etch}. As can be seen, R_{etch} for the first DBR is 91 nm/min. The other two samples are taken out of the chamber in every 7 minutes and the profile is measured after throughly rinsing the sample with distilled water for 30 s. For the second sample, $R_{\text{etch}} = 146$ nm/min. This means, ≈ 16 min is needed to etch the top 5 layer-pairs of an actual DBR (cf. Table 3.1). In case of third sample, $R_{\text{etch}} = 123$ nm/min resulting in ≈ 25 min for etching the bottom 6.5 layer-pairs of the actual DBR. Although both first and second samples have exactly same layer structure, the first sample has significantly lower R_{etch} compared to the second sample. The reason can be explained as follows. In order to protect the metallic surface of the chamber from Ar (strong mechanical etchant), a graphite substrate holder is used. However, Ar also etches the holder and carbon particles accumulate on the surface. If the carbon is not removed,R_{etch} is significantly reduced and the etch profile measurement is also misleading. The two scenarios (with and without rinsing) after 35 min etching are illustrated in Fig. 3.10 (insets). It is also observed that the increasing of the refractive index of SiN_x layer causes a shift towards higher compressive stress and a decreasing R_{etch}. In addition, R_{dep} tends to decrease as the refractive index increases. One explanation could be that a lower rate of deposition increases the likelihood that the atoms will reach the most energetically favorable locations. This leads to a higher layer density and thus to a smaller etch rate, which also leads to a higher compressive mechanical stress value. A higher density also results in a larger refractive index. In both cases, no significant under-etching of the MEMS structure is observed.

TABLE 3.6: RIE parameters for DBR etching. With the following parameters, the gas combination etches at a rate of 150 (± 5) nm/min.

RF power	Pressure	Temp.	CF_4	CHF_3	Ar	O_2
75 W	300 mTorr	25 °C	25 sccm	25 sccm	25 sccm	50 sccm

Chip on Submount Packaging

The next step is to dice the wafer into single MEMS-VCSEL chips and afterwards, to mount on the Si submounts using electrically conductive glue. However, once the wafer

is diced, no photolithography step can be applied anymore. As already mentioned, TFG (Ni etchant) attacks the Au electrode of the MEMS, a protective layer is required to cover it. Therefore, a photolithography is carried out to cover the characteristic shape of the MEMS electrode with PR. The photomask used for this lithographic step should be slightly smaller than the Ni hard mask. Hence it does not cover the sidewall of the MEMS-DBR. If the PR covers the sidewalls, the etchant can not reach the Ni below the circular dish as well as the beams, thus the under-etching will not be successful.

Release of the MEMS

In the following step, a wet-etching of Ni is carried out in two parts: First, the sample is dipped into a diluted nitric acid (HNO_3) etch solution. In order to visually control the etch time, a dummy wafer with the sputtered Ni of the same thickness as the sacrificial layer is also dipped in the solution. A magnet stirrer creates turbulence in the solution to enhance the etch rate. As soon as the visible Ni on the dummy wafer is completely disappeared, the sample is taken out of the solution. That means, the exposed portion of Ni sacrificial layer around the characteristic shape of the MEMS-DBR is also removed. But the Ni underneath the circular dish and the beams remains. In the next part, the sample is dipped in TFG etchant and kept standstill until the MEMS are released. The release of the MEMS can be visually observed by checking the color contrast between the flexible beams and the fixed MEMS contact electrodes, as shown in Fig. 3.11. It is clear that all MEMS mirrors are not released at the same time. For some devices, where the MEMS-DBRs are already released, the ARC are exposed to the etchant for longer time. This can partially damage the surface of the ARC. Moreover, The VCSEL n-contact metal ring is also etched by the TFG once the MEMS is released. In addition, the Au contact bondpads are exposed to TFG for the entire etching time as they are not covered with PR. Therefore, longer etching time also causes damage to the electroplated

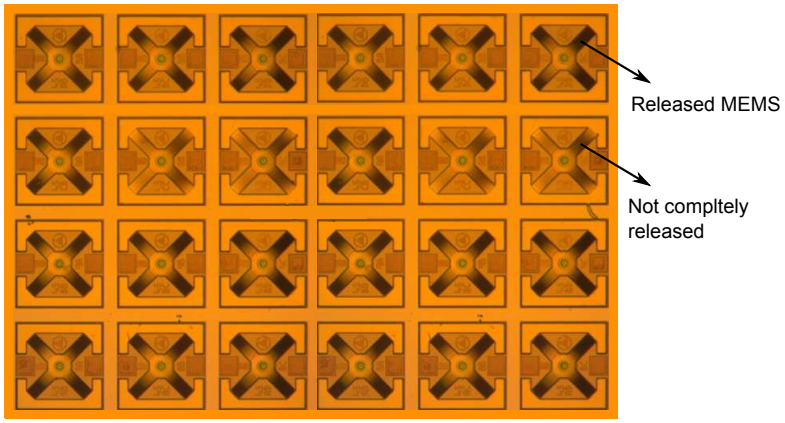

FIGURE 3.11: The release of the MEMS can be visually observed by looking at the beams – dark color indicates the Ni sacrificial layer is completely etched and the MEMS is released.

bondpads (although electroplated Au has significantly higher thickness compared to metal ring). So it is safe to take out the sample when ≈ 90% of the MEMS-DBRs are released. Afterwards, the sample is put in acetone in order to remove the PR on top of the MEMS electrode, followed by a isopropanol dip. The sample is kept in isopropanol until critical point drying.

Critical Point Drying

In the final step, the wafer is dried using a critical point drier to avoid the distortion of the MEMS due to surface tension effects (capillary force). First, the sample has to be placed in the specimen holder filled up with an intermediate fluid (i.e., isopropanol) which is miscible with liquid CO_2. After sealing the chamber, isopropanol begins to drain and is consequently replaced with liquid CO_2. The critical temperature (where both liquid and vapor phase coexist) of liquid CO_2 for a realizable pressure of around 83 bar is just above ambient temperature (around 32 °C). The temperature has to be increased slowly using a computer controlled ramp function for one hour to reach from 15 °C to 35 °C. When the temperature is raised above the critical temperature, liquid CO_2 changes to vapor without change of density (i.e., without surface tension effects). The wafer is taken out after the pressure is reduced to 1 bar. The complete surface micromachining process recipe of the MEMS-DBR is attached in Appendix C.

3.2 MEMS OAM-Filter: Structure and Fabrication

The MEMS tunable OAM-filter can be explained as a combination of two optical components: a wavelength tunable Fabry-Pérot optical filter and an optical OAM beam generator. The tunable filter utilizes the surface micromachined MEMS technology, as discussed in the previous section. The second component is a spiral phase plate (SPP) which can generate an optical OAM beam. Thus, the novel device can generate OAM beam at a defined wavelength generated by the MEMS tunable filter. Tuning of the filtered wavelength is obtained by varying the cavity length of the filter through electrothermal actuation of the top MEMS-DBR – i.e., the identical wavelength tuning principle as MEMS VCSEL.

Device structure

A cross-sectional view of a MEMS OAM-filter is shown in Fig. 3.12. The device comprises a double side polished (DSP) silicon substrate with an ARC on one side and a fixed bottom DBR, a variable air-gap, a movable MEMS-DBR and a SPP on the other side.

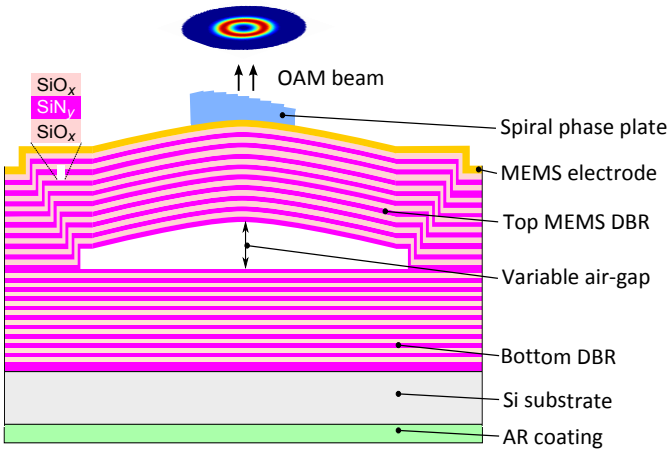

FIGURE 3.12: Cross-section of a MEMS tunable OAM-filter.

DSP wafers with controlled flatness characteristics are needed for devices where both side are used for processing and patterning. The ARC compensates the large discontinuity of the refractive index at the semiconductor/air interface, thus increases the portion of light coming in to (or going out of) the filter. A quarter wavelength ($\lambda_{\text{Bragg}}/4$ with $\lambda_{\text{Bragg}} = 1550\,\text{nm}$) thick ARC cancels out the reflection at the interface by destructive interference. The fixed bottom DBR is deposited and structured on the other side of the wafer. The MEMS-DBR is then surface micromachined on top of the bottom DBR. For electro-thermal actuation of the MEMS, a metal electrode is evaporated on its surface. A circular opening in the center of the electrode allows light to couple into the SPP, which is integrated on the MEMS-DBR.

Table 3.7 summarizes the structure of the MEMS OAM-filter with the layer properties of the dielectric DBRs. Apart from the SPP, the layer structure of top MEMS-DBR is identical for the MEMS VCSEL and the MEMS OAM-filter. The first layer of the bottom

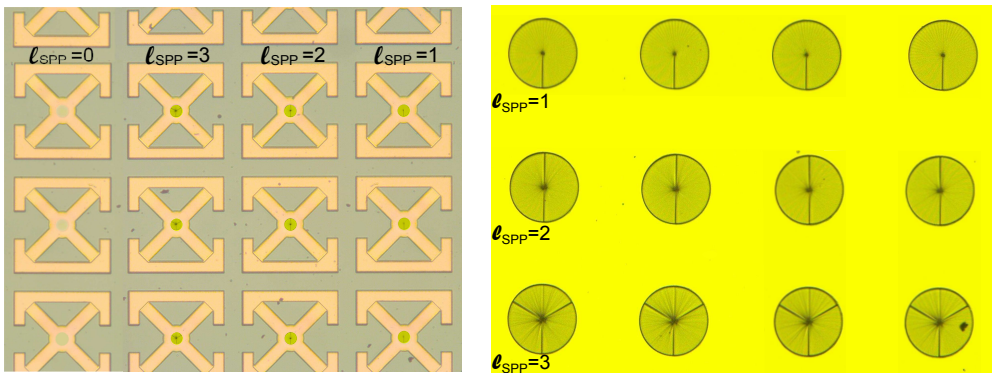

(a) (b)

FIGURE 3.13: (a) Optical images of a 2-D array of MEMS OAM-filters with SPP orders, $\ell_{\text{SPP}} = 1$, 2 and 3. The devices on the left column ($\ell_{\text{SPP}} = 0$) have no SPP. (b) Si wafer of 2-D arrays conjugate SPPs of corresponding orders.

TABLE 3.7: Layer structure of the MEMS OAM-filter. The Bragg layers are adapted for 1550 nm wavelength.

Polymer spiral phase plate (height of 5.5 µm)					
Au/Cr MEMS actuation electrode (40 + 10 nm)					
	Number of pairs	Material	Geometric thickness	Refractive index	Stress
Top MEMS-DBR	5	SiN_x	184 nm	1.94	-200 MPa
		SiO_y	269 nm	1.44	-110 MPa
	6	SiN_x	211 nm	1.82	+70 MPa
		SiO_y	269 nm	1.44	-110 MPa
	0.5	SiN_x	211 nm	1.82	+70 MPa
Initial air-gap ($\approx$ 4.5 µm)					
Bottom DBR	10	SiN_x	184 nm	1.94	-200 MPa
		SiO_y	269 nm	1.44	-110 MPa
	0.5	SiN_x	368 nm	1.94	-200 MPa
Double side polished Si substrate (thickness of $\approx$ 275 µm)					
SiN_x anti reflection coating (184 nm)					

DBR has direct contact with Si substrate. Since Si has a refractive index $n_{\mathrm{Si}} \approx 3.38$ at 1550 nm, the DBR has to start with optically thin SiO_y layer for proper phase matching. However, it turns out that SiO_y has poor adhesion to polished Si wafer. Therefore, an optically-transparent $\lambda_{\mathrm{Bragg}}/2$ SiN_x layer is first deposited, which is followed by 10 layer pairs with alternative sequence of compressive SiN_x and compressive SiO_y. The reason for choosing lesser pairs (in comparison to 11.5 pairs in the MEMS-DBR) for the bottom mirror is the inclusion of the compressive SiN_x with larger refractive index of 1.94. Hence, the refractive index contrast Δn is 0.5 for the entire layer-pair stack, and results in a maximum reflectivity R of 99.5% at λ_{Bragg}.

In this work, three different orders of SPPs (1, 2 and 3) are integrated on the MEMS. When a MEMS OAM-filters is employed in data transmission experiments, a conjugate SPP mask is required for the reception and conversion the optical vortex signal to a Gaussian beam. A conjugate SPP of order -1, for example, can be obtained by reversing the rotation of the corresponding SPP of order +1. The conjugate SPPs of order -1, -2, and -3 are fabricated on a DSP silicon wafers in a two dimensional array. Such an array of MEMS OAM-filters of three different orders is shown in Fig. 3.13 (a). The devices in the left-most column with no SPP on the MEMS representing the 0-th order ($\ell_{\mathrm{SPP}} = 0$). The conjugate SPP are fabricated in a bare Si wafer are shown in Fig. 3.13 (b).

Fabrication

The fabrication starts with an ICP-CVD deposition of a $\lambda_{\mathrm{Bragg}}/4$ thick SiN_x ARC layer. After the deposition is completed, the wafer is diced into 1 cm × 1 cm pieces. The ARC side of a wafer piece is then glued to glass substrate holder for the subsequent processing

steps. The bottom DBR comprising 10 pairs of SiN_x/SiO_y layers are deposited on the other side of the wafer piece. Then a 400 nm thick nickel (Ni) sacrificial layer is sputtered and laterally structured. The MEMS-DBR is then deposited. On top of the MEMS-DBR a gold (Au)/chromium (Cr) actuation electrode is evaporated. To accommodate the SPP, a circular opening in the Au/Cr layer is structured. Then, the top DBR is covered with a Ni hard etch mask and RIE etched to achieve the characteristic shape. Afterwards, both sacrificial layer and the etch mask are wet-etched and the device is dried using a critical point drier.

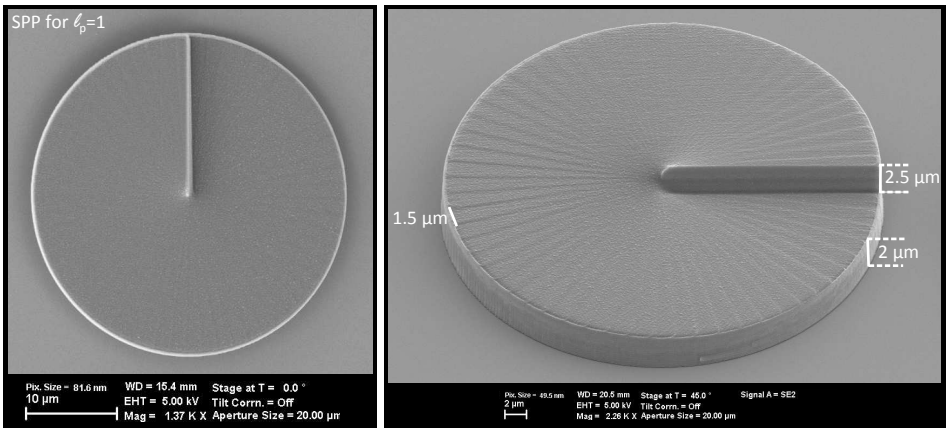

FIGURE 3.14: SEM images (top and side view) of a SPP of order 1 on a glass substrate.

In the following step, a three dimensional (3D) lithography system[†] is employed to write the SPPs on the MEMS. The SPP integration is carried out at the Institute of Applied Physics, Karlsruhe Institute of Technology, Germany. For mechanical stability, the chip is glued onto a sample holder and then fully covered by the liquid dip-in PR (Nanoscribe IP Dip). A computer-controlled sample stage allows for precise manipulation of the wafer position. In the dip-in configuration of the direct laser writing (DLW), the objective lens of the writing system is immersed in the PR [66]. This allows convenient writing on top of opaque substrates. The PR is designed such that single photons from the writing laser cannot be absorbed, but a two-photon absorption can induce polymerization. Since nonlinear processes scale with intensity, the polymerization occurs where the intensity is the highest, i.e., in the focal volume of the laser. Furthermore, the polymerization process exhibits a threshold behavior. Thus, only a volume within a certain iso-intensity surface given by the threshold intensity of the resist is polymerized. While the design height depends continuously on φ, the mask is divided into a fixed number of discrete steps. The geometry can be sliced into layers of equal height which can be exposed one after another using the rapid galvo-scanning technique. Figure 3.14 shows an exemplary SPP of order 1 fabricated on a glass substrate. The SPP has a total of 60 stair-steps with approx. 2.73 µm spacing between two consecutive steps at

[†]Photonic Professional GT, Nanoscribe GmbH, Germany

its circumference. The maximum height is approx. 4.5 µm with a height difference of 2.5 µm from the fist stair-step to the last one at the highest point. The diameter of the phase plate is 52 µm. The fabrication of a 52 µm-diameter SPP takes only five minutes.

Chapter 4

Characterization of MEMS VCSEL

This chapter demonstrates the suitability of the MEMS VCSEL for telecommunications applications at 1550 nm by a comprehensive set of characterizations. This includes static measurements of the tunable spectrum and the light–current–voltage (L-I-V) characterizations across the tunable range at different temperature levels. The far-field emission characteristics are recorded for the entire tuning range. The polarization behavior which is critical due to the circular waveguide geometry of the VCSEL is investigated with regard to Stokes parameters. The spectral linewidth is measured using delayed self-heterodyne method. To investigate the dynamic properties of the MEMS VCSEL measurements on the small-signal modulation and relative intensity noise are performed. MEMS tuning speed measurement in frequency domain completes the chapter.

4.1 Static Characterizations

Although a MEMS VCSEL offers ultra-wide, continuous single-mode wavelength tuning capability, its static characteristic parameters such as threshold current, maximum optical output power, thermal rollover current etc. are not uniform across the tuning range. Therefore, it is important to measure these parameters at different wavelengths, especially at the center and the two edges of the tuning range to observe the maximum deviation.

4.1.1 Electro-thermal Tuning

The MEMS VCSEL can be tuned in three different ways: (*i*) By applying a heating current to the MEMS electrode – i.e., electro-thermal actuation, (*ii*) by applying a voltage across two sides of the MEMS (MEMS electrode and VCSEL p-contact) – i.e.,

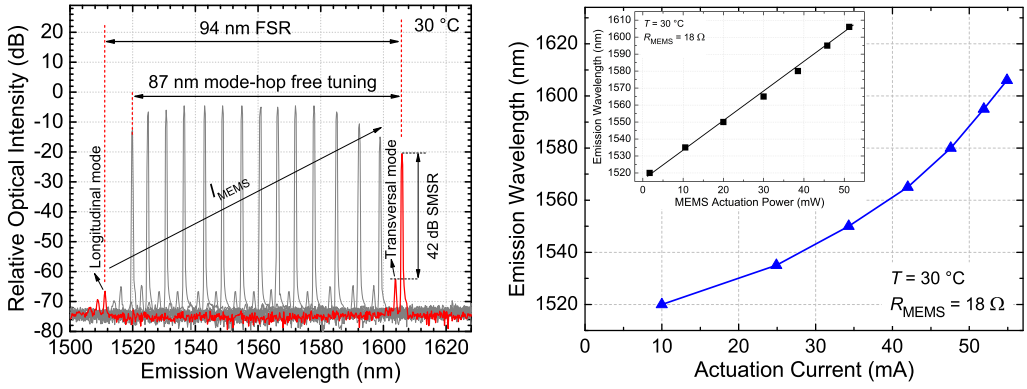

(a) (b)

FIGURE 4.1: (a) The continuous-wave (CW) tunable spectrum of a MEMS VCSEL at 30 °C is recorded by sweeping the actuation current I_{MEMS}. I_{bias} is set to 20 mA. The spectrum moves to higher wavelength values (red-shifted) with increasing I_{MEMS}. (b) Emission wavelength λ as a function of I_{MEMS}. Inset shows the linear relationship between emission wavelength and actuation power $P_{\mathrm{heat}} \propto \lambda$.

electro-static actuation, and (*iii*) by changing the substrate temperature – i.e., thermal tuning. In this section the spectral properties are investigated for the electro-thermal tuning scheme. As already discussed in Chapter 2, the actuation current I_{MEMS} forces the mirrors to expand upward. Hence, the initial air-gap as well the VCSEL cavity length are elongated and the emission wavelength is shifted towards higher values (red-shifted). For on-wafer characterizations, the wafer is mounted on a copper substrate using conductive liquid silver (Ag). The substrate is connected to a Peltier element for temperature stabilization. Since the change in the substrate temperature also alters the emission wavelength, it is important to distinguish between contributions of thermal and electro-thermal tuning of the laser. By keeping the substrate temperature fixed, the effect of only electro-thermal tuning can be observed. Two separate low-noise laser diode controllers[§] (LDCs) supply the laser bias current, I_{bias} and the MEMS actuation current, I_{MEMS}. In order to reduce the influence of the wavelength deviation due to self-heating it is important to set I_{bias} to a lower value adjacent to the threshold current. On the other hand, I_{bias} must be higher than the corresponding threshold currents for all emission wavelengths of the tuning range (threshold current is normally the lowest around the center and keeps increasing towards the edge, cf. Fig. 4.6 (a)). Therefore, I_{bias} is set to 20 mA which is higher than the highest threshold current for the entire tuning spectra. Due to the large beam waist,[*] light is butt-coupled (collimated and focused without any corrective optics) into a cone-lensed single-mode fiber (SMF) with a core diameter of 20 µm. The fiber output is connected to an optical spectrum analyzer (OSA)[†] with 0.08 nm spectral resolution. The tunable spectrum of a MEMS VCSEL

[§]ILX Lightwave LDC-3722B

[*]In comparison to a fixed wavelength VCSEL, the plane-concave resonator (resulting from the MEMS-DBR, air-gap, semiconductor cavity and the bottom DBR) generates a much larger beam waist. At 1560 nm emission, the calculated beam waist $2w_0 \approx 16$ µm.

[†]Agilent 86140A optical spectrum analyzer, 600–1700 nm

measured at a fixed heat-sink temperature of 30 °C is shown in Fig. 4.1 (a), where for each I_{MEMS} value, the emission spectrum is recorded. To sweep over the whole FSR without mode-hopping, the resonance wavelength is tuned to a particular longitudinal mode's (λ_m) initial value of 1520 nm corresponding to $I_{\mathrm{MEMS}} = 10$ mA. With a MEMS electrode resistance, $R_{\mathrm{MEMS}} = 18\,\Omega$, this referrers to an actuation power of $P_{\mathrm{heat}} = I^2_{\mathrm{MEMS}} \cdot R_{\mathrm{MEMS}} \approx 2$ mW. Now, for an increasing I_{MEMS} the lasing peak is continuously red-shifted and reaches up to 1607 nm at $I_{\mathrm{MEMS}} = 54$ mA (corresponding $P_{\mathrm{heat}} \approx 52$ mW). Figure 4.1 (b) shows the quadratic relationship between I_{MEMS} and the tunable emission wavelength λ. However, the actuation power, P_{heat} has a linear relationship with the air-gap length, L_{air}, thus also with λ according to: $\lambda \propto L_{\mathrm{air}} \propto P_{\mathrm{heat}} \propto \lambda$ (cf. Fig. 4.1 (b) [inset]). The criterion of continuous tuning range is set to a side-mode suppression ratio (SMSR) of > 30 dB between two consecutive longitudinal modes. Thus the device can be continuously tuned over 87 nm with a center wavelength of 1563 nm. The slope of the linear fitting, 1.74 nm/mW obtained from Fig. 4.1 (b) [inset] gives an indication of the efficiency of the tuning in terms of power dissipation. It is clear from Fig. 4.1 (a) that the laser does not lase across the entire FSR of 94 nm. The probable reason is as follows. During the wet-etching of the sacrificial layer (cf. Section 3.1), all the MEMS DBRs are not released at once. Those which are resealed earlier are exposed to the etchant for a longer time. The etchant solution attacks the ARC, although the etch rate is very slow. This can evidently limits the tuning range, as the ARC has impact on the FSR (thus on the tuning range) [73].

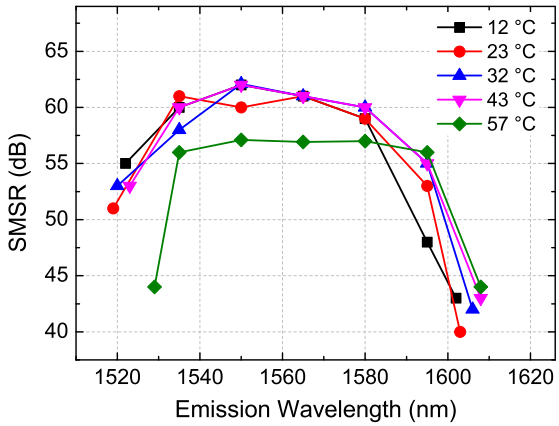

FIGURE 4.2: Side-mode suppression ratio (SMSR) values calculated from the tuning spectra, plotted as a function of wavelength for different substrate temperature.

The SMSR which describes the power ratio between the operating fundamental mode and the next higher order mode is measured from the spectra. For a tunable VCSEL the next higher order mode can refer either to the neighboring transversal mode (which is also spectrally located next to the main mode) or the next longitudinal mode which defines the FSR. In Fig. 4.1 (a), both suppressed higher order transversal mode/modes (at lower wavelength values adjacent to the lasing mode) and the next longitudinal mode are highlighted irrespective of spectral distance. Lasing power in any additional modes

represent noise in the WDM communication system. Therefore, higher SMSR is desired. In this work the single-mode operation defined by a SMSR of $> 30\,\mathrm{dB}$. Figure 4.2 shows the distribution of the SMSR values over the tuning range for five substrate temperature levels namely, 12 °C, 23 °C, 32 °C, 43 °C, and 57 °C. As water vapor condensation in the air-gap between MEMS-DBR and half-VCSEL can cause capillary-force related damage to the MEMS, the lower temperature level is kept at 12 °C. The upper limit is chosen in such a way that the lasing mode remains at the left edge of the tuning envelope for zero heating current (i.e., $I_{\mathrm{MEMS}} = 0\,\mathrm{mA}$). The MEMS VCSEL shows a very high SMSR value of $\geqslant 40\,\mathrm{dB}$ for the whole tuning range within the operating temperature regime. The reason for obtaining a high SMSR can be explained as follows. As mentioned in Chapter 2, gain guiding of the fundamental TEM_{00} mode for these devices is higher compared to higher order transversal modes. This is accomplished through confining electrical current laterally within a p^+-InGaAlAs/n^+-InGaAs BTJ aperture. The BTJ is highly conducting only in the center part of the device. In the outer part of the VCSEL mesa, a blocking ratio as high as 10000 can be achieved in the device's operating range [13]. At the right edge of the tuning range where the emission wavelengths are larger than the center wavelength, the cavity length has to be increased which results in a smaller RoC of the MEMS. Thus, the beam waist of the lasing beam is also reduced. Higher order transversal modes partially overlap with the BTJ and get access to the gain. Hence the SMSR is reduced. For smaller wavelengths the RoC becomes larger as the cavity length has to be decreased. The beam waist now is larger than the BTJ diameter, decreasing the differential gain of the lasing wavelength while the side-modes remain suppressed. Conclusively the SMSR decreases when moving from the center wavelength in either direction but still shows a highly single-mode emission across the entire tuning range.

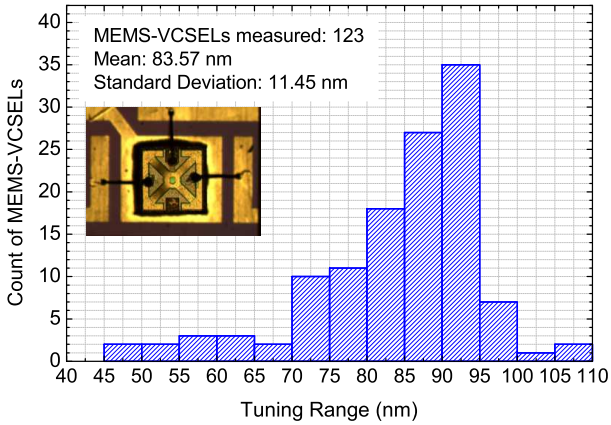

FIGURE 4.3: Tuning range distribution of 123 MEMS VCSELs from different positions of the wafer. The mean and standard deviation of the data set is 83.57 nm and 11.45 nm, respectively. The devices are measured after mounting and bonding to a silicon submount, as shown in the inset.

To show a statistical overview of the tuning range, 123 randomly selected MEMS VCSELs from the same wafer are characterized. As shown in Fig. 4.3, the mean and the standard deviation of the tuning range is 83.57 nm and 11.45 nm, respectively. The deviation of tuning range can be attributed to partial damage of the ARC during Ni sacrificial layer etching. MEMS-DBRs release at slightly different times depending on the position on the wafer. Those device, which are resealed early, are exposed to the etchant for a longer time and hence the ARC is partially etched. In addition, the factor contributing to the small deviation is the usual gradient in the thickness and density of the MEMS dielectrics during ICP-CVD deposition and results in an increasing mismatch between the DBR reflectivity maxima and the peak of the active material gain along the periphery of the wafer.

Thermal Effect on Tuning characteristics

A tunable laser which does not necessarily need an active cooling, at least for a fraction of the operation range, is highly desirable for any application due to the reduced power consumption. MEMS VCSELs developed in this work are designed and optimized for data transmission applications where the emission wavelength stabilization will be obtained either by an integrated solution within the package or by the optical line terminal (OLT) itself.[†] In some applications the wavelength of the devices may not be actively controlled for the sake of cost minimizations and compactness. Therefore, it is important to know the tuning characteristics as a function of the ambient temperature. In general, MEMS VCSELs do not show a homogeneous electro-thermal tuning behavior at a certain temperature. For instance, two adjacent on-wafer MEMS VCSELs often exhibit respective maximum tuning ranges at two different substrate temperatures. For investigating the thermal behavior a MEMS VCSEL is chosen which can be tuned across the whole FSR. Thus the temperature effect on of both tuning range and FSR can be observed. Figure 4.4 (a) shows the single spectrum as well as the spectral envelope of the tuning range, measured at fixed temperature of 20 °C and a constant $I_{\mathrm{bias}} = 20\,\mathrm{mA}$. The envelope is recorded with the OSA by holding the maximum of the spectrum while tuning the wavelength by increasing I_{MEMS}.

First, the longitudinal mode shifting due to temperature increment is measured. For a fixed wavelength VCSEL with same half-VCSEL material and structure, the thermal wavelength-shift is governed mainly by the refractive index change in the resonator and to lesser extent, by the thermal expansion of the semiconductor layers. The resultant effect pushes the wavelength to higher values at a rate, $d\lambda/dT = 0.09\,\mathrm{nm/K}$ [13].

[†]The integrated solution can be constructed by an additional monitor photo diode (the first photo diode measures optical power variations) in combination with an etalon. In the latter approach, the wavelength in measured at the OLT and an error signal is sent back to the network user over a pilot tone.

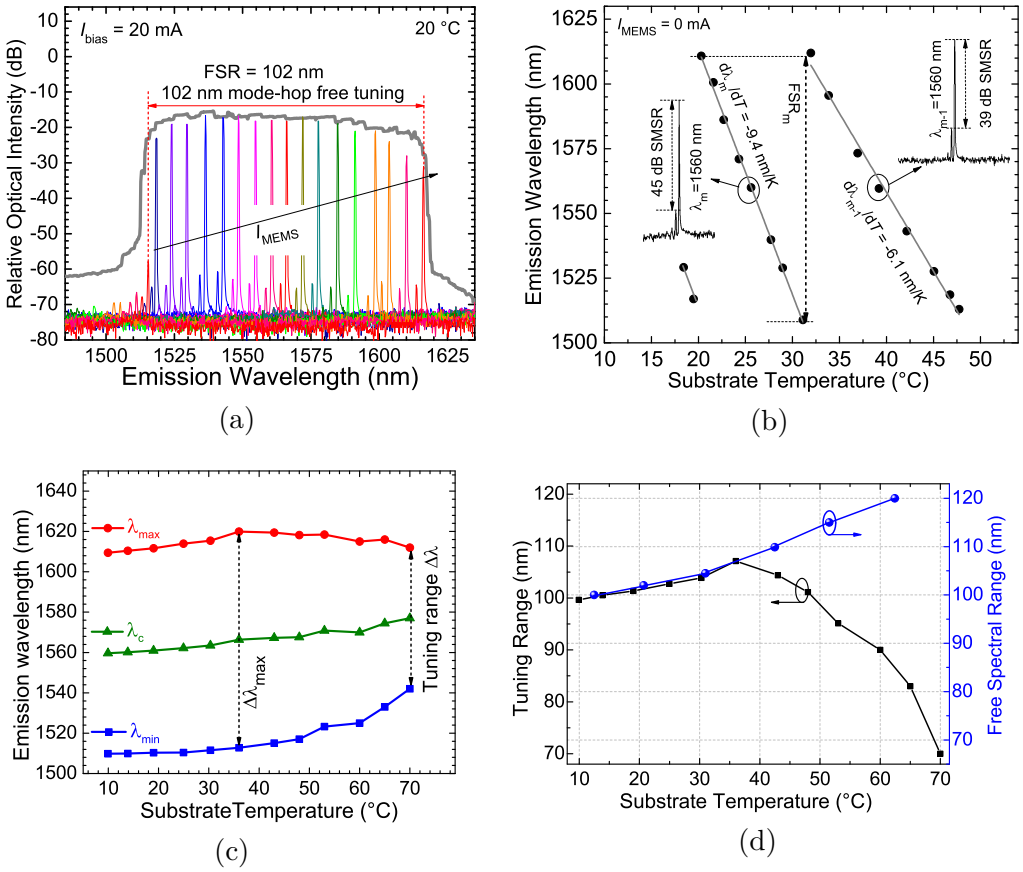

FIGURE 4.4: Thermal characteristics of a 14 µm aperture device. (a) Tunable emission spectra of a MEMS VCSEL measured at a constant laser current $I_{\mathrm{bias}} = 20\,\mathrm{mA}$, operating at 20 °C. (b) Wavelength-shift over temperature shown for two consecutive modes; I_{MEMS} is set to 0 mA. (c) Maximum (λ_{max}), minimum (λ_{min}) and center wavelength (λ_{c}) of the tuning range at different heat sink temperature. (d) Tuning range and the corresponding FSR as a function of temperature.

However, due to the presence of the expandable top mirror, blue-shifting due to cavity shrinkage with increasing temperature is typical for a MEMS VCSEL. As shown in Fig. 4.4 (b), the resonance wavelength λ_m (where integer m is the order of a certain longitudinal mode) shows a linear decrease with increasing temperature. A linear fit reveals a wavelength shift of $d\lambda_m/dT = -9.40\,\mathrm{nm/K}$. A temperature change of only 11 °C (from 20 °C to 31 °C) is sufficient to tune over the whole FSR. That means, one can set the emission wavelength only by changing the temperature, without applying any I_{MEMS}. When the temperature of the substrate is increased (at a fixed I_{MEMS}), the air-gap length is shortened. The reason behind this phenomenon are the different linear coefficients of thermal expansion α for the half-VCSEL structure and the MEMS dielectrics. As mentioned in Section 2, the half-VCSEL mainly consists of an Au substrate, BCB encapsulation and InP semiconductor with the coefficients $\alpha_{\mathrm{Au}} = 14.2 \times 10^{-6}\mathrm{K}^{-1}$, $\alpha_{\mathrm{BCB}} = 42 \times 10^{-6}\mathrm{K}^{-1}$ and $\alpha_{\mathrm{InP}} = 4.6 \times 10^{-6}\mathrm{K}^{-1}$, respectively. On the other hand, the dielectric materials $\mathrm{SiN}_x/\mathrm{SiO}_y$ of the MEMS-DBR have smaller coefficients of $\alpha_{\mathrm{SiN}} =$

$2.3\,\mathrm{x}\,10^{-6}\mathrm{K}^{-1}$ and $\alpha_{\mathrm{SiO}} = 0.5\,\mathrm{x}\,10^{-6}\mathrm{K}^{-1}$, respectively. Consequently, an increase in temperature of the whole device structure leads to a larger thermal expansion of the half-VCSEL compared to the MEMS-DBR. This causes the MEMS-DBR to be pulled down toward the half-VCSEL surface and thus reducing the length of the air-gap. Thus, with an increasing temperature the peak of λ_m is blue-shifted until it reaches the lower limit ($\approx$1508 nm) of the tuning envelope at 31 °C and eventually the next lower order mode λ_{m-1} starts to lase at the upper limit of the tuning range at 1612 nm. The RoC of the MEMS DBR also increases with increasing temperature. That means, the beam waist is increased and the BTJ accommodates neighboring transverse mode/modes which eventually obtain higher gain. Consequently, the SMSR of mode $m-1$ at 1560 nm is reduced by 6 dB in comparison to mode $m+1$ at the same emission wavelength.

Next, the deviation in the tuning range is determined by varying the temperature from 10 °C to 70 °C at a constant $I_{\mathrm{bias}} = 20$ mA. The spectral envelope is measured for determining the maximum (λ_{max}) and minimum (λ_{min}) values of the tuning wavelengths as well as the center (λ_{c}) of the tuning range. The results are summarized in Fig. 4.4 (c). As the peak material-gain wavelength shifts according to $d\lambda_g/dT \approx 0.6$ nm/K due to band-gap shrinkage, the initial lasing wavelength is also influenced. The lasing in a MEMS VCSEL starts only when the gain overcomes the cavity losses. Therefore, as the gain bandwidth shifts towards longer wavelength, λ_{min} also shifts towards longer wavelength. However, λ_{max} is not red-shifted as it is already limited by the DBR reflectivity bandwidth. The tuning range shown in Fig. 4.4 (d) increases from 99.5 nm at 10 °C to $\approx$ 107 nm at 36 °C. In this temperature regime the tuning range reaches to corresponding FSR values, meaning that the tuning range is limited by the FSR. Hence, the FSR must have increased due to cavity shrinkage in order to increase the tuning range. The reason behind the increment of the tuning range up to a certain extent and then a steep falling can be explained as follows. The gain bandwidth for laser inversion decreases with increasing temperature. However, the gain bandwidth is still broader than the FSR for thermal operation up to 36 °C. But with further temperature increment the gain bandwidth shrinks further as well as slightly shifts towards higher wavelength values. As a result, even though the FSR increases with higher temperature, the tuning range keeps shrinking at higher temperature regimes (above 36 °C in this case). By using Eqs. (2.19) and (2.20) from Chapter 2 and considering the measured wavelength $\lambda_m = \lambda_c = 1562$ nm with corresponding FSR = 102.75 nm at 25 °C, one can retrieve the order $m = 16$ (rounding up from 15.2, as mode number has be an integer value) of the lasing mode and the tuning efficiency $2/m = 0.125$ of the device [74]. In order to increase the continuous tuning range and thus, the FSR; m must be reduced at least by one order. That means, the cavity length L must decrease. However, to reduce m by 1, L (or the air-gap in particular) must to be reduced by a spectral distance equal to $\lambda_m/2 = 775$ nm for $\lambda_m = \lambda_c = 1550$ nm. According to Eqs. (2.19) and (2.20), reducing m from 16 to 15 will theoretically increase the FSR from 102.75 nm to $\approx$ 105 nm.

4.1.2 Light–Current–Voltage Measurement

The light–current–voltage (L-I-V) measurement of a laser relates the electrical input to the optical output and reveals many static characteristics which are important for data transmission experiments. With increasing I_{bias} above the lasing threshold or increasing ambient temperature a typical rollover occurs in the output power characteristics. The deviation from the linear increase of output power with current occurs due to higher carrier densities to maintain the threshold gain, carrier and current leakage effects, as well

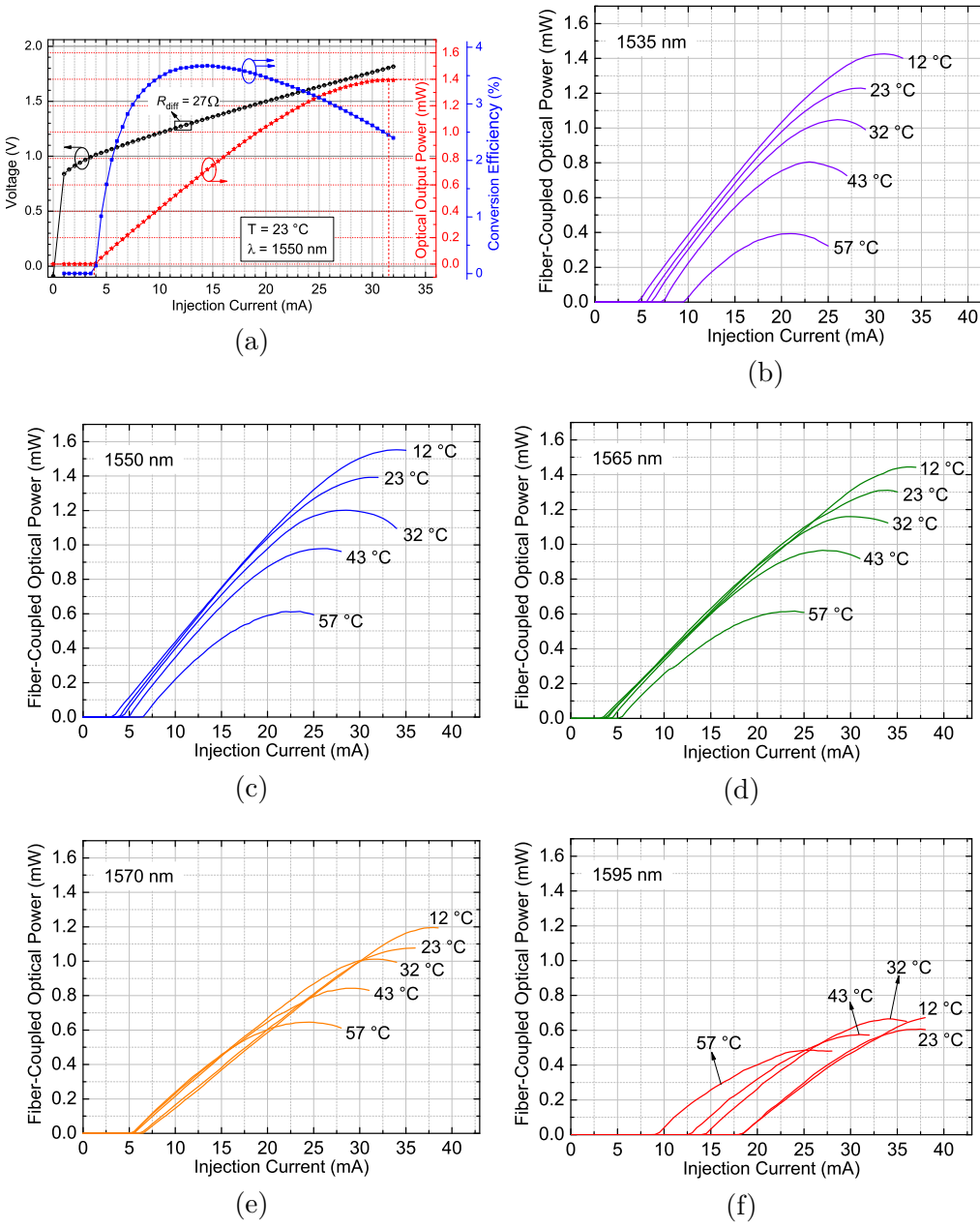

FIGURE 4.5: (a) Fiber coupled optical power (L) as a function of injection current I_{bias}, measured at a heat-sink temperature of 23 °C for 1550 nm emission wavelength. (b-f) L-I plots for five tuning wavelengths at different heat sink temperatures.

as increased non-radiative recombinations. Figure 4.5 (a) shows a *L-I-V* measurement plot of a MEMS VCSEL with 14 µm BTJ diameter, operating at heat-sink temperature of 23 °C. The device is emitting at 1550 nm for a $I_{\mathrm{MEMS}} \approx 35\,\mathrm{mA}$. I_{th} and fiber-coupled maximum optical power $P_{\mathrm{opt,max}}$ are 3.90 mA and 1.40 mW (obtained at thermal rollover current of 31.50 mA), respectively. The maximum power conversion efficiency of 3.70% occurs at a injection current of 14.50 mA. With respect to the corresponding photon energy at 1550 nm emission wavelength ($\equiv 0.8\,\mathrm{eV}$), the threshold voltage is only $\approx 100\,\mathrm{mV}$ higher. The differential series resistance R_{diff} ($=\Delta V/\Delta I$) is as small as 27 Ω (measured around 12 mA of injection current), which significantly reduces excess device heating and improves dynamic properties of the VCSEL. The measurements are carried out at five substrate temperature levels namely 12 °C, 23 °C, 32 °C, 43 °C, and 57 °C. At each temperature, the laser is tuned by varying I_{th} and the *L-I-V* data are recorded for five emission wavelengths (1535 nm, 1550 nm, 1565 nm, 1570 nm, and 1595 nm). At each temperature level, the lasing mode remains at λ_{min} of the tuning envelope for $I_{\mathrm{MEMS}} = 0\,\mathrm{mA}$. This allows to record the measurement data without any mode-hop across the tuning range. The *L-I* characteristics for five tuning wavelengths are shown in Fig. 4.5 (b-f). The temperature dependent lasing threshold currents I_{th} are retrieved from Fig. 4.5 (b-f) and summarized in Fig. 4.6 (a) as a function of the emission spectrum. The lowest $I_{\mathrm{th}} = 2.9\,\mathrm{mA}$ is achieved at 1550 nm for the lowest measured temperature of 12 °C. The general trend shows that I_{th} increases as the emission wavelength moves away from the center of the tuning range. A low I_{th} around the center of the tuning envelope refers to lower resonator losses and more efficient current guiding and conversion within the laser. As the peak material-gain wavelength of the active region is set to $\lambda_{\mathrm{Bragg}} = 1550\,\mathrm{nm}$, lower and higher wavelengths experience a lower gain. On the other hand, wavelengths away from λ_{Bragg} experience a lower reflectivity and thus higher cavity losses (cf., Fig. 3.5). One can also observe the red-shift of the characteristic "U" shape curves of the threshold values for higher wavelengths. At higher temperature, the peak material-gain wavelength of the active region decreases and is red-shifted due to bandgap shrinkage. From Fig. 3.4 (b), the wavelength shift of the material gain peak can be estimated as 0.59 nm/K. Because of differing gain and mode shifts with increasing device temperature, a mutual shift of lasing mode and gain spectrum occurs. Hence, I_{th} values for the shorter wavelengths show usual intrinsic loss related increment with increasing temperatures whereas those at longer wavelengths show a decrease due to favorable overlap with active material gain profile. The fiber-coupled maximum power $P_{\mathrm{opt,max}}$ and the corresponding rollovers currents retrieved from *L-I* plots are summarized as a function of emission wavelength in Fig. 4.6 (b). The characteristic shape of a upturned "U" with a common maxima around 1550 nm for all temperatures can be observed. As already mentioned, for longer wavelengths the reduction of material gain by higher temperature is partly compensated by the shift of the maximum gain towards those wavelengths, opposed to wavelengths on the left side of the spectrum, where the

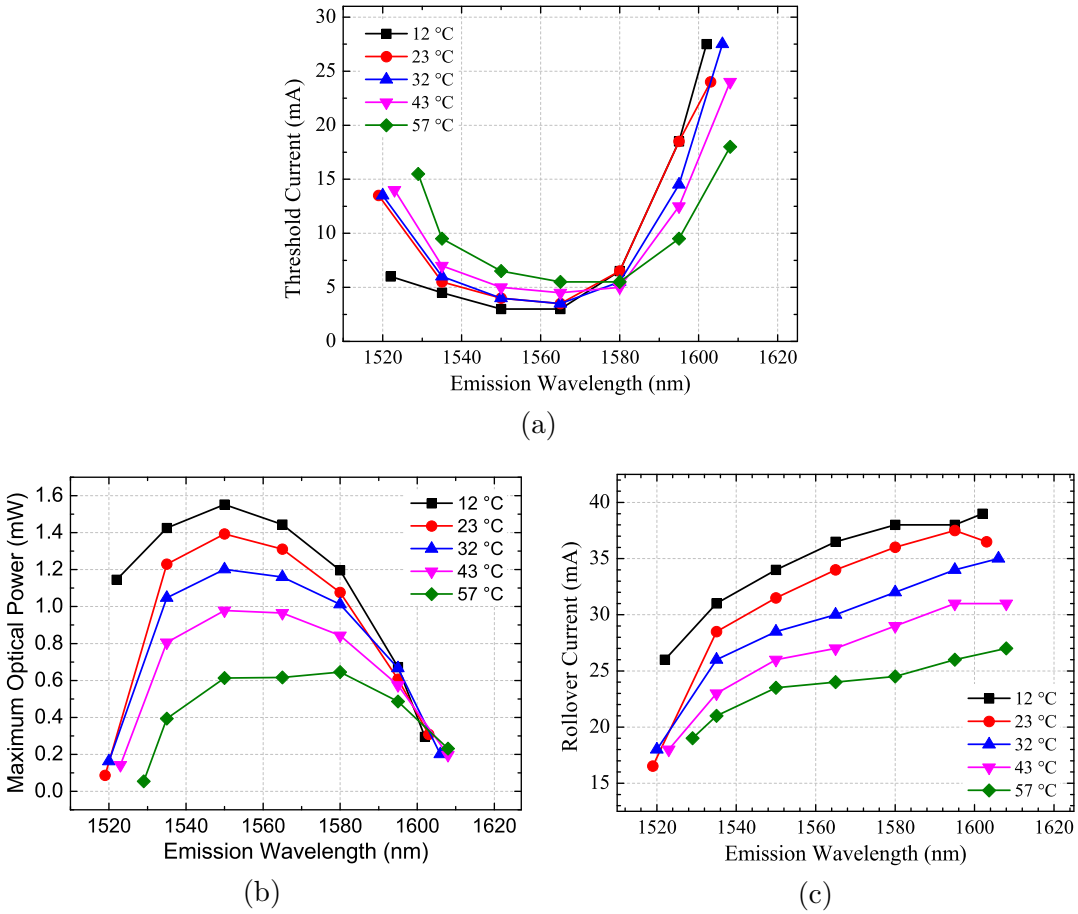

FIGURE 4.6: (a) Threshold currents (a), fiber-coupled maximum optical output powers (b), and corresponding thermal rollover current (c) measured at five heat sink temperatures and plotted as a function of tunable emission wavelengths.

red-shift intensifies the power reduction by temperature. As the spectral distance between the center wavelength and the material gain of the half-VCSEL increases, the upturned "U" shape becomes flattened. While comparing the curves for 12 °C and 23 °C at the λ_{min} edge, a drop of $P_{\mathrm{opt,max}}$ from 1.15 mW to 0.10 mW signifies that a change in temperature at his edge can be very crucial for optical output power. Figure 4.6 (c) shows the monotonous increase of the rollover current values with increasing emission wavelength and a decrease with increasing temperature.

The decrease in output power with increasing temperature can be better observed in Fig. 4.7 (a) where $P_{\mathrm{opt,max}}$ values obtained from the *L-I* characteristics for 1500 nm (Fig. 4.5 (c)) are plotted as a function of the heat sink temperature. The linear fit gives a slope $\mathrm{d}P_{\mathrm{opt,max}}/\mathrm{d}T \approx -0.021\,\mathrm{mW/K}$, which is the rate at which $P_{\mathrm{opt,max}}$ at 1550 nm decreases with increasing substrate temperature. The corresponding extrapolation of the measured data results in a maximum operating temperature of approximately 88 °C. As a comparison, the previous generation non-high-speed surface-micromachined MEMS VCSELs can be operated up to a temperature of 85 °C [40]. Figure 4.7 summarizes the slope values of $\mathrm{d}P_{\mathrm{opt,max}}/\mathrm{d}T$ for five emission wavelengths. As can be seen, the steepness

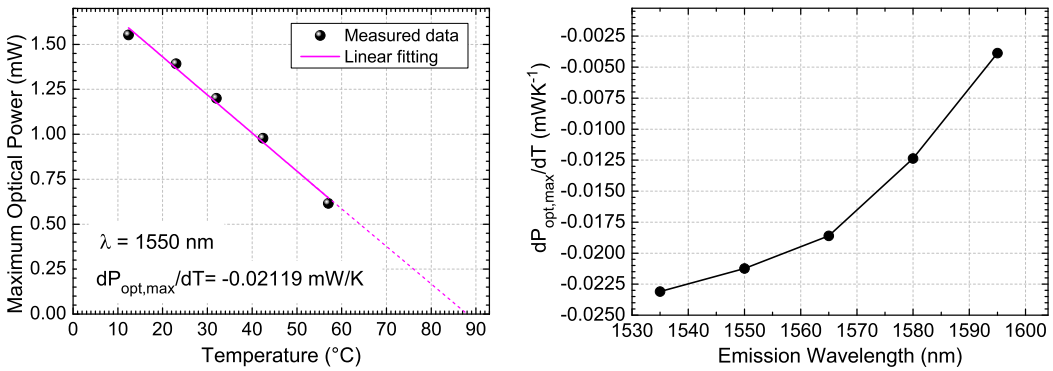

(a) (b)

FIGURE 4.7: (a) Maximum output power over temperature. The linear fit gives a slope $\mathrm{d}P_{\mathrm{opt,max}}/\mathrm{d}T \approx -0.021\,\mathrm{mW/K}$. (b) $\mathrm{d}P_{\mathrm{opt,max}}/\mathrm{d}T$ values plotted for different emission wavelengths.

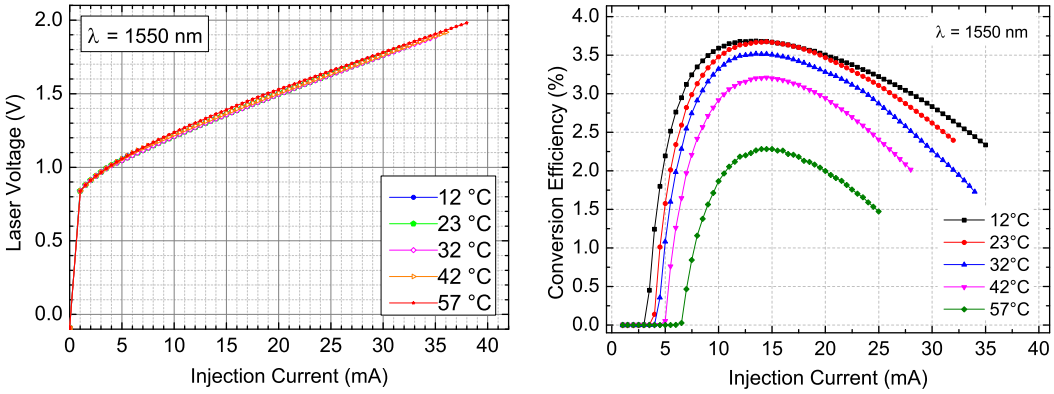

(a) (b)

FIGURE 4.8: (a) Laser voltages vs. injection current (V-I) characteristics of a 14 µm BTJ-diameter MEMS VCSEL. (b) corresponding fiber-coupled maximum optical output power on temperatures for different wavelengths.

of the slope for the corresponding wavelength increases with increasing wavelength values.

The voltage across the laser diode plotted against the injection current – i.e., the V-I characteristics are shown in Fig. 4.8 (a) for five wavelengths at 23 °C heat sink temperature. As can be seen, all the voltage curves remain close to each other. The voltage drop across the device stays below 2 V over the entire operation range indicating low series resistances (contact resistance plus laser resistance) in the device. The threshold voltage, a good measure for the voltage drop at hetero-barriers, is 0.85 V. Figure 4.8 (b) shows the calculated power conversion efficiency as a function of laser injection current, plotted for different heat sink temperatures. The differential quantum efficiency reaches its maximum near threshold current and decreases from there on. Higher temperatures reinforce the decay of the differential quantum efficiency with increased laser current significantly. In general, the conversion efficiency of the MEMS VCSEL is very low. This can be attributed to severals reasons: The dielectrics deposited in low temperature ICP-CVD are

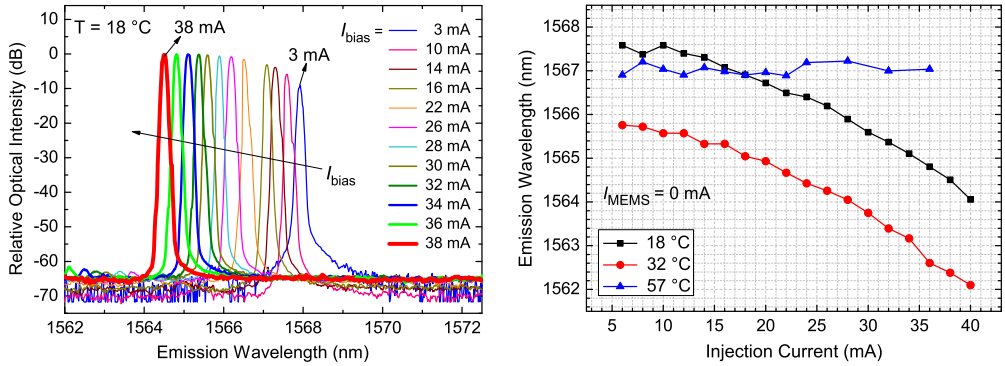

(a) (b)

FIGURE 4.9: (a) Emission spectrum recorded for increasing injection curret I_{bias} at a constant sunstrate teperature of 18 °C and zero I_{MEMS}. (b) Wavelength peaks versus I_{bias} at 18 °C, 32 °C, and 57 °C.

not of very high quality. The scattering causes a portion of light escaping from the resonator. Moreover, the light coming out from the half-VCSEL passes through air, where a portion of the light is absorbed. Typical single-mode fixed-wavelength VCSEL with flat top mirror can produce up to 7–8 mW which is factor ≈ 5 higher than the $P_{\text{opt,max}}$ of the MEMS VCSEL at 1550 nm. Also, the ARC damage related to the etching time of the sacrificial layer is a big concern for low output power and thus conversion efficiency. The MEMS are not released at the same time. Therefore, the MEMS which are released earlier are exposed to wet chemical etchant of the sacrificial layer can partially damage the ARC. This reduces the optical power significantly. The contact resistance of the bondpad increases after several on wafer probings, which contributes to the increment of the voltage and a decrease in the conversion efficiency of the device.

The wavelength drift due to change in the injection current is measured and shown in 4.9 (a). The substrate temperature is fixed at 18 °C and I_{MEMS} is set to zero. I_{bias} is increased gradually and the spectrum is recorded for each I_{bias} value. Unlike a fixed wavelength VCSEL, the wavelength is blue-shifted with increasing injection current. This is due to the same effect as described for temperature increment related blue-shift of the emission wavelength. As the half-VCSEL substrate is heated, it expands laterally. However as I_{MEMS} is kept at zero, the MEMS does not expand upwards. Therefore, with the expanding half-VCSEL substrate, the MEMS beams are also expanded and the cavity length becomes shorter. This results in a blue-shift in the emission wavelength. Figure 4.9 (b) summarizes the wavelength drift as a function of I_{bias} for three temperature levels namely, 18 °C, 32 °C and 57 °C. For temperatures of 18 °C and 32 °C a shift of roughly 3.5 nm within a current change up to 40 mA can be observed, whereas the emission wavelength is rather constant for injection current sweep at 57 °C. At higher temperature, the substrate expansion due to change in injection current is rather small compared to that due to substrate temperature itself, thus the additional heat generated by the injection current does not influence the emission wavelength. Small fluctuations in

the emission wavelengths can be attributed to the membrane movement due to on-wafer probing.

4.1.3 Far-Field Measurements

With an extended cavity consisting of an air-gap and a concave top mirror, MEMS-VCSEL resonator is more complicated than a plain Fabry-Pérot resonator. The three-dimensional electric field distribution of the longitudinal modes inside the resonator can be approximated by the radial symmetric Gaussian beam equation in cylindrical coordinates:

$$E(r,z) = E_0 \frac{w_0}{w(z)} \exp\left(-\frac{r^2}{w(z)^2}\right) \tag{4.1}$$

with spot size $w_0 = w(z = 0)$ of the Gaussian beam. The Gaussian beam diverges along the propagation direction, therefore $w(z)$ defines the beam radius r along the propagation axis z. The phase-front of the Gaussian beam transforms from a plane wave to a spherical wave for $z \to \infty$ according to

$$w(z) = w_0 \sqrt{1 + \left(\frac{z}{z_0}\right)^2}, \tag{4.2}$$

$$\text{and} \qquad R(z) = z_0 \left(\frac{z}{z_0} + \frac{z_0}{z}\right) = z\left(1 + \left(\frac{z_0}{z}\right)^2\right) \tag{4.3}$$

where z_0 is the Rayleigh length defined by $z_0 = \pi w_0^2/\lambda$ and $R(z)$ is radius of phase-front. Thus the Gaussian mode can be defined by $R(z) = \mathrm{RoC}(z)$ of the MEMS-DBR and the optical cavity length $L_\mathrm{o} = \sum L_i n_i$, so that the phase-fronts of the mode coincide with the mirror geometry [75]. Here, L_i is the geometrical resonator length and n_i the refractive index of the corresponding layer, respectively. For the MEMS VCSEL, the total cavity length consists of

$$L_\mathrm{o} = L_\mathrm{sc} + L_\mathrm{air} + L_\mathrm{t\text{-}DBR} + L_\mathrm{b\text{-}DBR}, \tag{4.4}$$

where L_sc is the geometrical lengths of semiconductor cavity, L_air is the air-gap, $L_{\mathrm{t-DBR}}$ and $L_{\mathrm{b-DBR}}$ are the penetration depths of MEMS- and bottom-DBR, respectively. This causes the plane phase-front at the fixed bottom mirror to gradually change to a spherical wave with a given spot size of

$$w_0 = \sqrt{\frac{\lambda}{\pi}\sqrt{L_\mathrm{o}(\mathrm{RoC} - \mathrm{L_o})}}. \tag{4.5}$$

Equation (4.5) gives a rough estimation of the beam waist of the Gaussian beam as it does not consider the multilayer VCSEL-structure [75]. Finally, the beam divergence can be calculated with a divergence angle θ_0, where

$$\theta_\mathrm{o} = \lim_{z\to\infty} \frac{w(z)}{z} = \frac{w_\mathrm{o}}{z_\mathrm{o}} = \frac{\lambda}{\pi w_\mathrm{o}}. \tag{4.6}$$

One of the most important aspects of VCSELs, in comparison to EELs, is their low beam divergence originating from the circular beam profile. Due to its rotational symmetry, the beam can be butt-coupled into the optical fiber – in most cases, without incorporating any corrective optics. This offers a cost efficient solution for packaging the devices. The divergence angle θ_0 of the VCSEL beam can be experimentally calculated from the spatial distribution of the radiated power in the far-field. In this section, the far-field pattern of a single-mode MEMS tunable VCSEL is recorded and the beam divergence is calculated. The VCSEL has an initial air-gap of 4.30 µm, RoC of 1030 µm and D_BTJ of 14.00 µm.

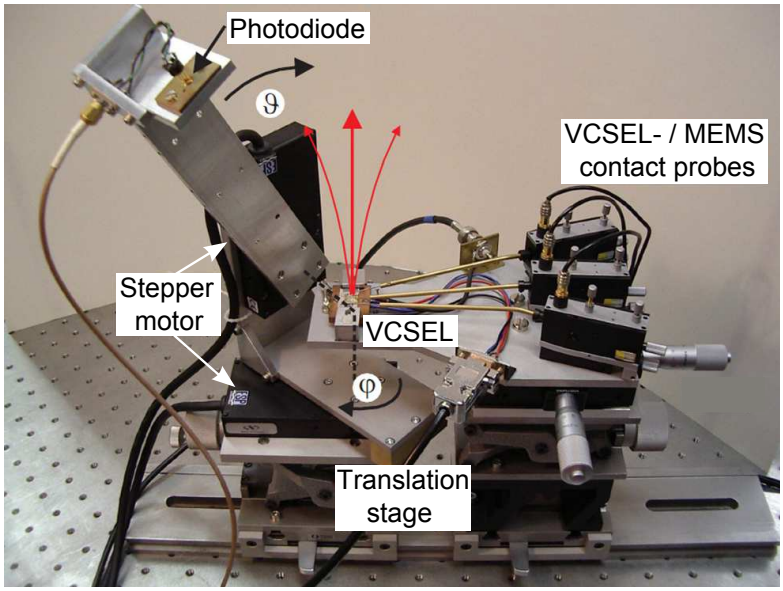

FIGURE 4.10: Far-field measurement setup.

The photograph of the measurement setup is shown in Fig. 4.10. The major parts of the setup comprises a commercially available InGaAs *p-i-n* photodiode (PD),[†] two computer-controlled rotation stages[‡] with built-in micro step drive stepper motors and a transimpedance amplifier (TIA).[§] The steppers are controlled by a motor driver.[¶]

[†]FGA21 InGaAs Photodiode from Thorlabs Inc., USA (2 mm active area, 0.88–1.05 A/W responsivity within 1400–1650 nm)

[‡]Newport PR50 Rotation Stage with 0.01° angular resolution

[§]HMS 564 low-noise transimpedance amplifier

[¶]ESP300 Motion Controller

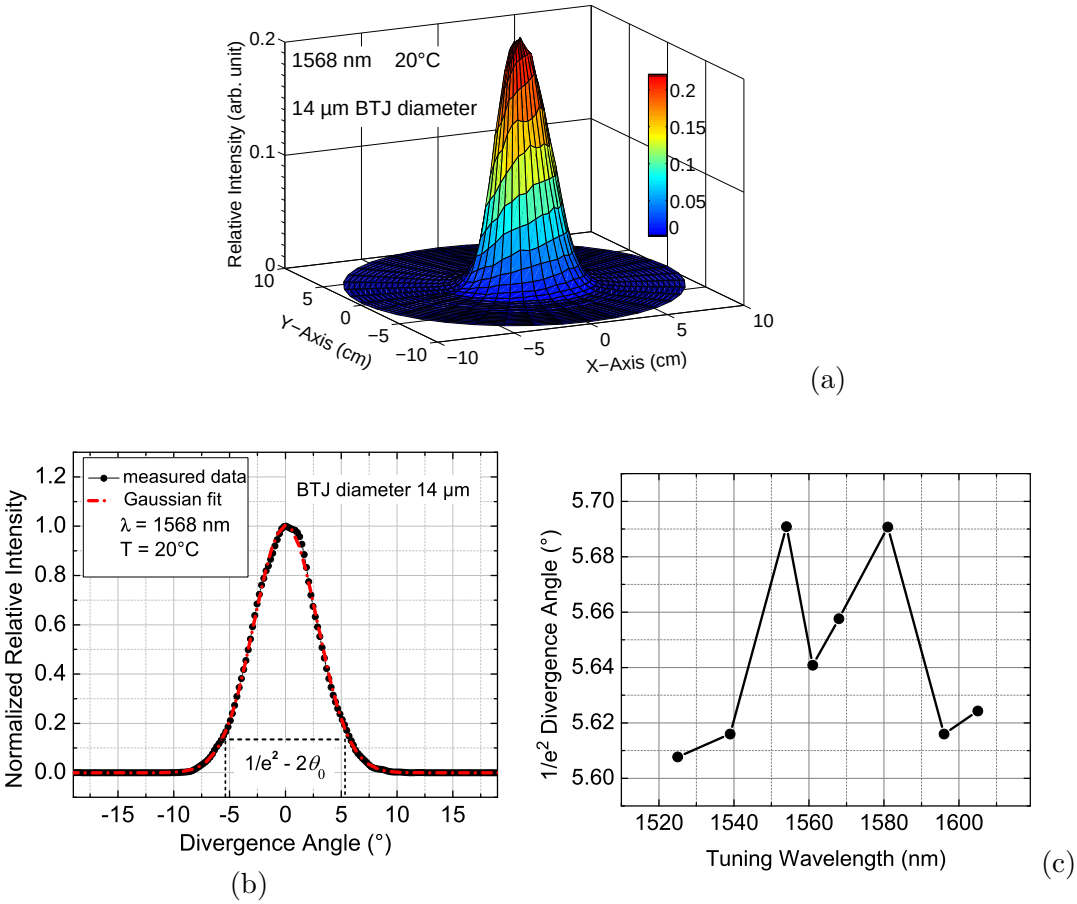

FIGURE 4.11: (a) Three dimensional color gradient of the far-field at 1568 nm emission wavelength at thermal rollover current of 35 mA and 20 °C heat sink temperature. (b) Relative optical intensity against divergence angle. (c) $1/e^2$ divergence angle for different tuning wavelengths.

The PD is mounted at a height of ≈ 20 cm above the MEMS VCSEL. The horizontally-mounted stepper motor provides the azimuthal rotation for the PD, as it is rotated from $-\varphi = -90°$ to $+\varphi = +90°$ with a resolution $\Delta\varphi = 5°$. For each φ value, the vertically-mounted stepper motor makes a spherical rotation from $-\vartheta = -30°$ to $+\vartheta = +30°$ polar angle with a resolution of $\Delta\vartheta = 0.2°$. The TIA converts the photocurrent into a voltage which is required for further processing for a complete three-dimensional field profile [76]. Figure 4.11 (a) shows the spatial mode characteristics mapped from far-field measurements for 1568 nm emission at $I_{\text{bias}} = 35$ mA and 20 °C heat sink temperature. At thermal rollover current of 35 mA, the MEMS VCSEL with the aforementioned membrane parameters still emits a circular symmetric, diffraction and refraction limited TEM_{00} beam. In comparison, a non-tunable VCSEL with a flat top DBR and a comparable half-VCSEL structure is highly multi-modal [76]. Even for a BTJ diameter of 6.5 µm the VCSEL lases with up to 9 transverse modes at thermal rollover of 12.5 mA. Consequently, multiple transverse modes overlap in far-field, forming an asymmetric,

doughnut-shaped beam (not shown here). Figure 4.11 (b) shows a randomly chosen one-dimensional cross-section far-field pattern of the corresponding three dimensional plot. The divergence angle θ_0 of the Gaussian fitting curve is 5.66° at the point where the intensity drops to $1/e^2$ (approx. 13.5%) of the highest peak. Despite this small divergence angle, efficient light-coupling is not possible without a lensed fiber due to the fact that the beam waist (inside the resonator) $2w_0 \approx 16\,\mu m$ is already larger than the standard SMF core $D_{core} = 8.2\,\mu m$. Considering the process parameters, the simulated penetration depths are approx. 1.5 µm and 2 µm for the MEMS- and bottom DBR, respectively. By using Eq. (2.71) and (2.72), one can calculate the spot size w_0 and the divergence angle θ_0. For $\lambda = 1568\,nm$ the calculated θ_0 is $\approx 5°$. However, the measured divergence angle does not perfectly match with the calculated far-field angle of 5°. This is due to the fact that Eq. (2.71) does not take into account the complicated coupled-cavity with multilayer structure of the MEMS VCSEL. Also the estimation is predominantly valid for passive optical resonators, neglecting apertures, guiding elements or refractive index steps inside the cavity. Figure 4.11 (c) shows the different divergence angles at different tuning wavelengths. Considering the measurement errors occurring from the vibration of the setup due to the stepper motors, it can be stated that the beam-divergence has a negligible amount of influence on the RoC of the MEMS for different tuning wavelengths.

4.1.4 Linewidth Measurements

Due to short-cavity related shorter photon life time, fixed wavelength VCSELs with flat top mirror show considerably larger linewidth compared to DFB lasers. A significant linewidth broadening arises when a movable MEMS is incorporated for wavelength-tuning. The typical linewidth of 1550 nm MEMS VCSELs reported in the literature are in the range of 40 MHz to 300 MHz employing a self-heterodyne technique [14, 77]. Due to its susceptibility of vibrations the MEMS mirror is exposed to unwanted vibrations, which can be simulated in two ways: acoustic coupling to external vibrations and through Brownian motion. The former can be significantly reduced by a well-designed mechanical isolation. However, the latter source is inevitable; any mirror movement will frequency-modulate the VCSEL and eventually degrade the linewidth performance. There are other factors such as radiation pressure, radiometric pressure and cavity extension in MEMS VCSEL which are also contributing to the linewidth broadening [77]. The radiometric pressure occurs due to intrinsic absorption of the MEMS-DBR. Consequently, a small temperature difference between the two sides of the DBR builds up and the mirror tends to move toward the cooler side resulting in an extension in the cavity length. By designing a mirror with lower absorption and by vacuum-packaging the devices, one can reduce this effect. Radiation pressure related MEMS fluctuation occurs when the mirror reflectivity is very high, which is the case for the MEMS-DBR.

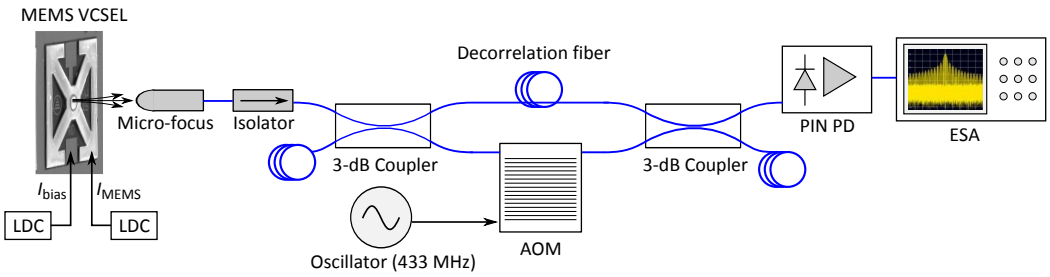

FIGURE 4.12: Linewidth measurements based on delayed self-heterodyne (DSH) method using fiber-based Mach-Zehnder interferometer.

High cavity power can deflect the MEMS-DBR upwards resulting in the shift in the emission towards longer wavelengths.

Linewidth measurement of an on-wafer MEMS VCSEL requires careful attention to a number of factors. Optical feedback from the MEMS mirror as well as from the fiber facet creates chaotic noise in the resonator [78] and make it difficult to reproduce the experimental results. Additional Gaussian noise is added from the photodiode and the spectrum analyzer. In this experiment the linewidth of a unpackaged on-wafer MEMS VCSEL is determined by using delayed self-heterodyne (DSH) interferometer technique, where the optical frequency of one arm is offset with respect to other. If the delay exceeds the coherence time of the laser, the combining beams interfere as if they originated from two independent lasers offset in frequency. The setup is shown in Fig. 4.12. The emitted light of the VCSEL is coupled into a polarization-maintaining fiber (PMF) with the help of micro-focus optics[‖] combining a lens system and a collimator. The lens system is AR coated which helps to minimize the back reflection of the light. The collimated light is then passed through an in-line isolator[**] in order to reduce optical reflections and back scattered feedback from the following connector stages. The output from the isolator is divided into two paths using a optical coupler. One of the beams is delayed by a 5 km long decorrelation fiber (time delay = 25 µs). This sufficiently long fiber allows for measuring linewidths and noise influences with a frequency above 40 kHz [14]. The other beam experiences an offset of 150 MHz by an acousto-optic modulator (AOM). The beat spectrum signal (the power density spectrum) captured by an electrical spectrum analyzer (ESA) yields the convolution of the linewidth. The measurements are averaged 100 times on the ESA. With a stable commercial laser, the setup is verified.

A Voigt profile fitting, which is the convolution of the Lorentzian and the Gaussian profiles, is helpful to separate two contributions individually. Figure 4.13 (a) shows the measured DSH beat signal of a MEMS VCSEL with $I_{\text{bias}} = 26\,\text{mA}$ and $I_{\text{MEMS}} = 0\,\text{mA}$, operating at an ambient temperature of 22 °C corresponding to 1548 nm emission. The linewidth is strongly influenced by a Gaussian behavior at the vicinity of the maximum,

[‖] Micro-focus optics from Schäfter + Kirschhoff GmbH, Hamburg, Germany
[**] General Photonics double stage in-line isolator, 40 dB isolation, 3 dB insertion loss

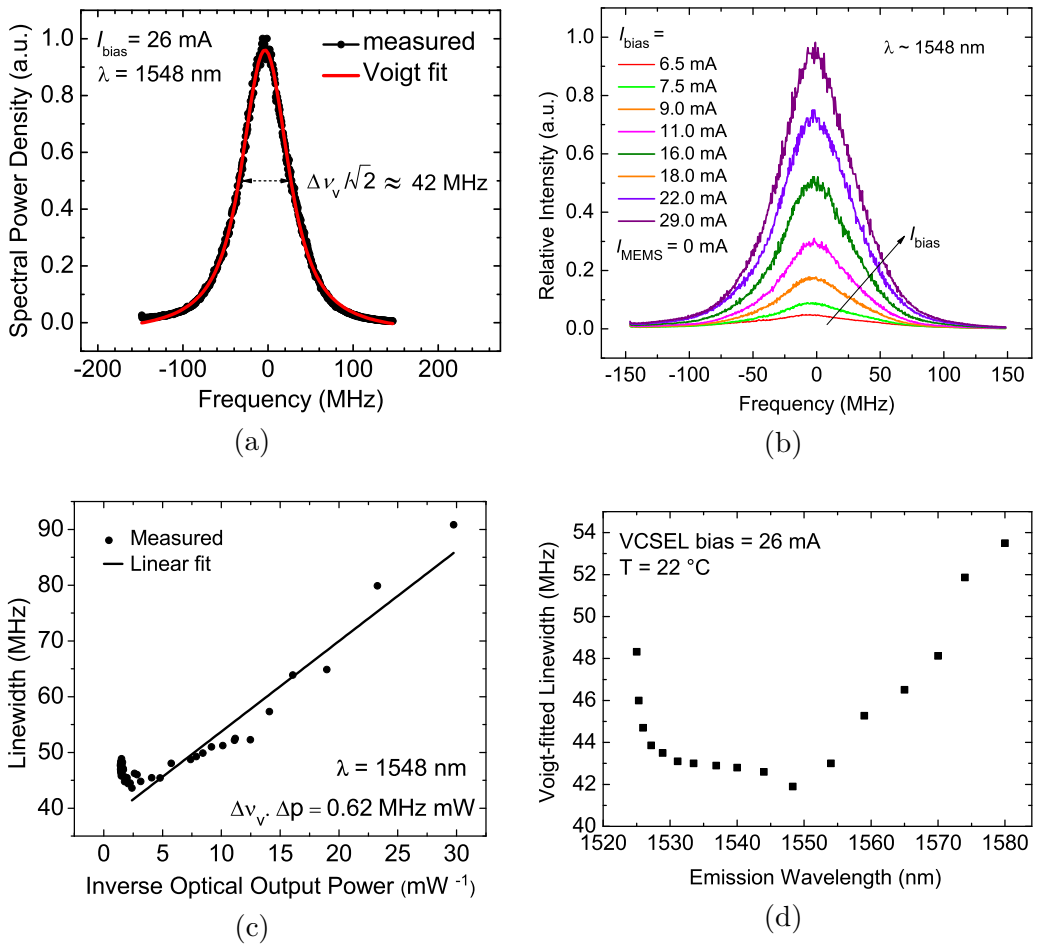

FIGURE 4.13: (a) Normalized power density spectrum of the beat note of self-heterodyne linewidth measurement of an MEMS VCSEL with a fiber delay length of 5 km. The total linewidth of this VCSEL is extracted to be 42 MHz. (b) Power density spectra of the beat signals for different operating currents. (c) Linewidth over the inverse optical power. (d) Voigt-fitted linewidth for different tuning wavelengths.

whereas the Lorentzian term is more dominant at distant frequencies. This allows the mathematical description of the laser spectrum as a Voigt rofile with strong Gaussian dominance. Therefore, the experimental data (black dots) are fitted with a Voigt profile (red curve). The Gaussian dominated linewidth $\Delta\nu_\mathrm{B}$ is estimated as the full-width half-maximum (FWHM) of the Voigt profile divided by a factor of $\sqrt{2}$, which eventually means $\Delta\nu_\mathrm{B} = 1/\sqrt{2} \cdot \mathrm{FWHM_{DHS}} = 42\,\mathrm{MHz}$.

Thermal noise related MEMS fluctuation results in a frequency fluctuation $\Delta\nu_\mathrm{rms}$ of the emission wavelength according to:

$$\Delta\nu_\mathrm{rms} = \frac{2|\Delta\nu_\mathrm{FSR}|}{\lambda_0}\sqrt{\frac{\mathrm{k_B}\,T_0}{k_\mathrm{m}}} \approx \frac{2c_0|\Delta\lambda_\mathrm{FSR}|}{{\lambda_0}^3}\sqrt{\frac{\mathrm{k_B}\,T_0}{k_\mathrm{m}}} \tag{4.7}$$

where $\Delta\nu_\mathrm{FSR}/\Delta\lambda_\mathrm{FSR}$ are free-spectral ranges (FSR) of the VCSEL cavity, $\mathrm{k_B}$ is Boltzmann constant, k_m is the spring constant of the MEMS-DBR, T_0 is the temperature,

c_0 is the speed of light and λ_0 is the emission wavelength [77]. The MEMS-DBR has a k_m value of 1350 N/m which is very close to the Comsol-Multiphysics-simulated value of 1300 N/m. Considering $\Delta\lambda_{FSR} \approx 71$ nm, $k_m = 1350$ N/m, $T_0 = 295$ K and $\lambda_0 = 1555$ nm one obtains $\Delta\nu_{rms} \approx 19$ MHz. In general, the frequency noise spectrum due to spontaneous emission is white and the resultant spectral shape is Lorentzian. If the intrinsic Lorentzian linewidth $\Delta\nu_L$ is smaller than the average fluctuation of the $\Delta\nu_{rms}$, an average linewidth $\overline{\Delta\nu}$, based on Gaussian distribution of the fluctuations can be defined as

$$\Delta\nu_B = 2\sqrt{2|\ln(0.5)|\Delta\nu_{rms}^2} \approx 2.35\Delta\nu_{rms} = 44.65\text{MHz}. \tag{4.8}$$

The measured $\Delta\nu_B$ is close to what has been obtained from Eq. (4.2) and is significantly less than the previously reported values for a packaged MEMS VCSEL in [79]. This is due to the fact that the smaller dimensions of the MEMS result in a larger k_m. Also the half-VCSELs used in this experiments have compressively strained quantum wells active region. The effect of free carrier plasma on linewidth degradation is lower in compressively strained quantum well devices in comparison to unstrained wells [80]. The power density spectrum of the DSH beat signal for diffident I_{bias} is shown in Fig. 4.13 (b). Figure 4.13 (c) shows the Voigt fitted linewidth $\Delta\nu_v$ over the inverse optical power $1/P$ for 1548 nm emission, where the linewidth increases linearly with $1/P$. A linear fit reveals a linewidth-power product of $\Delta\nu_v \cdot \Delta P = 0.62$ MHz mW. Figure 4.13 (d) is a plot of Voigt fitted linewidths for different tuning wavelengths. The dip in 1548 nm emission accounts for the maximum optical output power at this wavelength.

From the relationship between the Voigt spectrum with the Lorentzian and Gaussian spectra:

$$\Delta\nu_v = \frac{1}{2}\left(1.069\Delta\nu_L + \sqrt{0.867\Delta\nu_L^2 + 4\Delta\nu_B^2}\right) \tag{4.9}$$

one can also retrieve $\Delta\nu_L$ using so-called reference points away from the center. Since $1/f$ noise related broadening is endured mostly in the vicinity of the maximum, the 3-dB width strongly affected by Gaussian component is misleading. The 20-dB linewidth is characteristically dominated by the Lorentzian contribution and can be used for an educated estimation of $\Delta\nu_L$. Using this value as initial estimation, new 3-dB $\Delta\nu_L$ of 21 MHz is calculated. For comparison, the intrinsic linewidth estimated from the Lorentzian part of the Voigt fit is very close to the linewidth ($\approx$ 17 MHz) of a 1550 nm commercial non-tunable VCSEL with the similar basic structure [**?**]. The linewidth can further be reduced for narrow-linewidth applications like optical coherence tomography (OCT) by increasing the stiffness of the mirror (i.e. higher spring constant k_m) and by increasing both reflectivity of the MEMS-DBR as well as by increasing the air-gap (i.e.

longer resonator; higher Q factor). The linewidth can be significantly reduced by using a wavelength locked packaged MEMS VCSEL.

4.1.5 Polarization Measurements

MEMS VCSELs emit Gaussian beam profile with circular symmetry mainly due to their inherent quasi-circular resonator geometry. This cylindrical waveguide type resonator geometry also offers an interesting basis for polarization studies, specially the origin of a certain polarization selection. In general, the polarization properties are primarily determined by the polarization properties of the gain or, to be specific, by the interband optical transition matrix element [81], and by the geometric properties of the optical cavity. The polarization of the VCSEL emission ideally reflects the selection rules of the QWs' optical transition symmetry. Therefore, in principle, the emitted light should exhibit a circularly polarized state of light [82]. In EELs the anisotropic cavity shape as well as the mutual perpendicular direction between the carrier injection and light emission fix the polarization in a direction parallel to the active layer growth. However in VCSELs, due to vertical emission in reference to the wafer growth, the transition strength is the same for all polarization directions perpendicular to the direction of light emission [83]. Furthermore, the quasi-cylindrical symmetry of the VCSEL's structure leads to a trivial waveguide anisotropy. The gain and optical properties of VCSELs are isotropic for all polarizations perpendicular to the direction of light emission and therefore there is no intrinsic polarization selection mechanism in VCSELs. However, there are few mechanisms which can break the symmetry. Among them optically induced birefringence in the cavity and the mirrors [84], unintentional stress during manufacturing [85, 86], thermal effects [87, 88], and dichroism [89] are responsible for restricting the circularly polarized emission to linearly polarized emission. In this section the polarization characteristics of a tunable MEMS VCSEL is analyzed in terms of the Stokes vector parameters.

The Stokes parameters are a set of values that describe the polarization state of electromagnetic radiation. They are mathematically convenient alternative to the more common description of incoherent or partially polarized radiation in terms of its total intensity, degree of polarization (DOP), and the shape parameters of the polarization ellipse. The effect of an optical system on the polarization of light can be determined by constructing the Stokes vector for the input light and applying Müller calculus, to obtain the Stokes vector of the light leaving the system. The experiment uses the concept and setup mentioned by A. Molitor *et al.* in [90]. Figure 4.14 illustrates a schematic drawing of the experimental setup. The vertically emitted light is first collimated by a lens and then passed through a combination of a revolving quarter wave plate* and a fixed linear

*Quarter wave plate from B. Halle Nachfl. GmbH, Germany

polarizer.[†] Any linearly polarized light that strikes the quarter wave plate will be divided into two components with different indices of refraction. Thus it can convert linearly-polarized light to circularly polarized light and vice versa. The plane of the incident light is adjusted in a way that it makes 45° angle with the optical axis. Finally the light is detected by a photo detector which is connected to a computer. The intensity is measured and recorded as a function of the angle β (in radian) which is angle between the horizontal axis aligned with the crystal axis [110] and the fast axis of the quarter-wave plate. A fit to the obtained data depicted in the inset of Fig. 4.14 enables to derive four Stokes parameters S_0, S_1, S_2, and S_3, as well as the degree of polarization (DOP).

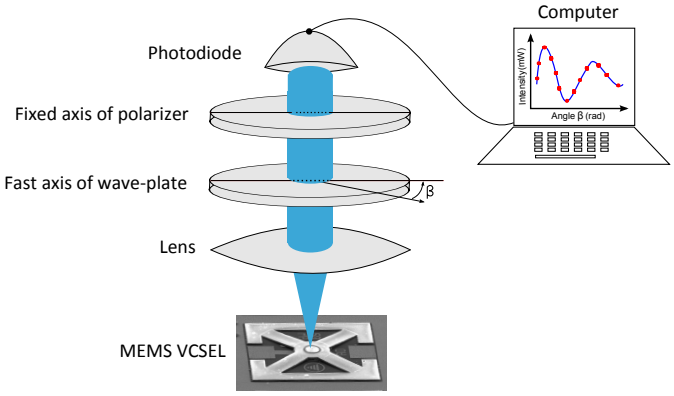

FIGURE 4.14: Sketch of the experimental setup for polarization measurements using Stokes vector parameters. The emitted light is collimated by a lens, passes a combination of a quarter-wave plate with revolvable fast axis and a polarizer with fixed transmission axis and is finally detected by a photo detector.

The first Stokes parameter S_0 represents the total intensity of the incident light. The S_1 parameter defines the linear horizontal (crystal axis [110]) or vertical (crystal axis [-110]) polarization. The S_2 parameter describes the amount of linear +45° or -45° polarization and S_3 describes the amount of right or left circular polarization contained within the investigated light beam. Now, the DOP can be calculated from the ratio of the sum of the three Stokes parameters S_1, S_2, and S_3 to the first Stokes parameter S_0. The Stokes vector of the detected light S'' at the detector can be calculated considering the effect of a quarter-wave plate and a linear polarizer on the Stokes vector of the VCSEL's emitted light S' using Müller matrix formalism, as:

$$S'' = \mathbf{M}_p * \mathbf{M}_{wp} * S'. \tag{4.10}$$

Here, $\mathbf{M}_p$ and $\mathbf{M}_{wp}$ represent the 4×4 Müller matrices for a linear polarizer and a quarter-wave plate, respectively. The first Stokes parameter of the detected light S_0'' can be simplified to this mathematical expression:

$$S_0''(\beta) = S_0' - S_1' * \frac{1 + \cos(4\beta)}{2} + S_2' * \frac{\sin(4\beta)}{2} + S_3' * \sin(2\beta)\,. \tag{4.11}$$

[†]Glan-Thompson polarizing prism, B. Halle Nachfl. GmbH

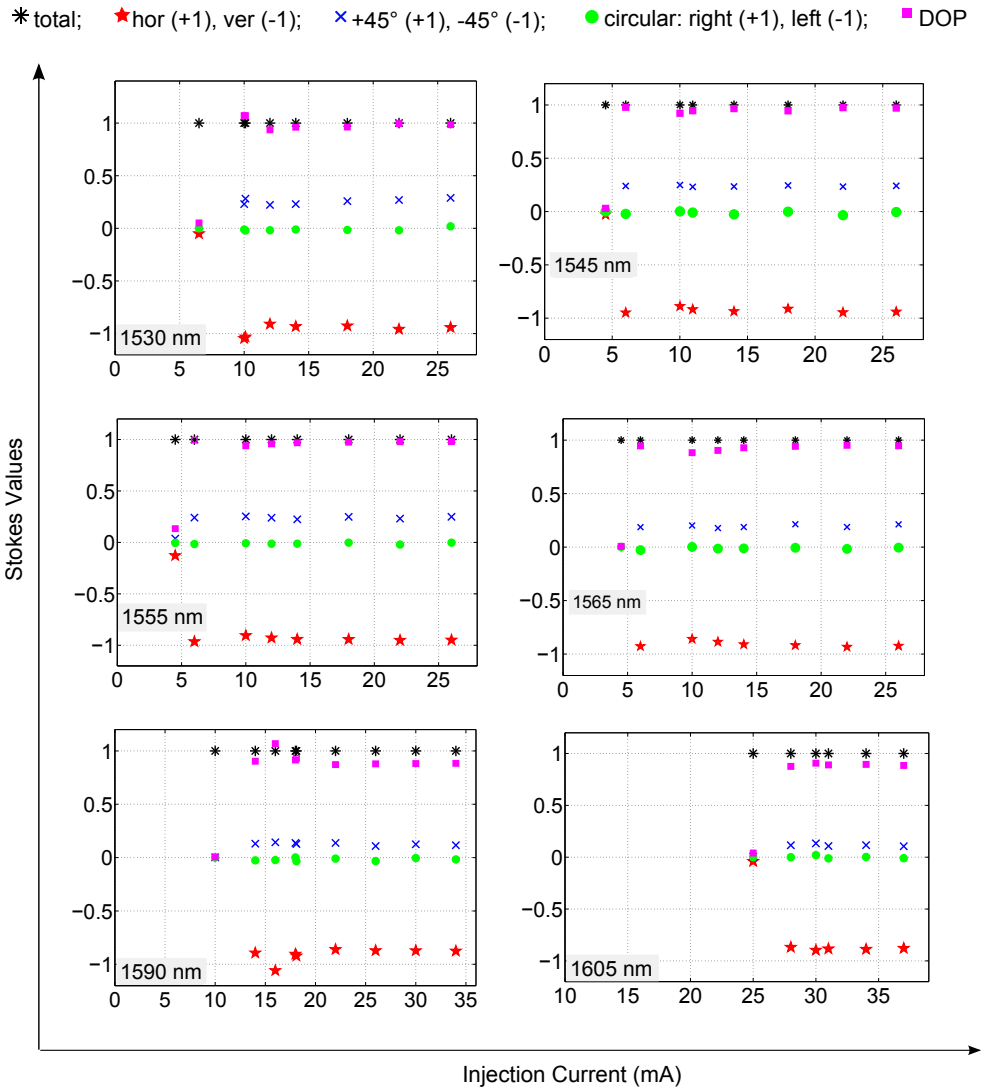

FIGURE 4.15: Normalized Stokes polarization parameters S_1 (red star), S_2 (blue cross), and S_3 (green circle) together with DOP (magenta square) as a function of laser injection current I_{bias} recorded at six emission wavelngths.

The unknown Stokes parameters S_0', S_1', S_2' and S_3' can be extracted by fitting the function within a multi-parameter fit to the measured intensity $S_0''(\beta)$ [91, 92]. By normalizing all four Stokes parameters to the total intensity S_0', S_1, S_2, and S_3 only take values between -1 and +1, whereas S_0 is constantly equal to 1 and is not depicted in the figures for the sake of clarity.

The polarization analysis is carried out for six different wavelengths namely, 1530 nm, 1545 nm, 1555 nm, 1565 nm, 1590 nm, 1605 nm. The heat sink temperature is set to 20 °C. The wavelengths are set by applying I_{MEMS}, whereas the I_{bias} is swept from 0 mA till the thermal rollover is reached. The measured normalized Stokes parameters, DOP and the total polarization are shown in Fig. 4.15 for different tuning wavelengths as a function of laser injection current. S_1 (red stars), S_2 (blue crosses), S_3 (green circles) and DOP (magenta squares) describe linear horizontal or vertical, linear with an orientation of

+45° or -45°, right or left circularly polarized light, and the amount of polarized light, respectively. Just below the lasing threshold (the lowest I_{bias} values in the plots) all these values are very close to zero, representing an unpolarized state of light due to the spontaneous emission. While increasing I_{bias} above the laser threshold, the state of polarization is constant which is represented by a dominant contribution of $S_1 = -1$. A small amount of S_2 of $\approx +0.2$ can be visible, reflecting a small misalignment of the lens and the subsequent stages with respect to the crystalline axis of the MEMS VCSEL. The DOPs for different emission wavelengths are calculated from the normalized Stokes values. A stable linear polarization together with a resulting high value of the DOP has been observed across the entire tuning range. As can be seen in 4.16, the DOPs are close to 1, reflecting a fully polarized state of light. This measurement with the injection current dependence of the Stokes parameters unveils the complete information about the orientation of the linear polarization, the amount and orientation of the circular polarization as well as the amount of polarized light in general. The polarization state in VCSELs can be controlled by introducing anisotropy in the waveguide or by providing a polarization dependent gain or loss, so that only one polarization state is sustained. The probable reason for polarization stability of this device can be attributed to the tilting of the suspended dish due to process related imperfections. Due to a misalignment in photolithography, the beams holding the MEMS can be slightly different in lateral dimensions. Based on the type of initial asymmetries, a significant mechanical movement of the membrane can cause a substantial tilt which in turn can favor only one polarization. However, this results may vary from device to device within the same wafer. Because of the cylindrical resonator geometry, the stability of the polarization is can be a fundamental problem for data transmission applications. By integrating a surface grating with dimensions in the sub-wavelength range – commonly known as sub-wavelength grating (SWG), direction-dependent mirror losses can be implemented. This defines the polarization of the VCSEL and stabilizes it under difficult conditions

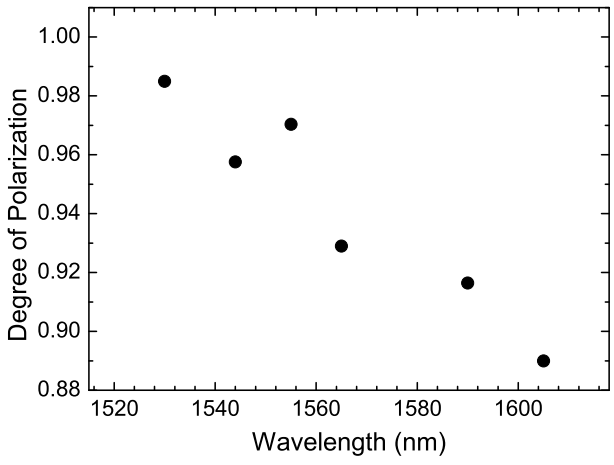

FIGURE 4.16: Degree of Polarization (DOP) of the device for six wavelngths.

such as modulation or feedback [14]. Alternatively, one can intensionally fabricate an elliptical MEMS dish to support one polarization mode [76].

4.2 Dynamic Characterizations

In this section, the MEMS VCSEL is characterized in terms of its dynamic response to small-signal modulation and relative intensity noise (RIN) behaviors. Both of these measurements give an estimation of the large-signal data transmission bandwidth in dynamic operation.

4.2.1 Small-Signal Modulation Response

In small-signal modulation experiment, the laser is modulated with a very small-amplitude sinusoidal signal around the bias point. By converting the modulated optical output to a photocurrent and by evaluating so-called scattering parameters (S-parameters) response with a network analyzer one can characterize the device in terms of small-signal behavior.

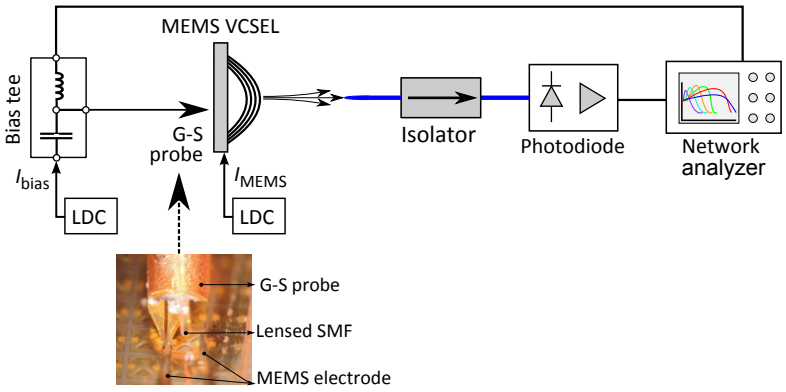

FIGURE 4.17: Setup for measuring the small-signal transfer function. The microscope image shows how the MEMS VCSEL is contacted on-wafer with a coplanner ground-signal (G-S) probe for dynamic measurements. The light output is butt-coupled to lensed single-mode fiber.

The experimental setup is shown in Fig. 4.17. The vector network analyzer (VNA)[†] is calibrated up to the end of the high-frequency (HF) ground-signal (G-S) probe,[‡] which is used for contacting the VCSEL bondpad. The calibration takes the frequency response of all electric components in between the VNA and the probe into account, thus compensates the losses due to impedance mismatch of the HF cables and connectors as a reference to 50 ohm system. A bias-tee[*] combines the small-signal sinusoidal modulation

[†] Agilent Technologies E5071C ENA
[‡] Cascade Microtech ACP40-GS-150 probe (40 GHz)
[*] Picosecond Pulse Labs (20 GHz)

current supplied by the VNA and the DC biasing component I_{bias} provided by an external current source LDC. In on-wafer configuration, the MEMS VCSELs can be directly probed due to their microstrip layout and coplanar connectivity. Thus one can get rid of additional potential parasitics from the bonding wires and the submount. The signal (S) of the G-S probe is supplied to the n contact pad of the VCSEL and the ground (G) is connected to the p contact pad (common backside p metal) of the neighboring VCSEL, as shown in Fig. 4.17. However, as far as single device is concerned, they are not apt for on-wafer coplanar probing as the VCSEL contacts are placed at opposite sides of the MEMS dish. The MEMS is probed separately with contact needles. The optical output is coupled into a micro-focus lensed SMF. The collimated light is then passed through an in-line isolator to reduce optical reflections and back scattered feedback. The output of isolator is fed to a high-speed photodiode.[§] The electrically converted output is then sent back to the second port of VNA. A comparison of the input and received output signal enables S-parameter analysis, with S_{21} representing the transfer function. The experiment is carried out for different bias currents and for different emission wavelengths, each at two temperature levels, 12 °C and 57 °C. To ensure the VCSEL is being modulated in the small-signal regime, the input electrical power is kept under -20 dBm.

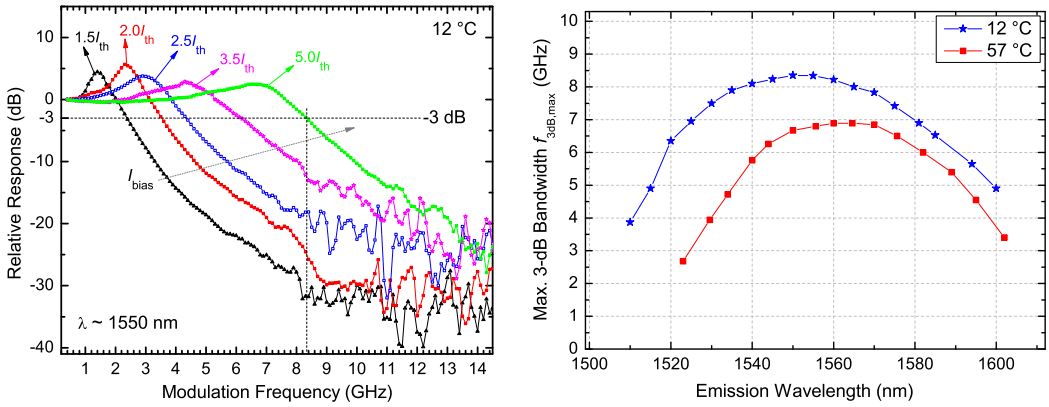

(a) (b)

FIGURE 4.18: (a) Small-signal modulation response of a 14 µm BTJ-diameter MEMS VCSEL for different injection currents above $I_{\text{th}} \approx 3.00$ mA. The laser is emitting at around 1550 nm at a heat sink teperature of 12 °C. (b) Maximum 3-dB bandwidths $f_{\text{3dB,max}}$ for different emission wavelengths at 12 °C and 57 °C.

Figure 4.18 (a) shows the small-signal modulation response of the MEMS tunable VCSEL operating at 12 °C and emitting at 1550 nm emission wavelength. Ideally, the laser exhibits a typical second-order low-pass behavior. Taking additional electrical parasitics into account the total transfer function H(f), as shown in Eq. (2.64), results in a three-pole filter function including relaxation-oscillation frequency f_{R}, intrinsic damping γ and parasitic roll-off f_{p}. The resonance peak shifts towards higher frequencies for

[§]Anritsu MN4765A O/E Calibration Module, 3-dB bandwidth 65 GHz, responsivity 0.7 A/W

increasing I_{bias} values above laser threshold. This is because the output power and photon density increase with increasing current above threshold. For $I_{\text{bias}} = 5I_{\text{th}} \approx 15\,\text{mA}$ ($I_{\text{th}} = 3.00\,\text{mA}$), a maximum 3-dB bandwidth, $f_{\text{3dB,max}}$ of 8.35 GHz is obtained. The modulation response curves in Fig. 4.18 (a) also reveal that the resonance peak flattens and broadens out with increasing bias, as the damping present through γ increases in proportion to f_{R}^2. With increasing current, the damping becomes large enough that the response drops below the 3-dB cutoff at frequencies less than f_{R}. Using the formula in Eq. (2.34) combined with the definition of γ (neglecting γ_0), one can determine the maximum modulation bandwidth for low damping. $f_{\text{3dB,max}}$ for different tuning wavelengths at two temperature levels namely, 12 °C and 57 °C are retrieved and plotted in Fig. 4.18 (b). In both temperatures, $f_{\text{3dB,max}}$ shows a upturned "U" shape characteristics, with a clearly visible red-shift for the measured values at 57 °C. At 12 °C, the lowest value of $f_{\text{3dB,max}} = 3.88$ GHz can be found at the shortest measured wavelength of 1510 nm; whereas for 57 °C, this is reduced to 2.68 GHz which is obtained at the emission wavelength of 1523 nm.

Figure 4.19 (a) summarizes the 3-dB cutoff frequency of the small-signal transfer function H(f) against the square root of the current above threshold, $(I - I_{\text{th}})^{1/2}$. The curves represent four tuning wavelengths (1515 nm, 1535 nm, 1555 nm, and 1575 nm) at 12 °C. The measured data are fitted in lower current regime with a linear straight line equation which passes though the origin (0,0). The slope is denoted as the modulation current efficiency factor (MCEF). The same measurements are retreated at 57 °C and the extracted MCEF values for two temperature levels are summarized in Fig. 4.19 (b). At 12 °C the highest value of MCEF = 2.62 GHz/mA$^{1/2}$ can be found at 1555 nm emission. It is evident that MCEFs at 57 °C for longer wavelengths do not decrease very much in comparison to those at 57 °C. The steep flanks at the edges of the spectrum reflect

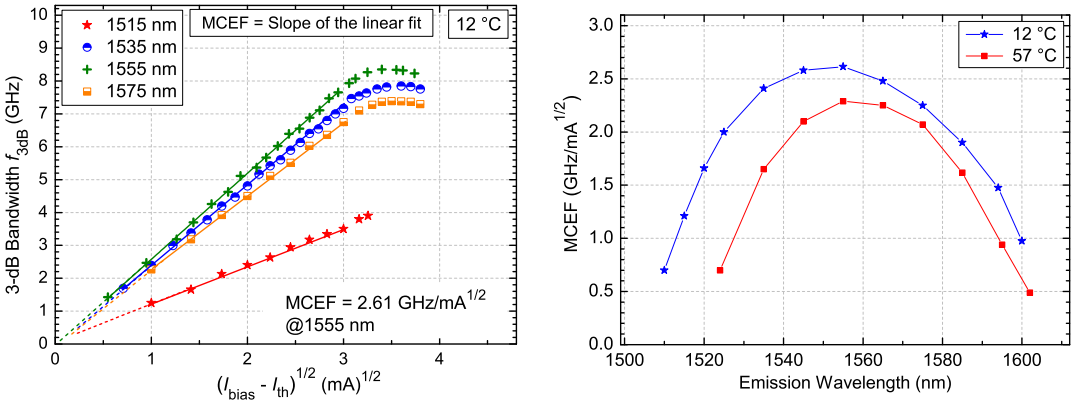

(a) (b)

FIGURE 4.19: (a) Small-signal 3-dB modulation bandwidth f_{3dB} as a function of $(I - I_{\text{th}})^{1/2}$, shown for 12 °C. (b) The slopes of the plots (f_{3dB} versus $(I - I_{\text{th}})^{1/2}$) are the corresponding MCEF values, which are plotted as a funtion of emission wavelength for two heat sink temeratures: 12 °C and 57 °C.

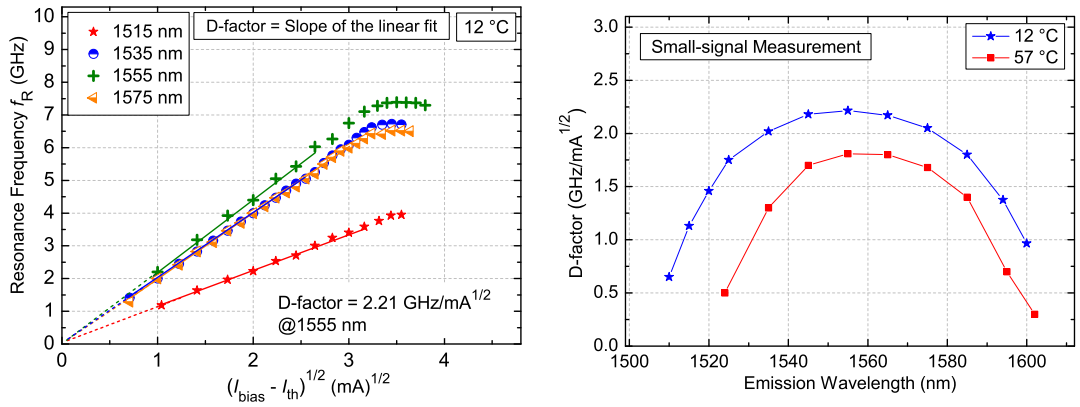

FIGURE 4.20: Resonance frequency f_R against the square root of the bias-current above threshold $(I - I_{th})^{1/2}$ shown for 12 °C (b) The slopes of the plots (f_R versus $(I - I_{th})^{1/2}$) are the corresponding D-factor values plotted as a funtion of emission wavelength for two heat sink temeratures: 12 °C and 57 °C.

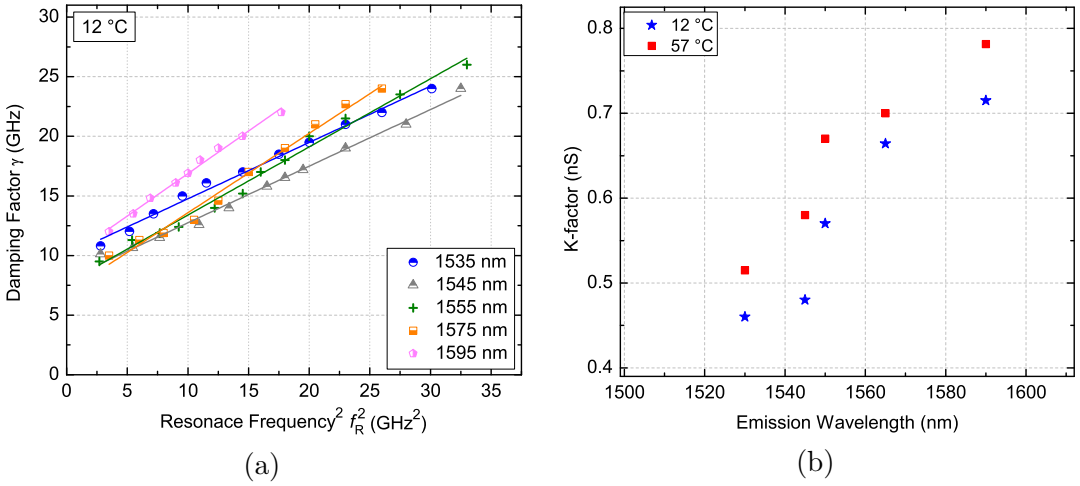

FIGURE 4.21: (a) Intrinsic damping factor γ vs. square of f_R plot shown for 12 °C. and (b) The K-factors that are obtained from a linear fit to the data, obtained for 12 °C and 57 °C for different tuning wavelengths.

the low differential gain in this area. The plots of the resonance frequencies f_R as a function of $(I - I_{th})^{1/2}$ for five tuning wavelengths at 12 °C are shown in Fig. 4.20 (a). The data points are fitted with linear equations crossing through the origin. The slope quantifying the increase of f_R with increasing I_{bias} in lower self-heating regime is the corresponding D-factor. Due to intrinsic heating at higher injection currents the gain of the active region decreases and the resonance frequency converges into its maximum, shown by the saturation of the otherwise linear slope. As expected, the laser shows its absolute maximum resonance frequency of 7.39 GHz at 12 °C for the center wavelength of 1555 nm. The corresponding maximum D-factor is 2.22 GHz/mA$^{1/2}$. The derivation from the linear region is due to the thermal damping effect. The same measurements are also carried out at 57 °C and the D-factors for the measured tuning wavelengths at two temperatures are compared in Fig. 4.20 (b). The effect of reduced resonance frequency

by decreased gain becomes especially obvious for the measurement at 57 °C. The drop of the MCEF from 2.62 GHz/mA at 12 °C to 2.29 GHz/mA at 57 °C is less significant in comparison to changes in the corresponding D-factor values (from 2.22 GHz/mA at 12 °C to 1.81 GHz/mA at 57 °C). This indicates an improved intrinsic and parasitic damping for the SC half-VCSELs at elevated temperatures. The latter refers to a high *RC*-parasitics-limited parasitic roll-off frequency f_P with a maximum value (obtained from the fitting curves of the measured small-signal-modulation response) of 5.90 GHz at 57 °C and at 1555 nm emission. Therefore, the modulation bandwidth of the VCSEL is limited by intrinsic and thermal damping, since the modulation bandwidth limit is much higher for a solely parasitically limited VCSEL [13]. In general, the relatively overall small D-factors are probably due to a large cavity length resulting from the incorporated air-gap as well as high penetration depth into the MEMS DBR and the large current aperture. To further enhance the 3-dB bandwidth of S_{21} response, a larger D-factor is desirable. It can be improved with a shorter cavity length design, fine-tuning of the refractive indexes of the DBR dielectrics, reduction of the aperture size, and reduction of the optical losses by implementing a proper ARC.

The damping rate versus the resonance-frequency f_R squared for five tuning wavelengths at 12 °C are plotted in Fig. 4.21 (a). By extracting the slope one can obtain the so-called K-factor. In general, higher wavelengths resulting from the longer cavity lengths have larger K-factor value. The half-VCSELs used in these experiments have much shorter cavity length compared to that of previous generation VCSELs [22]. Moreover, the enhancement of differential gain of the highly strained quantum-wells are supportive factors for low K-factors. In comparison to D-factor, K-factor is relatively insensitive to changes in temperature. This is due to the fact that the free-carrier absorption increases at high temperatures, because of increased phonon scattering rates leading to reduced carrier relaxation times. Meanwhile, differential gain is reduced. These two effects cancel out, leading to a temperature-stable K-factor. However, a reduction in photon-lifetime is expected to have an even stronger effect on the K-factor. Therefore, MEMS VCSEL resonator structure with a shortened air-gap and cavity length will further reduce the K-factor. Table 4.1 summarizes the small-signal parameters of the MEMS VCSEL operating at 1555 nm emission wavelength.

TABLE 4.1: Device parameters of the MEMS VCSEL at 1555 nm emission, derived from the small-signal analysis.

Maximum 3-dB bandwidth $f_{3dB,max}$	8.35 GHz
Maximum resonance frequency f_R	7.39 GHz
Modulation current efficiency factor (MCEF)	2.62 GHz/$\sqrt{\text{mA}}$
D-factor	2.21 GHz/$\sqrt{\text{mA}}$
K-factor	0.58 nS

4.2.2 Relative Intensity Noise (RIN)

The relative intensity noise (RIN) measurement provides an alternative method to determine the intrinsic small-signal parameters of a semiconductor laser. The measurement setup is illustrated in Fig. 4.22. The fiber-coupled laser light is fed to a PIN PD through an in-line isolator. The optical feedback from the subsequent connectors and reflectors appear as an external cavity that can tremendously influence the RIN. The feedback-induced intensity noise repeats with periodical resonance at spectral distance of $\Delta f = \mathrm{c}/2nL_{\mathrm{ec}}$, where c is speed of light, n is refractive index of the medium and L_{ec} the external cavity length. The electrical output from the photodiode is divided by a bias tee where the DC component is measured with a voltmeter and the AC noise component is fed into an ESA. The RIN is defined as the noise power within a bandwidth of 1 Hz normalized to the average (DC) power and is thus independent of the losses between the laser and the PIN PD. The ESA has a bandwidth of 2 MHz which adds 63 dBm to the electrical spectrum. This can be compensated by normalizing the RIN value with respect to Δf. The measured offset voltage V_{DC} is converted to $P_{0,el}$ by assuming a 50 Ω system. This leads to the computation of the RIN by the measuring quantities as follows:

$$\frac{\mathrm{RIN}}{\Delta f} = 20 \cdot \log_{10}\left(\frac{\sqrt{10^{(P_{\mathrm{el}}-63\,\mathrm{dB})/10} \cdot \frac{50\,\Omega}{1000}}}{V_{\mathrm{DC}}}\right) \tag{4.12}$$

In practice, the intensity noise which is measured using the aforementioned setup includes additional noise sources such as dark current from the PD, thermal noise from the electrical components (amplifier and ESA), $1/f$ noise, and shot noise. Figure 4.23 (a) shows the measured RIN spectra of the MEMS VCSEL evaluated in accordance with Eq. (4.12) at $I_{\mathrm{bias}} = 1.5I_{\mathrm{th}} = 4.65\,\mathrm{mA}$. The emission wavelength and the operating temperature are set to 1550 nm and 12°C, respectively. The low-frequency range in which the $1/f$ noise of the receiver dominates, is not shown here. A power density spectrum with RIN = -138 dB/Hz with a relaxation resonance peak at 3.85 GHz is achieved. The electrical power spectrum measurement is repeated for different I_{bias} values and plotted in Fig. 4.23 (b). The measurement is repeated for different tuning emission wavelengths.

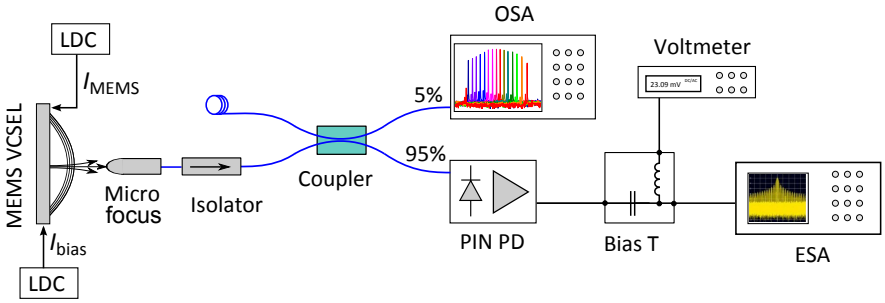

FIGURE 4.22: Experimental setup for RIN measurement.

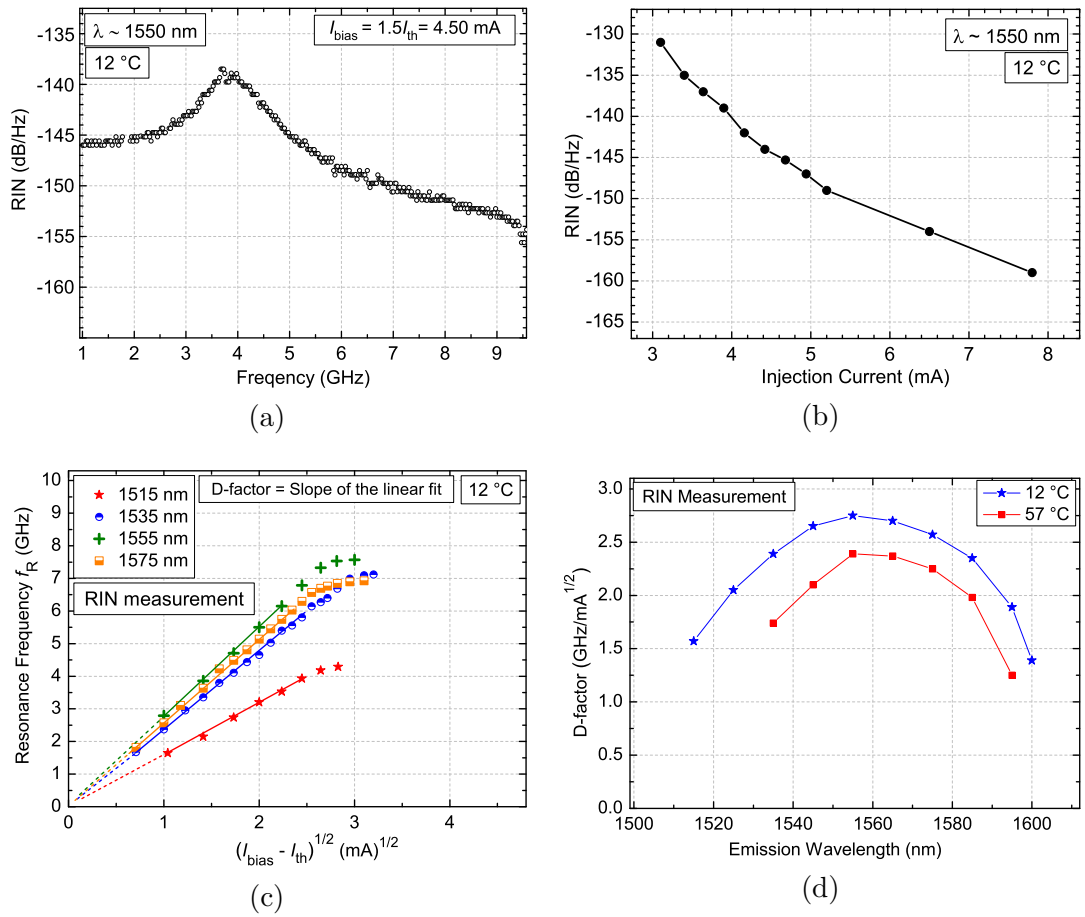

FIGURE 4.23: (a) RIN spektum at 1550 nm emission for $I_{\text{bias}} = 1.5I_{\text{th}}$. (b) RIN values as a function of bias-current. (c) resonance frequency f_{R} against the square root of the bias-current above threshold $(I - I_{\text{th}})^{1/2}$ for 15 °C, (d) Calculted D-factors for the RIN measurement.

The resonance frequencies f_{R} retrieved from the measurements are plotted as a function of $\sqrt{I - I_{\text{th}}}$, as shown in Fig. 4.23 (c). The data points in the linear region are fitted with a linear function where the slope gives the D-factor of the device. The value of D-factor = 3.05 GHz/mA$^{1/2}$ at 1555 nm shows a good agreement with the D-factor obtained from the small-signal modulation response. As the emission wavelength is tuned towards the edges of the tuning range, the dynamic behavior is strongly influenced by the effective spectral gain distribution. In general, the resonance frequency f_{R} saturates (not shown here) due to the internal heating at high operating currents. Figure 4.23 (d) summarizes the D-factors for different tuning wavelengths obtained from the RIN measurements at two temperature levels. Due to increasing SNR at elevated temperature, the precision of finding the resonance peak is highly reduced for the 57°C measurements. When heated to 57°C, both the small-signal and the RIN measurements show a decrease in the D-factor, which is due to a decrease in the differential gain at elevated temperatures.

The significant decrease in the maximum resonance frequency during the small-signal

measurement may be an indication of an additional limitation caused by charge carrier transport into the active zone or lateral diffusion via the relatively large aperture. It can be shown that the RIN measurement does not just prove the similar behavior as the small signal modulation but actually gives a very good estimation for the relevant f_{R}. It is assumed that the maximum of the RIN power density spectrum corresponds in good approximation ($Bf^2 \gg A$, cf. Section 2.2.2) to the actual relaxation oscillation frequency, whereas the small-signal frequency response due to attenuation generally reflects a somewhat lower resonance frequency. The measured $f_{\mathrm{3dB,RIN}}$ is slightly larger than $f_{\mathrm{3dB,S21}}$ which can be attributed to the additional the parasitic effects of the contact pad included in the small-signal measurement. Finally, it should be noted that there are other methods for characterizing the dynamic laser properties. On the one hand, the transient response in the time domain can be observed, but the influence of the parasitic elements must be small. In the case of dominant parasites, the modulation of the charge carriers can also be optically induced in order to characterize the intrinsic modulation behavior. An estimation of the resonance frequency of the VCSEL, with the exclusion of parasitic effects, can already take place by a simple measurement of the optical spectrum. The narrow emission line of a single-mode laser is accompanied by satellite peaks, whose spectral distance or width and intensity correspond to the resonant frequency or attenuation of the relaxation oscillations. If these features are sufficiently pronounced, these sidebands may already be resolved with an OSA [22].

4.2.3 Tuning Speed

The tuning speed of the MEMS VCSEL plays an important role in several applications such as OCT and gas sensing. In order to monitor transient processes and to avoid fluctuating measurement conditions like beam steering (refractive index fluctuations in the measurement path) during sensing applications, scan rates of 100 Hz or higher are usually desired [19]. In this section, the tuning speed of a electro-thermally actuated MEMS VCSEL is investigated by applying a sinusoidal modulated signal which is added to a DC heating current $I_{\mathrm{MEMS}} = 25\,\mathrm{mA}$. Figure 4.24 depicts the frequency response of the device. The I_{bias} is fixed at 20 mA during the whole experiment whereas the operation temperature is set to 22 °C. The modulation depth decreases 10 dB/decade for higher frequency corresponding to a low pass filter of first order,

$$\Delta\lambda(f) = \frac{\Delta\lambda_0}{\sqrt{1 + (3\frac{f}{f_{\text{3-dB}}})^2}} \tag{4.13}$$

with maximum tuning range of $\Delta\lambda_0$, the modulation frequency f, 3-dB frequency $f_{\text{3-dB}} = \sqrt{3}/(2\pi\tau)$ where τ is the thermal time constant. For the device with $\Delta\lambda_0 = 70\,\mathrm{nm}$, a fit reveals $\tau = 1.37\,\mathrm{ms}$. At the characteristic cut-off frequency of $f_{3-\mathrm{dB}} = 200\,\mathrm{Hz}$ the device covers half of its initial tuning range. With increasing frequencies, the heat inside the

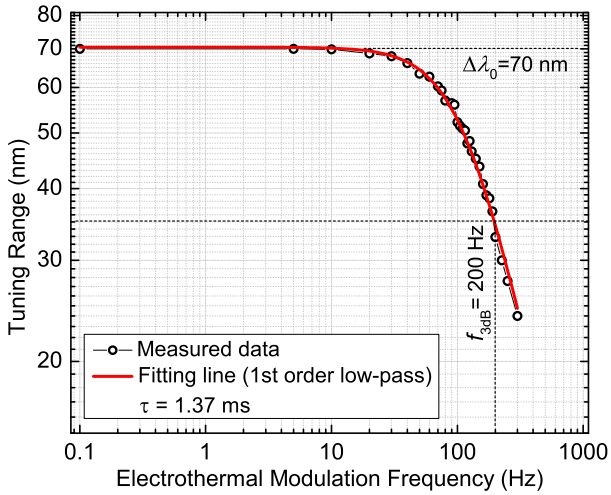

FIGURE 4.24: Frequency response of the MEMS under electro-thermal actuation. The static tuning range of 70 nm reduces to half at a modulation frequency $f_{3\text{-dB}} = 200Hz$.

MEMS is not fully dissipated during the modulation cycle and the tuning range converges towards zero around the central wavelength.

Chapter 5

Applications of MEMS VCSELs

The capability of having wide tuning range makes the MEMS VCSELs ideally suited for a wide range of applications. Depending on the application, their performance features such as static electro-optical parameters, small-signal modulation behavior, MEMS tuning speed etc. are optimized. As the MEMS VCSELs developed in this work are designed for optical data transmission, the main focus of this chapter is set on the short-reach fiber transmission application. In addition, the scope of these high-speed optical sources is investigated for two applications namely dispersion spectroscopy and tunable terahertz (THz) signal generation.

5.1 Optical Data Transmission

In order to evaluate the rigorous performance in an optical fiber based data transmission system, modulation analysis in so-called large-signal domain is essential. In this section, transmission experiments at 10 Gbit/s and 12.5 Gbit/s data rates are performed in back-to-back (BTB) configuration and bit error rates (BERs) are recorded as a function of received optical power. Afterwards, standard single-mode fiber (SSMF) of different lengths are installed in order to emulate the real-time system performance. The above mentioned experiments are carried out using on-wafer, directly-modulated devices. Finally, a packaged MEMS VCSEL is used for transmission experiments at 10 Gbit/s for an SSMF length up to 40 km without any dispersion compensation.

5.1.1 Back-to-Back Transmission

In direct current modulation scheme, the electrical signal containing the information is directly combined with the driving current I_{bias} as large-signal, thus modulating its

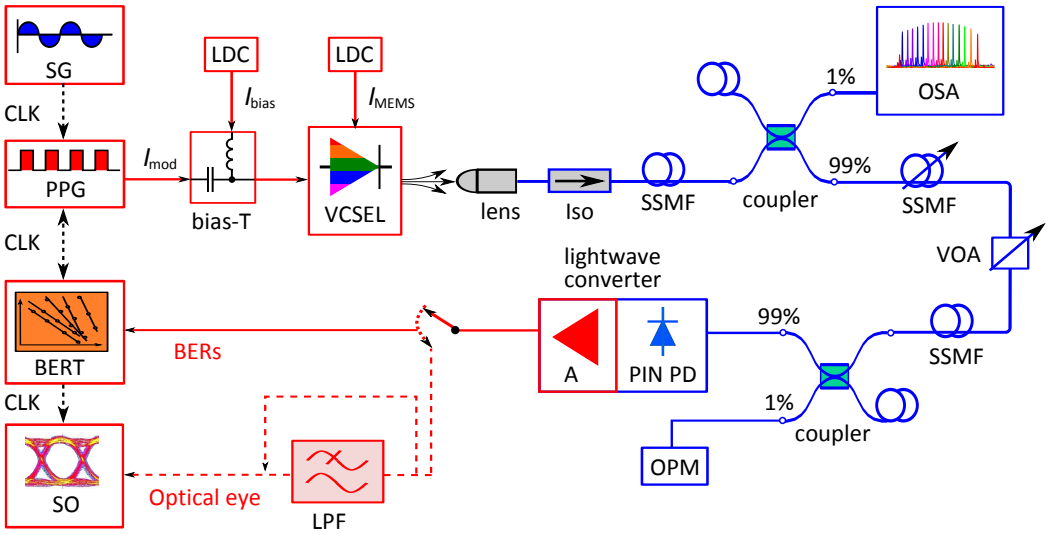

FIGURE 5.1: Experimental setup for large-signal data transmission. SG: signal generator, PPG: pulse pattern generator, LDC: laser diode controller, Iso: isolator, SSMF: standard single-mode fiber, OSA: optical spectrum analyzer, VOA: variable optical attenuator, PIN PD: *p-i-n* photodiode, A: preamplifier, OPM: optical power meter, LPF: electrical low-pass filter, BERT: bit-error rate tester, SO: sampling oscilloscope. The maximum operating frequency of 12.5 Gbit/s of the BERT is the maximum data transmission capacity of the setup.

optical output. In order to exclude any bandwidth limitations imposed by the optical fiber, the experiment is conducted in BTB configuration using an SSMF of only ≈ 5 m length. The experimental setup is shown in Fig. 5.1. The on-wafer chip with its coplanar connectivity is directly contacted by the G-S probe (see Fig. **??**). The bias-tee combines I_{bias} set by the laser diode controller (LDC) and the AC modulation signal, I_{mod}. The AC input branch of the bias-tee comes from a pulse pattern generator (PPG)* which provides the binary digital signal with a variable peak-to-peak voltage, V_{pp}. For this experiment, a non-return-to-zero (NRZ) modulation format with variable pseudo-random-binary-sequence (PRBS) is used. An external signal generator (SG) which generates the modulation frequency is fed to the PPG. The emitted light of the VCSEL is coupled into the SSMF with the help of AR coated micro-focus optics. The modulated optical output of the VCSEL is passed through an in-line isolator. The output is split and fed to several devices using couplers. In the first coupler stage, 99% of fiber output of the VCSEL is fed to a fiber coupled variable optical attenuator (VOA), which is connected to the measurement-controlling computer via GPIB connection. The remaining 1% of the light is inserted to an optical spectrum analyzer (OSA) for monitoring the emission wavelength. The output of the VOA is further split by the second coupler, with 10% being coupled out to an optical power meter (OPM). The OPM is calibrated to match the power of the remaining 90% signal, which is the received optical power for BER measurements. The 90% branch is connected to a lightwave converter† which converts

*Advantest D3186 pulse pattern generator, 150 Mbit/s to 12.5 Gbit/s
†Agilent 11982A lightwave converter

the optical signal back to an electrical signal. It combines a *p-i-n* photodiode (PIN-PD) with a low-noise preamplifier to provide a general-purpose front-end for lightwave frequency- and time domain measurements. The presence of a preamplifier in front of the oscilloscope can be critical to boost the electrical signal detected by the photodiode above the noise floor of the oscilloscope. The electrical output is alternatively connected to either a bit error rate tester (BERT)[‡] or to a sampling oscilloscope (SO).[§] The SO scans the data signal and generates the optical eye diagram from the transmitted bits, by means of which the transmission system can be visually adjusted for the best qualitative performance. The low-pass filter (LPF) within the path is helpful for removing the low frequency components and thus smoothing the eye diagram. The BERT is synchronized with the PPG as well as the clock generator, and connected to the PC via GPIB. It computes the BER values by comparing the bit sequence with the received signal.

Data transmission experiments at 10 Gbit/s are carried out for different emission wavelengths. In the first experiment, the influence of different PRBS word lengths on the BER is investigated for a fixed emission wavelength of 1550 nm. The length[*] of the PRBS generated from the PPG is given by the expression, $2^x - 1$, where x lies between 7 and 31. I_{bias} and V_{pp} are set to 25 mA and 1.5 V (optimized by observing the eye diagram), respectively. Figure 5.2 (a) summarizes BER measurements at 1550 nm emission and 20 °C substrate temperature for three different word lengths ($2^x - 1$; x = 7, 15, and 31). One can see the BER curves are shifted towards right for increasing word lengths. That means, signals with longer word lengths require higher received optical plower at a given BER value and bit rate. The power penalty at BER = 10^{-9} between $2^{31} - 1$ and $2^7 - 1$ word-length BER curves is 0.75 dB. A PRBS signal with a longer word length has a larger effective signal bandwidth due to increased low-frequency spectral components. In the corresponding eye-diagrams recorded at BER < 10^{-9}, one can identify narrower traces for $2^7 - 1$ word length compared to $2^{31} - 1$ curve. This corresponds to a lower effective bandwidth, thus a rather limited/small number of possible transitions. The vertical eye opening is also reduced for $2^{31} - 1$ word length, requiring more received optical power, i.e., lower signal-to-noise ratio (SNR) for a certain bit rate. As the long bit-patterns are only required by long-haul applications (also requires significantly long experiment-time), word lengths of $2^{15} - 1$ are predominantly used for the following measurements. In order to investigate the receiver-sensitivity, the tunable VCSEL output is externally modulated with a Mach-Zehnder modulator (MZM) with $2^{31} - 1$ word length. At a fixed BER value of BER = 10^{-9}, the power penalty for $2^{31} - 1$ word-length curve with

[‡]Advantest D3286 Error Detector, up to 12.5 Gbit/s

[§]Agilent infiniium DCA 86100B wideband oscilloscope

[*]The PRBS of x-th order gives an indication of the size of the sequence, whereas $(2^x - 1)$ is the maximum number of bits that are in the sequence. If N bits of data are segmented into every possible word of length x, one can list every possible combination of 0s and 1s for a x-bit binary word, with the exception of the all-0s word. The sequence can be stretched to infinity by repeating it after N elements, but it will then be cyclical and thus called "pseudo-random".

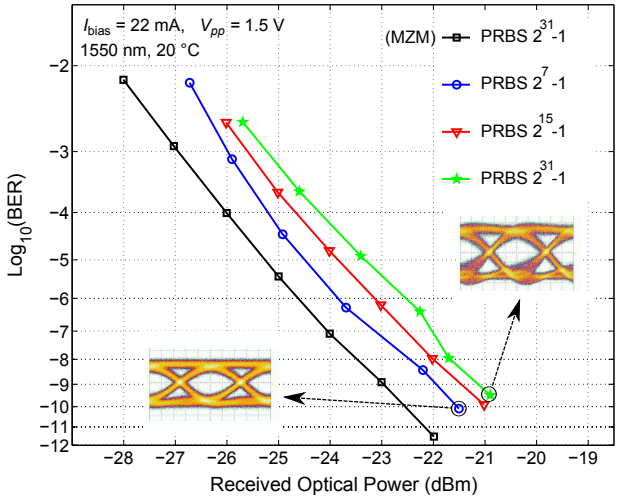

(a)

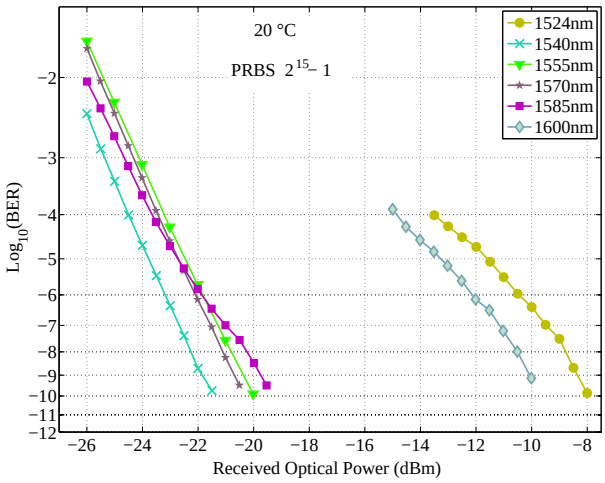

(b)

FIGURE 5.2: BER performance as a function of received optical power, operation at 10 Gbit/s NRZ direct modulation in back-to-back configuration. (a) BER curves for three PRBS word lengths with reference to a MZM, measured to 1550 nm emission. (b) BER performance for six tunable emission spectra with a fixed PRBS length of $2^{15} - 1$.

reference to MZM is 1.70 dB. This can be attributed to lower SNR and overshooting distortions, which is confirmed from the corresponding optical eye diagrams.

Next, the BER measurement at 10 Gbit/s is conducted while tuning the emission wavelength. Although the device can be tuned across 87 nm range (centered at 1563 nm) with a SMSR > 40 dB, quasi error-free transmission at 10 Gbit/s rate can only be achieved for a tuning range of 76 nm. Figure 5.2 (b) shows the BER plots of six tuning wavelengths including two edges of the emission spectra (1524 nm and 1600 nm). As can be seen, the four wavelengths representing the central region of the emission spectra (1540 nm, 1555 nm, 1570 nm, and 1585 nm) lie close to each other. This means the performance of the device in this region can be well assumed before installation and

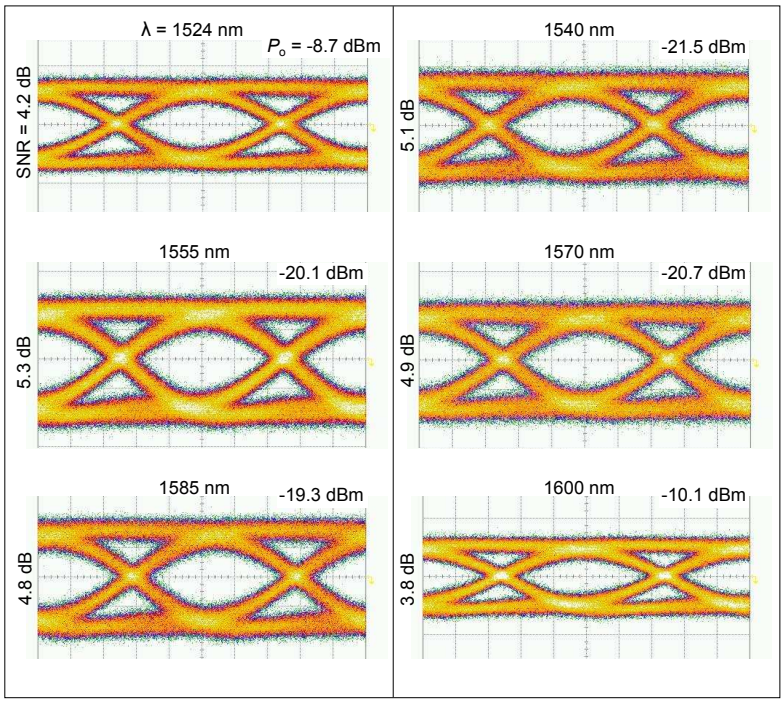

FIGURE 5.3: Optical eye diagrams including SNRs and corresponding recieved optical powers for six tunable emission spectum. The eyes are recorded for quasi error-free transmission at 10 Gbit/s.

will not require significant alteration of the driving condition in case the wavelength is required to be adjusted within this region. One can also see the deteriorating performance of the laser at the two spectral edges, as it demands significantly increased optical power for achieving a BER of 10^{-9}. This shifts the respective curves to the right side of the plot. The wavelengths on the edges of the tuning range have significantly high power penalties in reference to those around the center, following the trend of the small-signal modulation response (center wavelengths have larger 3-dB bandwidths of S_{21}) of the device. In comparison to central wavelengths, the wavelengths at the edge of the spectra have reasonably higher threshold current, lower rollover current and lower slope efficiency (cf. Fig. 4.5). As a result, the dynamic range of the laser significantly reduced as far as the large-signal modulation is concerned. This is directly translated to the overshooting distortions on the received optical signal. For choosing an optimal bias point for a certain modulation amplitude, the eye-openings are observed carefully. The optical eye diagrams of the corresponding wavelengths used in BER measurement are shown in Fig. 5.3. The eye for each wavelength refers to lowest measured BER value of the corresponding curve. Changing relevant parameters such as I_{bias} and V_{pp} causes an immediate change in the opening of the eye diagram, thus helps to fine-tune the system performance. As can be seen, at the two edges (i.e., 1524 nm and 1600 nm) of the tuning range, the SNR values are smaller compared to the rest of the wavelengths. However, even with a SNR of 3.80 dB at 1600 nm emission, quasi error-free transmission is possible for $2^{15} - 1$ long words.

From Fig. 4.5, it is evident that each emission wavelength has a slightly optimal operation point concerning dynamic measurements. Especially, I_{bias} has to be set for each wavelength and temperature level. Consequently the modulation V_{pp} needs to be adjusted, so that it remains within the linear region of the *L-I* curve. However, I_{bias} optimized by observing the optical eyes are higher than the expected value (from Fig. 4.5 plots). The optimal bias points are rather close to the respective CW thermal roll-over. A bias point near thermal rollover refers to a lasing operation in a strongly non-linear regime. For 10 Gbit/s NRZ large signal operation across the whole tuning range, the MEMS VCSEL is expected to have a S_{21} 3-dB bandwidth of $\approx$7 GHz (70% large signal modulation frequency). However, as shown in Fig. 4.18 (b), the device has as low as $\approx$4.3 GHz S_{21} 3-dB bandwidth at 1600 nm emission wavelength at 12 °C (it should be slightly lower for 20 °C). This suggests that neither the static *L-I* curves are impeccably representative for setting up the large-signal bias point nor the small-signal 3-dB bandwidth gives an perfect estimation about large-signal bandwidth for these lasers. This phenomenon can be explained as follows. Large-signal modulation can be compared to pulsed operation, especially if the modulation amplitude is large enough to switch the laser completely off. When the device is driven with 50% duty cycle pulses under large-signal modulation, the thermal rollover occurs at higher pump currents compared to CW operation. That means, the thermal budget is significantly larger for a 50% duty cycle pulsed operation. The InP-based half-VCSELs are mostly thermally limited, therefore, the modulation response is over-damped and has a smooth shape favoring higher data-rate [93]. If one considers only the small-signal analysis, performance of these BCB VCSELs could be underestimated by common rules of thumb.

In order to investigate the BER performance at elevated temperature, the MEMS VCSEL is modulated at 10 Gbit/s while changing the substrate temperature from 12 °C to 55 °C. For four temperature levels, namely 12 °C, 27 °C, 41 °C and 55 °C the wavelength is tuned in 5 nm step by adjusting I_{MEMS} and the corresponding BER values are recorded as a function of the received optical power. Figure 5.4 (a) shows the shortest (λ_{min}) and the longest (λ_{max}) emission wavelengths (at each temperature level), for which the BERT is still capable of receiving quasi error-free 10 Gbit/s data. One can see that the BER curves at 12 °C require lower received signal power compared to other curves. At elevated temperature the overall cavity loss is increased, whereas the signal power is reduced by lower material gain. Intrinsic heating sets a limit to the compensation of increased noise level by higher driving current. A summary of the λ_{min} and λ_{max} as well as the corresponding tuning range ($\lambda_{\mathrm{max}} - \lambda_{\mathrm{max}}$) at 10 Gbit/s operation for the aforementioned temperatures is shown in Fig. 5.4 (b). As can be seen, the tuning range at 10 Gbit/s operation is shrinking with increasing temperature (from 74 nm at 12 °C to 60 nm at 55 °C). However, the contribution of the shrinkage coming mostly from the lower wavelength edge λ_{min}, which is converging towards the center wavelength. This can be attributed to the typical red-shift of the material gain. The red-shift of the

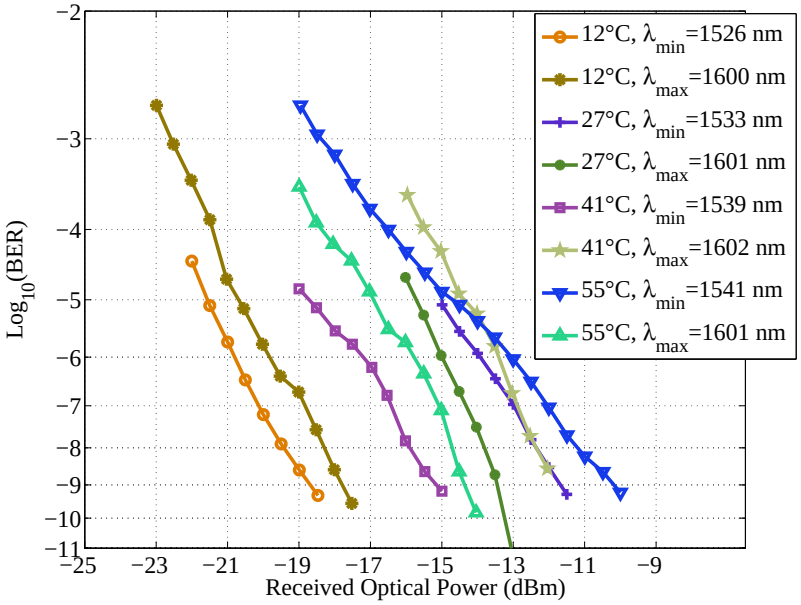

(a)

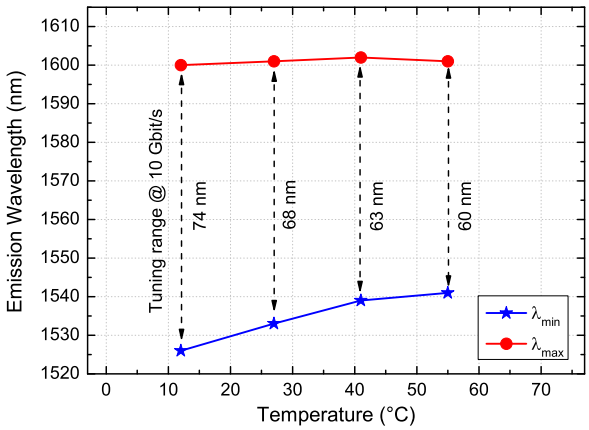

(b)

FIGURE 5.4: (a) Minimum and maximum wavelength for quasi error-free transmission in dependency of temperature operated in BTB configuration. (b) Tuning range as well as the minimum/maximum wavelengths (at which 10 Gbit/s transmission rate can be obtained) as functions of substrate temperature.

gain cannot exceed the subsequent λ_{max}, but causes the lower limit of the tuning range to increase. The overall change in 10 Gbit/s-operation tuning range due to change in temperature is still very small. This proves that the transmission capabilities of the SC MEMS VCSELs are very robust even under non ideal temperature conditions, which lowers the requirements for high quality temperature control for a packaged device.

Figure 5.5 shows the measured BER performance at 12.5 Gbit/s, which is the limiting bit-rate supported by BERT setup. Quasi error-free (BER $< 10^{-9}$) operation for 60 nm

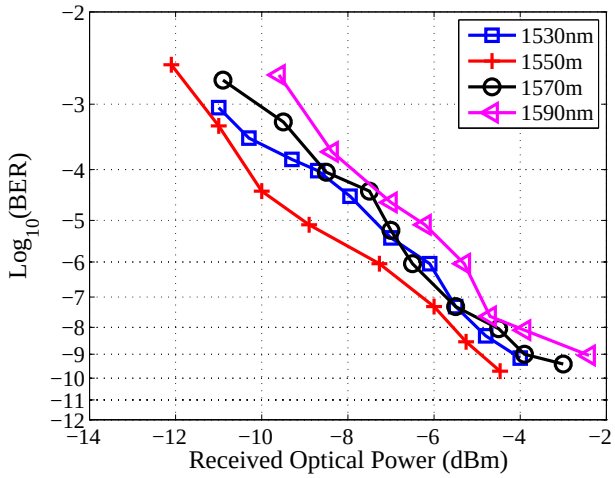

FIGURE 5.5: BER performance as a function of received optical power for BTB 12.5 Gbit/s NRZ direct modulation.

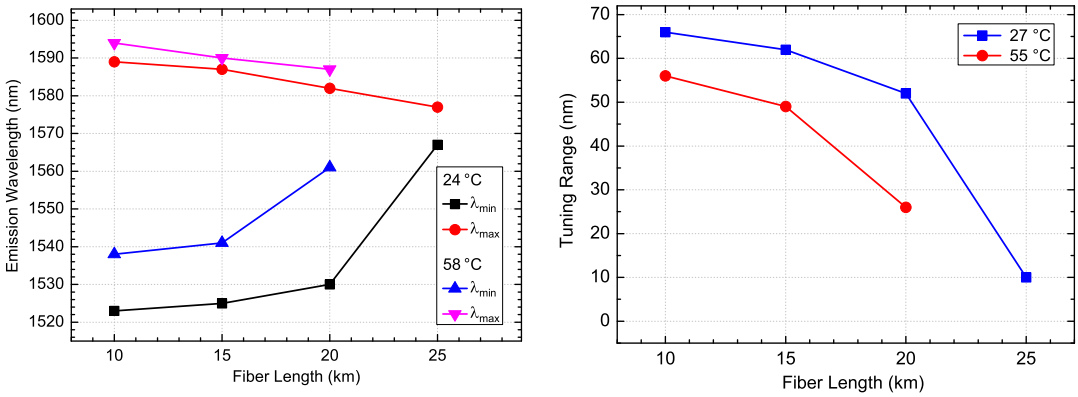

FIGURE 5.6: (a) The shortest (λ_{min}) and the longest (λ_{max}) emission wavelengths capable of transmitting error-free 10 Gbit/s transmission are plotted as a function of the fiber length at two temperature levels. (b) Corresponding tuning range achieved for 10 Gbit/s transmission at same temperature levels.

continuous tuning range (1530 nm to 1590 nm) is still achieved, which is the state-of-the-art tuning range for such bit rate. The results also suggest the compatibility of the MEMS tunable VCSEL as a potential source for 16 Gbit/s standard applications.

5.1.2 Data Transmission Using Single-Mode Fiber

After performing the BTB transmission experiments, SSMF of different lengths are installed to the experimental setup (cf. Fig.5.1) to simulate a real data transmission environment. The BER curves are recorded for different fiber lengths of 10 km, 15 km, 20 km and 25 km. For each fiber length, the maximum tuning range is retrieved for 10 Gbit/s quasi error-free transmission. The experiments are conducted at two temperature levels of 24 °C and 58 °C.

Figure 5.6 (a) shows λ_{min} and λ_{max} for 10 Gbit/s transmission as a function of the fiber length. For both temperatures, λ_{min} converges more rapidly to the center of the tuning range for increasing fiber length. Both waveguide- and material dispersion decrease with increasing wavelength. Consequently, longer wavelengths experience less pulse broadening along the fiber propagation, the signal quality suffers less and transmission is possible over longer distances at those wavelengths. The poor performance of the VCSEL on the tuning edge of its emission spectrum still causes the upper edge wavelength to shift towards the center wavelength, where higher optical power performance can compensate the dispersion and attenuation losses. Figure 5.6 (b) shows that the product of tuning range and fiber length is reduced significantly for 58 °C curves. Comparing the steep slopes of the curves beyond 15 km of fiber length, one can clearly see that dispersion and other transmission length dependent losses come into concern in that regime. The increasing temperature degrades the device performance for both longer and shorter wavelengths due to increased intrinsic losses and thermal noise. As the red-shift of the material gain and dispersion both favor longer wavelength, the center wavelength of the tuning range is also red-shifted for both higher temperatures and longer transmission lengths. However, the tuning range for a 20 km transmission line at 58 °C is still 27 nm – which is achieved by direct modulation, without any signal recovery methods, filtering or dispersion compensation.

5.1.3 Applications using Packaged MEMS VCSEL

After successfully dicing, gluing to the submount wafer and bonding the MEMS and the VCSEL pads to the submount, a few devices have been packaged to form TOSA (Transmitter Optical Sub-Assembly) with a standard LC connector. A flex cable is later soldered to the pins of the TOSA, via which the modulation signal can be fed. The MEMS VCSEL used for this experiment is characterized with a continuous tuning of $\approx$92 nm (from 1518 nm to 1610 nm). The fiber coupled optical power P_{opt}, SMSR and corresponding MEMS actuation power $P_{MEMS} = I^2_{MEMS} \times R_{MEMS}$ for a constant I_{bias} are recorded as a function of the tunable spectrum and shown in Fig. 5.7. As can be seen, the actuation power is not perfectly linear (orange line with star symbol), which is due to partial ARC damage the half-VCSEL. P_{opt} is over 1 mW in a range of 52 nm, which reaches the specification mentioned in Appendix D. The SMSR is $>$45 dB across the entire tuning range.

Fiber Transmission

Before explaining the measurement setup and the experimental results, a low-cost tunable MEMS VCSEL based WDM-PON concept is briefly discussed. The details of the setup

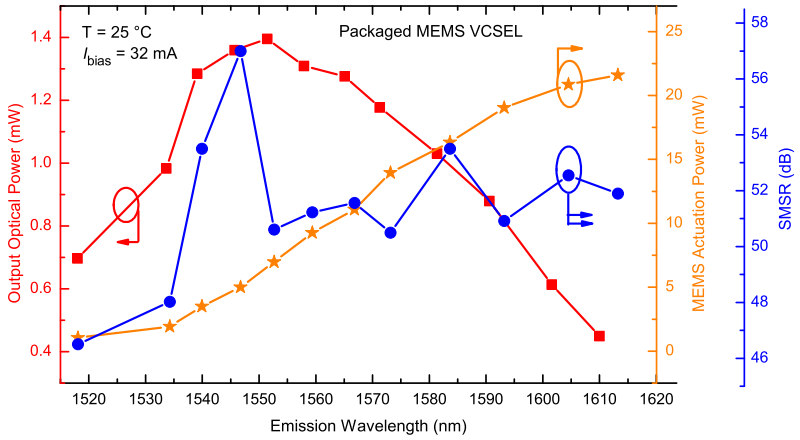

FIGURE 5.7: Fiber-coupled power, SMSR and corresponding MEMS actuation power $P_{\mathrm{MEMS}} = I^2_{\mathrm{MEMS}} \times \mathrm{R}_{\mathrm{MEMS}}$ of a packaged MEMS VCSEL plotted against its tunable emission wavelength.

and the experiment are explained in [94]. The WDM-PON is illustrated in Fig. 5.8 (a). The main aspect of the proposed WDM-PON system is a centralized wavelength-locker enabled autonomous tuning of the MEMS VCSEL in the tail-end equipment (TEE). The centralized locker is shared by all TEEs. In this way, it eliminates the necessity of wavelength-controlling for individual transmitter and reduces the system cost [95]. The optical distribution network (ODN) can be based on a tree or dropline architecture. The wavelength multiplexing (MUX) and demultiplexing (DEMUX) are realized by arrayed waveguide gratings (AWG). In case the feeder fiber length is significantly longer than the drop fibers (the differential end-to-end reach is typically under 5 km), a single dispersion-compensating fiber (DCF) in the head-end allows optimization of the chromatic dispersion for all channels. Droplines use optical add/drop multiplexers in several locations. In case the differential reach matches the for MFH specifications of 20 km. a single DCF is installed and optimized for the entire range of relevant reach. Thus, both architectures can be supported [94].

Figure 5.8 (b) shows the experimental setup. The experiment is mainly focused on the upstream application for MFH and MBH. Therefore, a limited reach of up to 40 km is considered. The packaged MEMS VCSEL is directly modulated at 10.3125 Gbit/s with $2^{31} - 1$ bit long PRBS signal. The tuning range has been limited to 33 nm (1529 nm to 1592 nm) to compensate a decrease of the optical power at two edges of the tuning range. The I_{bias} and the V_{pp} are set to 22 mA and 1 V, respectively and are kept constant for all measurements. The modulated signal is coupled into an SSMF and is transmitted over a maximum distance of 40 km. The accumulated dispersion at the OLT is compensated by a DCF matched to 40 km for all transmission lengths. It is worth to mention that the G.metro standard considers an optional erbium-doped fiber amplifier (EDFA) in upstream direction to reduce the requirements at the tail-end tunable transmitter. As the cost of EDFA and DCF will be distributed among all subscribers, the approach is

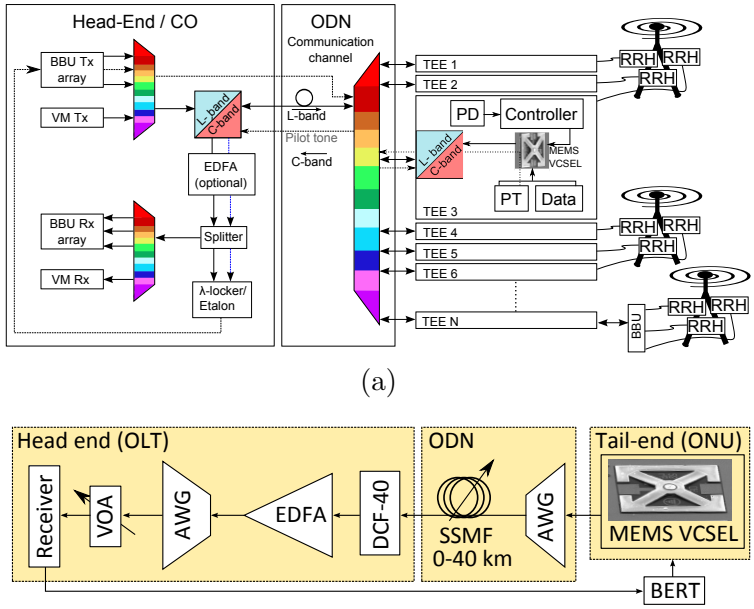

FIGURE 5.8: (a) A concept of a WDM-PON system based on low-cost tunable MEMS VCSEL. TX: transmitter, RX: receiver, AWG: arrayed waveguide grating, PD: photodetector, PT: pilot-tone. (b) Experimental setup. VOA: variable optical attenuator, EDFA: Erbium-doped fiber amplifier, SSMF: standard single-mode fiber„ DCF: dispersion compensating fiber, AWG: arrayed waveguide gratings, BERT: bit-error rate tester, OLT: optical line terminal, ODN: optical distribution network, optical ONU: optical network unit.

still cost efficient. Now, the dispersion compensated signal is finally launched into an SFP receiver on an evaluation board via a VOA. The electrical signal is connected back to the BERT to evaluate the BER performance.

Figure 5.9 (a) shows the BER as a function of the received optical power for BTB without DCF for four wavelengths (1529 nm, 1548 nm, 1567 nm, and 1592 nm), thus constituting a tuning range of of 63 nm. The BTB measurements show a wavelength dependent receiver sensitivity. In order to evaluate the system performance in an actual application case, the I_{bias} and the V_{pp} are not changed while tuning the wavelength. Figure 5.9 (b) shows the experimental results for the SMF transmission between 0–40 km with a constant dispersion compensation matched to 40 km SMF. That means, a transmission length of 0 km refers to simplest case where the signal is launched directly into the DCF. Comparing the BERs at 10^{-9}, the receiver sensitivities after 40 km SSMF transmission and BTB show similar results. This is expected due to the DCF matched to 40 km. For transmission lengths between 0 km and 30 km the receiver sensitivity varies < 1 dB for a particular wavelength. For G.metro MFH applications, the differential reach is limited to 20 km. This leads to a system optimization of the DCF. From Fig.5.9 (b), it can be seen that the smallest deviation of the receiver sensitivity for a 20 km transmission range is between 10 km and 30 km. This means that the optimum DCF should be matched to 30 km SSMF. The receiver sensitivity varies within 1.75 dB

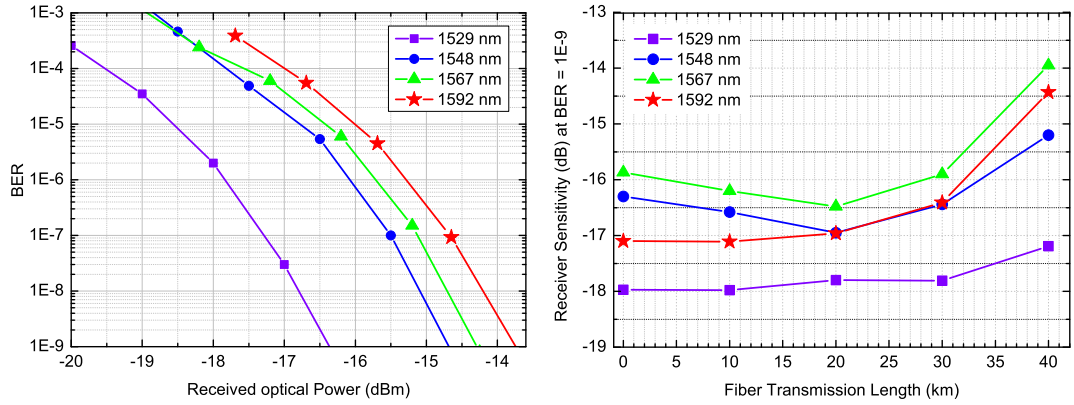

(a) (b)

FIGURE 5.9: (a) Back-to-back BER performance vs. received power for various wavelengths. (b) Receiver sensitivity measured as BER vs. receied optical power for different emission wavelengths after 1-40 km standard single-mode fiber (SSMF) and dispersion compensating fiber (DCF) matched to 40 km SSMF [**?**].

over the whole tuning range and all transmission reaches. Taking into consideration that the VCSEL settings are kept constant for all wavelengths and transmission lengths, the results are very promising. In other applications such as MBH and enterprise access where longer differential reaches are required, transmission is still possible with slightly increased penalties [**?**].

Application as Colorless ONU Transmitter

A. Gatto *et al.* has employed the fabricated MEMS VCSEL in a so-called colorless optical network unit (ONU) transmitter. The experimental results are published in [96]. Implementation of discrete multi-tone (DMT) modulation in combination with direct detection facilitate to overcome the bandwidth limitation of the MEMS VCSEL (≈ 7 GHz small-signal modulation bandwidth) and allow to employ a standard receiver suitable for 10 Gb/s operation. As a result, an upstream transmission beyond 25 Gbit/s using an SSMF of 20 km has been archived without any chromatic dispersion compensation. This shows the potential of the MEMS VCSEL as a high-bandwidth, low-cost, reduced-footprint ONU source in time and wavelength multiplexed-PON (TWDM-PON) system [96].

Application in SDN-Enabled Flexible Optical Metro Networks

M. S. Moreolo *et al.* has proposed and experimentally validated for the first time the potential of a directly modulated MEMS VCSEL in software-defined networking (SDN)-enabled sliceable bandwidth variable transceiver (S-BVT) flexible optical metro networks [97]. The integration of the fabricated MEMS VCSEL provides improved performance

and functionalities which include saturating the spectral voids with fine granularity. Using the proposed module, a bit rate up to 33 Gbit/s with DMT in BTB configuration and > 20 Gbit/s up to 185 km 2-hop path using single-sideband (SSB) orthogonal frequency division multiplexing (OFDM) has been demonstrated.

5.2 Other Applications using MEMS VCSELS

The scope of a tunable MEMS VCSEL is investigated in dispersion spectroscopy based gas sensing and tunable terahertz (THz) signal generation. The laser dispersion spectroscopy takes the advantage of two major aspects of these MEMS VCSELs namely, ultra-wide tuning range and high-speed direct modulation capability. On the other hand, tunable THz systems using electro-thermally actuated VCSEL is benefited from its moderately faster tuning speed and almost constant output power for a wide tuning range (excluding the wavelengths around the edges), in comparison to thermally tuned DFB laser based systems.

5.2.1 Heterodyne Phase Sensitive Dispersion Spectroscopy

The Kramers-Kronig relations indicate that both optical absorption and dispersion are linked to molecular resonances and consequently, are function of the respective gas concentration [98]. These informations are particularly interesting for different spectroscopic techniques to detect gases present in a medium and for estimating their concentration, temperature or pressure. Tunable lasers have already been key components in traditional absorption-based spectroscopic methods such as tunable diode laser absorption spectroscopy (TDLAS) [99]. Wide tuning range of the MEMS VCSEL is very attractive for multi-species gas analysis and suitable for high-density gas spectroscopy. However, the performance has been constrained by their characteristic non-monotonic output power fluctuations. The optical intensity decreases as the emission wavelength moves away from the center wavelength towards the edges of the tuning range (see Fig. 5.12). This significantly impacts measurements with substantial background noise such as dust, rain or fog where detected light intensity is expected to fluctuate. In such cases, a detailed calibration process of the non-linear intensity profile of every individual device employed in the system is crucial. Moreover, additional reference intensity characterizations of the sub-system together with a model for the expected intensity transmitted through the sample are possibly required. Thus, the complexity of the measurement setup and its operation increases considerably.

Dispersion spectroscopy methods are based on the measurement of optical dispersion associated to refractive index variations with wavelength that are inherent to molecular transitions. They offer significant advantages over classical methods:

- The refractive index changes are linearly dependent on the gas concentration, hence offer an extended dynamic range to dispersion spectroscopy sensors.
- It is possible to overcome baseline and normalization problems typical in absorption-based approaches [22], hence suitable for calibration-free operation.
- The dispersion spectroscopic method is inherently immune to optical power fluctuations. Therefore, the wavelength-dependent non-linear intensity profile does not affect the measurement technique.

VCSEL based phase-sensitive detection technique has recently been demonstrated by P. Martín-Mateos *et al.* in [100]. In this so-called heterodyne phase sensitive dispersion spectroscopy (HPSDS) method, the optical phase shift produced by a spectral feature has been successfully measured using a fixed wavelength VCSEL with thermal tuning of few nanometers. MEMS tunable VCSEL based dispersion spectroscopy has not been reported in literature. Due to its wide tunability, a MEMS VCSEL has potential for multi-species spectroscopy with more flexibility in terms of measurement range. In this work a multi-species gas sensing is performed in cooperation with P. Martín-Mateos, Universidad Carlos III de Madrid. The HPSDS method is demonstrated for the concurrent detection of three gas samples namely hydrogen cyanide (HCN), acetylene (C_2H_2) and carbon monoxide (CO) using a 92 nm-continuously-tunable MEMS VCSEL.

Principle of operation

The HPSDS method is based on the optical phase shift produced by the spectral feature [101]. The refractive index in the vicinity of a molecular transition with a center ω_c has the form:

$$n(\omega) = n_0 + s\frac{\omega_c - \omega}{(\omega_c - \omega)^2 + (\gamma/2)^2} \tag{5.1}$$

where s is a variable dependent of the spectral line and γ is the FWHM of the spectral feature. The graphical representation of Eq. (5.1) is shown in Fig. 5.10 (a). The dispersion profile can be characterized by ω_c and the FWHM [100]. When a multi-tone optical signal, it interacts with such a molecular transition; each optical tone encounters a slightly different value of refractive index. This eventually induces optical phase shifts (among them), which can be measured and used to calculate the concentration of gas. More specifically, the phase shift at the center wavelength of the spectral line is directly proportional to the concentration of the gas [102]. A laser modulated by an external

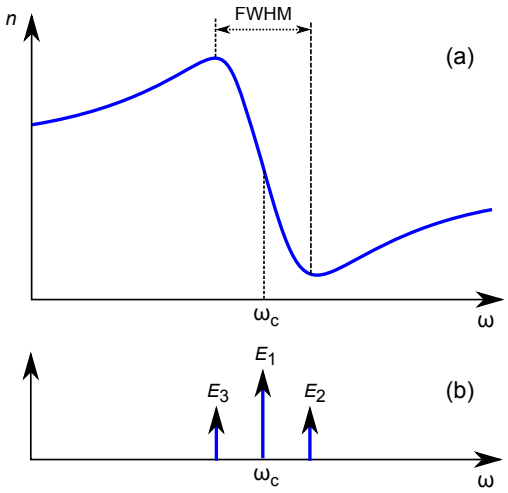

FIGURE 5.10: (a) Refractive index in the vicinity of a molecular transition with center ω_c. (b) Spectrum of an intensity modulated optical carrier centered in the dispersion line.

intensity modulator at a frequency ψ (rad/s) generates an optical spectrum consisting of a carrier E_1 and two sidebands E_2 and E_3 as follows:

$$E_1 = A_1 \cos \omega_0 t \tag{5.2}$$

$$E_2 = A_2 \cos (\omega_0 + \psi) t \tag{5.3}$$

$$E_3 = A_3 \cos (\omega_0 - \psi) t \tag{5.4}$$

where ω_0 is the optical frequency in rad/s. This is shown in Fig.5.10 (b). As the signal propagates through a dispersive medium, each frequency component travels at a marginally different phase velocity. At a propagation distance L from the emitter, three optical phase-modified signals can be expressed as:

$$E_1 = A_1 \cos \omega_0 t - \phi_1 \tag{5.5}$$

$$E_2 = A_2 \cos (\omega_0 + \psi_1) t - \phi_2 \tag{5.6}$$

$$E_3 = A_3 \cos (\omega_0 - \psi_1) t - \phi_3 \tag{5.7}$$

where

$$\phi_1 = \frac{\omega_0 L}{c} [n(\omega_0) - 1] \tag{5.8}$$

$$\phi_2 = \frac{\omega_0 L}{c} [n(\omega_0 + \psi_1) - 1] \tag{5.9}$$

$$\phi_3 = \frac{\omega_0 L}{c} [n(\omega_0 - \psi_1) - 1] \tag{5.10}$$

where $n(\omega)$ is the refractive index of the medium at ω and c is the speed of light in vacuum. When the signal imposes on a square-law photodetector (with sufficient electrical

bandwidth) two beat notes are generated as follows:

$$I_{12} \propto \frac{A^2{}_1}{2} + \frac{A^2{}_2}{2} + A_1 A_2 \cos \psi_1 t - (\phi_2 - \phi_1), \tag{5.11}$$

$$I_{13} \propto \frac{A^2{}_1}{2} + \frac{A^2{}_3}{2} + A_1 A_3 \cos \psi_1 t - (\phi_1 - \phi_3). \tag{5.12}$$

The phase of the resulting beat note (of frequency ψ_1) can be expressed as:

$$\phi_0 = \arctan \frac{A_2 \sin(\phi_2 - \phi_1) + A_3 \sin(\phi_2 - \phi_1)}{A_2 \cos(\phi_2 - \phi_1) + A_3 \cos(\phi_2 - \phi_1)}. \tag{5.13}$$

The above expression can be simplified to a great extent if the absorption in the gaseous medium is considered negligible – which is valid for low gas concentration. Since the amplitudes of the optical tones are equal, the amplitudes of two beat notes are also equal ($A_2 = A_3$) resulting in:

$$\phi_0 = \frac{\phi_2 - \phi_3}{2} \tag{5.14}$$

As reported in [100], the approximation introduces an accuracy error of 0.85% while validating the experimental results. Substituting Eqs. (5.9) and (5.10) with Eq. (5.14), the following expression concerning the beat note phase and the refractive indexes at the two optical frequencies is achieved:

$$\phi_0 = \frac{\omega_0 L}{2c}[n(\omega_0 + \psi_1) - n(\omega_0 - \psi_1)] \tag{5.15}$$

Equation (5.15) allows to determine the refractive index profile of the medium as a function of the wavelength, and eventually the species concentration and other different parameters of the gas [100]. Since the only factor considered for the estimation of gas-concentration is the phase-shift among optical signals, the actual power emitted by the laser at different tuning wavelengths has no effect on the received signal. Thus, despite its contribution to the SNR of the measurement, it has no influence on the estimation of concentration itself. Therefore, the output of the sensor is independent from the optical output power profile of the laser, and does not require any calibration process or additional reference measurement paths. However, in order to recover the dispersion spectrum proper selection of the modulation frequency is required. The relationship between modulation frequency and the maximum output phase are explained in [100].

Experiential Setup

The experimental setup of the HPSDS system is depicted in Fig. 5.11. It is based on radio-frequency (RF) down-conversion heterodyning using a MEMS tunable VCSEL. Two low noise current sources supply I_{bias} and I_{MEMS}. The tuning spectra of the MEMS

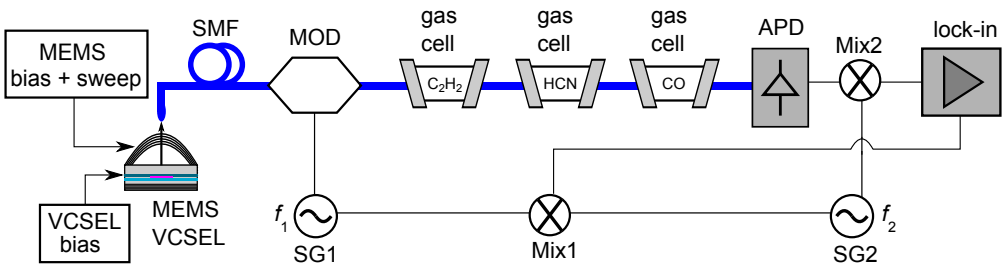

FIGURE 5.11: Experimental setup of the HPSDS system based on a MEMS-VCSEL. MOD: Optical intensity modulator, SG: Signal generator, Mix: Frequency mixer, APD: Avalanche photodiode, Lock-in: Lock-in amplifier.

VCSEL used for this experiment is shown in Fig. 5.12. The dotted line which refers to the continuous spectra of the tunable emission clearly shows a non-monotonic optical intensity profile with fluctuations of up to 17 dB from the center to the edge of the tuning envelope. For fast sweeping of the emission wavelength, a triangular signal $V_{\text{MEMS-AC}}$ corresponding to $I_{\text{MEMS-AC}}$ with a frequency $f = 50\,\text{Hz}$ and a duty cycle of 50% is connected to I_{MEMS} in series. The DC portion of the I_{MEMS} is referred to an offset current $I_{\text{offset}} = 41\,\text{mA}$ corresponding to the center of the tuning range ($\approx 1560\,\text{nm}$) is added on top of the triangular signal to confirm that the overall $I_{\text{MEMS}} = I_{\text{offset}} + I_{\text{MEMS-AC}}$ never drops below zero level. The peak-to-peak voltage amplitude of $V_{\text{MEMS-AC}}$ is set in way that the two edges of the tunning range correspond to two peaks of $V_{\text{MEMS-AC}}$. The emit-

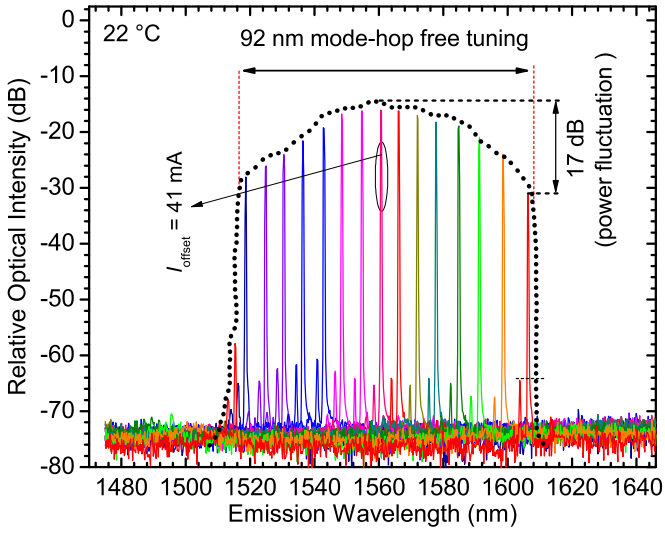

FIGURE 5.12: Tunable emission spectrum of the MEMS VCSEL. The dotted line refers to the continuous spectra with intensity fluctuations of up to 17 dB.

ted light is coupled to a lensed SMF (20 μm core diameter). The output light is intensity modulated[†] with signal generator (SG1) with a frequency of $f_1 = 1.5\,\text{GHz}$, which is in accordance with the linewidth of the targeted spectral lines for CO and HCN. The generated three tone HPSDS signal is then sent through the gaseous samples[‡]: HCN (3.11 dB

[†]LN65S-FC optical intensity modulator, Thorlabs Inc.
[‡]All gas samples are from Wavelength References Inc, Oregon, USA

absorption at 1536 nm) and CO (188 mdB absorption at 1568 nm) at ambient pressure of 740 Torr and C_2H_2 (8 dB absorption at 1530 nm) at a lower pressure of 50 Torr. The optical signal with phase information is detected by a high-speed avalanche photodiode (APD) with a 3-dB bandwidth of ≈10 GHz. The electrically converted output of the APD is fed to a mixer MIX1[¶] in order to down-convert the 1.5 GHz beat note to an intermediate frequency (IF) f_2 within the range of the lock-in amplifier[*] employed in the experiment. A second mixer MIX2 of same type is used to extract the reference signal for the lock-in amplifier.

Results and Discussion

Figure 5.13 shows a comparative scenario between direct absorption spectrum which is labeled as TDLAS and the HPSDS outcome of the gas samples. The TDLAS trace shows the parabolic intensity profile envelope as well as an additional non-uniform ripple in the power. This makes baseline-removing very complicated (and even harder for wavelength modulation techniques). On the contrary, this ripple is completely inexistent on the actual HPSDS signal, which is shown in the lower part of the inset on Fig. 5.13 (labeled as HPSDS). However, the optical intensity modulator used in the experiments has given rise to a small baseline signal that would be completely negligible on a narrower range architecture. Nonetheless, due to its spectral shape, it can very easily be fitted and removed by data processing, even though the use of a well-balanced intensity modulator would remove it completely. The final HPSDS signal for a measurement spanning from 1516 nm to 1598 nm (82 nm) can be found in the main plot of Fig. 5.13, where complete rotational-vibrational spectra of CO, HCN and (except for a few lines) C_2H_2 are shown. For a rapid differentiation between different analytes, the envelope of the HPSDS signal for each gas has been highlighted in different colors. As said before, the troughs of the HPSDS spectrum provide a direct measure of concentration.

It has been thus validated that it is possible to take advantage of the wide tuning range of MEMS-VCSELs for implementing a very simple dispersion spectrometer for detecting multi-analytes at different pressures. Since the only parameter used for the estimation of concentration is the phase-shift between optical signals, the actual power emitted by the laser has no effect on the output signal and, hence no influence on the estimation of concentration (apart from its contribution to the SNR of the measurement). As the system is analyzes several gases with a single laser source, the effect of a sample at a pressure different to which the system is optimized to operate has also been investigated. The C_2H_2 cell has a pressure lower to that of the CO and HCN cells. Hence the resultant linewidth of C_2H_2 resonances is approximately one third of those from CO

[¶]ZFM-11+, Mini-Circuits Inc., New York, USA
[*]Signal recovery 7265 dual phase DSP lock-in amplifier, 1 mHz to 250 kHz

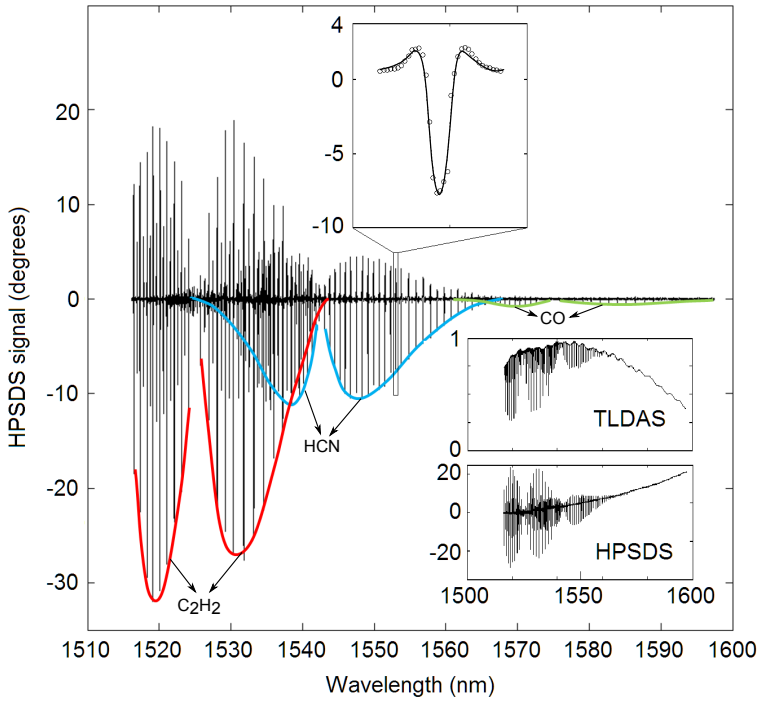

FIGURE 5.13: HPSDS phase signal of three samples for the entire spectral range. HPSDS signal is shown in degrees. A absorption spectroscopy signal in arbitrary units is also highlighted. Inset diagrams show comparative scenario between direct absorption spectrum (TDLAS) and the HPSDS outcome.

and HCN and this induces a comparatively more symmetrical HPSDS signal as reffed to the difference between the HPSDS signal for C_2H_2 and the signal for CO and HCN on Fig. 5.13. Nonetheless, the analyzing capability of the systems remains intact not only for multiple species but also gas samples at different pressures. The much lower pressure on one of the cells employed in the experimental validation reduces the limit of detection achievable exclusively for the given sample only by a factor of two. As a limitation, the wide wavelength range swept by the MEMS-VCSEL put a lot of strain on the performance of the optical intensity modulator in comparison to thermally tuned laser with much narrow tuning range. Therefore, one should carefully consider the stabilization of the temperature and the bias point. The MEMS VCSEL also provides the system with other distinctive advantages. As an example, it offers the means for simple wavelength referencing. The concentration of the sample is linearly related to the HPSDS output. When several samples (from the same or different gases) are measured one after the other, the result is equal to the sum of the individual contributions. This allows sending an HPSDS interrogation signal through a sample that has been already propagated through a gas reference cell, in order to retrieve the wavelength axis on detection. The HPSDS signal containing the concentration information can be later recovered by simply subtracting the calibrated or simulated wavelength reference spectrum. Beyond that, the wide tuning and the great number of lines analyzed open many new possibilities for obtaining an optimum accuracy in the estimation of concentration, as using the fitted

envelope of the whole bands or multi-line averaging approaches, instead of using single troughs of the HPSDS signal. These opportunities should ultimately improve accuracy and the limit of detection of the spectroscopic setup.

5.2.2 Tunable Terahertz (THz) Generation

In the electromagnetic spectrum terahertz (THz) radiation (0.3 to 10 THz) is positioned between infrared and microwave radiation and shares some common properties with each of them. THz radiation travels in a line of sight, can penetrate a wide variety of non-conducting materials and is non-ionizing. A diverse range of applications can be addressed which employ THz radiation. Among them, non-invasive medical diagnosis, health care, pharmaceutical quality control, high-frequency communications, homeland security, and earth and space science applications [103, 104]. For applications where a large frequency exposure of up to few THz or a high spectral resolution is necessary, heterodyne photomixing of two CW lasers is frequently used [105]. A small change in the emission wavelength provided by a tunable laser can be inferred into a remarkable frequency changes in the microwave range by heterodyne superposition with a second laser of fixed wavelength. In principle, a MEMS VCSEL with a tuning range of 60 nm centered at 1550 nm can cover the electromagnetic spectrum from DC to 7 THz. Both laser sources should deliver approximately the same power. Two lasers at frequencies ν_1 and $\nu_2 = \nu_1 + \nu_{\mathrm{THz}}$ drive an ultra-fast photodiode (PD) or a photoconductor that generates an ac current oscillating with the difference frequency of THz. An appropriate antenna converts the ac current into a THz emission. On the receiver side, a photoconductor mixes the received THz signal with the optical envelope of the beat signal that is used for the THz generation, leading to a down-conversion of the THz field to a dc photocurrent as a read-out signal. Although the bandwidth of the state-of-the-art photomixing systems reach up to ≈ 3 THz, commercial narrow-linewidth telecom-wavelength DFB lasers are limited to a tuning range of 0.6 THz. Several DFB lasers with appropriately chosen emission wavelengths can cover a frequency span of up to 3 THz [106]. External cavity lasers with a tuning range of several THz is relatively bulky and expensive. The MEMS VCSELs developed in this work are investigated as an potential alternative source for widely tunable THz generation. M. T. Haidar *et al.* has demonstrated that the a single tunable VCSEL has the potential to replace the above mentioned optical source due to its cost- and energy-efficiency, extremely fast tunability (in case of electro-static actuation) and circular-symmetric mode profile which allows efficient fiber coupling [107]. The experimental setup and results are summarized in Appendix E.

Chapter 6

Tunable MEMS OAM-Filter

A tunable MEMS OAM-filter proposed in this work is a passive optical component capable of generating/receiving an orbital angular momentum (OAM) beam of a specific order for a certain wavelength range around the design wavelength of 1550 nm. In this chapter some basic characteristic properties of the device including the quality of the generated OAM beams are investigated. The filters are employed for simultaneous wavelength and OAM multiplexing/demultiplexing of 10 Gbit/s data streams. The setups used for OAM beam generation/detection and data transmission are described. Experimental results of the BER performance measurements are discussed.

6.1 MEMS Filter Characterization

As discussed already in Section 3.2, the MEMS OAM-filter consists of a tunable Fabry-Pérot (FP) resonator with an integrated micro-sized spiral phase plate (SPP) on top of the movable MEMS mirror. In order to investigate the performance of the complete device it is, therefore, important to evaluate the performance of the FP filter without/with SPPs separately. First, the transmission characteristics of the MEMS filter (without SPP, i.e., $l_{\mathrm{SPP}} = 0$) is investigated. The experimental setup is shown in Fig. 6.1. An semiconductor optical amplifier (SOA) is used as a broadband optical source. The light is focused on the anti-reflection coated (ARC) side of the MEMS filter via a SMF coupled lens system. The transmission spectrum of the filter is coupled to a second lens system and then fed to an OSA. The use of the SMF supports to suppress the side modes. For aligning the filter to the lens system the reflected power is measured, which is accomplished by a 3-dB coupler. By maximizing the reflected power, the filter is first aligned to the focal plane of the lens system. For further optimization of the alignment, the transmission spectrum is observed in the OSA at a high resolution ($= 0.1$ nm) and then

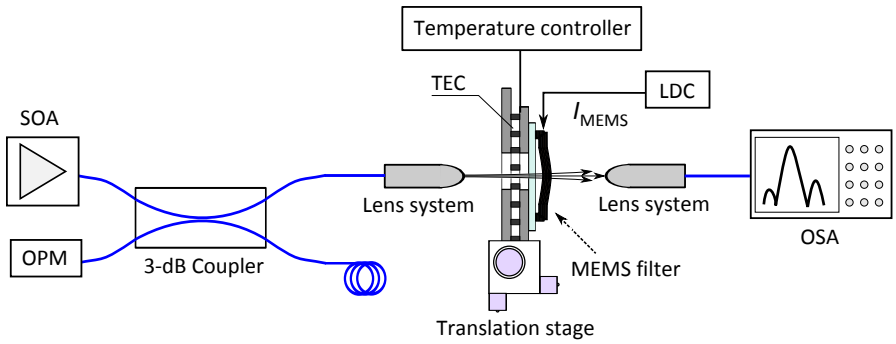

FIGURE 6.1: Experimental setup for characterizing the transmission characteristics of a MEMS tunable Fabry-Pérot filter.

the SMSR with respect to higher order resonator modes is maximized. A thermoelectric cooler (TEC) element is used for changing the temperature of the copper substrate holder. Similar to MEMS VCSELs, the tuning of the filtered wavelength is obtained by altering the FP cavity length – which can be obtained either by the electro-thermal actuation of the MEMS electrode or simply by changing the substrate temperature. Figure 6.2 (a) shows the transmission spectra of a MEMS tunable FP filter measured at 29 °C. In case of electro-thermal tuning the spectra is red-shifted with an increasing MEMS current I_{MEMS} (thus with increasing actuation power). The free-spectral range (FSR) of the resonance mode m is 135 nm. The shape of the intensity envelope follows the trace of the SOA. The side mode on the left side of the main resonance mode can be reduced or even removed by proper alignment of of the lens system to MEMS filter. The filter shows a full-width at half-maximum (FWHM) bandwidth of 0.19 nm at 1550/,nm. Figure 6.2 (b) shows the electro-thermal tuning of two consecutive modes. It is clear that the mode-hop occurs only at the edge of the tuning range.

The resonance wavelength of the filter can also be tuned simply by changing the substrate temperature. Figure 6.2 (c) shows the typical dependence of the filter resonance wavelength on the wafer temperature. Unlike electro-thermal actuation, this tuning scheme provides blue-shifting of the resonance wavelength (see Section 4.2). Thermal tuning of the resonance wavelength is particularly helpful in cases where the setup has limited space in the test-bench. The complexity of the setup can be reduced by getting rid of two additional contact needles and their translation stages. As can be seen, the resonance wavelength is tuned from 1548 nm to 1508 nm corresponding to substrate temperature of 16 °C and 29 °C, respectively. The measured data are fitted with a straight line with a slope $\mathrm{d}\lambda/\mathrm{d}T = -3.24\,\mathrm{nm/K}$. In comparison to the MEMS VCSEL ($\mathrm{d}\lambda/\mathrm{d}T = -9.4\,\mathrm{nm/K}$), the value of this negative slope is significantly lower. This is due to the lower coefficients of thermal expansion of Si substrate ($\alpha_{\mathrm{Si}} = 2.6\,\mathrm{x}\,10^{-6}\mathrm{K}^{-1}$) compared to InP/BCB ($\alpha_{\mathrm{InP}} = 4.6\,\mathrm{x}\,10^{-6}\mathrm{K}^{-1}$ and $\alpha_{\mathrm{BCB}} = 42\,\mathrm{x}\,10^{-6}\mathrm{K}^{-1}$) based VCSEL

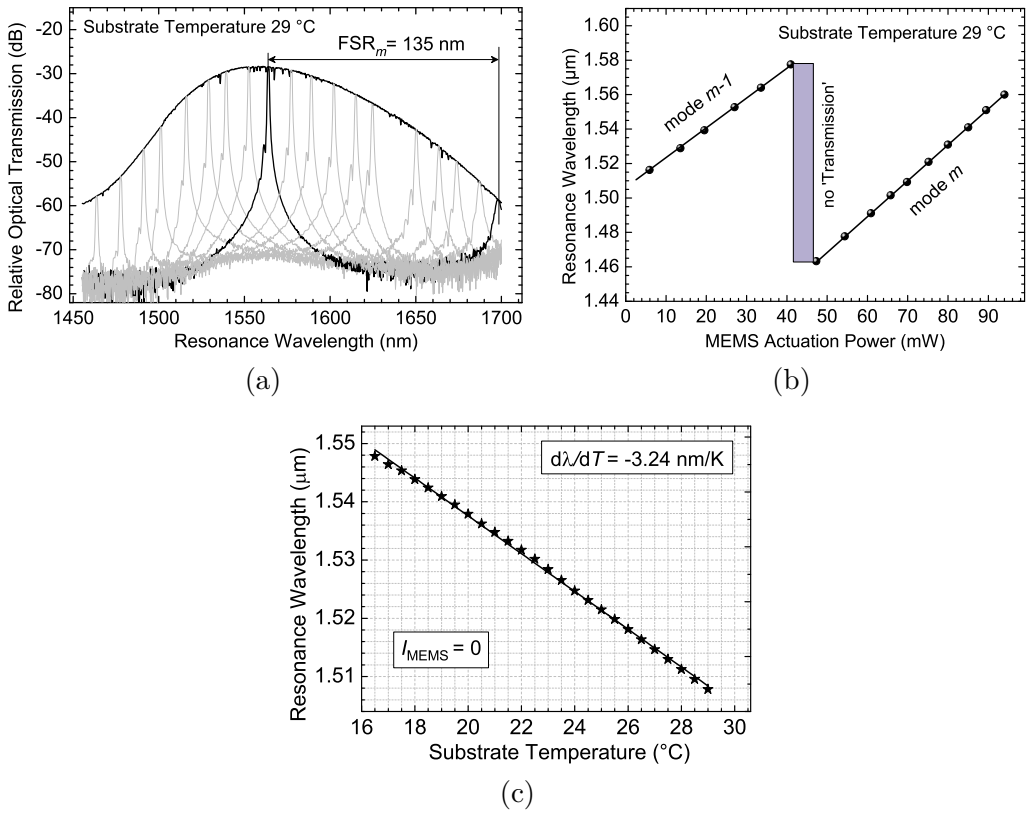

FIGURE 6.2: (a) Tuning spectra of a MEMS tunable Fabry-Pérot optical filter. (b) Tuning wavelength vs. MEMS actuation power, and (c) Tuning wavelength as a function of substrate temperature.

wafer. In order to go beyond 1548 nm, the substrate temperature has to be lowered further. This is harmful to the filter as it could allow the atmospheric vapor to condensate and eventually destroy the MEMS. However, 40/,nm of mode-hop free tuning can still be achieved for filters with different orders of SPPs. It is worth mentioning that the FSR and the transmission characteristics of the MEMS filter do not change after integrating the SPP mask on its upper DBR. Provided that both the DBRs have sufficiently large reflectivity bandwidths, FSR is the ultimate limiting factor for obtaining a wide mode-hop free tuning. For the following experiments, tuning the resonance wavelength of the MEMS OAM-filter is realized with thermal tuning.

6.2 OAM beam Generation and Detection

Experimental Setup

Figure 6.3 shows the experimental setup for testing the functionality of the proposed MEMS OAM-filters [37]. A tunable external cavity laser (ECL) is used for sweeping the emission wavelength which will eventually pass through the filter. The ECL covers the wavelength range which is supported by the filter transmission window shown in

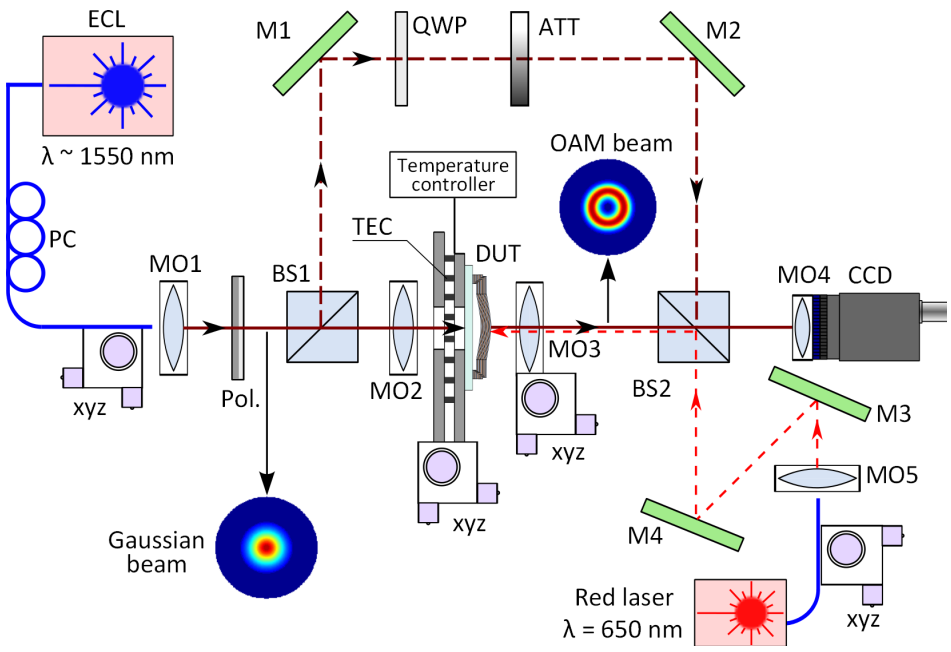

FIGURE 6.3: Experimental setup for generation, detection and characterization of different OAM modes. ECL: External cavity laser, PC: Polarization controller, xyz: Three axis positioning stage, MO1-MO5: Microscope objectives, POL: Polarizer, BS1-BS2: Beam splitters, M1-M4: Mirrors, QWP: Quarter wave plate, ATT: Variable attenuator, TEC: Thermoelectric cooler , DUT: Device under test, CCD: Charge coupled device camera.

Fig. 6.2 (c). The SMF polarization controller (PC) installed at the output of ECL allows optimizing the state of polarization to maximize the power after the polarizer (POL). A microscope objective MO1 then collimates the optical output from the fiber. The polarizer along the fiber path ensures linear polarization of the beam at the input of the MEMS OAM-filter. The light from the ECL is incident upon the wafer from the ARC side of the substrate. First, the phase profiles of the OAM beams transmitted through the MEMS OAM-filter are determined using Mach-Zehnder interferometry. This technique enables capturing the fringe patterns between the transmitted OAM beam and the reference flat-wavefront Gaussian beam. To reconstruct the phase distributions from fringe patterns, a parallel interference between the OAM beam and a reference beam is applied [**?**]. This approach captures two fringe patterns for each phase profile measurement. The beam splitter BS1 as well as the mirrors M1 and M2 prepare the reference beam parallel to the OAM beam, both are then combined with BS2 to obtain fringe patterns on the near-infrared (NIR) charge coupled device (CCD) camera. Microscope objectives MO4 and MO5 provide sufficient magnification of the images to be captured by the camera. The Gaussian beam traveling the longer path is already linearly polarized. Hence the quarter wave plate allows introducing the additional $\pi/2$ phase shift with reference to OAM beam by aligning its fast or slow axis with the electric field vector of the incident light. [108**?**]. The variable attenuator ATT is used to make the power of the reference

beam comparable with that of the beam, emitted from the filter. Microscope objective MO3 provides a collimated output by matching the beam waist of its aperture with the curvature of the MEMS mirror. For preliminary alignment of the filter with the input IR beam, the fiber coupled red light laser is used, which can precisely point on the MEMS dish of a definite device on the wafer. The light beam from the red light laser, previously aligned with the IR beam by means of mirrors M3, M4, is also transmitted through the beam splitter BS2. Final precise positioning of the filter and optimization of the incidence angle of the input beam is provided by controlling the output power and the "doughnut" shaped intensity profile of the beam generated by the filter.

Intensity and Phase Distribution

The main resonance mode of the FP resonator is Gaussian in the case of a MEMS filter without SPP and possesses the highest intensity, whereas the 1st side-mode is defined as the mode with second highest intensity after the main mode. The dependence of the transmittance on the resonance wavelength for the main mode of MEMS filters are shown in Fig. 6.4. The output power of the modes emitted through the filters are

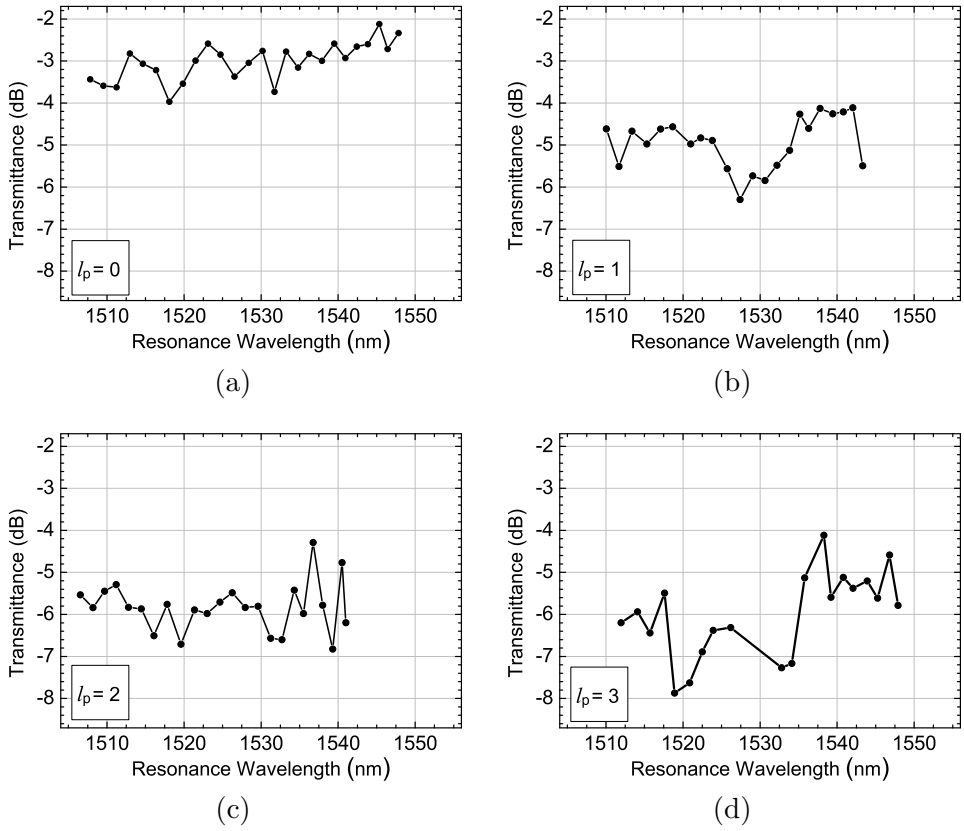

FIGURE 6.4: Transmittance of the SPP modes with $l = 0$, 1, 2 and 3 as a function of resonance wavelength.

estimated in free-space from the camera images in order to avoid the influence of non-optimal coupling of higher-order modes with the fiber on the power measurement results. To obtain correct power estimations, the nonlinearity of the camera response and the wavelength dependence of the camera output have been taken into account. As can be seen, the transmittance of each device fluctuates to a small extent around an average value and does not demonstrate any significant decay over the whole measured range of wavelengths. Table 6.1 summarizes the average transmittance of four MEMS OAM-

TABLE 6.1: Average transmittance of four MEMS OAM-filters.

	Average transmittance (dB)			
SPP type	no SPP	$l_{SPP} = 1$	$l_{SPP} = 2$	$l_{SPP} = 3$
Main mode	-3.01	-4.94	-5.83	-6.01
1st side-mode	-15.14	-14.59	-12.78	-13.88

filters. It is evident that the average transmittances of the MEMS OAM-filters with SPPs are slightly lower than that of a MEMS filter without SPP ($l_{SPP} = 0$). For the filter with $l_{SPP} = 1$ this difference is 1.93 dB. This reduction can be readily explained by the additional absorption and scattering of the light by the SPP itself. As the SPPs of different azimuthal orders have the same construction and their average thickness is also the same, the lower values of transmittance obtained for the devices with $l_{SPP} = 2$ and 3 can be explained by the methodological inaccuracy when measuring the power with the camera, as the higher order OAM modes lead to the broadening of the lateral field distribution, and as a result some part of beam energy cannot be effectively distinguished from the noise level due to the limited sensitivity of the camera.

The transmittance of the side-modes have also been investigated. As mentioned already, they are highly dependent on the alignment of the filter with respect to the input beam. When capturing images of the beams transmitted through the MEMS filters, input beam alignment is kept in order to maximize the transmittance for the main resonance mode. The transmittances for the 1st side-modes averaged over the measured tuning ranges are also shown in Table 6.1. However, for the most practical cases these values of side-mode transmittance captured for the free space radiation are not important. For example, if the MEMS OAM-filter is used as an OAM- and wavelength-selective device for detecting channel signals in a OAM-wavelength-multiplexed transmission system, only the received mode corresponding to the opposite azimuthal order of SPP at the main resonant wavelength of MEMS-filter can be transformed to the Gaussian mode and coupled to the SMF. In the case of integration of such MEMS mirror with SPP to the VCSEL for wavelength-tunable direct OAM beam generation, the resulting SMSR will be defined mostly by the RoC of the MEMS-DBR as well as the optimal overlapping of the lasing Gaussian transverse mode with the active region.

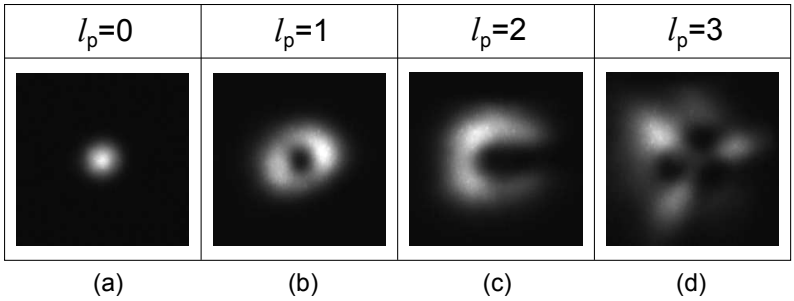

FIGURE 6.5: Intensity distributions for the main resonance mode of the MEMS OAM-filters with the 4 azimuthal orders ($l_p = 0$, 1, 2, and 3) at a resonance wavelength of 1540 nm.

Figure 6.5 shows the intensity distributions of the main resonator mode captured at the output of simple MEMS-filter and those with SPPs of azimuthal orders $l_p = 1$, 2, 3. All images correspond to a same resonance resonance wavelengths of 1540 nm. As there is no visible difference in the shape of intensity distributions obtained for each device over the tested wavelength range (except the overall beam intensity), for the sake of brevity only intensity distributions for one wavelength are shown. Phase distributions extracted from the captured fringe patterns are shown in Fig. 6.6, where for each device three phase distributions corresponding to three different wavelengths namely, the center and the two edges of the corresponding measured tuning range are represented. However, as follows from Fig. 6.5 (c),(d) and Fig. 6.6 (d)-(i), the beams at the output of MEMS OAM-filter of azimuthal orders $l_p = 2$ and $l_p = 3$ have non-uniform intensity distribution

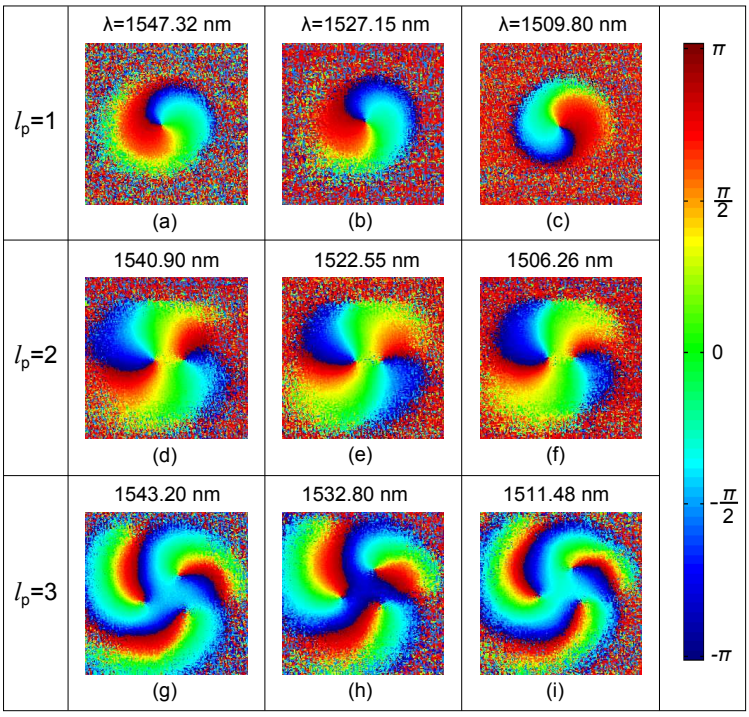

FIGURE 6.6: Measured phase distributions for the main resonance mode of the MEMS OAM-filters with the 3 azimuthal orders ($l_p = 1$, 2, 3) at different resonance wavelengths.

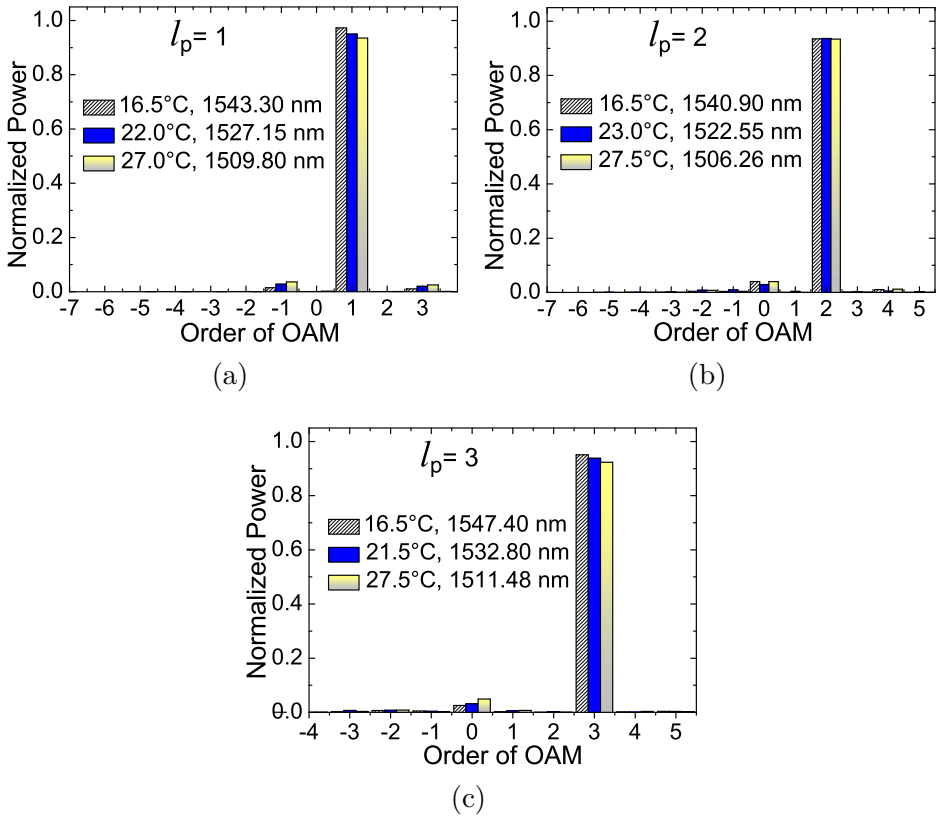

FIGURE 6.7: Normalized power of OAM states in the generated vortex beams using SPPs of orders 1 (a), 2 (b) and 3 (c), respectively.

over the "doughnut" mode profile and the corresponding non-symmetry in the phase distributions. It is worth to mention that the peculiarity does not change with the temperature and the corresponding resonant wavelength. Therefore, these non-ideal amplitude distributions can be attributed to the non-ideal symmetry of upper MEMS DBR convexity resulting in a deviation of the center of the transmitted beam from the geometrical center of MEMS filter aperture. As the SPP is aligned to the geometrical center of the filter aperture, such behavior of the filter leads to some displacement between the output beam and SPP.

Figure 6.7 shows the normalized OAM spectra, obtained by expanding the experimental phase distributions (see Fig. 6.6) in terms of angular harmonics $\exp(il\varphi)$. Two possible factors affecting the purity of the generated OAM states are:

- Phase profile distortion due to output beam displacement, which is present for the whole range of resonant wavelengths.
- Reduction of the efficiency of mode conversion from the Gaussian mode to the OAM modes as the resonance wavelength goes down from the designed SPP wavelength of 1550 nm.

But the tunability band is relatively small compared to the central wavelength, and as a result the OAM state purity degrades only by 3.8% (from 0.9726 to 0.9353) over a wavelength range of 33.60 nm for the device with $l_{\mathrm{SPP}} = 1$, and by 0.0279 (from 0.9512 to 0.9233) over the wavelength range of 35.92 nm for the device with SPP $l_p = 3$. For the device with $l_{\mathrm{SPP}} = 2$, there is no significant improvement of OAM beam quality when increasing the wavelength (the normalized power of OAM $l_{\mathrm{SPP}} = 2$ proves to be 0.9353 at 1540.9 nm and 0.9336 at 1506.26 nm), which can be explained by the technological properties of current device or by an inaccuracy when measuring the phase distributions. On the whole, as can be seen from Fig. 6.6, the output beams retain their vortical structure over the whole considered wavelength range, and even for the MEMS OAM-filter of azimuthal order $l_{\mathrm{SPP}} = 3$ the normalized power of OAM state $l_p = 3$ is not lower than 0.9233.

6.3 Optical Data Transmission Experiments

Experimental Setup

In order to perform wavelength- and OAM-multiplexed transmission experiments, a prototype of an optical communication system is constructed. The key components of the system comprises a typical tunable ECL as transmitter, a WDM multiplexer (WDM-MUX), a free-space OAM multiplexer (OAM-MUX), and a receiver, where simultaneous demultiplexing of wavelengths and spatial channels is provided by the MEMS OAM-filter. Figure 6.8 shows the complete setup used for digital data transmission experiments. Two tunable ECLs (λ_1, λ_2) feeding the WDM-MUX generating two information channels with a variable wavelength difference ($\Delta\lambda = \lambda_2 - \lambda_1$). The first channel operating at λ_1 is considered to carry the desired signal, i.e., the information signal to be transmitted. The second channel operating at λ_2 is considered as neighboring interfering channel, which is also carrying data of same bandwidth as the first channel. Measurements of BER performance have been performed for the desired channel only. Two different modulation schemes are utilized in this experiment. The first one is a on-off keying (OOK) modulation which is a simplified form of intensity modulation. The second modulation scheme is binary phase-shift keying (BPSK) which uses the phase modulation of the carrier signal. It employs two phases that are separated by 180 °. Two polarization controllers PC1 and PC2 allow optimizing the state of polarization of the laser signals which are then independently modulated by two separate Mach-Zehnder modulators (MZMs) or phase modulator (PM) in case of OOK and BPSK, respectively.

The modulators are operated at data rate of 10 Gbit/s, driven by a PRBS word lengths of 2^{31}–1 and 2^{23}–1, respectively. Modulators MZM1 and MZM2 used for OOK provide extinction ratios of 9.2 dB and 9.46 dB, respectively. In the case of BPSK phase

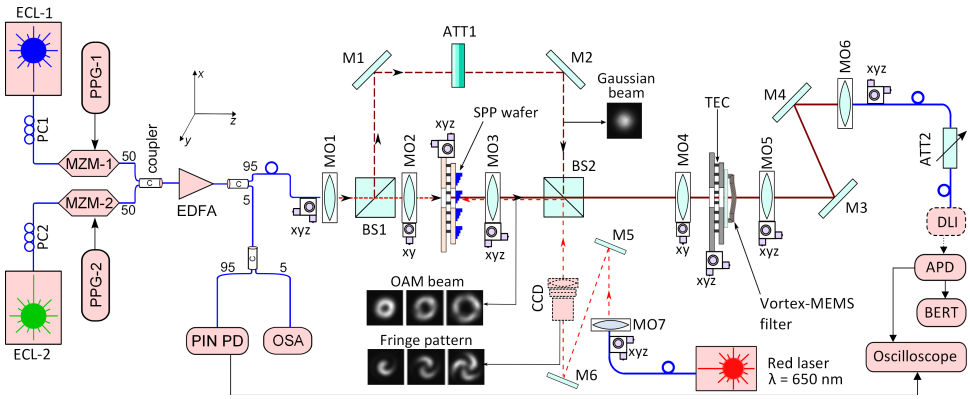

FIGURE 6.8: Schematic drawing of the experimental setup for the BER measurements.

modulators (PM) are used instead of MZMs. The independent modulated channels are coupled together to an erbium-doped fiber amplifier (EDFA) by using a 50/50 coupler. 95% of the fiber-output pre-amplified signal is collimated by microscope objective MO1. This collimated output is split by beam splitter BS1 to generate two separate paths for the WDM signal. One signal is passed through a simple SPP mask[†] (non-tunable, fabricated on a Si wafer) which generates the OAM beam corresponding to the azimuthal order of SPP. The other path passing through mirror M1, variable attenuator ATT and mirror M2 remains as a Gaussian beam. Microscope objective MO2 serves to match the beam waist with the SPP, and MO3 collimates the output OAM beams. Another 5% portion of the generated WDM signal is split between the *p-i-n* photodiode (PIN PD) (95%) and optical spectrum analyzer (OSA) (5%). By connecting the digitizing oscilloscope to the output of PIN, initial eye-diagrams of individual WDM-channels can be captured in order to optimize the channel performance. The OSA serves to monitor the spectrum of the generated WDM signals in order to ensure that WDM channels have equal powers and are separated with a desirable wavelength spacing $\Delta\lambda$. The total output power of EDFA is kept at the level of 20 dBm. As MEMS OAM-filter itself filters out all the undesired wavelengths including the amplified spontaneous emission (ASE) noise of the EDFA, no optical band-pass filter is used after EDFA.

A path difference of 35 cm between Gaussian beam and OAM beam is formed providing a 1.17 ns delay between OAM-multiplexed channels. Beam splitter BS2 provides multiplexing of Gaussian and OAM beams; thus forming four independent information channels. Variable attenuator ATT1 allows for adjusting the ratio between powers transmitted in Gaussian and OAM channels. First, it is required for compensation of higher losses in the path of OAM channel compared with that of Gaussian channel due to SPP and MO2, MO3. Moreover, as the experiments show, power in the Gaussian channel should be additionally reduced to some extent relative to the OAM channel in order

[†]As shown in Fig. 3.13, the non-tunable SPPs used at the transmitter side have the same construction as SPPs of the MEMS OAM-filters, but are deposited directly on a double side polished (DSP) Si substrate. The other side of the wafer is covered by an ARC, on which the input beam is incident upon.

to provide stable detection of both these spatial channels. This can be explained by different efficiency of beam coupling to the MEMS filters for Gaussian and OAM mode. The position of ATT1 is kept the same when receiving the Gaussian and OAM channels and their power difference after BS2 is kept at 1.45 dB throughout the experiments.

The fiber coupled red light laser beam is used for preliminary alignment of the SPP to the input IR beam. The red light is focused on the SPP with proper azimuthal order. The beam from the red light laser, previously aligned with the IR beam by means of mirrors M5 and M6, is also transmitted through the beam splitter BS2. For precise alignment of the SPPs, intensity distribution of its output beam is monitored using the CCD camera, placed after BS2. Also the use of CCD-camera facilitates alignment of OAM-MUX in order to have Gaussian and vortex channels propagating parallel over the same spatial free space link. As the elements BS1, BS2, M1 and M2 form a Mach-Zehnder interferometer, it is convenient to control coincidence of Gaussian and vortex channels from the fringe patterns at the output of OAM-MUX – as in the lower inset in Fig. 6.8. When aligning OAM-MUX, its feeding fiber is connected directly to the laser without modulators and WDM-MUX to have coherent radiation for contrast fringe patterns. The multiplexed signal is transmitted over a short free space link of $\approx 23\,\text{cm}$ between BS2 and MO4. At the receiver side the multiplexed signal is focused by MO4, which matches the beam waist with the RoC of the MEMS-DBR of the filter, and then incident to the SPP. The azimuthal order of SPP corresponds to the opposite topological charge of the vortex beam when receiving the OAM channel, and the MEMS-filter without SPP is used when receiving the Gaussian channel. Tuning of the filters is realized by controlling the substrate temperature with a TEC element. MO5 provides collimation of the beam transmitted through the MEMS-filter, and MO6 provides coupling of this beam to the standard SMF, which serves as a spatial filter supporting only the Gaussian mode, and also as a link to the photo-detector. Mirrors M3, M4 provide alignment of the MEMS-filter output beam to the fiber. Detection of the received signal is provided by an avalanche photodiode (APD); in case of BPSK a delay line interferometer (DLI) is used before the APD.

Data Transmission Results

In this section capability of the transmission system employing the MEMS OAM-filter is evaluated in terms of BER performance. The experimental setup allows to measure BER values as a function of received optical power (ROP) for different number of information channels in order to determine the penalties while simultaneous WDM and OAM multiplexing/demultiplexing is performed. For the first proof-of-concept experiment four different cases have been considered. They are as follows.

- Case 1: One channel (reference BER curve for one wavelength and each OAM alone).
- Case 2: Two spatial channels at the same wavelength but different OAMs,
- Case 3: Two wavelength channels without extra OAM multiplexing,
- Case 4: Four channels where two spatial and two wavelength channels are Combined.

The BER results are summarized in Fig. 6.9. The series of BER measurements mentioned above are implemented for both OAM- and Gaussian channels. During the measurements the received channel has the wavelength in the range from 1536 nm to 1544 nm. The BER curves at other wavelengths are expected to be similar across the MEMS OAM-filters tuning range. The spacing between channels in wavelength domain is fixed and equals to 0.8 nm.

In case of two transmitted OAM channels, the measured one is tagged as (Rx). For example, when two channels with $\ell = 0$ and $\ell = 1$ are being transmitted at the same wavelength, the sign $\ell(\mathrm{Rx}) = 0$ means that the Gaussian channel is measured, and the sign $\ell(\mathrm{Rx}) = 1$ denotes measuring of the OAM channel. This notation is used for all figures. In order to verify that OAM/wavelength multiplexing with proposed devices is independent of the modulation formats, the similar sets of BER vs. ROP values are recorded for each format (OOK and BPSK). In Fig. 6.9, the left column (a, c, e) corresponds to OOK modulation, and the right column (b, d, f) is referred to BPSK modulation. All complex modulation formats represent combinations of amplitude and phase modulations. In case of BPSK the power budget is limited to the lower values (up to -27 dBm) because of the losses in the DLI. In order to avoid the noise due to ASE, no amplifier is used at the receiver side. Consequently, in case of BPSK ROP margin does not permit to demonstrate error-free transmission using the setup. However, the BER values are lower compared with OOK at the same ROPs according to the theoretical predictions. Extrapolation of BER curves for higher ROPs in case of BPSK can show error-free transmission analogously to the demonstrated BER curves in case of OOK. In reference to the optical transmission network (OTN) standard, BER below 3.8×10^{-3} is essential for successful transmission utilizing so-called forward error correction (FEC) with 7% overhead (OH). However, as far as short-reach optical links and data center interconnects are concerned this BER threshold is not practical due to large overhead and high latency of the FEC. For example, the IEEE 802.3bm standard implies FEC with 2.7% OH Reed-Solomon (RS) code with 100 ns latency. As a consequence, the FEC needs a BER threshold at 1.42×10^{-5} to realize an output BER value smaller than 10^{-15} [109–111]. Therefore, in case of OOK modulation shown in Fig. 6.9 (a, c, e) the BER limit at 1.42×10^{-5} is also considered. In order to evaluate the performance of transmission system while demultiplexing wavelength and OAM channels using MEMS

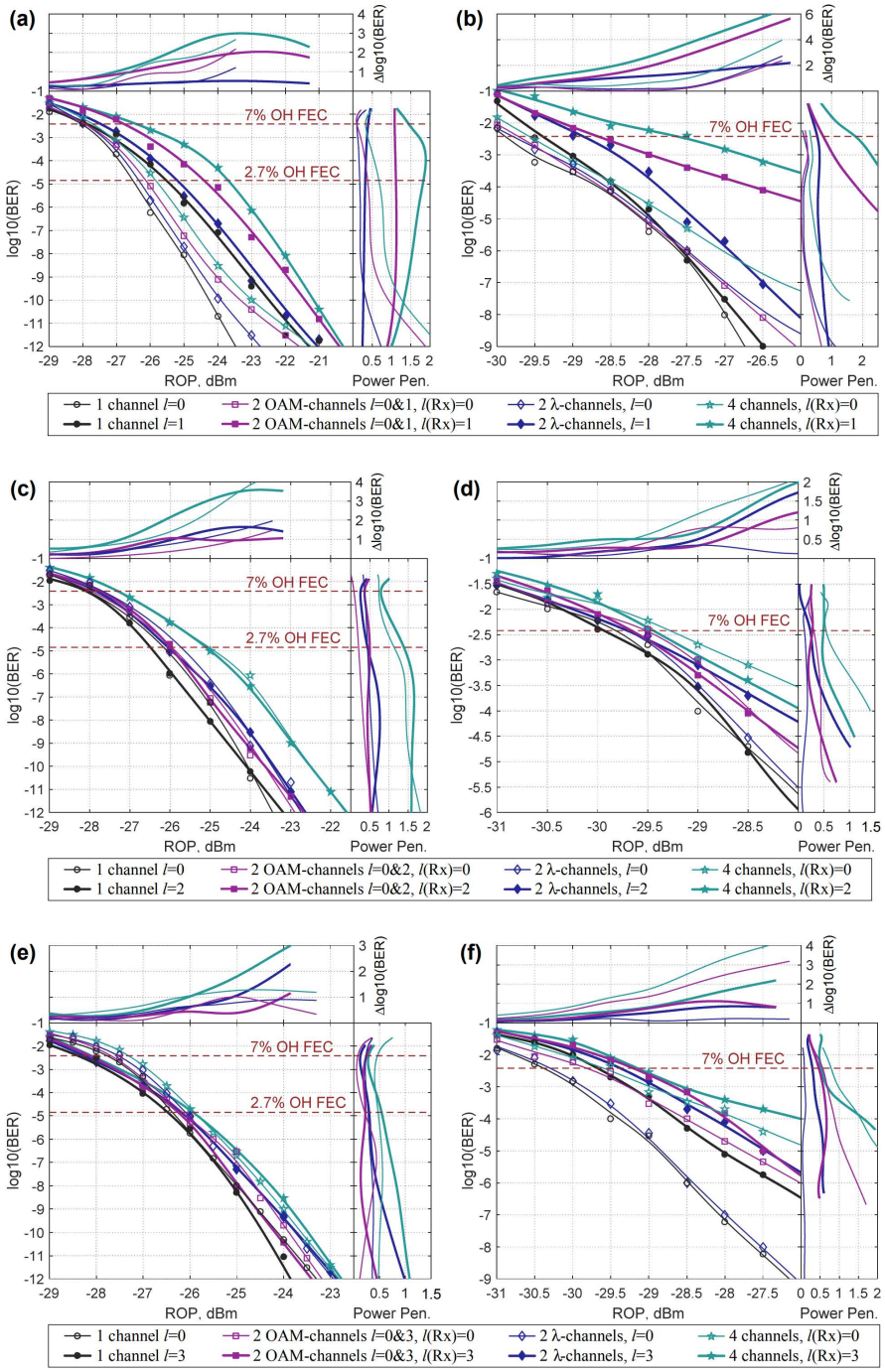

FIGURE 6.9: BER vs. ROP curves and penalties for demultiplexing wavelength and OAM channels when transmitting the Gaussian channel and the OAM channel of order: (a),(b) $l_p = 1$; (c),(d) $l_p = 2$; and (e),(f) $l_p = 3$. The left [(a),(c),(e)] and the right [(b),(d),(f)] columns correspond to OOK and BPSK modulations, respectively.

OAM-filters, the BER and ROP penalties over the whole measured range of ROP is calculated. A general assumption can be made that the closer azimuthal orders of the transmitted OAM channels, the higher BER and power penalties. The lowest penalties appear in case of maximum OAM separation, namely with $l_p = 3$ and $l_p = 0$, as can be seen in Fig. 6.9 (e). For less OAM separation the BER and power penalties generally

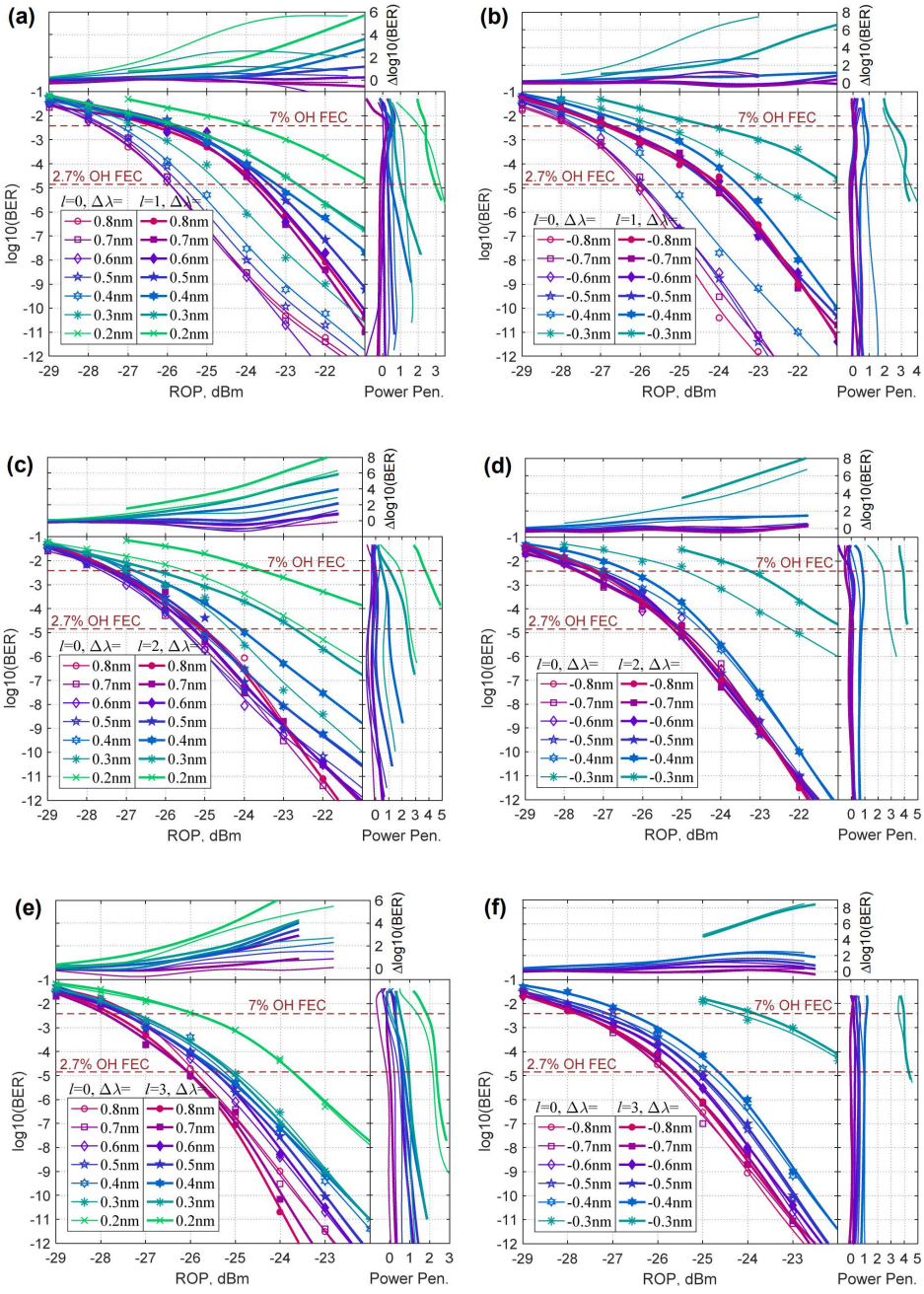

FIGURE 6.10: BER vs. ROP curves and penalties for OOK modulation when four (two wavelength and two OAM) channels are being transmitted for different spacing between wavelength channels. Each graph corresponds to transmission of the Gaussian channel and the OAM channel of order: $l_p = 1$; (c),(d) $l_p = 2$; and (e),(f) $l_p = 3$. The left column [(a),(c),(e)] and the right column [(b),(d),(f)] correspond to the cases when the received channel has higher and lower wavelength, than the filtered channel, respectively.

increase. Power penalty values calculated at the FEC BER thresholds for the case of four (two wavelength and two OAM) channels for OOK and BPSK are summarized in the Table 6.2.

In order to estimate the selectivity of the MEMS OAM-filters in the wavelength domain, the performance of the system for different spacing $\Delta\lambda$ between wavelength

TABLE 6.2: Penalties at the FEC BER thresholds for four (two OAM and two wavelength) channels, $\Delta\lambda = 0.8$ nm.

Modulation		OOK		BPSK
BER threshold		7% OH HD-FEC	2.7% OH RS FEC	7% OH HD-FEC
l(Tx) = 0, 1	l(Rx) = 0	0.33	0.68	0.32
	l(Rx) = 1	1.45	1.83	1.77
l(Tx) = 0, 2	l(Rx) = 0	0.73	1.13	0.54
	l(Rx) = 2	0.79	1.39	0.49
l(Tx) = 0, 3	l(Rx) = 0	0.46	0.47	0.79
	l(Rx) = 3	0.29	0.54	0.52

channels in case of OOK modulation is investigated. Figure 6.10 shows the corresponding BER measurement results. The devices were tested for the case of simultaneous multiplexing of two wavelength and two OAM channels, and $\Delta\lambda$ was decreasing from 0.8 nm with the step of 0.1 nm while the wavelength channels remained separable. As before, values of BER in both the OAM channel and the Gaussian channel were measured. Penalties were calculated relative to the case of largest spacing $\Delta\lambda = 0.8$ nm.

From the filter transmittance shown in Fig. 6.2 (a), it is evident that the device has a non-symmetric bandwidth from the peak of the resonance wavelength. At the right side (towards longer wavelength) of the peak, transmittance value falls more abruptly compared to the left side. Depending on the spectral position of the adjacent channel, this asymmetric property of the spectrum can influence the BER performance. Therefore, two scenarios are investigated in this work. The influence of both smaller and longer wavelengths in reference to the channel under investigation have been tested. This is shown in Fig. 6.10, where the left (a, c, e) and the right (b, d, f) columns correspond to the smaller and the longer wavelength (relative to the received channel), respectively. It is clearly visible that the MEMS filter suppresses the non-resonant channel differently depending on the positioning of the suppressed channel. The performance deterioration due to crosstalk between two wavelength channels becomes evident for $\Delta\lambda \leq 0.5$ nm in the case when the received channel has longer wavelength than the filtered channel. When the received channel has smaller wavelength than the filtered channel, the crosstalk is noticeable for $\Delta\lambda \leq 0.4$ nm. In the former case the received signal remains detectable with the BER values lower than 7% OH FEC threshold even with $\Delta\lambda = 0.2$ nm. However, in the latter case the quality of the received signal degrades rapidly with diminishing the spacing between wavelength channels beyond 0.4 nm. Nevertheless, wavelength channels in the latter case still can be demultiplexed when $\Delta\lambda = 0.3$ nm. Therefore, the overall behavior of filters in wavelength domain suggests its reasonable usage with the 50 GHz DWDM frequency grid. Table 6.3 summarizes maximum ROP penalties (among both placement scenarios of wavelength channels mentioned above) when multiplexing the Gaussian beam and OAM beams of azimuthal orders $l_p = 1$, 2 and 3. From the exper-

TABLE 6.3: Maximum penalties at the FEC BER thresholds for multiplexing four channels, $\Delta\lambda = 0.4\,\text{nm}$ in reference to $\Delta\lambda = 0.8, \text{nm}$.

BER threshold		7% OH HD-FEC	2.7% OH RS-FEC
$l(\text{Tx}) = 0, 1$	$l(\text{Rx}) = 0$	0.62	0.84
	$l(\text{Rx}) = 1$	0.83	0.48
$l(\text{Tx}) = 0, 2$	$l(\text{Rx}) = 0$	0.35	0.63
	$l(\text{Rx}) = 2$	0.84	1.00
$l(\text{Tx}) = 0, 3$	$l(\text{Rx}) = 0$	0.62	0.94
	$l(\text{Rx}) = 3$	1.15	1.00

iments, it can be validated that the performance of the MEMS OAM-filters in both wavelength and OAM domains is analogous – the larger spacing between channels in each multiplexing domain the better the transmission system performance (lower BER and power penalties), and vice versa. In order to fully characterize the functionality of the presented filter construction, it is necessary to make tests with more OAM channels. In this case an impact of their cross talk will be characterized closer to the real transmission conditions.

Chapter 7

Summary and Outlook

The first part of this thesis aimed for an electrically-pumped, high-speed, widely-tunable VCSEL emitting around the telecom wavelengths of 1550 nm. Wavelength tuning is realized with electro-thermal actuation of a movable MEMS based top DBR, which is integrated to the basic half-VCSEL structure by means of surface micromachining. A comprehensive characterization of the fabricated MEMS VCSELs are carried out, highlighting their potential applications and demonstrate the versatility of the demonstration of practical short reach optical fiber communications.

A brief history of VCSELs as laser sources for high-speed communication have been provided in Chapter 1. The chronological evolution of the tunable VCSELs and their diverged applications are discussed. Prior to the detailed characterization of the devices, some basic concepts of the VCSEL structure and tuning mechanism based on Fabry-Pérot (FP) resonator is briefed in Chapter 2. Investigating small-signal modulation response is an important part of this thesis. The response is described as three-pole transfer function comprising the intrinsic damping limit due to the resonant carrier-photon interaction and the extrinsic limit which is attributed to the parasitic elements of the VCSEL device. In addition, temperate increases via current induced self-heating imposes thermal limit. Some aspects of optical data transmission such as large-signal modulation, BER, and optical eye digram are also illustrated.

A ultra-wide tunable emission in the range of ≈ 100 nm has been archived in this work – thanks to the large gain-bandwidth of the active material, significantly short half-VCSEL cavity length and large reflectivity stop bandwidth of the DBRs. For a properly designed MEMS-VCSEL, FSR is the ultimate limit for further increasing the mode-hop free tunability. The details of the surface micromachining process is described in Chapter 3. The SiN_x/SiO_y based MEMS DBR is deposited using a low-temperature ICP-CVD and processed directly on the surface of the half-VCSEL. The implementation

of the DBR mirror layers promises an even larger tuning range due to the large stop band, as well as the small air gap lengths in the range of 4–5µm. The mechanical stress and the air-gap length can be adjusted via the deposition parameters and the thickness of the sacrificial layer. Due to challenges in terms of technological compatibility between the high-speed half-VCSEL from Vertilas GmbH and the MEMS technology of the TU Darmstadt a number of technological solution approaches have been investigated in this work. In the end, a robust and reproducible process flow has been developed targeting large-volume fabrication.

The tunable VCSEL is characterized in terms of its static and dynamic properties and discussed in Chapter 4. By using a concavely bent DBR mirror, only the desired fundamental Gaussian mode can be excited even with 14 µm buried tunnel junction diameter (VCSEL aperture). This plane-concave geometry increases the SMSR and guarantees stable optical properties over the whole tuning range. In continuous-wave operation at room temperature, the device is characterized with a side-mode suppression of more than 40 dB for the entire tuning range. The *L-I-V* characteristics of a typical device shows output power larger of 1.4 mW and threshold current of 2.9 mA for the center of the emission around 1550 nm at room temperature. Various temperatures are applied to the heat sink and the static performance is evaluated in details. At thermal rollover current, the MEMS VCSEL emits a circular symmetric, diffraction and refraction limited TEM_{00} beam which is advantageous for coupling into the optical fiber. The divergence angle of the Gaussian fitting curve is 5.66°, measured at $1/e^2$ the point where the intensity drops to of the highest peak. A narrow emission line and a high tuning speed are two opposing properties, as the movable MEMS is subject to Brownian noise. Using self-heterodyne method with a fiber delay-length of 5 km, the linewidth of an MEMS VCSEL is extracted. The Gaussian dominated linewidth is estimated to be 42 MHz. This is a factor two lower in comparison to the the previous generation non-high-speed MEMS VCSELs [40], and is attributed to the increased the spring constant (stiffness) and reduced dimension of the MEMS. The intrinsic linewidth estimated from the Lorentzian contribution (far away from the center peak) of the Voigt fit is 21 MHz. A stable linear polarization together with a resulting high value of the degree of polarization (DOP) has been observed across the entire tuning range. No switching of the polarization modes has been observed for the entire bias operation. The probable reason for polarization stability of this device can be attributed to a slightly different RoCs of the MEMS-DBR in two directions, originating from the process related imperfections. For the first time, the dynamic properties of a surface-micromachined MEMS VCSELs with direct modulation capacity in the wavelength range around 1550 nm are investigated. The results are discussed in detail in Chapter 5. The maximum modulation bandwidth of $f_{3dB,max}$ = 8.35 GHz at the center emission as well as $f_{3dB,max}$ of 3.88 GHz across a tuning range of 90 nm has been demonstrated.

Chapter 5 deals with applications of the fabricated MEMS-VCSEL. In order to determine it capacity in large-signal domain, data transmission experiments are performed in back-to-back configuration. For a medium PRBS word length of $2^{15} - 1$, a quasi error-free transmission at 10 Gbit/s is achieved for a continuous tuning range of 76 nm by directly modulated device. Maximum transmission of 12.5 Gbit/s, which is the limiting bit-rate supported by BERT setup is also demonstrated. Quasi error-free (BER $< 10^{-9}$) operation for 60 nm continuous tuning range (1530 nm to 1590 nm) is still achieved, which is the state-of-the-art tuning range for such bit rate. Using a packaged MEMS VCSEL, error-free transmission of 10 Gbit/s direct modulation over 40 km SSMF for the tuning range of more than 60 nm. This is more than suitable for the proposed converged MFH and MBH network application utilizing the G.metro novel WDM-PON system with differential reaches of up to 40 km.

The second component propped and experimentally validated in this thesis is a FP MEMS OAM-filter. This novel wavelength-tunable micro-sized components with integrated SPPs are suitable for distinguishing different OAM modes for a broad tuning range around 1550 nm emission. Some basic fundamental of OAM modes and their generation technique using SP are described in Chapter 2. The top MEMS-DBR fabrication is identical for the MEMS VCSEL and OAM -filter. The SPP integration technique is briefly discussed in Chapter 3. Four devices with OAM orders of $l_p = 0$ (no SPP on MEMS), 1, 2 and 3 have been investigated in Chapter 5. They are capable of generating/receiving the OAM beam of corresponding order over a continuous tuning range of more than 30 nm, for which the designed SPPs work with $> 92\%$ mode purity. The system performance is evaluated while multiplexing two wavelength channels (with 0.8 nm spacing) and two OAM channels (Gaussian beam is combined with OAM beams of azimuthal orders $l_p = 1,\ 2,\ 3$). Experimental results have shown that in the case of intensity modulation penalties do not exceed 1.45 dB and 1.83 dB at the 7% and 2.7% OH FEC BER thresholds, respectively. With the ROP up to -20 dBm the error-free transmission (BER$>10^{-12}$) is demonstrated. In the case of phase modulation, penalties do not exceed 1.77 dB at the 7% OH FEC BER threshold. Moderate penalties when shifting wavelength channels as close as 0.4 nm (1.15 dB and 1 dB at the above mentioned BER thresholds respectively) suggest usage of the proposed devices with the 50 GHz DWDM frequency grid. At the same time, transmission tests when multiplexing Gaussian beam with OAM beams of different orders demonstrate the behavior of the MEMS OAM-filter in OAM domain generally similar to that in the wavelength domain – the larger the distance between multiplexed channels, the better the transmission system performance. The proposed device is suitable for dense on-chip integration and is dedicated for the next generation optical links in both long-haul and short-range scenarios, simultaneously utilizing three degrees of freedom of the electromagnetic waves: wavelength, polarization, and OAM.

7.1 Future Work

UWB Pulse Generation Utilizing MEMS VCSEL

Directly modulated MEMS VCSELs can be used for reconfigurable wired-wireless converged networks with high data rates. This network concept require simple and low-cost solutions for the generation of the ultra-wide band (UWB) signal in the optical domain. Direct modulation of VCSEL in combination with optical filtering enable a low-cost generation of such UWB pulses.

UWB offers high data rate with low power consumption, high efficiency of space-frequency spectrum, interference mitigation, immunity to multi-path fading, and penetration capability through obstacles. It is well suited for the communication between fixed access points connected to data backbone and large numbers of wireless sensors in their vicinity. Due to the low power consumption resulting in small transmission range of up to ten meters, the number of radio interfaces in the deployment area increases. Each antenna can be addressed via an optical fiber channel which is defined by the optical wavelength. Such UWB-over-fiber (UWBoF) networks make all-optical UWB signal generation highly desirable. To generate an appropriate spectrum, the optical pulse shapes need to be derivatives of a Gaussian pulse. The first derivative is referred to as a monocycle, whereas the second derivative is known as doublet. The spectrum of the fifth order derivative of a Gaussian pulse fits perfectly into the FCC mask. However, its generation in the optical domain is rather complex compared to the monocycle or doublet. With additional filtering (electrical filter or appropriate antenna transfer function), the spectrum of the monocycle or doublet can be adapted to the FCC mask at low cost. There exists a manifold of techniques to generate the derivatives of Gaussian pulses in the optical domain. However, most of them are rather complex and costly. As a first attempt, generation of UWB pulses using direct modulation of a DFB laser and optical filtering has been demonstrated [112, 113]. The setup executes an derivative operation which generates monocycles, if the DFB laser is electrically modulated with a Gaussian driving signal. As a future work, the use of widely tunable MEMS-VCSEL for all optical monocycle generation in UWBoF WDM-PON can be interesting topic for investigation.

SPP Integration to MEMS VCSEL

In this work, a new wavelength-tunable micro-component for simultaneous selection of the waves with different wavelengths and values of OAM MEMS-based FP filter with integrated spiral phase plate. As one step forward, one can integrate the SPPs within the aperture of a MEMS-DBR of the MEMS VCSELs, the linearly polarized Gaussian

beam emitted by the VCSEL can be directly converted into a beam carrying specific OAM modes and their superposition states with high efficiency and high beam quality. With direct modulation facility of the fabricated MEMS VCSELs, OAM-VCSEL will open a new horizon in the field of OAM-based optical and quantum communications, especially for short reach data interconnects. Apart from wavelength and OAM beam selectivity, one can add a third degree of freedom namely, polarization preference – simply by fabricating an elliptical MEMS. The proposed OAM-VCSELs will generate high-purity OAM modes while maintaining advantages in cost and power efficiency.

Increasing Tuning Range using SiO_y/SiC-Based MEMS-DBR

In order to increase the reflectivity bandwidth of the MEMS-DBR, SiO_y/SiC-based dielectrics can be used. The simulation using transfer-matrix method shows promising results [114]. A continuous tuning range of electrically pumped MEMS-VCSEL can be extended to $>140\,\text{nm}$. The high refractive index contrast of $\Delta n > 1$ between SiO_y and SiC reduces required number of layer pairs to 11 and broadens the stopband width of the reflectivity up to 448 nm for $R > 99.5\,\%$, which is more than a factor of two compared to the material system SiN_x/SiO_y (23 layers, 216 nm for $R > 99.5\,\%$) used for the current MEMS-VCSELs. The smaller number of DBR-layers enables a significant reduction of the overall mirror thickness, which enables a further miniaturization of the device and thus an increase of the free spectral range (FSR), the ultimate limit for continuous wavelength tuning.

Acronyms

2-D	Two dimensional
Ag	Silver
AM	Amplitude modulation
APD	Avalanche photodiode
ARC	Antireflection coating
ASE	Amplified spontaneous emission
Au	Gold
AWG	Arrayed-waveguide grating
BBU	Baseband Unit
BCB	Benzocyclobutane
BER	Bit error rate
BERT	Bit error rate tester
BPSK	Binary phase-shift keying
BTB	Back-to-back
BTJ	Burried tunnel junction
CCD	Charge coupled device
CGH	Computer generated hologram
Cr	Chrome
CVD	Chemical vapor deposition
CW	Continuous-wave
DBR	Distributed Bragg reflector
DC	Direct current
DFB	Distributed feedback
DI	Deionized

DLW	Direct laser writing
DOE	Diffractive optical element
DSH	Delayed self-heterodyne
DUT	Device under test
EBL	Electron beam lithography
ECL	External cavity laser
EDFA	Erbium-doped fiber amplifier
EEL	Edge emitting laser
ER	Extinction ratio
ESA	Electrical spectrum analyzer
FBG	Fiber Bragg grating
FEC	Forward error correction
FH	Fork holograms
FIB	Focused ion beam
FP	Fabry-Pérot
FSR	Free spectral range
FTTH	Fiber-to-the-home
GaAs	Gallium Arsenide
GPIB	General purpose interface bus
G-S	Ground-signal
HCG	High contrast grating
HNO_3	Nitric acid
HCl	Hydrochloric acid
HPSDS	Heterodyne phase sensitive dispersion spectroscopy
ICP-CVD	Inductively coupled plasma chemical vapor deposition
InP	Indium Phosphide
IR	Infrared
ISI	Inter-symbol interference
LAN	Local area network
Laser	Light amplification by stimulated emission
L-I-V	Light–current–voltage
LG	Laguerre-Gaussian
LIDAR	Light detection and ranging

LTG	Low Temperature Grown
MBE	Molecular Beam Epitaxy
MDM	Mode division multiplexing
MEMS	Micro-electro-mechanical system
MLSPP	Multi-level spiral phase plate
MMF	Multimode fiber
MUX	Multiplexer
MZM	Mach-Zehnder modulator
Ni	Nickel
NIR	Near infrared
NRZ	Non return to zero
OAM	Orbital angular momentum
OCT	Optical coherence tomography
OOK	On-off keying
OTN	Optical transmission network
OV	Optical vortex
PD	Photodiode
PDM	Polarization division multiplexing
PMD	Phase modifying devices
PON	Passive optical network
PR	Photoresist
PRBS	Pseudo-random bit sequence
QW	Quantum well
RF	Radio frequency
RIE	Reactive ion etching
RIN	Relative intensity noise
RoC	Radius of curvature
ROP	Received optical power
RS	Reed-Solomon
SAM	Spin angular momentum
SC	Short-cavity
SDM	Space division multiplexing
SDN	Software-defined networks

SSMF	Standard single-mode fiber
SEM	Scanning electron microscope
Si	Silicon
SiC	Silicon Carbide
SiN$_x$	Silicon Nitride
SiO$_x$	Silicon Oxide
SLM	Spatial light modulators
SMSR	Side-mode suppression ratio
SNR	Signal-to-noise ratio
SOA	Semiconductor optical amplifier
SPP	Spiral phase plate
SWG	Subwavelength grating
TDLAS	Tunable diode laser spectroscopy
TEE	Tail-end equipment
THz	Terahertz
TIA	Transimpedance amplifier
TOSA	Transmitter optical subassembly
VCSEL	Vertical-cavity surface-emitting laser
VNA	Vector network analyzer
VOA	Variable optical attenuator

Symbols

n	Refractive index
$L_{\mathbf{0}}$	Resonator length (geometric)
L	Resonator length (optical)
$L_{\mathbf{tot}}$	Total resonator length
c	Speed of light ($2.99792458 \times 10^{8}\ \mathrm{m \cdot s^{-1}}$)
e	Electron charge ($1.60217646 \times 10^{-19}\ \mathrm{C}$)
E	Electric field
ε	Permittivity
ε_0	Absolute permittivity ($8.8541878 \times 10^{-12}\ \mathrm{F \cdot m^{-1}}$)
ε_{eff}	Effective permittivity
ε_r	Relative permittivity
η	Quantum efficiency
η_i	Internal quantum efficiency
λ	Wavelength
τ_c	Carrier life-time
ν	Frequency
Z_0	Free space impedance
Z_{load}	Load impedance
z	Penetration depth

Appendix A

Differential Analysis of the Rate Equations

In order to obtain the dynamic behavior of lasers in response to current modulation, time derivatives of the rate equations are generated. By assuming that dynamic changes in the carrier and photon densities deviated from steady state values are very small, one can obtain small-signal modulation transfer functions. Taking I_{L}, N, S and g as dynamic variable into account, the differentials of Eq. (1) and (2) develops to:

$$d\left[\frac{dN}{dt}\right] = \frac{\eta_{\mathrm{i}}}{qV}\, dI_{\mathrm{L}} - \frac{1}{\tau_{\Delta n}}\, dN - v_{\mathrm{g}} g\, dS - S v_{\mathrm{g}}\, dg, \tag{A.1}$$

$$d\left[\frac{dS}{dt}\right] = \left[\Gamma v_{\mathrm{g}} g - \frac{1}{\tau_{\mathrm{p}}}\right] dS + S\Gamma v_{\mathrm{g}}\, dg + \frac{\Gamma}{\tau'_{\Delta n}}\, dN, \tag{A.2}$$

where

$$\frac{1}{\tau_{\Delta n}} = \frac{dR_{\mathrm{sp}}}{dN} + \frac{dR_{\mathrm{nr}}}{dN} + \frac{dR_{\mathrm{l}}}{dN} \approx A + 2BN + CN^2, \tag{A.3}$$

$$\frac{1}{\tau'_{\Delta n}} = \frac{dR'_{\mathrm{sp}}}{dN} \approx 2\beta_{\mathrm{sp}} BN + \frac{d\beta_{\mathrm{sp}}}{dN} BN^2. \tag{A.4}$$

All the unstimulated carrier decay recombination processes can be summarized as:

$$R_{\mathrm{rec}} = R_{\mathrm{sp}} + R_{\mathrm{nr}} + R_{\mathrm{l}} = \frac{N}{\tau} \approx BN^2 + AN + CN^3. \tag{A.5}$$

where N/τ is estimated by the polynomial $BN^2 + AN + CN^3$ where the terms estimate defect, spontaneous (R_{sp}) and Auger recombinations, respectively.

The differential carrier lifetime $\tau_{\Delta n}$ depends on the local slope dR/dN where as the total carrier lifetime τ depends on the overall slope R/N. The gain variation dg can be

further expanded to

$$dg = a\,dN - a_{\mathrm{p}}\,dS, \tag{A.6}$$

by assuming that it s affected by both carrier and photon density variation. The gain is also inversely proportionate to $(1+\varepsilon S)$, where ε is known as gain compression factor. Thus one can approximate gain by:

$$g(N,S) = \frac{g_0}{1+\varepsilon S}\ln\left(\frac{N+N_{\mathrm{s}}}{N_{\mathrm{tr}}+N_{\mathrm{s}}}\right). \tag{A.7}$$

With this expression the gain derivatives become:

$$a = \frac{\partial g}{\partial N} = \frac{g_0}{(N+N_{\mathrm{s}})(1+1+\varepsilon S)} \equiv \frac{a_0}{1+\varepsilon S}. \tag{A.8}$$

Here a_0 is defined as nominal differential gain— the value of a with zero photon density. Replacing dg with Eq. (8), the differential rate equations become:

$$\frac{d}{dt}(d\,N) = \frac{\eta_{\mathrm{i}}}{qV}\,dI_{\mathrm{L}} - \Psi_1\,dN - \Psi_2\,dS, \tag{A.9}$$

$$\frac{d}{dt}(d\,S) = \Psi_3\,dN - \Psi_4\,dS, \tag{A.10}$$

where the rate coefficients referred to

$$\Psi_1 = \frac{1}{\tau_{\Delta n}} + v_{\mathrm{g}}aS, \qquad \Psi_2 = \frac{1}{\Gamma\tau_{\mathrm{p}}}\frac{R'_{\mathrm{sp}}}{S} - v_{\mathrm{g}}a_{\mathrm{p}}S \tag{A.11}$$

$$\Psi_3 = \frac{\Gamma}{\tau'_{\Delta n}} + \Gamma v_{\mathrm{g}}aS, \qquad \Psi_4 = \frac{\Gamma R'_{\mathrm{sp}}}{S} + \Gamma v_{\mathrm{g}}a_{\mathrm{p}}S \tag{A.12}$$

The rate coefficients allows to conveniently describe the differential rate equations in a compact matrix format:

$$\begin{bmatrix} dN \\ dS \end{bmatrix} = \begin{bmatrix} -\Psi_1 & -\Psi_2 \\ +\Psi_3 & -\Psi_4 \end{bmatrix} \begin{bmatrix} dN \\ dS \end{bmatrix} + \frac{\eta_{\mathrm{i}}}{qV}\begin{bmatrix} dI \\ 0 \end{bmatrix} \tag{A.13}$$

Now for small signal analysis, a small AC current I_1 is considered which is superimposed with the DC current I_0 above threshold. Under steady state conditions, the lasers carrier density and photon density would respond with some harmonics of the

drive frequency f. Using derivatives:

$$I = I_0 + I_1 \exp(j\omega t) \;\Rightarrow\; dI(t) = I_1 \exp(j\omega t) \tag{A.14}$$

$$N = N_0 + N_1 \exp(j\omega t) \;\Rightarrow\; dN(t) = N_1 \exp(j\omega t) \tag{A.15}$$

$$S = S_0 + S_1 \exp(j\omega t) \;\Rightarrow\; dS(t) = S_1 \exp(j\omega t) \tag{A.16}$$

Setting $d/dt \rightarrow j\omega$ and rearranging Eq. (15) one obtains:

$$\begin{bmatrix} \Psi_1 + j\omega & \Psi_2 \\ -\Psi_3 & \Psi_4 + j\omega \end{bmatrix} \begin{bmatrix} N_1 \\ S_1 \end{bmatrix} + \frac{\eta_{\mathrm{i}} I_{\mathrm{L1}}}{qV} \begin{bmatrix} 1 \\ 0 \end{bmatrix} \tag{A.17}$$

with the determinant

$$\Delta \equiv \begin{vmatrix} \Psi_1 + j\omega & \Psi_2 \\ -\Psi_3 & \Psi_4 + j\omega \end{vmatrix} = \Psi_2\Psi_3 + \Psi_1\Psi_4\omega^2 + j\omega(\Psi_1\Psi_4) \tag{A.18}$$

Applying Cramer's rule to obtain small-signal carrier and photon densities in terms of modulation current:

$$N_1 = \frac{\eta_{\mathrm{i}} I_{\mathrm{L1}}}{qV} \cdot \frac{1}{\Delta} \begin{vmatrix} 1 & \Psi_2 \\ 0 & \Psi_4 + j\omega \end{vmatrix} = \frac{\eta_{\mathrm{i}} I_{\mathrm{L1}}}{qV} \cdot \frac{\Psi_4 + j\omega}{\omega_{\mathrm{R}}^2} H(\omega), \tag{A.19}$$

$$S_1 = \frac{\eta_{\mathrm{i}} I_{\mathrm{L1}}}{qV} \cdot \frac{1}{\Delta} \begin{vmatrix} 1 & \Psi_2 \\ 0 & \Psi_4 + j\omega \end{vmatrix} = \frac{\eta_{\mathrm{i}} I_{\mathrm{L1}}}{qV} \cdot \frac{\Psi_3}{\omega_{\mathrm{R}}^2} H(\omega), \tag{A.20}$$

where the modulation is conveniently described in terms of two parameter modulation transfer function:

$$H(\omega) = \frac{\omega_{\mathrm{R}}^2}{\Delta} \equiv \frac{\omega_{\mathrm{R}}^2}{\omega_{\mathrm{R}}^2 - \omega^2 + j\omega\gamma} \tag{A.21}$$

ω_{R} is defined as relaxation oscillation frequency and γ as the damping factor. Comparing Eq. and , the following relations can be made:

$$\omega_{\mathrm{R}}^2 \equiv \Psi_2\Psi_3 + \Psi_1\Psi_2 = \frac{\upsilon_{\mathrm{g}} a S}{\tau_{\mathrm{p}}} + \left[\frac{\Gamma \upsilon_{\mathrm{g}} a_p S}{\tau'_{\Delta N}} + \frac{\Gamma R'_{\mathrm{sp}}}{S\tau_{\Delta N}}\right]\left(1 - \frac{\tau_{\Delta N}}{\tau'_{\Delta N}}\right) + \frac{1}{\tau'_{\Delta N}\tau_{\mathrm{p}}} \tag{A.22}$$

$$\gamma = \Psi_1 + \Psi_4 \equiv= \upsilon_{\mathrm{g}} a S \left[1 + \frac{\Gamma a_p}{a}\right] + \frac{1}{\tau_{\Delta N}} + \frac{\Gamma R'_{\mathrm{sp}}}{S} \tag{A.23}$$

In practice, the expression of ω_{R}^2 can be reduced to a single term. For example, the last term is small compared to the first for $SV_p > n_{\mathrm{sp}}$ and thus can be ignored above threshold condition. Moreover, above threshold, the term with $1/S$ can also be ignored.Finally,

the relation $a/\tau_p \gg \Gamma a_p/\tau_{\Delta N}$ also applies, making the modified and simpler expression for ω_{R}^2.

$$\omega_{\mathrm{R}}^2 = 4\pi^2 f_{\mathrm{R}}^2 = \frac{v_{\mathrm{g}} a S}{\tau_{\mathrm{p}}} \tag{A.24}$$

Appendix B

Photolithography Masks

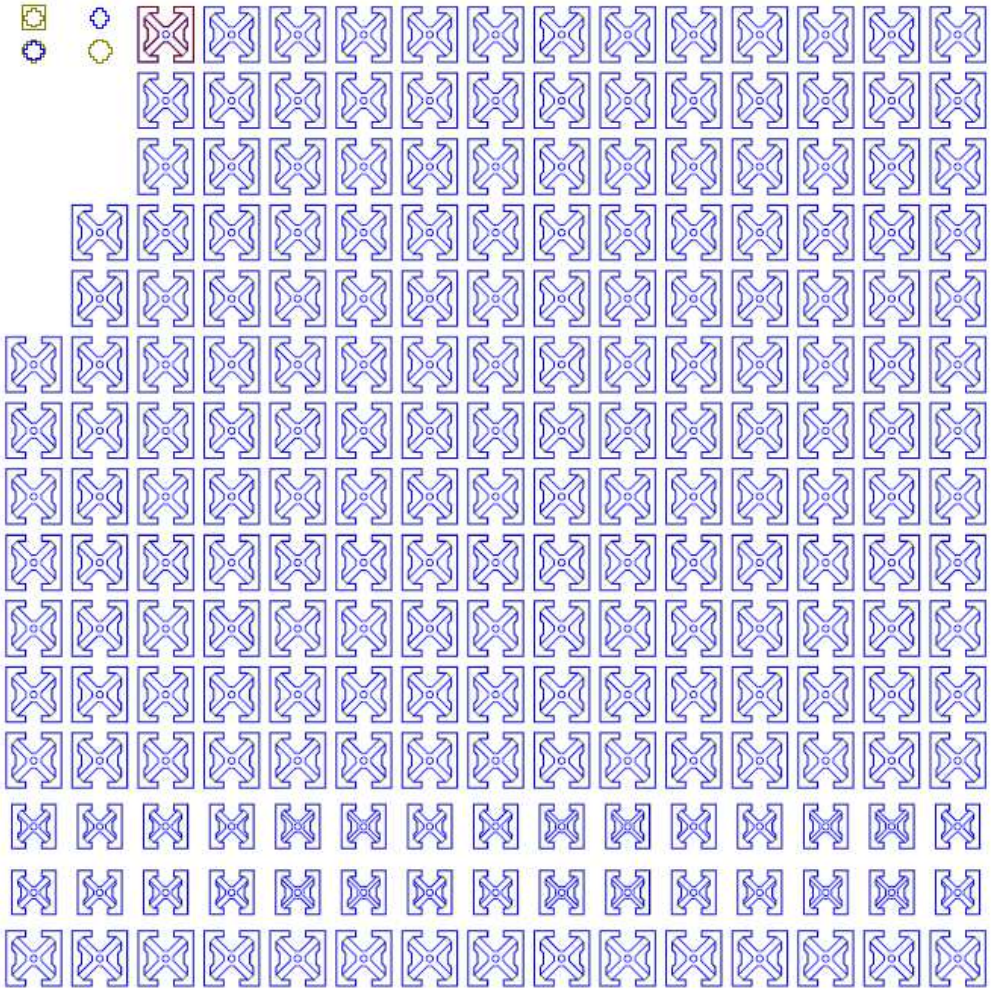

FIGURE B.1: A unit cell showing the overlay of all photolithography masks used in MEMS surface micromachining.

Appendix C

MEMS Surface Micromachining Process

Ni sacrificial layer sputtering and structuring

Sputtering Ni

• Mounting on a glass holder,

• 12 min of Ni sputtering with pressure $p = 320 \times 10^{-4}$ mbar and RF power $P_{\mathrm{RF}} = 2\,\mathrm{kW}$ for an estimated thickness of 400 nm

Photolithography

• Spin coating of PR (AZ 1518) at 6000 rpm for 40 s,

• Softbaking in two steps: 2 min in 90 °C + 2 min in 120 °C hotplate,

• UV exposure 23 s with the mask for sacrificial layer,

• Developing in Clariant AZ 400K : H_2O (1 : 4) for 30 s and stopping the reaction with DI H_2O bath for 30 s,

• Drying with N_2

Wet-chemical etching of Ni

• $\approx$ 2 min in buffered HNO_3 ($HNO_3 : H_2O = 1 : 30$) at 50 °C and stopping the reaction with an H_2O bath for 30 s,

PR removal

• Immersing in *N*-Methyl-2-pyrrolidone(NMP) at 50 ° for 1 min, and then thoroughly rinse with DI H_2O

• Drying with N_2

Deposition of MEMS-DBR dielectric layers

Single layer deposition

• 3 SSP Si wafers are used for depositing two SiN_x (tensile and compressive) and one SiO_y layers separately. They are used for extracting the deposition time, refractive index and the stress values for the final DBR layer deposition

DBR deposition

• Mounting the sample on a 2-inch Si substrate,

• DBR layer deposition according to:

SiN_x (tensile) $\Rightarrow N_2 : SiH_4 = 6.0 : 6.7$; $p = 7.9$ mTorr, $P_{ICP} = 200$ W,

SiN_x (compressive) $\Rightarrow N_2 : SiH_4 = 6.0 : 6.5$; $p = 8.8$ mTorr, $P_{ICP} = 200$ W,

$SiO_y \Rightarrow N_2O : SiH_4 = 12.0 : 3.0$; $p = 7.5$ mTorr, $P_{ICP} = 500$ W, $P_{ICP} = 500$ W,

• un-gluing the sample from the Si substrate by heating up to 100 °C and again mounting on a glass holder,

• Cleaning with NMP at 50 ° for 1 min, and then thoroughly rinse with DI water

MEMS electrode evaporation and structuring

Cr/Au evaporation

• Install the sample in Balzers metalization chamber on the rotating mount, then 10 nm Cr at 0.4 Å/min, followed by 40 nm Au at 0.7 Å/min

Au galvanization

• 2 µm Au galvanization (externally)

Photolithography

• Spin coating of PR (AZ 1518) at 6000 rpm for 40 s,

• Softbaking in two steps: 2 min in 90 °C + 2 min in 120 °C hotplate,

• UV exposure 23 s (mask for elelctrode),

• Developing in Clariant AZ 400K : H_2O (1 : 4) for 30 s and stopping the reaction with a DI water bath for 30 s,

• Drying with N_2

Wet-chemical etching of Cr/Au

• Spray 2 times the Au etchant [mixture of 82.3 g of ceric ammonium nitrate ($(NH_4)_2[Ce(NO_3)_6]$), 45 ml of nitric acid (HNO_3) and 500 ml of deionized water (H_2O)] with a syringe and rinse with DI water for 1 min,

• Spray 2 times standard perchloric acid ($HClO_4$) based Cr etchant and rinse with DI water for 1 min,

• Cleaning with NMP at 50 ° for 1 min, and then thoroughly rinse with DI water

Ni hard mask sputtering and structuring

Sputtering Ni

• 6 min of Ni sputtering with $p = 320 \times 10^{-4}$ mbar and P_{RF} power = 2 kW for a thickness of 200 nm

Photolithography

• Spin coating of PR (AZ 1518) at 6000 rpm for 40 s,

• Softbaking in two steps: 2 min in 90 °C + 2 min in 120 °C hotplate,

• UV exposure 23s (mask for hard-mask),

• Developing in Clariant AZ 400K : H_2O (1 : 4) for 30 s and stopping the reaction with an H_2O bath for 30 s,

• Drying with N_2

Wet-chemical etching of Ni

• 1 min in buffered HNO_3 ($HNO_3 : H_2O = 1 : 30$) at 50 °C and stopping the reaction with a water bath for 30 s,

PR removal

• Immersing in NMP at 50 ° for 1 min, and then thoroughly rinse with DI water,

• Drying with N_2

Structuring the MEMS-DBR

RIE etching

• RIE etching according to:

RF power	Pressure	Temp.	CF_4	CHF_3	Ar	O_2
75 W	300 mTorr	25 °C	25 sccm	25 sccm	25 sccm	50 sccm

• Cleaning with DI water after each 10 min, and measuring the etch depth in the DekTak,

• after the final round, drying with N_2

Removing Ni sacrificial layer: part 1

Partial Ni wet etching

• Etching of exposed sacrificial Ni layer around the MEMS-DBR: 2 min in buffered HNO_3 ($HNO_3 : H_2O = 1 : 30$) at 50 °C and water bath for 30 s,

• Drying with N_2

Mounting on a submount

Photolithography

• Spin coating of PR (AZ 1518) at 6000 rpm for 40 s,

• Softbaking in two steps: 2 min in 90 °C + 2 min in 120 °C hotplate,

• UV exposure 23s (same mask for hard-mask),

• Developing in Clariant AZ 400K : H_2O (1 : 4) for 30 s and stopping the reaction with an H_2O bath for 30 s,

• Drying with N_2

Dicing and mounting on submount

• Performed at an external facility

Removing Ni sacrificial layer: part 2

• Under-etching of Ni until (approx. 2–3 hours) the MEMS is resealed: in TFG at 50 °C

PR removal

• Immersing in NMP at 50 ° for 1 min, and then thoroughly rinse with DI water,

• Immerse the Si submount sample in isopropanol

Releasing the MEMS-DBR

Critical point drying

• Filling the transfer boat with adequate isopropanol so that the sample is fully immersed,

• Flushing the chamber with CO_2,

• Increasing the temperature from 15 °C to 38 °C at a ramp of 2 °C in every 3 min,

• taking out of the chamber after releasing the pressure and mounting the Si submount on a Cu holder for electro-optical characterizations

Appendix D

TOSA Packaging and Characterizations

The MEMS VCSELS developed in this work are mainly targeted for an compact SFP+ transceiver module where some predefined specification are to be met. An sketch of such a SFP+ module is shown in Fig. D.1. After on-wafer testing few MEMS VCSELs are packaged (TO-46 based LC TOSA package).

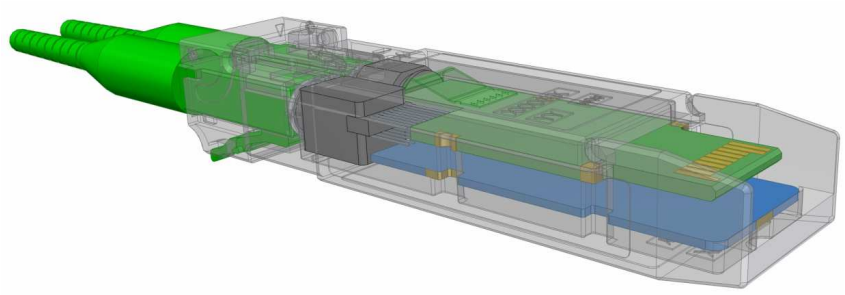

FIGURE D.1: Optimal space utilization of an SFP+ module by two printed circuit boards on both sides (green and blue).

TABLE D.1: Measured basic electro-optical characteristics of the first batch of TOSAs.

TOSA	T (°C)	I_L (mA)	Tuning (nm)	SMSR (dB)	For 50 nm tuning range		
					Fiber coupled power (dBm)	Variation (dB)	SMSR (dB)
1	24.8	35	84	41	>0.0	1.25	45
2	24	30	91	36	>-2.9	1.22	45
3	26	30	91	33	>-1.2	0.94	45
4	25.7	35	81	45	>-0.6	1.32	45
5	11.4	30	71	42	>-3.7	1.5	45

Several components and functions needed to be integrated inside a small TO-46 based LC TOSA package. These include a thermoelectric cooler (TEC), a thermistor and a

monitoring diode. Only one control signal is required to tune the laser without mode hops across the full tuning range. In total, only 8 pins are required for the described functionality. An overview of the measured DC properties is given in Table D.1.

The temperature in the second column is set via the Peltier element in the TOSA. As the performance (output power, threshold current) at the edges of the tuning range fluctuates, the first set of analysis is limited to 50 nm range which is defined by the project milestone. Within this 50 nm, the optical power in the glass fiber should be greater than -3 dBm (0.5 mW), varying by less than 1.5 dB. The four best TOSAs meet this specification. For all TOSAs, SMSR is greater than 45 dB. In the case of tuning ranges > 90 nm, the SMSR is reduced at the edges because of the mode competition.

Appendix E

MEMS VCSEL-based THz Photomixing

The THz photomixing experiment employs two laser diode sources for generating the beat signal. One laser is a commercially available DFB laser and the other one is a SC MEMS VCSEL developed in this work. The experimental setup is illustrated in Fig. E.1. The emission wavelength of the MEMS VCSEL is set to 1525 nm corresponding to $I_{\text{bias}} = 20\,\text{mA}$, $I_{\text{MEMS}} = 0\,\text{mA}$ and a substrate temperature of 20 °C. The optical power of the VCSEL is coupled to a polarization-maintaining (PM) fiber through a lens system and an optical isolator aligned to the slow axis of the PM fiber. The measured fiber-coupled optical power is 1.5 mW. An in-house built wavelength locker which collects 1% of the VCSEL output power is used for locking and sweeping the emission wavelength [23]. The remaining power is fed to the 95% port of a 95/5 PM coupler, where the 5% port is fed from DFB laser set at ≈ 40 mW fiber coupled output power. The intentional unequal coupling from the two lasers diodes balances the power levels at the output port of the coupler. A gain-flattened PM-EDFA* amplifies the combined power to ≈ 44 mW, which drives a *p-i-n* photomixer†. The THz emission is radiated in the free space by a built-in antenna. A photoconductor receives the THz emission using homodyne detection with a lock-in amplifier (time constant $\tau_{\text{LIA}} = 30$ or 300 ms). The THz frequency bandwidth of the setup is limited to 2.75 THz which is set by the dynamic range of the detector-source pair at the given laser power [107]. To demonstrate the continuous tunability and frequency coverage of the homodyne THz setup, MEMS-VCSEL is tuned and stabilized by the control circuit to a particular wavelength between 1533.41 nm and 1570.41 nm covering the whole amplification range of the EDFA. First, the MEMS VCSEL is locked to 1533.41 nm. Optical beating of the MEMS VCSEL with the longest DFB laser wavelength of 1558.57 nm generates a bandwidth of 3.14 THz. A

*PriTel, Model PMFA-20-IO
†WIN-PD from Fraunhofer-Institut für Nachrichtentechnik / TOPTICA Photonics

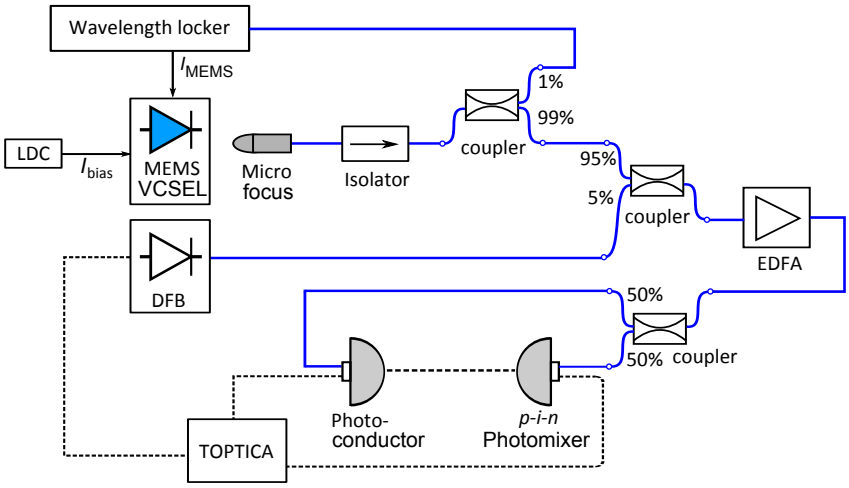

FIGURE E.1: Schematic of the THz setup, broadband tunability is obtained by employing a tunable MEMS VCSEL.

subsequent temperature tuning of the DFB laser in steps of 100 MHz is carried out over its tuning range of 550 GHz, i.e., from 1558.57 to 1554.16 nm. Subsequently, the control circuit tunes and locks the MEMS VCSEL to a longer wavelength with a step of 3-4 nm (corresponding to either 400 or 500 GHz steps) followed by repeated temperature tuning of the DFB laser. The wavelength step size of the VCSEL ensures overlap of the individual DFB sweeps to get a continuous spectrum without any interruption. A scan with $\lambda_{\text{MEMS-VCSEL}} < \lambda_{\text{DFB}}$ is shown in Fig. 17, where the individual DFB sweeps are indicated by color sequences. The swept THz bandwidth from 3.14 THz to dc is limited solely by the noise floor of the photomixing system to 2.75 THz. Since the setup is operated in ambient air, several water lines are clearly visible. To ensure rapid data acquisition, most data are recorded with $\tau_{\text{LIA}} = 30$ ms. Only for the three traces above 1.95 THz (the green, black, and green traces in Fig. 17) is 300 ms used to reduce the noise floor and extend the THz bandwidth. For $\tau_{\text{LIA}} = 300$ ms, a dynamic range of 87.5

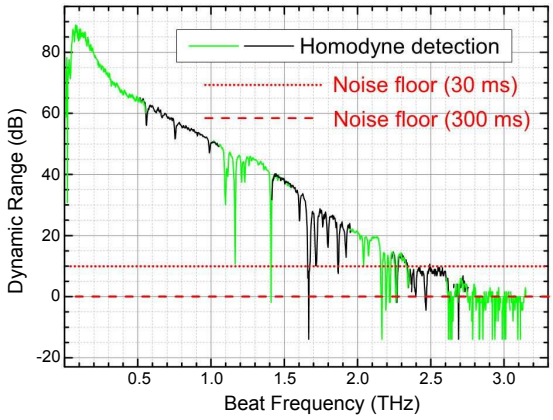

FIGURE E.2: Homodyne detection of 2.75 THz using a MEMS VCSEL and a DFB laser ($\lambda_{\text{VCSEL}} < \lambda_{\text{DFB}}$ [107]. The individual DFB sweeps are indicated by color sequences.

dB is obtained at 0.1 THz, while this drops to 50.3 dB at 1 THz. For 30 ms, the dynamic range is 10 dB smaller, as also shown in Fig. E.2. In a similar way, a scan from dc to 1.99 THz for $\lambda_{\text{MEMS-VCSEL}} > \lambda_{\text{DFB}}$. In this case, the THz bandwidth is limited by the bandwidth of the PM-EDFA to a maximum difference frequency of 1.99 THz. Therefore, the measurement demonstrates a fully covered bandwidth of 4.74 THz (2.75 THz 1.99 THz). Improved photomixers with an extended bandwidth should allow for a sweep up to a THz bandwidth of 4.74 THz using the present optical system with an appropriately chosen DFB diode featuring a wavelength at the edge of the EDFA gain region.

Bibliography

[1] R. Kompfner, "Optics at Bell laboratories – optical communications," *Appl. Opt.*, vol. 11, no. 11, pp. 2412–2425, 1972.

[2] T. H. Maiman, "Stimulated optical radiation in ruby," *Nature*, vol. 187, pp. 493–494, 1960.

[3] I. Hayashi, M. B. Panish, P. W. Foy, and S. Sumski, "Junction lasers which operate continuously at room temperature," *Appl. Phys. Lett.*, vol. 17, no. 3, pp. 109–111, 1970.

[4] M. Horiguchi and H. Osanai, "Spectral losses of low-OH-content optical fibres," *Electron. Lett.*, vol. 12, no. 12, pp. 310–312, 1976.

[5] L. A. Coldren, S. W. Corzine, and M. L. Mašanović, "A phenomenological approach to diode lasers," in *Diode Lasers and Photonic Integrated Circuits*, ch. 2, pp. 45–90, Hoboken, New Jersey: John Wiley and Sons, Inc., 2012.

[6] R. Michalzik, "VCSELs: A research review," in *VCSELs: Fundamentals, Technology and Applications of Vertical-Cavity Surface-Emitting Lasers* (R. Michalzik, ed.), ch. 1, pp. 3–15, Berlin, Heidelberg: Springer Berlin Heidelberg, 2013.

[7] K. Iga, "Surface-emitting laser–its birth and generation of new optoelectronics field," *IEEE J. Sel. Topics Quantum Electron.*, vol. 6, no. 6, pp. 1201–1215, 2000.

[8] H. Soda, K. Iga, C. Kitahara, and Y. Suematsu, "GaInAsP/InP surface emitting injection lasers," *Jpn. J. Appl. Phys.*, vol. 18, pp. 2329–2330, 1979.

[9] F. Koyama, S. Kinoshita, and K. Iga, "Room-temperature continuous wave lasing characteristics of a GaAs vertical cavity surface-emitting laser," *Appl. Phys. Lett.*, vol. 55, pp. 221–222, 1989.

[10] M. Orenstein, A. C. Von Lehmen, C. Chang-Hasnain, N. G. Stoffel, J. P. Harbison, J. P. Florez, E. Clausen, and J. E. Jewell, "Vertical-cavity surface-emitting

InGaAs/GaAs lasers with planar lateral definition," *Appl. Phys. Lett.*, vol. 56, pp. 2384–2386, 1990.

[11] B. Tell, Y. H. Lee, K. F. Brown-Goebeler, J. L. Jewell, R. E. Leibenguth, M. T. Asom, G. Livescu, L. Luther, and V. D. Mattera, "High-power CW vertical-cavity top surface-emitting GaAs quantum well lasers," *Appl. Phys. Lett.*, vol. 57, pp. 1855–1857, 1990.

[12] D. Kuchta, A. Rylyakov, F. Doany, C. Schow, J. Proesel, C. Baks, P. Westbergh, J. Gustavsson, and A. Larsson, "A 71 Gb/s NRZ modulated 850 nm VCSEL-based optical link," *IEEE Photon. Technol. Lett.*, vol. 27, no. 6, pp. 577–580, 2015.

[13] M. Müller, W. Hofmann, T. Gründl, M. Horn, W. P, R. Nagel, E. Roenneberg, G. Böhm, D. Bimberg, and M.-C. Amann, "1550-nm high-speed short-cavity VCSELs," *IEEE J. Sel. Topics Quantum Electron.*, vol. 17, no. 5, pp. 1158–1166, 2011.

[14] Y. Rao, W. Yang, C. Chase, M. Huang, D. Worland, S. Khaleghi, M. Chitgarha, M. Ziyadi, A. Willner, and C. Chang-Hasnain, "Long-wavelength VCSEL using high-contrast grating," *J. Sel. Topics Quantum Electron.*, vol. 19, no. 4, p. 1701311, 2013.

[15] C. Gierl, T. Gruendl, P. Debernardi, K. Zogal, C. Grasse, H. A. Davani, G. Böhm, S. Jatta, F. Küppers, P. Meissner, and M.-C. Amann, "Surface micromachined tunable 1.55 μm-VCSEL with 102 nm continuous single-mode tuning," *Opt. Express*, vol. 19, no. 18, pp. 17336–17343, 2011.

[16] S. Paul, C. Gierl, J. Cesar, M. Malekizandi, C. Neumeyr, M. Ortsiefer, and F. Küppers, "10-Gb/s direct modulation of widely tunable 1550-nm MEMS VCSEL," *IEEE J. Sel. Top. Quantum Electron.*, vol. 21, no. 6, pp. 436–443, 2015.

[17] H. Li, D. Phillips, X. Wang, Y. Ho, L. Chen, X. Zhou, J. Zhu, S. Yu, and X. Cai, "Orbital angular momentum vertical-cavity surface-emitting lasers," *Optica*, vol. 2, no. 6, pp. 547–552, 2015.

[18] K. Grobe, M. H. Eiselt, S. Pachnicke, and J.-P. Elbers, "Access networks based on tunable lasers," *J. Lightwave Technol.*, vol. 32, no. 16, pp. 2815–2823, 2014.

[19] B. Kögel, H. Halbritter, S. Jatta, M. Maute, G. Bohm, M. C. Amann, M. Lackner, M. Schwarzott, F. Winter, and P. Meissner, "Simultaneous spectroscopy of NH_3 and CO using a >50 nm continuously tunable MEMS-VCSEL," *IEEE Sensors Journal*, vol. 7, no. 11, pp. 1483–1489, 2007.

[20] V. Jayaraman, D. D. John, C. Burgner, M. E. Robertson, B. Potsaid, J. Y. Jiang, T. H. Tsai, W. Choi, C. D. Lu, P. J. S. Heim, J. G. Fujimoto, and A. E. Cable, "Recent advances in MEMS-VCSELs for high performance structural and functional SS-OCT imaging," in *Proc. SPIE*, vol. 8934, pp. 8934 – 8934 – 11, 2014.

[21] B. V. Hoe, G. Lee, E. Bosman, J. Missinne, S. Kalathimekkad, O. Maskery, D. J. Webb, K. Sugden, P. V. Daele, and G. V. Steenberge, "Ultra small integrated optical fiber sensing system," *Sensors*, vol. 33, no. 16, pp. 12052–12069, 2017.

[22] K. Benjamin, *Mikromechanisch weit abstimmbare Oberflaechen-emittierende Laserdioden für Sensoranwendungen.* German dissertation, Technische Universität Darmstadt, Darmstadt, 2014.

[23] M. T. Haidar, S. Preu, S. Paul, A. E. C. Gierl, J. Cesar, and F. Küppers, "Widely tunable telecom MEMS-VCSEL for terahertz photomixing," *Opt. Lett.*, vol. 40, no. 9, pp. 4428–4431, 2015.

[24] B. Behroozpour, N. Quack, P. Sandborn, S. Gerke, W. Yang, C. Chang-Hasnain, M. C. Wu, and B. E. Boser, "Method for increasing the operating distance of MEMS LIDAR beyond brownian noise limitation," in *2014 Conference on Lasers and Electro-Optics (CLEO) - Laser Science to Photonic Applications*, pp. 1–2, 2014.

[25] A. Caliman, A. Mereuta, G. Suruceanu, V. Iakovlev, A. Sirbu, and E. Kapon, "8 mW fundamental mode output of wafer-fused VCSELs emitting in the 1550-nm band," *Opt. Express*, vol. 19, no. 18, pp. 16996–17001, 2011.

[26] K. Zogal, S. Paul, C. Gierl, P. Meissner, and F. Küppers, "Up to 12-Gbps transmission over 6.3-km SMF using a directly modulated bulk micromachined MEMS tunable VCSEL," in *2015 European Conference on Optical Communication (ECOC)*, pp. 1–3, Sept 2015.

[27] H. Sano, A. Matsutani, and F. Koyama, "Athermal and tunable operations of 850 nm VCSEL with thermally actuated cantilever structure," in *35th European Conference on Optical Communication, ECOC*, (Vienna, Austria), pp. 1–2, 2009.

[28] V. Jayaraman, G. D. Cole, M. Robertson, A. Uddin, and A. Cable, "High-sweep-rate 1310 nm MEMS-VCSEL with 150 nm continuous tuning range," *Electron. Lett.*, vol. 48, no. 14, pp. 867–869, 2012.

[29] T. Pfeiffer, "Next generation mobile fronthaul and midhaul architectures," *IEEE/OSA Journal of Optical Communications and Networking*, vol. 7, pp. B38–B45, November 2015.

[30] M. H. Eiselt, "Remotely controllable WDM-PON technology for wireless fronthaul/backhaul application," in *Proc. OECC*, p. ThA3, 2016.

[31] J. Gutiérrez, N. Maletic, D. Camps-Mur, E. García, I. Berberana, M. Anastasopoulos, A. Tzanakaki, V. Kalokidou, P. Flegkas, D. Syrivelis, T. Korakis, P. Legg, D. Markovic, G. Lyberopoulos, J. Bartelt, J. K. Chaudhary, M. Grieger, N. Vucic, J. Zou, and E. Grass, "5G-XHaul: a converged optical and wireless solution for 5G transport networks," *Transactions on Emerging Telecommunications Technologies*, vol. 27, no. 9, pp. 1187–1195, 2016.

[32] N. Bozinovic, Y. Yue, Y. Ren, M. Tur, P. Kristensen, H. Huang, A. E. Willner, and S. Ramachandran, "Terabit-scale orbital angular momentum mode division multiplexing in fibers," *Science*, vol. 340, pp. 1545–1548, 2013.

[33] A. E. Willner, H. Huang, Y. Yan, Y. Ren, N. Ahmed, G. Xie, C. Bao, L. Li, Y. Cao, Z. Zhao, J. Wang, M. P. J. Lavery, M. Tur, S. Ramachandran, A. F. Molisch, N. Ashrafi, and S. Ashrafi, "Optical communications using orbital angular momentum beams," *Adv. Opt. Photon.*, vol. 7, pp. 66–106, Mar 2015.

[34] A. Jesacher, C. Maurer, A. Schwaighofer, S. Bernet, and M. Ritsch-Marte, "Near-perfect hologram reconstruction with a spatial light modulator," *Opt. Express*, vol. 16, pp. 2597–2603, 2008.

[35] M. W. Beijersbergen, R. P. C. Coerwinkel, M. Kristensen, and J. P. Woerdman, "Helical-wavefront laser beams produced with a spiral phaseplate," *Opt. Commun.*, vol. 112, no. 5, pp. 321–327, 1994.

[36] A. Turnbull, D. A. Roberson, G. M. Smith, L. Allen, and M. J. Padgett, "Generation of free-space Laguerre-Gaussian modes at millimetre-wave frequencies by use of a spiral phaseplate," *Opt. Commun.*, vol. 127, no. 5, pp. 183–188, 1996.

[37] S. Paul, V. S. Lyubopytov, M. F. Schumann, J. Cesar, A. Chipouline, M. Wegener, and F. Küppers, "Wavelength-selective orbital-angular-momentum beam generation using MEMS tunable Fabry-Perot filter," *Opt. Lett.*, vol. 41, pp. 3249–3252, Jul 2016.

[38] V. S. Lyubopytov, A. P. Porfirev, S. O. Gurbatov, S. Paul, M. F. Schumann, J. Cesar, M. Malekizandi, M. T. Haidar, M. Wegener, A. Chipouline, and F. Küppers, "Simultaneous wavelength and orbital angular momentum demultiplexing using tunable MEMS-based Fabry-Perot filter," *Opt. Express*, vol. 25, pp. 9634–9646, May 2017.

[39] N. Hodgson and H. Weber in *Laser Resonators and Beam Propagation*, Berlin, Germany: Springer-Verlag, 2005.

[40] C. Gierl, *Mikromechanisch weit abstimmbare oberflaechen-emittierende Laser mit Vertikalresonator*. German. dissertation, Technische Universität Darmstadt, Darmstadt, 2014.

[41] K. J. Ebeling, "Integrated optoelectronics," Berlin, Germany: Springer-Verlag, 2005.

[42] D. M. Kuchta, F. E. Doany, L. Schares, C. Neumeyr, A. Daly, B. Kögel, and J. R. M. Ortsiefer, "Error-free 56 Gb/s NRZ modulation of a 1530 nm VCSEL link," 2015.

[43] R. Olshansky, P. Hill, V. Lanzisera, and W. Powazniak, "Frequency response of 1.3 μm InGaAsP high speed quantum-well semiconductor lasers," *IEEE J. Quantum Electron.*, vol. 23, pp. 1410–1418, 1987.

[44] A. Kern, *Monolithically integrated transceiver chips for bidirectional optical data transmission*. Dissertation, Universität Ulm, Ulm, 2015.

[45] M. S. R. Allen, L.; Beijersbergen and J. Woerdman, "Orbital angular momentum of light and the transformation of Laguerre-Gaussian laser modes," *Phys. Rev. A*, vol. 45, pp. 8185–8189, 1992.

[46] C. H. Schmitz, K. Uhrig, J. P. Spatz, and J. E. Curtis, "Tuning the orbital angular momentum in optical vortex beams," *Opt Express*, vol. 14, no. 15, pp. 6604–12, 2006.

[47] G. Gibson, J. Courtial, M. J. Padgett, M. Vasnetsov, V. Pasko, S. M. Barnett, and S. Franke-Arnold, "Free-space information transfer using light beams carrying orbital angular momentum," *Opt. Express*, vol. 12, pp. 5448–5456, Nov 2004.

[48] J. E. Curtis and D. G. Grier, "Structure of optical vortices," *Phys. Rev. Lett.*, vol. 90, p. 133901, 2003.

[49] A. Nicolas, L. Veissier, L. Giner, E. Giacobino, D. Maxein, and J. Laurat, "A quantum memory for orbital angular momentum photonic qubits," *Nat. Photon.*, vol. 8, pp. 234–238, 2014.

[50] A. Mair, A. Vaziri, G. Weihs, and A. Zeilinger, "Entanglement of the orbital angular momentum states of photons," *Nature*, vol. 412, pp. 313–316, 2001.

[51] M. Dienerowitz, M. Mazilu, P. J. Reece, T. F. Krauss, and K. Dholakia, "Optical vortex trap for resonant confinement of metal nanoparticles," *Opt. Express*, vol. 16, pp. 4991–4999, Mar 2008.

[52] M. Gecevičius, R. Drevinskas, M. Beresna, and P. G. Kazansky, "Single beam optical vortex tweezers with tunable orbital angular momentum," *Appl. Phys. Lett.*, vol. 104, p. 231110, 2014.

[53] M. R. Dennis, R. P. King, B. Jack, K. O'Holleran, and M. J. Padgett, "Isolated optical vortex knots," *Nature Physics*, vol. 6, pp. 118–121, 2010.

[54] G. Foo, D. M. Palacios, and J. G. A. Swartzlander, "Optical vortex coronagraph," *Opt. Lett.*, vol. 30, pp. 308–3310, 2005.

[55] S. Fuerhapter, A. Jesacher, S. Bernet, and M. Ritsch-Marte, "Spiral interferometry," *Opt. Lett.*, vol. 30, pp. 1953–1955, 2005.

[56] S. Fürhapter, A. Jesacher, S. Bernet, and M. Ritsch-Marte, "Twisting of light around rotating black holes," *Nat. Phys.*, vol. 7, pp. 195–197, 2011.

[57] D. S. Simon and A. V. Sergienko, "Two-photon spiral imaging with correlated orbital angular momentum states," *Nat. Photon.*, vol. 85, no. 4, p. 043825, 2012.

[58] N. R. Heckenberg, R. McDuff, C. P. Smith, and A. White, "Generation of optical phase singularities by computer-generated holograms," *Opt. Lett.*, vol. 17, pp. 221–223, 1992.

[59] R. K. Tyson, M. Scipioni, and J. Viegas, "Generation of an optical vortex with a segmented deformable mirror," *Appl. Opt.*, vol. 47, pp. 6300–6306, 2008.

[60] G. Ruffato, M. Massari, and F. Romanato, "Compact sorting of optical vortices by means of diffractive transformation optics," *Opt. Lett.*, vol. 42, no. 3, pp. 551–554, 2017.

[61] W. Chen and Q. Zhan, "Realization of an evanescent Bessel beam via surface plasmon interference excited by a radially polarized beam," *Opt. Lett.*, vol. 34, pp. 722–724, 2009.

[62] F. Bouchard, H. Mand, M. Mirhosseini, E. Karimi, and R. W. Boyd, "Achromatic orbital angular momentum generator," *New J. Phys.*, vol. 16, p. 123006, 2014.

[63] G. Biener, A. Niv, V. Kleiner, and E. Hasman, "Formation of helical beams by use of Pancharatnam-Berry phase optical elements," *Opt. Lett.*, vol. 27, pp. 1875–1877, 2002.

[64] L. Marrucci, C. Manzo, and D. Paparo, "Optical spin-to-orbital angular momentum conversion in inhomogeneous anisotropic media," *Phys. Rev. Lett.*, vol. 96, p. 163905, 2006.

[65] X. Cai, J. Wang, M. J. Strain, B. Johnson-Morris, M. S. J. Zhu, J. L. O'Brien, M. G. Thompson, and S. Yu, "Integrated compact optical vortex beam emitters," *Science*, vol. 338, p. 363–366, 2012.

[66] M. Schumann, T. Buckmann, N. Gruhler, M. Wegener, and W. Pernice, "Hybrid 2D-3D optical devices for integrated optics by direct laser writing," *Light Sci. Appl.*, vol. 3, p. e175, 2014.

[67] M. Ortsiefer, W. Hofmann, J. Rosskopf, and M.-C. Amann, "Long-Wavelength VCSELs with Buried Tunnel Junction," in *VCSELs: Fundamentals, Technology and Applications of Vertical-Cavity Surface-Emitting Lasers* (R. Michalzik, ed.), ch. 8, pp. 321–351, Berlin, Heidelberg: Springer Berlin Heidelberg, 2013.

[68] G. R. Hadley, "Effective index model for vertical-cavity surface-emitting lasers," *Opt. Lett.*, vol. 20, pp. 1483–1485, 1995.

[69] C. Grasse, M. Müller, G. Boehm, R. Enzmann, Y. Xu, M. Goerblicha, R. Meyer, M. Ortsiefer, and M.-C. Amann, "Planarization of overgrown tunnel junctions for InP-based VCSEL by MOVPE," in *Eur. Workshop Metalorgan. Vapor Phase Epitaxy*, (Ulm, Germany), 2009.

[70] T. Gruendl, K. Zogal, M.Mueller, R.Nagel, S. Jatta, K. Geiger, C. Grasse, G. Boehm, M. Ortsiefer, P. Meissner, and M.-C. Amann, "High-speed and high-power vertical-cavity surface-emitting lasers based on InP suitable for telecommunication and gas sensing," 2010.

[71] P. Debernardi, B. Kögel, K. Zogal, P. Meissner, M. Maute, M. Ortsiefer, and G. Böhm, "Modal properties of long-wavelength tunable MEMS-VCSELs with curved mirrors: comparison of experiment and modeling," *IEEE J. Sel. Topics Quantum Electron.*, vol. 44, no. 4, pp. 391–399, 2008.

[72] S. M. Jatta, "Plasmaunterstützte Abscheidung von dielektrischen Schichten zur Entwicklung von mikromechanisch abstimmbaren optischen Komponenten," Darmstadt: Phd Thesis, TU Darmstadt, 2011.

[73] P. Debernardi, B. Kögel, K. Zogal, P. Meissner, M. Maute, M. Ortsiefer, and G. Böhm, "Modal properties of long-wavelength tunable MEMS-VCSELs with curved mirrors: comparison of experiment and modeling," *IEEE J. Sel. Topics Quantum Electron.*, vol. 44, no. 4, pp. 391–399, 2008.

[74] C. Gierl, T. Gründl, S. Paul, K. Zogal, M. T. Haidar, P. Meissner, M.-C. Amann, and F. Küppers, "Temperature characteristics of surface micromachined MEMS-VCSEL with large tuning range," *Opt. Express*, vol. 22, no. 11, pp. 13063–13072, 2014.

[75] P. Tayebati, P. Wang, D. Vakhshoori, C.-C. Lu, M. Azimi, and R. N. Sacks, "Half-symmetric cavity tunable microelectromechanical VCSEL with single spatial mode," *Photon. Technol. Lett.*, vol. 10, no. 12, pp. 1679–1681, 1998.

[76] B. Kögel, M. Maute, H. Halbritter, F. Riemenschneider, G. Böhm, M.-C. Amann, and P. Meissner, "Long-wavelength MEMS tunable vertical-cavity surface-emitting lasers with high sidemode suppression," *Journal of Optics A: Pure and Applied Optics*, vol. 8, no. 7, p. S370, 2006.

[77] H. Halbritter, C. Sydlo, B. Koegel, F. Riemenschneider, H. L. Hartnagel, and P. Meissner, "Impact of micromechanics on the linewidth and chirp performance of MEMS-VCSELs," *IEEE J. Sel. Topics Quantum Electron.*, vol. 13, no. 2, pp. 367–373, 2007.

[78] Y. C. Chung and Y. H. Lee, "Spectral characteristics of vertical-cavity surface-emitting lasers with external optical feedback," *IEEE Photon. Technol. Lett.*, vol. 3, no. 7, pp. 597–599, 1991.

[79] S. Paul, C. Gierl, T. Gruendl, K. Zogal, P. Meissner, M.-C. Amann, and F. Kueppers, "Far-field emission characteristics and linewidth measurements of surface micro-machined MEMS tunable VCSELs," in *Proc. SPIE 8639, Vertical-Cavity Surface-Emitting Lasers XVII, 86390H*, pp. 1–2, Feb 2013.

[80] Y. Huang, S. Arai, and K. Komori, "Theoretical linewidth enhancement factor alpha of Ga/sub 1xx/In/sub x/As/GaInAsP/InP strained-quantum-well structures," *IEEE Photon. Technol. Lett.*, vol. 5, no. 2, pp. 142–145, 1993.

[81] S. L. Chuang, "Physics of photonic devices," Wiley Series in Pure and Applied Optics, ch. 13, pp. 639–666, Hoboken, NJ, USA: John Wiley & Sons, 2009.

[82] M. San Miguel, Q. Feng, and J. V. Moloney, "Light-polarization dynamics in surface-emitting semiconductor lasers," *Phys. Rev. A*, vol. 52, pp. 1728–1739, Aug 1995.

[83] S. W. Corzine, R.-H. Yan, and L. A. Coldren, "Chapter 1 - Optical Gain in iii–v Bulk and Quantum Well Semiconductors," in *Quantum Well Lasers* (P. S. Zory, ed.), pp. 17–96, San Diego: Academic Press, 1993.

[84] R. F. M. Hendriks, M. P. van Exter, J. P. Woerdman, A. van Geelen, L. Weegels, K. H. Gulden, and M. Moser, "Electro-optic birefringence in semiconductor vertical-cavity lasers," *Appl. Phys. Lett.*, vol. 71, no. 18, pp. 2599–2601, 1997.

[85] A. K. J. van Doorn, M. P. van Exter, and J. P. Woerdman, "Strain-induced birefringence in vertical-cavity semiconductor lasers," *IEEE J. Quantum Electron.*, vol. 34, pp. 700–706, 1998.

[86] F. M. di Sopra, M. Brunner, and R. Hövel, "Polarization control in strained T-bar VCSELs," *IEEE Photon. Technol. Lett.*, vol. 14, pp. 1034–1036, Aug 2002.

[87] C. Degen, I. Fischer, W. Elsäßer, L. Fratta, P. Debernardi, G. P. Bava, M. Brunner, R. Hövel, M. Moser, and K. Gulden, "Transverse modes in thermally detuned oxide-confined vertical-cavity surface-emitting lasers," *Phys. Rev. A*, vol. 63, p. 023817, Jan 2001.

[88] S. Balle, E. Tolkachova, M. S. Miguel, J. R. Tredicce, J. Martín-Regalado, and A. Gahl, "Mechanisms of polarization switching in single-transverse-mode vertical-cavity surface-emitting lasers: thermal shift and nonlinear semiconductor dynamics," *Opt. Lett.*, vol. 24, pp. 1121–1123, Aug 1999.

[89] M. P. van Exter, R. F. M. Hendriks, and J. P. Woerdman, "Physical insight into the polarization dynamics of semiconductor vertical-cavity lasers," *Phys. Rev. A*, vol. 57, pp. 2080–2090, Mar 1998.

[90] A. Molitor, S. Hartmann, and W. Elsaesser, "Stokes vector characterization of the polarization behavior of vertical cavity surface emitting lasers," *Opt. Lett.*, vol. 37, no. 22, pp. 4799–4801, 2012.

[91] H. G. Berry, G. Gabrielse, and A. E. Livingston, "Measurement of the Stokes parameters of light," *Appl Opt.*, vol. 16, no. 12, pp. 3200–3205, 1977.

[92] B. Schaefer, E. Collett, R. Smyth, D. Barrett, and B. Fraher, "Measuring the Stokes polarization parameters," *Am. J. Phys*, vol. 75, no. 2, pp. 163–168, 2007.

[93] W. Hofmann, M. Müller, A. Nadtochiy, C. Meltzer, A. Mutig, G. Böhm, J. Rosskopf, D. Bimberg, M.-C. Amann, and C. Chang-Hasnain, "22-Gb/s long wavelength VCSELs," *Opt. Express*, vol. 17, pp. 17547–17554, Sep 2009.

[94] C. Wagner, J. Zou, M. Ortsiefer, C. Greus, C. Neumeyr, K. Grobe, M. Eiselt, S. Paul, J. Cesar, F. Küppers, J. J. V. Olmos, and I. T. Monroy, "Full C-band tunable MEMS-VCSEL for next generation G.metro mobile front- and

backhauling," in *2017 Optical Fiber Communications Conference and Exhibition (OFC)*, pp. 1–3, March 2017.

[95] S. Pachnicke, J. Zhu, M. Lawin, A. Wonfor, M. Eiselt, R. Cush, R. Turner, P. Firth, M. Wale, R. V. Penty, I. H. White, and J. P. Elbers, "Novel WDM-PON system with shared wavelength locking and full C-band tunability," in *Photonic Networks; 15. ITG Symposium*, pp. 1–5, May 2014.

[96] A. Gatto, P. Parolari, C. Neumeyr, and P. Boffi, "Beyond 25 Gb/s directly-modulated widely tunable VCSEL for next generation access network," in *Optical Fiber Communication Conference*, p. Th1E.2, Optical Society of America, 2018.

[97] M. S. Moreolo, L. Nadal, J. M. Fabrega, F. J. Vilchez, R. Casellas, R. M. noz, C. Neumeyr, A. Gatto, P. Parolari, and P. Boffi, "Modular SDN-enabled S-BVT adopting widely tunable MEMS VCSEL for flexible/elastic optical metro networks," in *Optical Fiber Communication Conference*, p. M1A.7, Optical Society of America, 2018.

[98] J. Hayden, P. Martín-Mateos, P. Acedo, and B. Lendl, "A quantitative comparison of dispersion- and absorption-spectroscopic gas sensing," 2017.

[99] J. Reid, J. Shewchun, B. K. Garside, and E. A. Ballik, "High sensitivity pollution detection employing tunable diode lasers," *Appl. Opt.*, vol. 17, pp. 300–307, Jan 1978.

[100] P. Martín-Mateos and P. Acedo, "Heterodyne phase-sensitive detection for calibration-free molecular dispersion spectroscopy," *Opt. Express*, vol. 22, pp. 15143–15153, Jun 2014.

[101] D. Roschdestwensky, "Anomale dispersion im natriumdampf," *Ann. Phys.*, vol. 344, no. 12, pp. 307–345, 1912.

[102] P. Martín-Mateos, J. Hayden, P. Acedo, and B. Lendl, "Heterodyne phase-sensitive dispersion spectroscopy in the mid-infrared with a quantum cascade laser," *Analytical Chemistry*, vol. 89, no. 11, pp. 5916–5922, 2017. PMID: 28480710.

[103] M. Tonouchi, "Cutting-edge terahertz technology," *Nat. Photonics*, vol. 1, pp. 97–105, 2007.

[104] A. Y. Pawar, D. D. Sonawane, K. B. Erande, and D. V. Derle, "Terahertz technology and its applications," *Drug Invention Today*, vol. 5, no. 2, pp. 157 – 163, 2013.

[105] S. Preu, G. H. Döhler, S. Malzer, L. J. Wang, and A. C. Gossard, "Tunable, continuous-wave terahertz photomixer sources and applications," *Journal of Applied Physics*, vol. 109, no. 6, p. 061301, 2011.

[106] A. J. Deninger, A. Roggenbuck, S. Schindler, and S. Preu, "2.75 THz tuning with a triple-DFB laser system at 1550 nm and InGaAs photomixers," *Journal of Infrared, Millimeter, and Terahertz Waves*, vol. 36, pp. 269–277, Mar 2015.

[107] M. T. Haidar, S. Preu, J. Cesar, S. Paul, A. S. Hajo, C. Neumeyr, H. Maune, and F. Küppers, "Systematic characterization of a 1550 nm microelectromechanical (MEMS) tunable vertical cavity surface emitting laser (VCSEL) with 7.92 THz tuning range for terahertz photomixing systems," *J. Appl. Phys.*, vol. 123, no. 2, p. 023106, 2018.

[108] I. Kaminow, T. Li, and A. E. Willner, *Optical Fiber Telecommunications Volume VIB, Sixth Edition: Systems and Networks*. Academic Press, 6th ed., 2013.

[109] J. Petrilla, "100G SR4 and RS (528, 514, 7, 10) FEC," tech. rep., Avago Technologies, 2012.

[110] "IEEE standard for ethernet - amendment 3: physical layer specifications and management parameters for 40 Gb/s and 100 Gb/s operation over fiber optic cables," tech. rep., IEEE 802.3bm-2015, 2015.

[111] V. S. Lyubopytov, A. P. Porfirev, S. O. Gurbatov, S. Paul, M. F. Schumann, J. Cesar, M. Malekizandi, M. T. Haidar, M. Wegener, A. Chipouline, and F. Küppers, "Simultaneous wavelength and orbital angular momentum demultiplexing using tunable MEMS-based Fabry-Perot filter," *Opt. Express*, vol. 25, pp. 9634–9646, May 2017.

[112] Q. Le, D. Briggmann, , and F. Küppers, "Generation of UWB pulses using direct modulation of semiconductor laser and optical filtering," *Electron. Lett.*, vol. 49, pp. 1171–1173, August 2013.

[113] C. Gierl, Q. T. Le, C. Damm, and F. Küppers, "Generation of uwb pulses utilizing directly modulated tunable MEMS-VCSEL," in *2015 IEEE Topical Conference on Wireless Sensors and Sensor Networks (WiSNet)*, pp. 41–43, Jan 2015.

[114] C. Gierl, K. Zogal, S. Paul, and F. Küppers, "Tunable MEMS-VCSEL with 140-nm tuning range using tuning range using SiO/SiC-based MEMS-DBR," 2014.

Publications

Journals

1. **S. Paul**, P. M.-Mateos, N. Heermeier, F. Küppers, and P. Acedo, "Multispecies heterodyne phase sensitive dispersion spectroscopy over 80 nm using a MEMS-VCSEL," *ACS Photonics*, vol. 4, no. 11, pp. 2664-−668, Oct. 2017.

2. **S. Paul**, V. Lyubopytov, M. Schumann, A. Chipouline, J. Cesar, A. Chipouline, M. Wegener, and F. Küppers, "Wavelength-selective orbital angular momentum beam generation using MEMS tunable Fabry-Perot filter," **(Editor's Pick)**, *Optics Letters*, vol. 48, no. 7, pp. 394−396, Jul. 2016.

3. **S. Paul**, M. T. Haidar, J. Cesar, M. Malekizandi, B. Kögel, C. Neumeyr, M. Ortsiefer, and F. Küppers, "Far-field, linewidth and thermal characteristics of a high-speed 1550-nm MEMS tunable VCSEL," *Optics Express*, vol. 24, no. 12, pp. 394−396, May 2016.

4. **S. Paul**, C. Gierl, J. Cesar, Q. T. Le, M. Malekizandi, B. Kögel, C. Neumeyr, M. Ortsiefer, and F. Küppers, "10-Gb/s direct modulation of widely tunable 1550-nm MEMS VCSEL," *IEEE Journal of Selected Topics in Quantum Electronics*, vol. 21, no. 6, pp. 394−396, Nov 2015.

5. M. T. Haidar, S. Preu, J. Cesar, **S. Paul**, A. Hajo, H. Maune, C. Neumeyr, and F. Küppers, "Systematic characterization of a 1550 nm microelectromechanical (MEMS)-tunable vertical-cavity surface-emitting laser (VCSEL) with 7.92 THz tuning range for terahertz photomixing systems," **(Featured Article)**, *Journal of Applied Physics*, vol. 123, no. 2, p. 023106, Jan. 2018.

6. C. Wagner, A. Dochhan, M. H. Eiselt, K. Grobe, M. Ortsiefer, C. Gréus, C. Neumeyr, **S. Paul**, J. Cesar, F. Küppers, J. J. V. Olmos, and I. T. Monroy, "26-Gbps

DMT transmission using full C-band tunable VCSEL for converged PONs," *IEEE Photonics Technology Letters*, vol. 29, no. 17, pp. 1058−13072, Jun. 2017.

7. V. Lyubopytov, A. P. Porfirev, S. O. Gurbatov, **S. Paul**, M. F. Schumann, J. Cesar, M. Malekizandi, M. T. Haidar, M. Wegener, A. Chipouline, and F. Küppers, "Simultaneous wavelength and orbital angular momentum demultiplexing using tunable MEMS-based Fabry-Perot filter," *Optics Express*, vol. 25, no. 9, pp. 394−396, Mar. 2017.

8. M. T. Haidar, S. Preu, **S. Paul**, C. Gierl, J. Cesar, A. Emsia, and F. Küppers, "Widely tunable telecom MEMS-VCSEL for terahertz photomixing," *Optics Letters*, vol. 40, no. 9, pp. 4428−4431, Sep. 2015.

9. C. Gierl, T. Gründl, **S. Paul**, K. Zogal, M. T. Haidar, P. Meissner, M.-C. Amann, and F. Küppers, "Temperature characteristics of surface micromachined MEMS-VCSEL with large tuning range," *Optics Express*, vol. 22, no. 11, pp. 13063−13072, Jun. 2014.

10. A. Kern, **S. Paul**, D. Wahl, A. A.-Samaneh, R. Michalzik, "Single-fiber bidirectional optical data links with monolithic transceiver chips," *Advances in Optical Technologies*, vol. 2012, no. 18, pp. 13063−13072, Sep. 2011.

11. A. Kern, **S. Paul**, W. Schwarz, D. Wahl, R. Blood, R. Michalzik, "Bidirectional multimode fiber interconnection at Gb/s data rates with monolithically integrated VCSEL–PIN transceiver chips," *IEEE Photonics Technology Letters*, vol. 23, no. 15, pp. 1058−13072, Sep. 2011.

Conference Proceedings

12. **S. Paul**, J. Cesar, M. Malekizandi, M. T. Haidar, C. Neumeyr, M. Ortsiefer, and F. Küppers, "Towards a SFP+ module for WDM applications using an ultra-widely-tunable high-speed MEMS-VCSEL," in Vertical-Cavity Surface-Emitting Lasers XXI, Kent D. Choquette; Chun Lei, Editors, Proceedings of SPIE Vol. 10122 (SPIE, Bellingham, WA 2017), 1012209.

13. **S. Paul**, V. S. Lyubopytov, M. F. Schumann, J. Cesar, M. Malekizandi, M. T. Haidar, A. P. Porfirev, S. O. Gurbatov, M. Wegener, A. Chipouline, F. Küppers, "Vortex-MEMS filters for wavelength-selective orbital angular momentum beam generation," in Complex Light and Optical Forces XI, David L. Andrews; Enrique

J. Galvez; Jesper Glückstad, Editors, Proceedings of SPIE Vol. 10120 (SPIE, Bellingham, WA 2017), 101200G.

14. **S. Paul**, J. Cesar, M. T. Haidar, M. Malekizandi, M. Ortsiefer, B. Kögel, C. Neumeyr, F. Küppers, "Thermal characteristics, linewidth and far-field measurements of high-speed widely-tunable MEMS-VCSEL," in European VCSEL Day 2016, Darmstadt, Germany, 2016.

15. **S. Paul**, J. Cesar, M. T. Haidar, C. Gierl, B. Koegel, C. Neumeyr, M. Ortsiefer, F. Küppers, "Ultra wide mode-hop free tuning around 1550-nm telecom wavelength using high-speed MEMS-VCSELs **(Best Paper Award)**," in 20th Microoptics Conference 2015 (MOC '15), Fukuoka International Congress Center, Fukuoka, Japan, 2015.

16. **S. Paul**, K. Zogal, C. Gierl, P. Meissner, F. Küppers, "Up to 12-Gbps transmission over 6.3-km SMF using a directly modulated bulk micromachined MEMS tunable VCSEL," in European Conference on Optical Communication (ECOC), Valencia, Spain, 2015.

17. **S. Paul**, C. Gierl, J. Cesar, F. Küppers, B. Kögel, J. Rosskopf, M. Görblich, Y. Xu, C. Neumeyr, M. Ortsiefer, "7-GHz Small-signal Modulation Response of a Surface micromachined BCB MEMS VCSEL with $>$ 50-nm continuous tuning," in CLEO/Europe-EQEC 2015, Munich, Germany, 2015.

18. **S. Paul**, C. Gierl, J. Cesar, Q. T. Le, M. Malekizandi, F. Kueppers, B. koegel, J. Rosskopf, C. Gréus, M. Görblich, Y. Xu, C. Neumeyr, M. Ortsiefer, "High speed surface micromachined MEMS tunable VCSEL for telecom wavelengths," in Conference on Lasers and Electro-Optics (CLEO), San Jose, CA, USA, 2015.

19. **S. Paul**, C. Gierl, A. Molitor, Franko Küppers, "Stokes parameters of 1550 nm MEMS tunable VCSEL," in European VCSEL Day 2014, Rennes, France, 2014.

20. **S. Paul**, C. Gierl, T. Gründl, K. Zogal, P. Meissner, M.-C. Amann, F. Küppers, "Far-field emission characteristics and linewidth measurements of surface micromachined MEMS tunable VCSELs," in Vertical-Cavity Surface-Emitting Lasers XVII, Kent D. Choquette; James Guenter, Editors, Proceedings of SPIE Vol. 8639 (SPIE, Bellingham, WA 2013), 86390H.

21. **S. Paul**, C. Gierl, K. Zogal, P. Meissner, F. Küppers, "Widely tunable surface micro-machined MEMS VCSELs in the range of 1.55 and 1.95 μm," in European VCSEL Day 2012, Berlin, Germany, 2012.

22. J. Cesar, **S. Paul**, and M. T. Haidar, B. Corbett, A. Chipouline, F. Küppers, "Surface micromachined MEMS-tunable PIN-photodiodes around 1550-nm," in Conference on Lasers and Electro-Optics (CLEO), San Jose, CA, USA, 2017.

23. M. Ortsiefer, C. Gréus, J. Rosskopf, **S. Paul**, J. Cesar, C. Neumeyr, F. Kueppers, "Ultra wide mode hop free tuning of long-wavelength MEMS VCSELs **(Post Deadline Paper)**," in 3rd International Workshop on Infrared Technologies, Olching, Germany, 2016.

24. T. Haidar, E. Polat, **S. Paul**, C. Gierl, J. Cesar, A. Chipouline, F. Küppers, "Tunable semiconductor fiber ring laser with Integrated MEMS-Tunable Fabry-Perot Filter," in CLEO 2016 - Conference on Lasers and Electro-Optics, San Jose, California, USA, 2016.

25. J. Cesar, **S. Paul**, F. Küppers, B. Kögel, C. Gréus, C. Neumeyr, M. Ortsiefer, I. Ibrahim, J. Schmidt, M. Eiselt, "Weit abstimmbare Sender (MEMS-VCSEL) bei 1550 nm für photonische Netze.," in 17. ITG-Fachtagung Photonische Netze 2016, Leibzig, Germany, 2016.

26. J. Cesar, **S. Paul**, F. Küppers, T. Kusserow, "SiC-SiO_2 MEMS-DBR based widely tunable optical filters around 1550 nm with narrow FWHM," in CLEO/Europe-EQEC 2019, Munich, Germany, 2019.

27. C. Gierl, K. Zogal, **S. Paul**, F. Küppers, "Tunable MEMS-VCSEL with >140-nm tuning range using tuning range using SiO_2/SiC-based MEMS-DBR," in Vertical-Cavity Surface-Emitting Lasers XVIII, James Guenter; Chun Lei, Editors, Proceedings of SPIE Vol. 9001 (SPIE, Bellingham, WA 2014), 900107.

28. C. Gierl, T. Gründl, K. Zogal, **S. Paul**, C. Grasse, G. Böhm, P. Meissner, M.-C. Amann, and F. Küppers, "Widely tunable MEMS-VCSELs operating at $>70\,^{\circ}$C," in Vertical-Cavity Surface-Emitting Lasers XVII, Kent D. Choquette; James Guenter, Editors, Proceedings of SPIE Vol. 8639 (SPIE, Bellingham, WA 2013), 86390G.

29. K. Zogal, T. Gruendl, C. Gierl, **S. Paul**, C. Grasse, P. Meissner, M.-C. Amann, F. Küppers, "Widely tunable singlemode surface micro-machined MEMS-VCSELs operating at 1.95 μm," in Vertical-Cavity Surface-Emitting Lasers XVII, Kent D. Choquette; James Guenter, Editors, Proceedings of SPIE Vol. 8639 (SPIE, Bellingham, WA 2013), 86390C.

30. A. Kern, **S. Paul**, D. Wahl, A. Hein, R. Rösch, W. Schwarz, R. Michalzik, "6 Gbit/s full-duplex multimode fiber link with monolithic VCSEL-PIN transceiver chips," in 37th European Conference and Exhibition on Optical Communication (ECOC), Geneva, 2011, pp. 1–3

31. A. Kern, D. Wahl, **S. Paul**, M. T. Haidar, R. Blood, W. Schwarz, R. Michalzik, "7 Gbit/s data transmission over 500 m multimode fiber with monolithically integrated bidirectional VCSEL-based transceiver chips," in CLEO: 2011 - Laser Science to Photonic Applications, Baltimore, MD, 2011, pp. 1–2.

32. A. Kern, D. Wahl, **S. Paul**, M. Haidar, R. Blood, W. Schwarz, and R. Michalzik, "Up to 9 Gbit/s Data Transmission with Monolithically Integrated VCSELs and PIN Photodiodes," in CLEO/Europe and EQEC 2011 Conference Digest, OSA Technical Digest (CD) (Optical Society of America, 2011), paper CB1-4.

33. M. T. Haidar, **S. Paul**, C. Gierl, S. Preu, F. Küppers, "Ultra-broadband telecom MEMS-VCSEL for frequency-tunable terahertz generation with photomixers," in Infrared, Millimeter, and Terahertz waves (IRMMW-THz), Tucson, Arizona, USA, 2014.

Book

1. Spieker, C., Haas, O., Golde, K., Gierl, C., **Paul, S.** (2013). Aufgaben zur Elektrotechnik 2. Wechselströme, Drehstrom, Leitungen, Anwendungen der Fourier-, der Laplace -und der Z-Transformation. Berlin, Boston: Oldenbourg Wissenschaftsverlag.

Supervised Theses

Bachelor-thesis (D-2013/0815)

Fabrication and Characterization of a MEMS-Based Wavelength Tunable Fiber Ring Laser (German: Herstellung und Charakterisierung eines MEMS-basierten,Wellenlängen-abstimmbaren Faserringlasers) by Niels Heermeier (grade: 1.0)

Master-Thesis (2262-M)

Fabrication and Characterization of a MEMS-VCSEL for Optical High-Speed Communication (German: Herstellung und Charakterisierung eines MEMS-VCSEL für optische Hochgeschwindigkeitskommunikation) by Niels Heermeier (grade: 1.0)

Curriculum Vitae

Personal Information

Name:	Sujoy Paul
Date of birth:	01. January 1985
Place of birth:	Chittagong, Bangladesh

Eduaction

12/2011 – 06/2017	Ph.D. candidate in Electrical Engineering Institute for Microwave Engineering and Photonics (IMP) Technische Universität (TU) Darmstadt, Germany
03/2009 – 08/2011	M.Sc. in Communications Technology (Microelectronics major) Ulm University, Germany
04/2002 – 01/2016	B.Sc. in Electrical and Electronic Engineering American International University-Bangladesh, Bangladesh
02/1999 – 08/2001	Higher Secondary Certificate Chittagong College, Bangladesh
02/1999 – 08/2001	Secondary School Certificate Chittagong Govt. High School, Bangladesh

Employment

08/2017 – till now	Laser Chip Design Engineer (R & D) II-VI Laser Enterprise, Zürich, Switzerland
07/2014 – 06/2017	Scientific Staff IMP, TU Darmstadt, Germany
04/2010 – 11/2011	Research Assistant Institute of Optoelectronics, Ulm University, Germany
03/2006 – 02/2009	Junior Lecturer American International University Bangladesh

Scholarships and Awards

10/2015	Best paper award in 20th Micropoptics conference Fukuoka, Japan
01/2017	Travel grant to SPIE Photonics West San Francisco, California, United States
01/2006	Magna Cume Laude American International University Bangladesh
07/1999	11th position in combined merit list in Secondary School Certificate examination